2014

Los Alamos Space Weather Summer School Research Reports

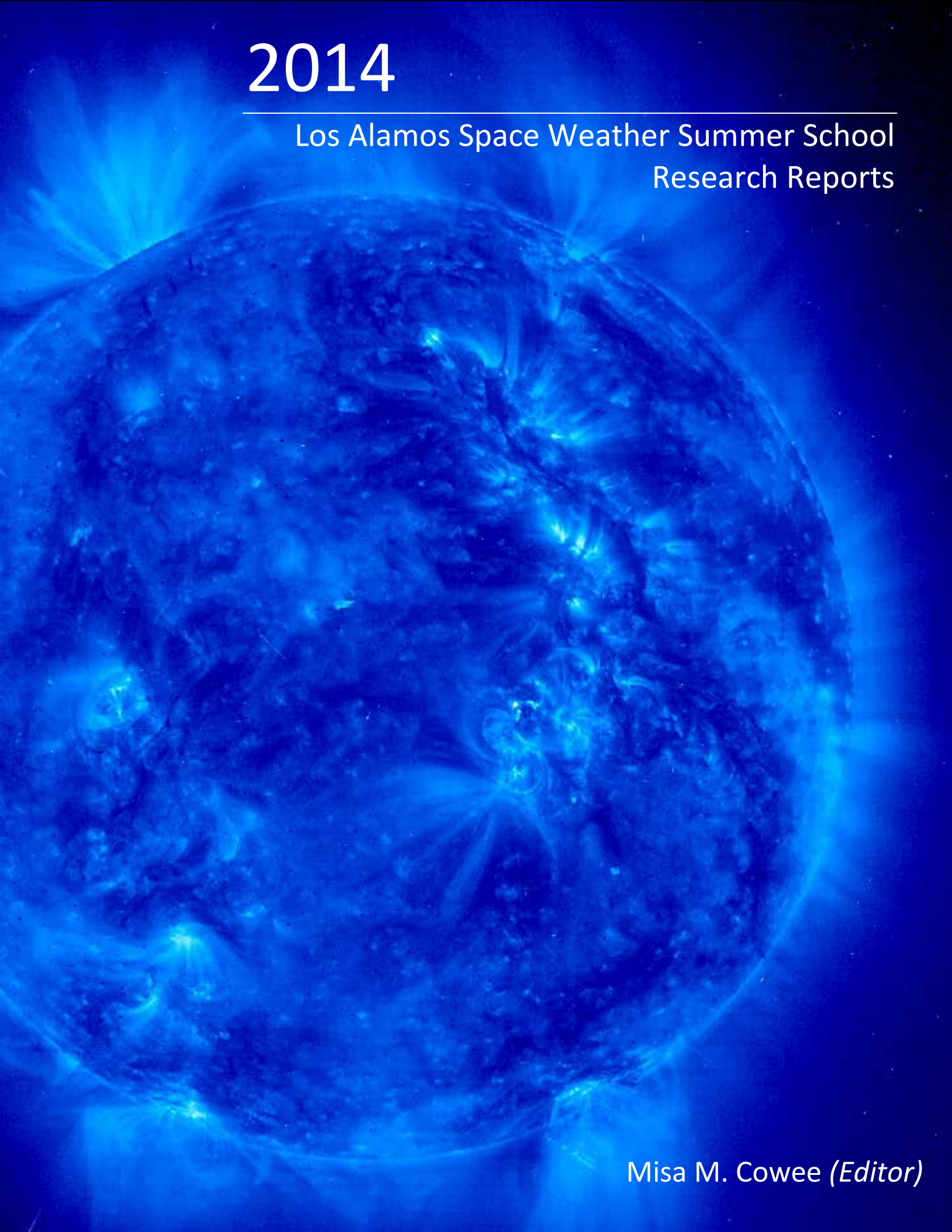

Misa M. Cowee *(Editor)*

Cover image: SOHO EIT image (sohowww.nascom.nasa.gov)

2014

Los Alamos Space Weather Summer School
Research Reports

Preface

The fourth Los Alamos Space Weather Summer School was held June 2nd – July 25th, 2014, at Los Alamos National Laboratory (LANL). With renewed support from the Institute of Geophysics, Planetary Physics, and Signatures (IGPPS) and additional support from Laboratory Directed Research and Development (LDRD), the National Aeronautics and Space Administration (NASA), the Defense Threat Reduction Agency (DTRA), and the Department of Energy (DOE) Office of Science, we hosted a new class of twelve students from various U.S. and foreign research institutions. The summer school curriculum includes a series of structured lectures as well as mentored research and practicum opportunities. Lecture topics including general and specialized topics in the field of space weather were given by a number of researchers affiliated with LANL.

Students were given the opportunity to engage in research projects through a mentored practicum experience. Each student works with one or more LANL-affiliated mentors to execute a collaborative research project, typically linked with a larger on-going research effort at LANL and/or the student's PhD thesis research. This model provides a valuable learning experience for the student while developing the opportunity for future collaboration.

This report includes a summary of the research efforts fostered and facilitated by the Space Weather Summer School. These reports should be viewed as work-in-progress as the short session typically only offers sufficient time for preliminary results. At the close of the summer school session, students present a summary of their research efforts, and a panel honors the best presenter with an all-expenses-paid trip to a major conference to present their work. This year the winner was Ryan McGranaghan with "High-Latitude Conductivity Modeling and Important to the Magnetosphere-Ionosphere-Thermosphere System". Congratulations!

It has been a pleasure for me to take over the organization of the Los Alamos Space Weather Summer School this year. I am very proud of the work done by the students, mentors and lecturers—your dedicated effort and professionalism are key to a successful program. I am grateful for all the administrative and logistical help I have received in organizing the program, and to the previous director, Josef Koller, for assisting me in the transition.

Los Alamos, NM
December 2014

Dr. Misa Cowee
Summer School Director

2014

Los Alamos Space Weather Summer School
Research Reports

New students

Ryan Coder	*Georgia Institute of Technology*
Sebastian De Pascuale	*University of Iowa*
Wade Duvall	*Virginia Polytechnic Institute and State University*
John Haiducek	*University of Michigan*
William Hoey	*University of Texas at Austin*
Ryan McGranaghan	*University of Colorado Boulder*
Bo "Ivy" Peng	*KTH Royal Institute of Technology, Sweden*
Shreedevi Radhakrishna	*Space Physics Laboratory, Vikram Sarabhai Space Centre; University of Mysore, India*
Padmashri Suresh	*Utah State University*
Timothy Waters	*University of Nevada, Las Vegas*
Fei Xu	*Nanjing University of Information Science and Technology, China; University of Alabama Huntsville*

Returning students

R. Scott Hughes	*University of Southern California*
Quintin Schiller	*University of Colorado at Boulder*

2014

Los Alamos Space Weather Summer School
Research Reports

Project Reports

New Students

2014

Los Alamos Space Weather Summer School Research Reports

Returning Students

2014

Los Alamos Space Weather Summer School
Research Reports

Pictures

Class of 2014 Students and Mentors
(Students indicated in bold. Left to right, back row: ***William Hoey****, Yue Chen, Joseph Borovsky, Steven Morley, Gregory Cunningham,* ***Timothy Waters****, Andrew Walker, Xiangrong Fu; middle row:* ***Fei Xu****,* ***Ryan McGranaghan****,* ***Ryan Coder****,* ***R. Scott Hughes****,* ***John Haiducek****,* ***Sebastian DePascuale****; front row: Josefina Salazar,* ***Padmashri Suresh****,* ***Hong Zhao****, Misa Cowee,* ***Ivy Peng****,* ***Shreedevi Radhakrishna****, Yiqun Yu, Vania Jordanova. Not pictured: Gian Luca Delzanno,* ***Wade Duvall****, Reiner Friedel, Peter Gary, Humberto Godinez, John Leacock, Richard Linares, David Palmer, Richard Schirato and John Steinberg.*

2014

Los Alamos Space Weather Summer School
Research Reports

Lectures

LOS ALAMOS SPACE WEATHER SUMMER SCHOOL

2014

Los Alamos Space Weather Summer School
Research Reports

Sponsors

- Institute of Geophysics, Planetary Physics, and Signatures (IGPPS)
- Laboratory Directed Research and Development (LDRD)
- National Aeronautics and Space Administration (NASA)
- Defense Threat Reduction Agency (DTRA)
- Department of Energy - Office of Science (DOE-OSC)

Contact Information

Dr. Misa Cowee
Los Alamos Space Weather Summer School
P.O. Box 1663, MS D466
Los Alamos National Lab, NM 87545

http://www.swx-school.lanl.gov/

Publication Release

LA-UR 15-20136

Improved Models for Radiometric Attitude Estimation of Agile Space Objects

Ryan D. Coder

Georgia Institute of Technology, Atlanta, GA, 30332, USA

Abstract

This work details the beginning of several innovations are introduced to ameliorate error in space object attitude estimation. Specifically, a radiometric measurement noise model is developed to define the observation uncertainty in terms of optical, environmental, and sensor parameters. This reduces biases in the space objects' posterior state distributions. Additional planned models include a correlated angular rate dynamics model, adopted to decouple the effects of inertia and body torques for agile space objects. This novel dynamics model requires the adoption of marginalized particle filters to preserve computational tractability. The software framework is outlined, and simulated results are presented to demonstrate resultant reductions in agile space object attitude estimation error.

Keywords: debris, SSA, agile SO, attitude estimation, lightcurve inversion

1. Introduction

Improvements in Space Situational Awareness (SSA) were identified by the Rumsfeld Commission Report as a top priority to protect the US and its allies as well as maintain its economic and diplomatic objectives[1]. The high level activities of SSA include the detection, tracking, characterization, and analysis of space objects (SOs), as defined in Joint Publication 3-14, "Space Operations." [2]. Space objects are typically defined as active and inactive satellites, rocket bodies, and orbital debris [3]. To fully characterize space objects, it is necessary to obtain knowledge about both SO shape and attitude, which can inform SO payload capability or mission purpose. [4] For SO in low earth orbit, shape and attitude estimation is performed extensively using radar-based methods developed in the early 1980's [5]. The shape and attitude of large SO can also be estimated from resolved imagery taken by ground based optical sensors. However, when SO are too distant to be imaged by radar facilities or too small to be adequately resolved by ground based optical sensors, the only data currently available is unresolved images. [4]

Each unresolved image can be analyzed to determine the total amount of radiant flux reflected by the SO. A typical observation campaign of several images can then be used to create a light curve, a temporally resolved sequence of radiant flux measurements over a specified bandwidth. Because the total amount of flux reflected by the SO is dependent on the SO shape and attitude, estimating either the attitude or shape of the SO is possible using the observed light curve. [6] This process is referred to as light curve inversion, and was initially developed to characterize asteroids. [7]

Past efforts to characterize asteroids have used batch estimation methods, where attitude, angular rates, moments of inertia and shape model are all simultaneously estimated. [8, 9, 10, 11] Batch estimation requires that available light curves represent the asteroid in a variety of solar phase angles and attitudes relative to the observer. Batch estimation methods can also be applied to SOs. However, real time updates of SO activities are sometimes desired and sequential filtering schemes such as unscented Kalman filters (UKF) or particle filters (PF) are necessary. [12] The measurements ingested into such filters are frequently assumed to be corrupted by time-invariant, zero mean Gaussian white noise [13] whose covariance is based on historical observation data.[14] These arbitrarily selected covariances introduce unnecessary biases in the posterior SO state distributions, and previous work concluded that more accurate measurement noise models could alleviate discrepancies between observational and simulated data.

Email address: rcoder@gatech.edu (Ryan D. Coder)

[15] Recent work by the author can be leveraged to calculate photon counts from the SO and environment, which can be summed to determine contributions to the overall measurement noise. Therefore, the contribution of this work is to define a measurement noise model, based on SO and environmental parameters, which reduces these SO state distribution biases.

The first application of light curve inversion to SO attitude estimation, using a sequential filter, was performed by Hall et al. in 2005. [6] While the light curve inversion process is similar, there are several important differences between asteroids and man-made SOs. The first significant difference is that unlike asteroids, many SO have highly angular facets composed of several materials, each having different reflectance properties. This has led some researchers to separate the SO attitude from materials and shape properties, which are collectively referred to as the SO "shape model." [4] More recent work has proposed using multiple-model adaptive estimation to simultaneously estimate SO attitude and shape model. [16] Whether the shape model is estimated independently or simultaneously with the SO attitude, additional complexity is added in the case of non-convex shape models. In much of the asteroid literature, a host of restrictions are placed on the shape model, such as assuming a triaxial ellipsoid, [8, 17] in additional to assuming the asteroid is purely convex. [18, 19]. Due to the fact that local minima exist when inverting light curves of non-convex shapes, estimation of globally optimal non-convex shape models remain an open area of research. Consequently, the shape model of results presented in this work are also assumed to be convex.

Another difference is that the motion of SO is generally non-homogeneous compared to that of an asteroid. SO which are not actively controlled, are typically subject to many perturbative forces such as atmospheric drag, solar radiation pressure, and earth oblateness effects. [20] SO that can actively maneuver, typically referred to as "agile" SO, introduce new modeling complications. Nonzero torques, introduced by SO actuators, are difficult to discern from the normalized mass properties of the SO. Past work has assumed that SO angular rates can be modeled as process noise. [14] Aircraft tracking methods, however, have solved this problem by assuming simply that the acceleration is correlated exponentially over short periods of time. [21] In the future, this work will adopt this dynamics model model and apply it to the SO light curve inversion problem.

Unfortunately, it is known that the measurement function for SO light curve inversion is a non-linear function of attitude states. The resultant posterior distributions of SO states are potentially non-Gaussian, a situation where UKFs are inappropriate. [12] This has led to the adoption of particle filters, which do not require that the state distributions assume a Gaussian form. [14] As particle filters are computationally expensive, increasing the number of states is undesirable. Assuming that accelerations are exponentially correlated enlarges the SO attitude state space from 6 to 9 states when all 3 body axes are considered. This number of states becomes computationally infeasible for current state of the art PFs. However, "marginalized" particle filters (MPFs) have recently introduced whereby a standard Kalman Filter (KF) is utilized for linear subsets of the state space. [22] Since the angular rate dynamics are necessarily described by a linear set of equations, MPFs reduce the number of nonlinear states to 3, preserving the computational efficacy of state of the art PFs.

This work is organized as follows. A background on EO sensor noise and a radiometric model detailing the path of photons from the Sun to the EO sensor are presented in the Background section. The contribution of this work, the radiometric measurement noise model, is presented in the Methodology section, along with the light curve "simulator" necessary to generate synthetic test data. Results for the new measurement noise model along with the discussion are presented in the Results section.

2. Background

2.1. Noise Sources in EO Sensors

To develop a radiometric measurement noise model, it is important to first understand the various sources of noise in an SO image taken by a typical EO sensor. An excellent discussion on EO sensor noise sources is presented by Merline and Howell [23], and this work extracts the largest noise sources and presents them here along with a radiometric model in complementary notation. The most common sources of noise in a typical EO sensor are due both the observed scene and the sensor itself. The largest types of noise inherent in the image are Poisson or "shot" noise from the SO and background noise due to radiant sky intensity, i.e. light pollution. The largest noise contributors deriving from sensor construction and operation are dark current noise, read noise, and variance in digitization offset.

To quantify these noise sources, let the total signal of the SO in the sensor be defined in analog-to-digital units (ADU), which are commonly referred to as "counts," as shown in Eq. (1). [23]

$$S = \sum C_i - m\bar{n} - m\bar{d} \tag{1}$$

In Eq. (1), the SO signal , S, is calculated from the total counts, C_i, the number of pixels occupied by the SO, m, and the average background level, $\bar{n}$, and the digitization offset, $\bar{d}$. The subscript i is used to denote a pixel which lies in the array of pixels containing the SO, m. The digitization offset is an extremely small contributor to overall noise, such that it is neglected in the derivation presented here. Thus, to find the variance of the total, integrated signal a Taylor Series expansion is taken about the mean integrated signal, $\bar{S}$, as shown in Eq. (2). [23]

$$\sigma_S^2 = \sum_{i=1}^{m} \left(\frac{\partial S}{\partial C_i}\right)^2 \sigma_{C_i}^2 + \left(\frac{\partial S}{\partial \bar{n}}\right)^2 \sigma_{\bar{n}}^2 \tag{2}$$

It is emphasized that beginning with Eq. (2), the following equations are written in units of electrons and not ADU. So, the variance of the source signal, σ_S^2, the variance of the total signal, $\sigma_{C_i}^2$, and the variance of the background noise, $\sigma_{\bar{n}}^2$, are defined in units of electrons. Because all of the coefficients in Eq. (1) are constant, no terms higher than first order appear in Eq. (2). Additionally, the variance of the total signal and background are assumed to be uncorrelated and zero mean, therefore no covariance terms appear in Eq. (2). This Taylor series can also be equivalently rewritten as shown in Eq. (3). [23]

$$\sigma_S^2 = \sum_{i=1}^{m} \sigma_{C_i}^2 + m\sigma_{\bar{n}}^2 \tag{3}$$

In this study, the major contributors to background noise are assumed to be the shot noise from the SO and the radiant intensity of the background sky, C_S. This neglects counts from the dark current of the CCD, C_D, and read noise of the CCD, σ_r^2. Thus, the variance in the total signal in each i pixel is defined as shown in Eq. (4). [23]

$$\sigma_{C_i}^2 = (C_{i,\mathrm{SO}} + C_{i,\mathrm{S}})\, G \tag{4}$$

The shot noise and background sky noise have been converted from ADU to electrons via the CCD gain, G. The CCD gain defines the efficiency of a CCD sensor in converting electrons to ADU. The variance in the noise is defined as shown in Eq. (9). [23]

$$\sigma_{\bar{n}}^2 = \frac{1}{z^2} \sum_{j=1}^{z} \left(\sigma_{C_{j,\mathrm{S}}}^2 + \sigma_{C_{j,\circ}}^2\right) \tag{5}$$

The final new superscript, $\circ$, indicates that these counts are due to direct current (DC) bias. To quantity the signal reflected by the SO, one must also determine the average background noise and subtract it from the total signal. Because it is not possible with traditional CCDs to determine the source of individual electrons, the background noise level must be estimated. The simplest method for determining the background is to find the mean background noise from a random sample of z, "SO-free" pixels. [24] The subscript "j" is used to denote that these z pixels are a separate array from the m pixels occupied by the SO. Substituting Eqs. (4 - 9) into Eq. (3) yields a final expression for the variance in the integrated signal, as shown in Eq. (6). [23]

$$\sigma_S^2 = \sum_{i=1}^{m} \left[(C_i - C_i^{\circ})\, G\right] + \frac{m^2}{z^2} \sum_{j=1}^{z} \left[\left(C_j - C_j^{\circ}\right) G\right] \tag{6}$$

In Eq. (6), the first term is shot noise in the source integration while the second term is due to the radiant sky intensity. These terms can be simplified as shown in Eqs. (7 and 8). [23]

$$\sum_{i=1}^{m} \left[(C_i - C_i^{\circ})\, G\right] \simeq q_{\mathrm{SO}} t + m\left(q_{p,\mathrm{sky}}\right) \tag{7}$$

$$\sum_{j=1}^{z} \left[\left(C_j - C_j^{\circ}\right) G\right] \simeq z\left(q_{p,\mathrm{sky}}\right) \tag{8}$$

In Eqs. (7 - 8), q_{SO} is the photon flux reflected by the SO and $q_{p,\mathrm{sky}}$ is the photon flux per pixel from the background sky irradiance, both of which will be defined shortly. Additionally, t is the integration time, also called the exposure time, of the observation. The arrival process of photons incident on the CCD plane can be accurately modeled by a Poisson process. Since the mean and variance of a Poisson distribution are equal, the mean and variance of electrons generated in a CCD from a SO observation can be defined by Eq. (9), by combining Eqs. (7 and 8). [25]

$$\mu_{\mathrm{n}} = \sigma_{\mathrm{n}}^2 \approx q_{\mathrm{SO}} t + m \left(1 + \frac{m}{z}\right) \left[\left(q_{p,\mathrm{sky}}\right) t\right] \tag{9}$$

Eq. (9) shows that the noise present in images containing SO can be defined if one determines the photon flux due to the SO and background sky irradiance. Doing so first requires some basic radiometric definitions, which describe how photons originating from solar excitance reflect from SO through the atmosphere and optics to become incident on the EO sensor focal plane.

2.2. Radiometric Model

By convention, SO brightness is quantified using the apparent visual magnitude system, first developed by early astronomers. The system is unitless, logarithmic, and references the brightness of Vega as the scale's zero point. The resulting SO signature represented in the apparent visual magnitude system, $m_{v,\mathrm{SO}}$, is found using Eq. (10).[26]

$$m_{v,\mathrm{SO}} = m_{v,\odot} - 2.5 \log_{10} \left(M_{\mathrm{SO}}\right) \tag{10}$$

Please note that unless otherwise stated, this radiometric model uses standard SI units. The visual magnitude of the Sun is typically given as -26.73 and M_{SO} is the total radiant excitance of the SO, which is given by Eq. (11).

$$M_{\mathrm{SO}} = \frac{1}{R^2} \int_{\lambda_{\mathrm{LL}}}^{\lambda_{\mathrm{UL}}} M_{\oplus}\left(\lambda\right) F_r \left(\theta_I^B, \hat{s}, \hat{R}, \lambda\right) \mathrm{d}\lambda \tag{11}$$

In this equation, R is the distance from the SO to the observer, $M_{\oplus}\left(\lambda\right)$ is the spectral excitance of the Sun at the Earth integrated over wavelength λ, and F_r is the reflectance function from the SO towards the observer, from direction $\hat{\mathbf{s}}$, the unit vector from the Sun to the SO. The rotation from the inertial frame to the body frame of the SO necessary to calculate these unit vectors is denoted by θ_I^B. The spectral excitance of the Sun can be modeled using a black-body radiator assumption. [26]

$$M_{\odot}\left(\lambda\right) \simeq \frac{2\pi h c^2}{\lambda^5 \left[\exp\left(\frac{hc}{k\lambda T}\right) - 1\right]} \tag{12}$$

The constants h, c, and κ are Planck's constant, the speed of light, and Boltzman's constant respectively. The wavelength, λ, of interest is user defined and logically should include the bandwidth of EO sensor sensitivity. This excitance then travels to Earth, having been diminished by the distance between the two bodies, such that the solar excitance at Earth is given by Eq. (13). [26]

$$M_{\oplus}\left(\lambda\right) = \frac{r_{\odot}^2}{\left(1\ \mathrm{AU}\right)^2} M_{\odot}\left(\lambda\right) \tag{13}$$

The solar excitance at Earth is then partially reflected depending on the size, shape, and materials that compose the SO under observation. To construct simulated light curves, a bi-directional reflectance function (BRDF), F_r, must be selected. Previous work has examined the Blinn-Phong [27], Cook-Torrance [28], He-Torrance, [29], Ward [30], and Lafortune [31] BRDFs to determine how closely these BRDFs represent real materials. [32, 33] It was determined that He-Torrance and Cook-Torrance BRDFs were most representative of actual materials. This fact, combined with the readily available equations annotated by Holzinger, [14] led to the adoption of the Cook-Torrance BRDF for this work. Once the total flux of the SO had been calculated, the photon flux density above the Earth's atmosphere, Φ_{SO}, is given by Eq. (14).

$$\Phi_{\mathrm{SO}} = \frac{M_{\mathrm{SO}} \lambda}{hc} \times 10^{-0.4 m_{\odot}} \tag{14}$$

In Eq. (14), λ is a weighted average value and not a vector representing a spectral response. Therefore, a weighted average of $\lambda = 625$ nm is used, and the quantities h and c are Planck's constant and the speed of light respectively. This yields the photon flux density, Φ_{SO}, in photons/s/m^2. The next step is to model the light gathering capabilities of a proposed telescope system. For a ground-based sensing application, the photon flux captured by the optical system, q_{SO}, measured in e^-/s, is given by Eq. (15). [34]

$$q_{\text{SO}} = \Phi_{\text{SO}} \tau_{\text{atm}} \tau_{\text{opt}} \left(\frac{\pi D^2}{4} \right) \text{QE} \tag{15}$$

In Eq. (15), the aperture diameter of the telescope is D, while τ_{atm} and τ_{opt} are the transmittance of the atmosphere and optics assembly respectively. The quantum efficiency of the CCD is defined as QE. These two transmittances and the QE have physical different values for different wavelengths of light. In lieu of more detailed modeling, these three variables are defined to have values ranging from $\tau \in (0, 1]$ and $\text{QE} \in (0, 1]$. If higher fidelity models of these values are desired, the convolution of any combination of these three values could be utilized.

To accurately characterize noise due to background light, the local background radiant intensity, I_{sky}, whose major sources are moonlight and local light pollution, must be determined. In relatively light polluted areas, it is suggested that a sky sensor is utilized to directly measure this quantity. Otherwise, the radiant identity varies from $I_{\text{sky}} \in [15, 22]$ for urban to rural skies. Because I_{sky} is measured in units of m_v/arcsec^2, conversion to radiometric units is necessary. The total photon radiance at the telescope aperture due to background sky pollution, L_{sky}, in photons$/$s$/$m$^2/$sr, is given by Eq. (16). [34]

$$L_{\text{sky}} = \Phi_0 10^{-0.4 I_{\text{sky}}} \left(\frac{180}{\pi} \right)^2 3600^2 \tag{16}$$

One can now calculate the total incidence on the focal plane from the radiance at the telescope aperture the "camera equation" is used as defined by Eq. (17). [26]

$$E_{\text{sky}} = \frac{L_{\text{sky}}}{g} \tag{17}$$

Here, g defines the capability of the system to convert radiance from the aperture to the sensor focal plane, and has been defined for a singlet lens, valid for all focal lengths, as shown in Eq. (18). [26]

$$g = \frac{1 + 4 (ND)^2}{\tau_{\text{opt}} \pi} \tag{18}$$

In Eq. (18), the variable N defines the focal ratio of the optical system. It is very typical for SSA telescopes to utilize Cassegrainian-type optics. Thus, an additional term indicating the loss of photons due to the obstruction created by the secondary mirror and supporting structure, τ_s, is introduced. [26]

$$\tau_{\text{opt,c}} = \tau_{\text{opt}} \tau_s \tag{19}$$

A final expression for the photon flux per pixel resulting from background radiant intensity, $q_{p,\text{sky}}$, is expressed in e^-/s/pixel as shown in Eq. (20).

$$q_{p,\text{sky}} = \frac{L_{\text{sky}} \tau_{\text{opt}} \tau_s \pi \, (\text{QE}) \, p^2}{1 + 4N^2} \tag{20}$$

In Eq. (20), the EO sensor is assumed to have square pixels. For non-square pixels, p^2 can be replaced by the appropriate unit of area. The radiometric model developed defines the photon flux of SOs, in Eq. (15), and the background sky brightness, in Eq. (20), as a function of various environmental variables and SSA asset design parameters. With these two quantities defined, it is now possible to discuss how these quantities relate to the ability of an SSA asset, such as a Raven-class telescope, to successfully detect and track SOs.

3. Methodology

3.1. Data Flow

The emphasis of this work is to present novel models for reducing systematic error present in current attitude estimation algorithms when applied to agile SO. To demonstrate the ability of these novel methods to accomplish

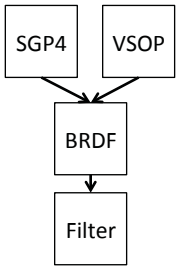

Figure 1: Lightcurve Simulator Flowchart

this goal, the simulated data must match observational data as closely as possible. Accordingly, the development of a physics based "light curve simulator" is presented in Fig. 1.

The first component of this simulator is the Simplified General Perturbations Propagator (SGP4). [35] This software calculates the position and velocity of actual SO by propagating the information from a two line element (TLE) file. The next piece of software critical to the simulator is the 1987 implementation of Variations Séculaires des Orbites Planétaires (VSOP87). [36] This enables the position of the Sun to be calculated with less than 1" error until 6000 A.D. The geometry necessary to define the reflectance of light can be defined using the the position of the Sun, observer, and SO. This geometry is used in the final part of the simulator, a bidirectional reflectance distribution function (BRDF) model. This particular work utilizes the Cook-Torrance BRDF model to calculate the total radiant flux of actual SO at various attitudes and positions in their orbit.

3.2. Dynamics Model

This work presents a simplified 2-DOF model, where only the attitude and attitude rate about the z-axis is considered. This is done only to maintain the computational efficacy of the code, as expansion to a full 6-DOF model mechanically is the same but simply takes longer run time. Accordingly, the continuous system time dynamics are given by Eq. (21) and Eq. (22), where the process noise $\mathbf{w}(t)$ is assumed to be additive, zero mean Gaussian white noise.

$$\dot{\mathbf{x}}(t) = \mathbf{F}\mathbf{x}(t) + \mathbf{G}\mathbf{w} \tag{21}$$

$$\mathbf{F} = \begin{bmatrix} 0 & 1 \\ 0 & 0 \end{bmatrix}, \mathbf{G} = \begin{bmatrix} 0 \\ 1 \end{bmatrix} \tag{22}$$

While the state appears linearly in the dynamics equations, the state appears non-linearly in the measurement function as defined by Eq. (24). As described in Eq. (24), this work will utilize the photon flux incident on the CCD for the measurements. This stands in contract to much of the literature in the field, which uses visual magnitudes. Inherently, there is no problem with using visual magnitudes, unless they are also used to specify $\mathbf{v}_k$ as time-invariant, zero mean Gaussian white noise. Unfortunately, this is typically done in the literature and yields inconsistent results for the measurement noise. Inspection of Eq. (10) reveals the visual magnitudes use a logarithmic scale such specifying $\mathbf{v}_k = 0.3$, for example, means that the noise present in the measurement is much greater for brighter objects than dimmer objects. It is possible to convert a visual magnitude noise to a noise specified in a flux rate if the flux of a 0th magnitude object is used, however, it is unclear in the literature if this is performed by the authors.

$$\mathbf{y}_k = \mathbf{H}_k\left(\mathbf{x}_k\right) + \mathbf{v}_k \tag{23}$$

$$\mathbf{y}_k = q_{\mathrm{SO}}\left(\theta_I^B(t_k), \hat{s}(t_k), \hat{R}(t_k), D, \tau, \mathrm{QE}\right) + \mathbf{v}_k \tag{24}$$

The contribution of this paper is developing a radiometric measurement function that captures the noise present in an image as a function of optical and environmental parameters. In Section 2, the mean and variance of the combination

of shot and background noise was developed. Therefore, one can define a time dependent zero mean Gaussian white noise as defined byEq. (25).

$$\mathbf{v}_k \sim \mathcal{N}\left(0, \sqrt{q_{\mathrm{SO}} t + m\left(1 + \frac{m}{z}\right)\left[\left(q_{p,\mathrm{sky}}\right) t\right]}\right) \tag{25}$$

4. Simulation Results

An unscented kalman filter is implemented to test the incorporation of the proposed, improved models. The results presented here are for "Test Case 1" which utilizes traditional additive time-invariant Gaussian white noise, as well as "Test Case 2" which incorporates the novel radiometric measurement noise model. These results are obtained from a TLE for the Galaxy 15 satellite on June 6th, 2014 at 10:19:21 UTC along with the shape model parameters presented in Table 1 . Fig. 2 shows the measurements of the Galaxy 15 satellite over the observation period, and

Table 1: Assumed Shape Model Parameters

Facet	A (m)	ξ	a	m
+X	2	0.5	0.1	0.3
+Y	2	0.5	0.2	0.3
+Z	2	0.5	0.3	0.3
-X	2	0.5	0.4	0.3
-Y	2	0.5	0.5	0.3
-Z	2	0.5	0.6	0.3

how the brightness of the SO changes with attitude. The green circles also indicate the exact measurements which are ingested in the measurement algorithm. The components of the novel measurement noise model are also illustrated. As expected, the shot noise varies proportionally to the total SO signature, while the background light pollution noise contribution remains constant.

Fig. 3 illustrates the results for the UKF incorporating the measurement noise model, where the dots denote the state estimate and the dashed lines indicate the 3σ bounds. Within one minute of observation, the attitude estimate of the SO converges to the actual attitude. It is found, as discussed previously, that the state distributions sometimes become non-Gaussian. In these cases, the UKF diverges as it is suitable only for Gaussian distributions. Therefore, future work will utilize the new measurement noise model with a PF. To quantify the uncertainty of the filtering

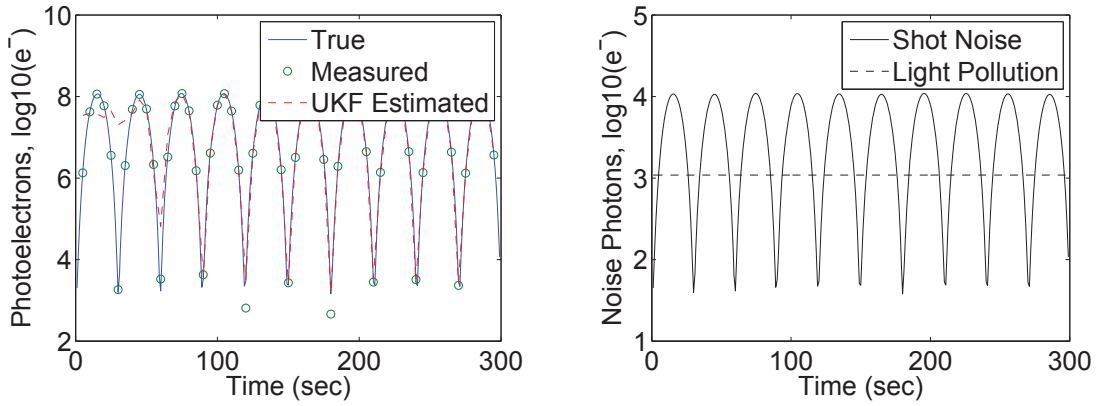

(a) True, Measured, and Estimated Signature

(b) Measurement Noise Components

Figure 2: Measurement Noise Model

algorithm when the true state is known, the root-mean-square-deviaiton (RMSD) is calculated and averaged for many

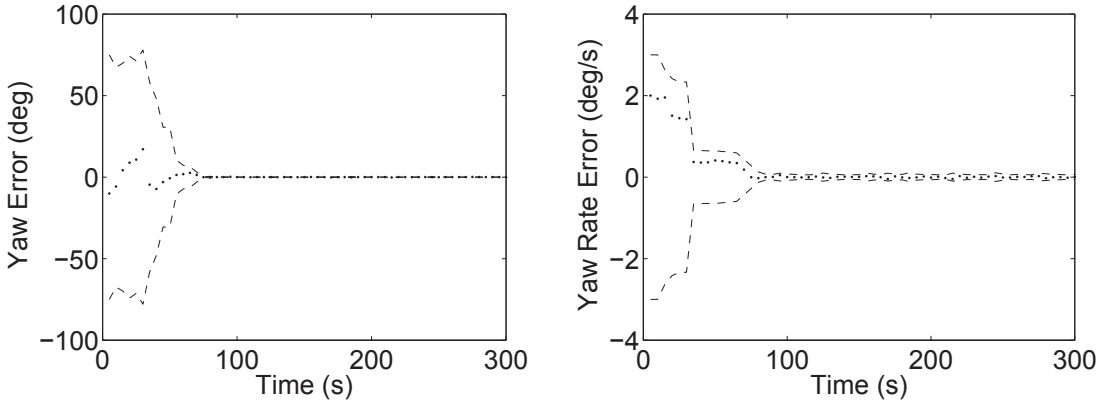

(a) Estimated Yaw Angle (b) Estimated Yaw Rate

Figure 3: Augmented UKF with Measurement Noise Model

runs of each algorithm. Table 2, computed for 50 runs of the UKF, shows the mean of each posterior distribution for the state of Test Case 2. It is important to note that a smaller RMSD does not necessarily indicate a better estimation algorithm. It could be the case that either the process noise $\mathbf{w}$ or measurement noise $\mathbf{v}_k$ did not adequately capture the true uncertainty of the problem. In this case, the analyst is lead to believe they know the SO state with a greater degree of certainty than is really the case.

Table 2: RMSD of UKF state estimation

	Test Case 1	Test Case 2
Yaw Angle Error (deg)	4.68	2.16
Yaw Rate Error (deg/s)	0.88	1.68

5. Conclusion

Physics based models can be utilized to remove biases inherent in traditional measurement noise models. It is anticipated that the implementation of a correlated angular rate dynamics model, and requisite marginalized particle filters, will enable the effect of inertial torques to be decoupled from the effects of actuator torques on SO angular acceleration. These three contributions will enhance the quality of information gleaned from scarce observation assets and further improve the state estimation of agile SO. By improving the quality of SSA, this work directly supports the U.S. responsibility to promote the peaceful use of space and support its domestic, economic, diplomatic and national security objectives.

References

[1] D. H. Rumsfeld, Commission to assess united states national security space management and organization, Tech. rep., Committee on Armed Services of the U.S. House of Representatives (January 2001).

[2] Joint Chiefs of Staff, Space operations, Tech. Rep. JP 3-14, United States Department of Defense (January 2009).

[3] G. Stokes, C. Von Braun, R. Sridharan, D. Harrison, J. Sharma, The space-based visible program, Lincoln Laboratory Journal 11 (2) (1998) 205–238. doi:10.2514/6.2000-5334.
URL http://dx.doi.org/10.2514/6.2000-5334

[4] D. Hall, B. Calef, K. Knox, M. Bolden, P. Kervin, Separating attitude and shape effects for non-resolved objects, in: The 2007 AMOS Technical Conference Proceedings, 2007, pp. 464–475.

[5] J. L. Walker, Range-doppler imaging of rotating objects, Aerospace and Electronic Systems, IEEE Transactions on (1) (1980) 23–52.

[6] D. Hall, J. Africano, P. Kervin, B. Birge, Non-imaging attitude and shape determination, in: Advanced Maui Optical and Space Surveillance Technologies Conference, 2005.

[7] H. Russell, On the light variations of asteroids and satellites, The Astrophysical Journal 24 (1906) 1–18.

[8] P. Magnusson, Distribution of spin axes and senses of rotation for 20 large asteroids, Icarus 68 (1) (1986) 1 – 39. doi:DOI: 10.1016/0019-1035(86)90072-2.
URL http://www.sciencedirect.com/science/article/B6WGF-47314T5-1BC/2/6685fef3fcbf63c7988bcf0b40280806

[9] J. Torppa, M. Kaasalainen, T. Michalowski, T. Kwiatkowski, A. Kryszczynska, P. Denchey, R. Kowalski, Shapes and rotational properties of thirty asteroids from photometric data, Icarus 164 (1) (2003) 364–383. doi:doi:10.1016/S0019-1035(03)00146-5.

[10] M. Kaasalainen, J. Torppa, Optimization methods for asteroid lightcurve inversion: I. shape determination, Icarus 153 (1) (2001) 24 – 36. doi:DOI: 10.1006/icar.2001.6673.
URL http://www.sciencedirect.com/science/article/B6WGF-458NDJD-16/2/31e30b320da3df56b6a26c8e32d4e014

[11] M. Kaasalainen, J. Torppa, K. Muinonen, Optimization methods for asteroid lightcurve inversion: Ii. the complete inverse problem, Icarus 153 (1) (2001) 37 – 51. doi:DOI: 10.1006/icar.2001.6674.
URL http://www.sciencedirect.com/science/article/B6WGF-458NDJD-17/2/b80412ec638b149747d7f9f08dc9de4e

[12] R. Van Der Merwe, A. Doucet, N. De Freitas, E. Wan, The unscented particle filter, in: NIPS, 2000, pp. 584–590.

[13] D. Simon, Optimal state estimation: Kalman, H infinity, and nonlinear approaches, Wiley, 2006. doi:10.1002/0470045345.
URL http://dx.doi.org/10.1002/0470045345

[14] M. J. Holzinger, K. T. Alfriend, C. J. Wetterer, K. Luu, C. Sabol, K. Hamada, A. Harms, Photometric attitude estimation for agile space objects with shape uncertainty, Journal of Guidance, Control, and Dynamics In Press.

[15] C. J. Wetterer, M. K. Jah, Attitude determination from light curves, Journal of guidance, control, and dynamics 32 (5) (2009) 1648–1651.

[16] R. Linares, J. L. Crassidis, M. K. Jah, H. Kim, Astrometric and photometric data fusion for resident space object orbit, attitude, and shape determination via multiple-model adaptive estimation, in: AIAA Guidance, Navigation, and Control Conference, 2010, aIAA 2010-8341.

[17] A. Cellino, V. Zappala, P. Farinella, Asteroid shapes and lightcurve morphology, Icarus 78 (2) (1989) 298–310.

[18] M. Kaasalainen, L. Lamberg, K. Lumme, E. Bowell, Interpretation of lightcurves of atmosphereless bodies. I - General theory and new inversion schemes, Astronomy and Astrophysics 259 (1992) 318–332.

[19] M. Kaasalainen, L. Lamberg, K. Lumme, Interpretation of lightcurves of atmosphereless bodies. II - Practical aspects of inversion, Astronomy and Astrophysics 259 (1992) 333–340.

[20] J. E. Prussing, B. A. Conway, J. E. Prussing, Orbital mechanics, Vol. 57, Oxford University Press New York, 1993.

[21] R. A. Singer, Estimating optimal tracking filter performance for manned maneuvering targets, Aerospace and Electronic Systems, IEEE Transactions on (4) (1970) 473–483.

[22] T. Schon, F. Gustafsson, P.-J. Nordlund, Marginalized particle filters for mixed linear/nonlinear state-space models, Signal Processing, IEEE Transactions on 53 (7) (2005) 2279–2289.

[23] W. Merline, S. B. Howell, A realistic model for point-sources imaged on array detectors: The model and initial results, Experimental Astronomy 6 (1-2) (1995) 163–210. doi:10.1007/BF00421131.
URL http://dx.doi.org/10.1007/BF00421131

[24] T. Schildknecht, Optical astrometry of fast moving objects using ccd detectors, in: Geodätisch-geophysikalische Arbeiten in der Schweiz, Vol. 49, 1994.

[25] W. W. Hines, D. C. Montgomery, C. M. Borror, D. M. Goldsman, Probability and statistics in engineering, Wiley, 2008.

[26] E. Budding, O. Demircan, Introduction to Astronomical Photometry, 2nd Edition, Cambridge Observing Handbooks for Research Astronomers, Cambridge University Press, 2007. doi:10.1017/CBO9780511536175.
URL http://dx.doi.org/10.1017/CBO9780511536175

[27] J. F. Blinn, Models of light reflection for computer synthesized pictures, SIGGRAPH Comput. Graph. 11 (1977) 192–198. doi:http://doi.acm.org/10.1145/965141.563893.
URL http://doi.acm.org/10.1145/965141.563893

[28] R. L. Cook, K. E. Torrance, A reflectance model for computer graphics, Computer Graphics 15 (3) (1981) 307–316.

[29] X. D. He, K. E. Torrance, F. X. Sillion, D. P. Greenberg, A comprehensive physical model for light reflection, SIGGRAPH Comput. Graph. 25 (1991) 175–186. doi:http://doi.acm.org/10.1145/127719.122738.
URL http://doi.acm.org/10.1145/127719.122738

[30] G. J. Ward, Measuring and modeling anisotropic reflection, SIGGRAPH Comput. Graph. 26 (1992) 265–272. doi:http://doi.acm.org/10.1145/142920.134078.
URL http://doi.acm.org/10.1145/142920.134078

[31] E. P. F. Lafortune, S. Foo, K. E. Torrance, D. P. Greenberg, Non-linear approximation of reflectance functions, in: Proceedings of the 24th annual conference on Computer graphics and interactive techniques, SIGGRAPH '97, ACM Press/Addison-Wesley Publishing Co., New

York, NY, USA, 1997, pp. 117–126. doi:http://dx.doi.org/10.1145/258734.258801.
URL http://dx.doi.org/10.1145/258734.258801
[32] S. H. Westin, H. Li, K. E. Torrance, A comparison of four brdf models, in: Eurographics Symposium on Rendering, 2004, pCG-04-2.
[33] A. Ngan, F. Durand, M. Wojciech, Experimental analysis of brdf models, in: Eurographics Symposium on Rendering, 2005.
[34] J. R. Shell, Optimizing orbital debris monitoring with optical telescopes, in: Advanced Maui Optical and Space Surveillance Technologies Conference, Space Innovation and Development Center, 2010.
[35] D. A. Vallado, P. Crawford, R. Hujsak, T. Kelso, Revisiting spacetrack report# 3, AIAA 6753 (2006) 2006.
[36] P. Bretagnon, G. Francou, Planetary theories in rectangular and spherical variables-vsop 87 solutions, Astronomy and Astrophysics 202 (1988) 309–315.

Assessment of the RAM-CPL coupled plasmaspheric density model using recent observations from the Van Allen Probes

Sebastian De Pascuale

Department of Physics & Astronomy, University of Iowa, Iowa City, IA, 52242

Vania Jordanova

Los Alamos National Laboratory, Los Alamos, NM 87545

Abstract

We simulate equatorial plasmaspheric electron densities in the inner-magnetosphere with a dynamical model (RAM-CPL) based on empirical parameters governing the source and loss processes of refilling and erosion. Pre-dawn and Post-dusk in situ measurements by the current Van Allen Probes (RBSP) mission during two geomagnetic events, from 15 - 20 January and 31 May - 5 June of 2013 respectively, provide a basis for model validation against globally opposed asymmetries in the drivers and response of the system. The twelve days of simulation captured mean density values regulated by geomagnetic activity up to the plasmapause boundary. Delayed erosion just inward of the plasmapause and decreased refilling outward of the boundary proved most challenging to model performance. To probe local density features, virtual RBSP satellites were tracked hourly through the simulated equatorial plasmasphere encountering steep gradients and low density values representative of the plasmapause. Over 80% of the virtual crossings for both events corresponded to actual RBSP observations of select criteria: either an average factor of 5 change in density within $\Delta L = 0.5$ or the outermost drop in density to a threshold value of 20 cm^{-3}. The RAM-CPL model produced plasmapause-like features to within .50 ± 0.13 R_E during January 15 - 20 and .55 ± 0.13 R_E during May 31 - June 5, 2013. We do not find, in general, any correlation between geomagnetic activity and deviation in simulated plasmapause locations from observed crossings. Other studies show that the formation of the plasmapause boundary is strongly driven by a convection electric field. The agreement between model and data presented in this paper suggests that an improved description of the electric potential governing convection could allow higher fidelity simulations at increased resolution.

Keywords: plasmaspheric erosion & refilling, convection electric field, Van Allen Probes, RBSP, EMFISIS, EFW

1. Introduction

Trapped by Earth's dipolar magnetic field and subsequently corotating with the planet, the plasmasphere constitutes an interface of cold, dense plasma ($\leq$ 20 eV, $10 - 10^4$ cm^{-3}, and primarily H^+) between the ionosphere and magnetosphere [*Lemaire and Gringuaz*, 1988]. Decades of consistent effort since its initial discovery [*Carpenter*, 1963] have shown the plasmasphere to be bounded by a plasmapause, a discontinuity in the radially decaying profile descibing equatorial densities [*Carpenter and Anderson*, 1992], whose position varies inversely with geomagnetic activity [*O'brien and Moldwin*, 2002] and inversely around dusk with magnetic local time (MLT) [*Chappell et al.*, 1970]. Furthermore, recent observations of the toroidal region demonstrate that the plasmasphere can exhibit a high degree of outer structure (e.g. plumes) whose formation depend on the time history of convective erosion from electric fields and of refilling from ionospheric outflow [*Darrouzet et al.*, 2008]. The global and local density content of this thermal plasma in the inner-magnetosphere is responsible for the collisional loss of ions and host to the plasma waves

Email addresses: sebastian-depascuale@uiowa.edu (Sebastian De Pascuale), vania@lanl.gov (Vania Jordanova)

that scatter electrons from the surrounding hot (>1 keV) ring current and radiation belts [*Lyons et al.*, 1972, *Fok et al.*, 1991 and *Jordanova et al.*, 1996].

A detailed perspective of the relationship between the plasma populations of the radiation belts, ring current, and plasmasphere is being offered by the current Van Allen Probes mission, formerly known as the Radiation Belt Storm Probes (and hereafter as RBSP A & B). The satellites are equipped with instrumentation designed to provide insight into the acceleration, transport, and loss of energetic particles in the inner-magnetosphere. At near equatorial (~10°) geostationary transfer orbits (period ~9h), the two lapping probes extend from a perigee of ~600 km to an apogee of ~5.8 R_E. Measurements of the electromagnetic environment allow direct contextualization of particle observations and associated plasma waves. The Electric Field and Waves (EFW) instrument [*Wygant et al.*, 2013] measures three-axis electric fields driving the system and the spacecraft potential that serves as a proxy of the ambient plasma density. A reliable determination of the electron number density is obtained from frequency signatures in spectral data captured by the Electric and Magnetic Field Instrument Suite and Integrated Science (EMFISIS) suite [*Kletzing et al.*, 2013]. These local in situ measurements can be compared to global models of the equatorial plasmasphere to constrain the dependence on key parameters.

Promoted by a host of specialized missions (multipoint, sounding, and imaging), the last decade of plasmaspheric research has focused on developing better understanding of the influence of geomagnetic events on the plasmasphere as a two-way coupling problem between the magnetosphere-plasmasphere and plasmasphere-ionosphere [*Ganguli et al.*, 2000]. Describing the dynamic morphology of the plasmasphere due to convective erosion progressing from the nightside is frustrated by obscure electric fields and the unknown original state of the system [*Singh et al.*, 2011]. Recent observations have introduced a variety of complex shapes attainable by the plasmapause that depend on these two factors. The recovery of the plasmasphere after an event occurs as the approach to diffusive equilibrium within magnetic flux tubes connected to the ionosphere, which receive outgoing flux on the dayside and are corotated into the nightside. Local asymmetries in these processes impact global evolution on extended timescales that are difficult to isolate with independent in situ data. Contextualizing select observations via modeling, however, can yield some insight into the history dependent behavior of the plasmasphere.

In this paper we assess the performance of equatorial plasmaspheric electron density simulations produced by RAM-CPL (cold plasma), a coupled component of the newly-developed ring current - radiation belts model, RAM-SCB [*Jordanova et al.*, 2006]. Two geomagnetic events on 15 - 20 January and 31 May - 5 June, 2013 during Van Allen Probes observations separated by a quarter sector in MLT from the pre-dawn to post-dusk regions are considered. Although the initial conditions of this study are static, the simulations are driven by an empirical description of the convection electric field chosen to reflect two distinct processes: mangetospheric dayside reconnection and subglobal current system feedback in the ionosphere. We use the K_p geomagnetic activity index to parameterize the evolution of the plasmasphere and define a plasmapause boundary to systematically contextualize actual and virtual observations. For both events, the agreement in plasmapause location for at least 80% of the encounters was reproduced to within 0.55 R_E.

The subsequent sections of this paper are organized in the following manner: we describe the RAM-CPL modeling scheme used in this study, characterize the global convection electric field driving the system, attribute simulation fidelity to observational features, and segregate model performance with a comparison of actual versus virtual plasmapause crossings. Space for displaying data is allocated conservatively; only observations from RBSP A will be used in reference against simulation intervals due to the close proximity (similarity) of the two Van Allen Probes satellites during the chosen events at the low resolution of this study (produced at the midpoint of the hour within 1hr MLT by 0.25 L bins).

2. Modeling Framework

We ran two simulations of the RAM-CPL plasmasphere in order to describe enhanced asymmetry in the convection electric field that produces erosion for in situ measurements obtained by the Van Allen Probes spacecraft (see **Figure 3**). The two-dimensional equatorial model of cold plasma density incorporates a parametric function of particle refilling due to ionosphere-magnetosphere coupling during **E** x **B** plasmaspheric evolution [*Rasmussen et al., 1992*]. Two empirically derived components, an initial condition and a time-dependent driver, are utilized to dynamically progress the simulated configuration of plasma throughout a geomagnetic event as illustrated in **Figure 1**.

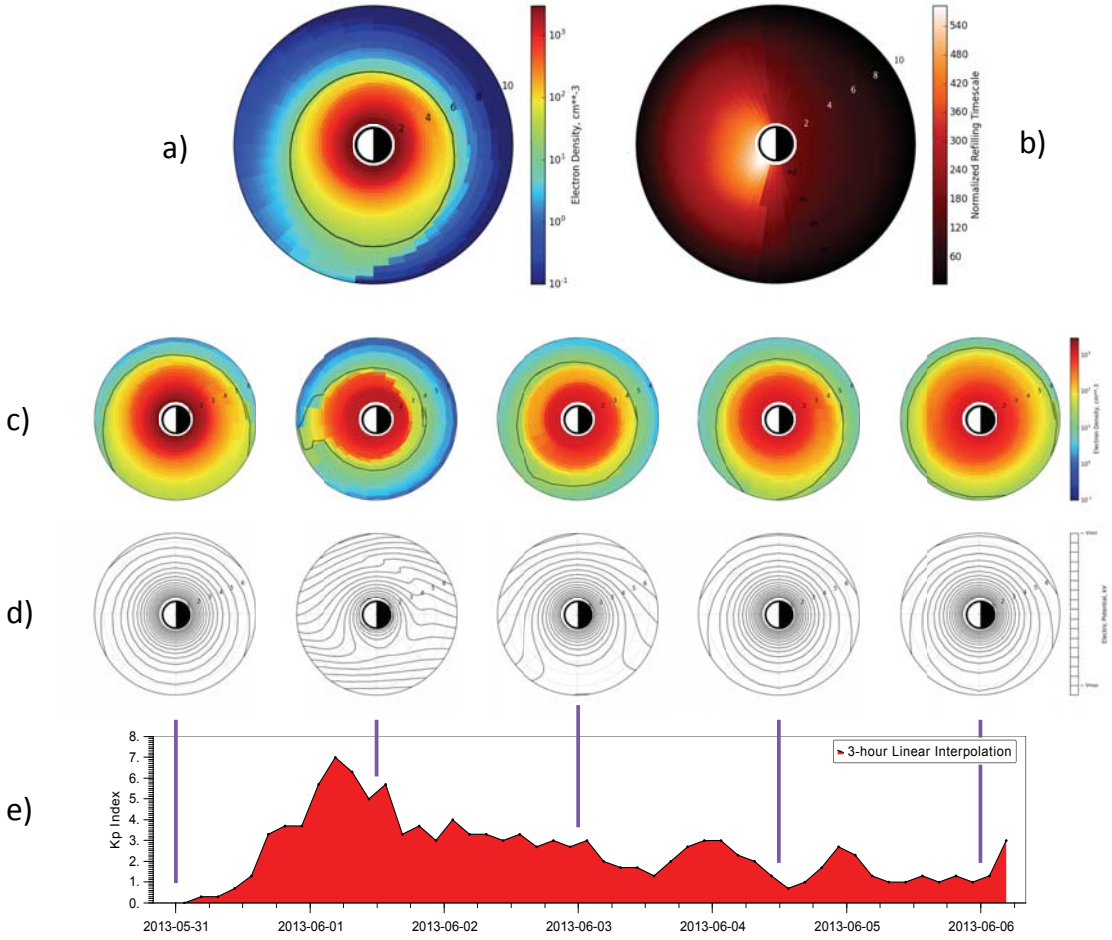

Figure 1: Overview of the two-dimensional density model of the plasmasphere (RAM-CPL) for the May 31 - June 5, 2013 simulation. Each plot is presented in the equatorial plane with the sun to the left and the earth at center. (a) RAM-CPL is initialized by an extended plasmasphere from 1.5 up to 10 R_E that is determined by refilling to saturation the system during a quiet-time interval ($K_p < 2$). (b) Empirical models of outgoing particle flux from the ionosphere yield the diurnally dependent rate of refilling, which is effective on the dayside. (c) The evolution of plasmaspheric densities driven by **E** x **B** convective motion is shown for select times up to 6.5 R_E in the range of Van Allen Probes orbits. A black line traces the 20 cm^{-3} density contour as a reference for the plasmapause. (d) In this study, convection due to geomagnetic activity is represented by a Volland-Stern and Subauroral Polarization Stream electric potential to emphasize asymmetric and enhanced flows in the night sectors. (e) The simulation is parameterized by a linear interpolation of the 3-hour K_p index.

2.1. Input Parameters

RAM-CPL accounts for the ionospheric origin of particles in the plasmasphere contained by the earth's corotating magnetic field. Outward flow along closed magnetic field lines into the refilling plasmasphere is balanced by the transport of plasma. While connected to the ionosphere, a magnetic flux tube element can change in volume and density. Convective motion, nevertheless, can separate this plasma source from the plasmasphere by venting the content of a flux tube open at the magnetopause of the magnetosphere into interplanetary space [*Rasmussen et al.*, 1992]. The predominant ion population in the plasmasphere is composed of H^+, which is balanced by an equal number of electrons assuming the quasi-neutrality of the plasma. This species is produced diurnally on the dayside ionosphere through the charge exchange reaction with oxygen, contributing to a limited upward flux of particles that sustains the plasmasphere. On the nightside, plasma freely exits downward back into the ionosphere at an equal rate unless electric fields convect plasma across magnetic field lines during geomagnetic storms [*Gordon et al.*, 1978].

A conservation equation describing the total number of ions in a flux tube is obtained by integration of the continuity equation such that along a field line the evolution of average plasma density is given by:

$$\frac{\partial \bar{n}}{\partial t} = \frac{F_N + F_S}{B_i V} - \text{transport}(L, \phi, t) \tag{1}$$

where F_N and F_S are the contribution of fluxes (positive upward) from the northern and southern ionospheres, respectively. Here, V is the volume per unit magnetic flux of a tube of plasma and B_i is the magnetic field at the conjugate ionosphere. It can be shown that under nominal conditions while refilling is underway, the average density $\bar{n}$ along a magnetic field line can be directly compared with measurements of the density n_{eq} taken near the equatorial plane of the magnetosphere, (i.e. $\bar{n} \approx n_{eq}$) [*Rasmussen et al.*, 1992].

The source term of plasmaspheric density evolution then readily yields a timescale τ_s for refilling, assuming that the approach to equilibrium depends on the variation from hemispheric saturation levels, n_N and n_S, according to:

$$\frac{F_N + F_S}{B_i V} = \sum_{N,S} \frac{n_s(L, \phi) - \bar{n}(L, \phi)}{\tau_s}. \tag{2}$$

Under these approximations, at the time when a flux tube is completely empty ($\bar{n} = 0$) the upward ionospheric fluxes are maximum such that the refilling timescale can be written as:

$$\tau_s = \frac{n_s(L, \phi) B_i V}{F_{ls}}. \tag{3}$$

In the RAM-CPL scheme, the limiting particle fluxes F_{ls} from the ionosphere are calculated analytically [*Richards and Torr*, 1985] and further parameterized by empirical models for neutral temperatures and densities (MSIS-86) [*Hadin*, 1987] as well as charged particle temperatures (IRI) [*Bilitza*, 1986].

Assuming a simplified model for the saturation of the plasmasphere [*Carpenter and Anderson*, 1992], which varies annually with the day of year, d, and the 13-month average sunspot number, $\bar{R}_s$, as:

$$n_{sat} = 10^{(-0.3145L + 3.9043)} + \text{variation}(d, \bar{R}_s), \tag{4}$$

we model the evolution of plasmaspheric equatorial density for each magnetic flux tube by specifying a constant refilling rate of τ_0 (**Figure 1 (b)**):

$$\frac{\partial n_{eq}}{\partial t} = \frac{n_{sat}(L) - n_{eq}(L, \phi)}{\tau_0(L, \phi)} - \text{transport}(L, \phi, t) \tag{5}$$

During geomagnetically active conditions, a time-variable convection electric field in conjunction with the corotation electric field of Earth will also change the distribution of density in the plasmasphere. The process of erosion begins on the scale of hours as a new mapping of the trajectories of magnetic flux tubes on open (closed) trajectories from the tail (Earth) to closed (open) ones such that refilling (venting) can now occur on the scale of days [*Nishida*, 1966; *Chen and Wolf*, 1972]. As a consequence, the outer boundary of the plasmasphere (the plasmapause) becomes distorted with time and can assume a variety of configurations (e.g. plumes) depending on the history of erosion and refilling. For a simple parameterization of convection, the shielded Volland-Stern potential [*Volland*, 1973; *Stern*, 1975] may be used:

$$\Phi_{VS} = -A(t) r^2 \sin(\phi) \tag{6}$$

where the coefficient A is normalized to the K_p geomagnetic activity index by [*Maynard and Chen*, 1975]:

$$A_{MC} = \frac{0.045}{\left(1 - 0.159 K_p + 0.0093 {K_p}^2\right)^3} \quad (kV/{R_E}^2) \tag{7}$$

To probe underlying asymmetries that drive convection, we consider separately the contribution of the Subauroral Polarization Stream (SAPS) phenomenon of inner-magnetosphere-ionosphere coupling [*Foster and Burke*, 2002]. SAPS arrises from feedback in a global electrical current circuit between the ring current and high-latitude ionosphere,

resulting in a radially narrow, westward flow channel for dusk-to-midnight magnetic local times (MLT) when mapped to the magnetospheric equatorial plane [*Burke et al.*, 1998; *Foster and Vo*, 2002]. An analytical model of this active-time effect is derived by *Goldstein et al.*, 2005 using average SAPS properties and is similarly dependent on K_p, where:

$$\Phi_{SAPS} = -F(r,\phi,t)G(\phi)V(t) \tag{8}$$

such that the SAPS channel location and width decrease with increasing K_p. The potential drop across the channel, however, increases with K_p, but peaks near dusk decreasing eastward across the nightside. In combination with a convection potential, such as the Volland-Stern empirical model, the SAPS effect tends to enhance duskside sunward plasma flows for high geomagnetic activity ($K_p > 4$; see **Figure 1 (d)**).

2.2. Two Event Case Study

The event intervals selected for the RAM-CPL model assessment of this study occur during Van Allen Probes observations that are separated by ~6 hours in MLT from the post-dusk to the pre-dawn sectors. During the 15 - 20 of January 2013 (RBSP apogee near 3hrs MLT), the RBSP spacecraft encountered 3 plumelike structures that were confirmed by plasmapause test-particle (PTP) simulations using a Volland-Stern and SAPS convection electric field [*Goldstein et al., 2014* (in press)]. That paper also reported a radial plasmapause agreement between actual and virtual observations of $0.40 \pm 0.05 R_E$. These results motivate a similar comparison performed by the RAM-CPL model with the new addition of global density information and the caveat of parameterizing in time solely by the K_p index. From the 31 of May through the 5 of June 2013 (RBSP apogee near 22hrs MLT), a significant increase in geomagnetic activity to a level of $K_p = 7$ produced asymmetric erosion in the plasmasphere followed by an extended period of recovery. We use these two RBSP observations (see **Figure 2**) together with a convection electric field model of the inner-magnetosphere to drive the RAM-CPL plasmaspheric density simulations and validate the limit of its applicability.

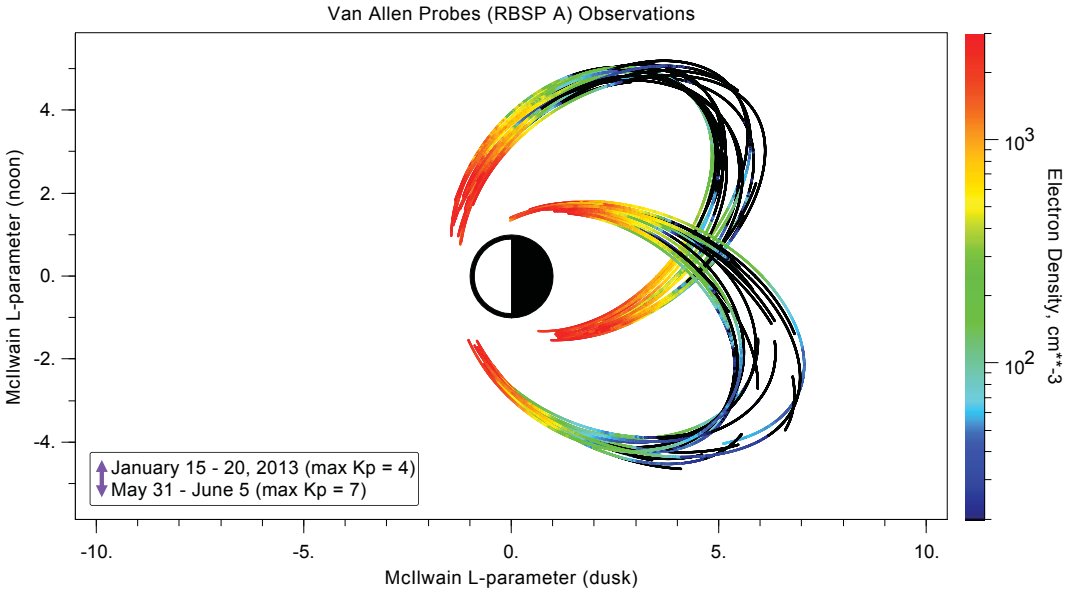

Figure 2: Observations from the RBSP A EMFISIS instrument of the local plasma electron density in logarithmic color scale during two geomagnetic events. The geostationary transfer orbit of the spacecraft can extend to nearly $L = 7$, while measurement limitations are exceeded by high densities lower than $L = 1.5$. During January 15 - 20, 2013 (upper) RBSP A was located in the pre-dawn MLT sector (around 3hrs), whereas precessing counter clockwise around Earth the later orbits of May 31 - June 5, 2013 (lower) occur in the post-dawn MLT sector (around 22hrs). On this figure, density values at or below 20 cm^{-3} are colored in black to give an indication of the plasmapause location for each orbital track through the plasmasphere.

3. Convection Electric Field Asymmetries

In this section we calculate for both observational events the corresponding component of the simulated convection electric field as measured by the RBSP EFW instrument. The sensors are comprised of four spin-plane booms 100 m across each pair and two 10 m separated spin-axis probes. To produce accurate measurements of the electric field, the EFW team utilizes a modified Geocentric Solar Ecliptic (mGSE) coordinate system such that the X mGSE component is along the spin-axis of the spacecraft and points within $\sim 37^\circ$ of the earth-sun line, while the spin-plane Y mGSE and Z mGSE components are processed separately to avoid mixing the quality of the signal between the short and long booms. If Sgse = $[S_{Xgse}, S_{Ygse}, S_{Zgse}]$ is the spin-axis unit vector in GSE coordinates and Zgse is the z-axis unit vector in that system, then:

$$\text{Ymgse} = -\frac{(\text{Sgse} \times \text{Zgse})}{\left\|\text{Sgse} \times \text{Zgse}\right\|} \tag{9}$$

and the angle α between the Ygse and Ymgse components follows as:

$$\alpha = \cos^{-1}\left(\frac{S_{Xgse}}{\sqrt{{S_{Xgse}}^2 + {S_{Ygse}}^2}}\right). \tag{10}$$

A linear fit was sufficient to capture the slow variation of this angle for the 6 day long events under study where, in terms of seconds s since the start of the simulation,:

$$\begin{array}{ll} \underline{15-20\ \text{January, 2013}} & \underline{31\ \text{May}-5\ \text{June, 2013.}} \\ \alpha = -1.89\times10^{-7}s + .13 & \alpha = -2.19\times10^{-7}s + 3.06 \end{array} \tag{11}$$

For the position of the RBSP spacecraft at an offset angle θ positive from the X GSE axis, we find that the Y mGSE equatorial model for the convection electric field in cylindrical coordinates in the GSE plane is given by:

$$E_{\text{Ymgse}} = (E_r \sin\theta + E_\theta \cos\theta)\cos\alpha \tag{12}$$

In the middle panel of **Figure 3 (b)** is displayed a comparison between the Y mGSE EFW measured electric field and that calculated from the Volland-Stern and SAPS convection model. The EFW measurement is spin-fit and eliminated of the motional electric field of the spacecraft, $E = v_{sc} \times B$, to supply an inertial frame of reference. It is observed that large deviations occur at the boundaries of an RBSP spacecraft orbit and during several intervals, such as 20 January, 2013 1800 - 2400 UT and 1 June, 2013 0800 - 1800 UT. No specific correspondence between the driving K_p index or resultant simulated densities is seen.

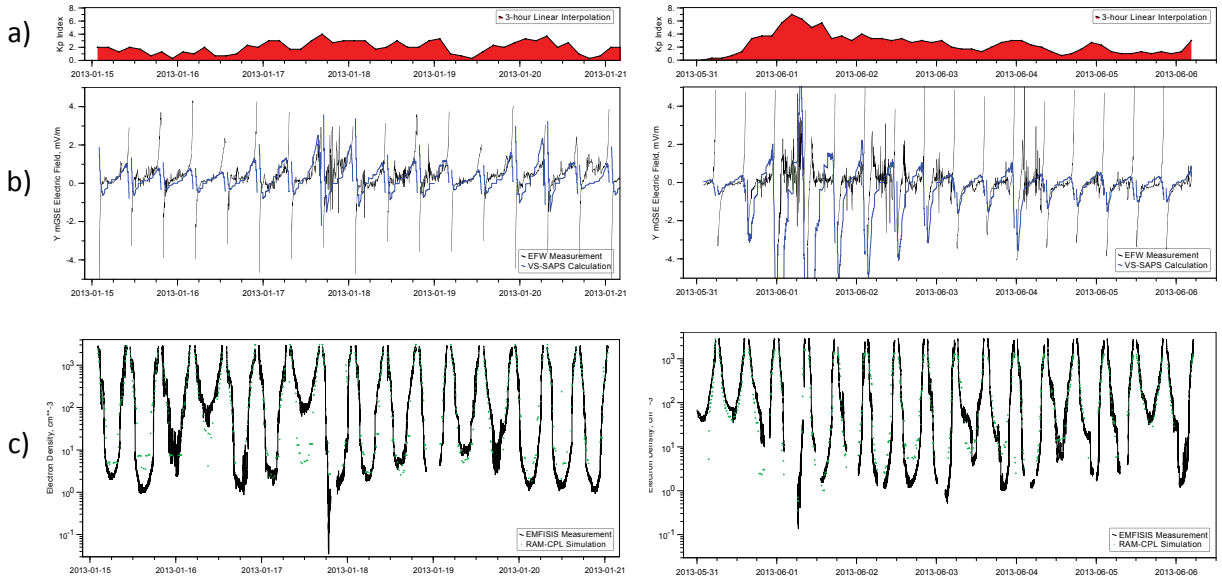

Figure 3: Virtual observations through the RAM-CPL hourly simulation of the January and June events of 2013 compared to in situ measurements by RBSP A. a) 3-hour K_p geomagnetic activity index used to parameterize in time, through linear interpolation, the Volland-Stern and SAPS convection electric field. b) Calculation of the Y mGSE component of the simulated (blue) electric field against the EFW spin-fit data as a proxy for the driver of erosion. c) EMFISIS determined electron density with simulated (green) plasmaspheric depletion and subsequent refilling. The January event exhibits a high degree of density structure due to the variability of geomagnetic activity, whereas the June event is better described by severe erosion and differential refilling.

4. Post-erosion Plasmaspheric Density Refilling

In general, the RAM-CPL plasmasphere shows a radial dependence in the agreement between actual observations and a virtual track through the hourly created simulations. The third panel of **Figure 3 (c)** seems indicates that low densities at or past the extent of the plasmasphere are difficulty to reproduce and, in particular, that variations in the K_p index parameterizing the model convection electric field do not have an exact correspondence with the behavior of the simulation. For example, on day 17 of the January event between 0600 - 1800 UT the densities are significantly underestimated during what appears to be a short reduction in geomagnetic activity. The interval is on the order of hours and two days into the simulation, too short for refilling to occur at large L and unlikely biased by the initial configuration. Rather, the plasmasphere seemingly undergoes convective transport not adequately captured by the Volland-Stern and SAPS potential in the pre-dawn MLT sector.

Alternatively, the June event illustrates asymmetric or delayed erosion of the plasmasphere in the post-dusk MLT sector. From 0600 until 1000 UT on day 3 of June, density in the plasmasphere reaches a threshold level possibly maintained by refilling, transport, or spacecraft passage through a large structure (eg. plume). RBSP A encounters a steep density gradient immediately after this feature indicative of the plasmapause. Later instances, such as the upturn in density at 1800 UT on the same day or at 2200 UT on day 4 of June, further motivate the conception that a sustained density structure remains after the severe erosion ($Kp = 7$) that marks the beginning of this event. To the extent that refilling may play a role in the formation of this feature, the RAM-CPL simulation failed to reproduce a leveling profile in the density.

The degree of merit attained by RAM-CPL is presented as the average density percent difference (normalized by the mean of the observed and simulated values) for outbound/inbound radial bins of 0.25 L in **Figure 4**. Success is deemed for cases at or below a factor of 2 (100%) difference. In the January event, the simulation matches higher densities at lower L values (< 3) far better by comparison than the June event during which a period (days 2-5) after the onset of high geomagnetic activity lower L values report greater and sustained difference. For both events, the simulation struggled most to match observations at steep density gradients. The disparity is noted by the connected dots labeling plasmapause crossings on the figures as defined in the next section. This behavior may not be surprising due to the low resolution of RAM-CPL used here and the balance between erosion and refilling at the furthest extent of the plasmasphere.

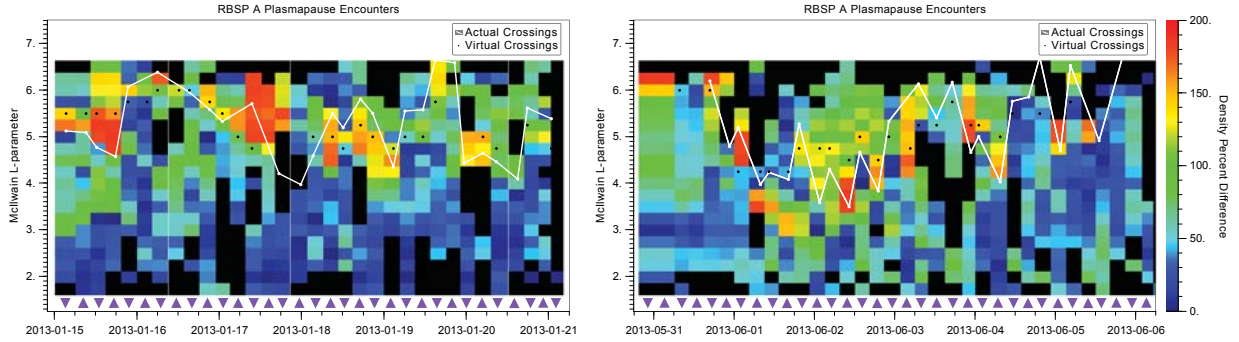

Figure 4: Density percent difference between simulated and measured plasmaspheric densities normalized by the mean value on a linear color scale. The binning corresponds to outbound/inbound passes as indicated by the purple triangles (down/up, respectively) for each column and .25 R_E increments in L for each row. Overmarked as black dots are virtual plasmapause crossings; actual plasmapause crossings are dots connected by the black line. Note that in both cases the plasmapause location is coincident with high percent difference. During the January event there is a steady improvement from lower (higher) to higher (lower) L values (densities) of greater simulation fidelity. For the June event, the alternating pattern of actual plasmapause encounters is representative of MLT dependent locations (from ~21 hrs on an outbound pass to ~24 hrs on an inbound pass).

5. Determination of Plasmapause Candidate Crossings

The plasmapause is a feature of the plasmasphere frequently noted but rarely consistently defined because its detection depends primarily on limited in situ spacecraft observations. For instance, one criteria examines the innermost sharp density gradient in a measured radial profile defined by a change of a factor of 5 or more within $\Delta L < 0.5$ [*Carpenter and Anderson*, 1992; *Moldwin et al.*, 2002]. Others have chosen a low density threshold such as the outermost occurrence in L of 20 cm^{-3} to identify the extent of the plasmasphere based on instrument sensitivity [*Goldstein et al.*, 2005; *Goldstein et al.*, 2014 (in press)]. We choose here the latter definition to analyze RBSP A EMFISIS measurements used in this study. **Figure 5** shows the radial difference between virtual and actual plasmapause determinations versus the K_p parameterization used to drive convection in the RAM-CPL simulation. We find that both simulations produced acceptable plasmapause locations to an accuracy of 0.50 ± 0.13 L (to within an L bin spacing) and 0.55 ± 0.13 L for the January and June events of 2013, respectively. No clear error dependence between simulations and observations on the driving geomagnetic activity index is shown.

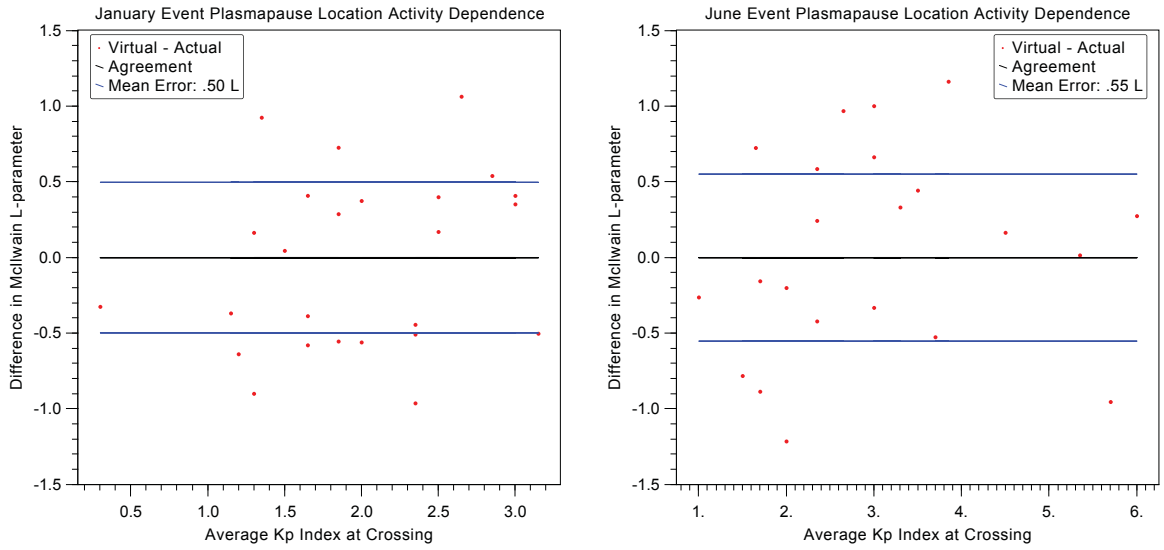

Figure 5: Difference in simulated and actual plasmapause locations versus the average (for each encounter) K_p activity index for the January and June events of 2013. Scatter is organized around perfect agreement (indicated by the black line) and within nominal performance (mean error indicated by the blue lines). There is no particular organization of outlying points for certain geomagnetic conditions.

6. Summary and Conclusions

This paper presents a two event case study for observations taken by the Van Allen Probes during 15 - 20 January and 31 May - 5 June, 2013 to assess the performance of the two-dimensional RAM-CPL plasmaspheric density model. A combined Volland-Stern and SAPS potential was chosen to drive the simulation and represent local asymmetries in the convection electric field that causes the erosion of the plasmasphere. Refilling was assumed to occur at a constant rate from empirical models of the outward ionospheric particle flux up to an average saturation density level. Significant virtual deviations from actual measurements were found, corresponding to diminished and asymmetric erosion on the pre-dawn and post-dusk MLT sectors of the January and June events of 2013 respectively. In these cases the location of the plasmapause as defined by the low density 20 cm^{-3} threshold marks the boundary past which low densities are overestimated by the RAM-CPL simulation. The virtual RBSP A satellite encountered 28 plasmapause crossings during the January event compared to 25 actual determinations for a model-data difference of $\Delta L_{AVG} = 0.50 \pm 0.13$, whereas 24 virtual crossings versus 22 actual plasmapause encounters were detected during the June event to an accuracy of $\Delta L_{AVG} = 0.55 \pm 0.13$.

The good agreement in plasmapause location between these low resolution RAM-CPL plasmasphere simulations and the Van Allen Probes observations is suggestive that the K_p parameterization of the convection electric field is, in general, adequate. Indeed, it is often reported that the mean behavior of the plasmapause varies linearly according to the K_p geomagnetic activity index [*Carpenter and Anderson*, 1992; *O'Brien and Moldwin*, 2003]. However, a higher resolution and longer simulated extension of this study is necessary to fully account for the disparities concerning enhanced refilling and asymmetric erosion. Improved timescales for the recovery of the plasmasphere are beyond the scope of this current work and dataset, but alternative convection electric field models are readily available. As utilized by *Goldstein et al.*, 2014 (in press) in the analysis of the January event, the Volland-Stern potential can be parameterized instead by the scaled solar wind electric field E_{SW} that is calculated from bulk flow during southward orientation of the interplanetary magnetic field (IMF). *Weimer*, 2005 has also proposed a well-developed empirical ionospheric model that can be mapped as a potential to the equatorial plane of the magnetosphere along magnetic field lines. The potential patterns in this model are significantly asymmetric in magnetic local time and exhibit small-scale structures that can promote sustained features in the plasmasphere. Full integration with the RAM suite for kinetic simulations of ring current evolution may require, rather, the coupling provided by self-consistently calculated electric and magnetic fields that can be implemented in the study of the plasmasphere [*Liemohn et al.*, 2004]. Evidence of disagreement between simulations and observations can still identify the importance of non-convective processes, whose detailed properties are not well-known.

References

Bilitza, D. (1986). International Reference Ionosphere: recent developments. Radio Sci 21, 343, 1986.

Burke, W.J., et al. (1998). Electrodynamics of the inner magnetosphere observed in the dusk sector by CRRES and DMSP during the magnetic storm of June 4-6, 1991. J of Geophys Res 105, 18, 391.

Carpenter, D.L. (1963). Whistler evidence of a "Knee" in the magnetospheric ionization density profile. J of Geophys Res 68, 1675 - 1682.

Carpenter, D.L. and Anderson, R.R. (1992). An ISEE/Whistler model of equatorial electron density in the magnetosphere. J of Geophys Res 97, A2, 1097-1108.

Chappell, Cr., Harris, K.K., Sharp, G.W. (1970). The morphology of the bulge region of the plasmasphere. J of Geophys Res 75, 19, 3848-3861.

Chen, A.J., and Wolf, R.A. (1971). Effects on the plasmasphere of a time-varying convection electric field. Planet Space Sci 20, 483-509.

Darrouzet, F. et al. (2008). Plasmaspheric density structures and dynamics: Properties observed by the CLUSTER and IMAGE missions. Space Sci Rev 14, 55-106.

Foster, J.C., and Burke, W.J. (2002). SAPS: A new categorization for sub-auroral electric fields, Eos Trans AGU 83, 36, 393.

Foster, J.C., and Vo, H.B. (2002). Average characteristics and activity dependence of the sub auroral polarization stream. J of Geophys Res 107. A12), 1475.

Fok, M.C., Kozyra, J.U., Nagy, A.F., Cravens, T.E. (1991). Lifetime of ring current particles due to Coulomb collisions in the plasmasphere. J of Geophys Res 96, 7861-7867.

Ganguli, G., Reynold, M.A., Liemohn, M.W., 2000. The plasmasphere and advances in plasmaspheric research. J of Atmos and Solar-Terrestrial Physics 62, 1647-1657.

Goldstein, J. Burch, J.L., and Sandel, B.R. (2005). Magnetospheric model of sub auroral polarization stream. J of Geophys Res 110, A09222.

Goldstein, J., De Pascuale, S., Kletzing, C., Kurth, W., Genestreti, K.J., Skoug, R.M., Larsen, B.A., Kistler, L.M., Mouikis, C., Spence, H. (2014). Simulation of Van Allen Probes plasmapause encounters. J of Geophys Res, doi:10.1029/2014JA020252, in press.

Gordon, C.W., Canuto, V., and Axford, W.I. (1978). The Earth, 1: The Upper Atmosphere, Ionosphere, and Magnetosphere. Gordon and Breach Science Publishers. 40.

Hedin, A.E. (1987). MSIS-86 thermospheric model. J Geophys Res 92, 4649.

Jordanova, V.K., Kistler, L.M., Kozyra, J.U., Khazanov, G.V., Nagy, A.F. (1996). Collisional losses of ring current ions. J of Geophys Res 101, A1, 111-126.

Jordanova, V.K., Miyoshi, Y.S., Zaharia, S., Thomsen, M.F., Reeves, G.D., Evans, D.S., Mouikis, C.G., and Fennell, J.F. (2006). Kinetic simulations of ring current evolution during the Geospace Environment Modeling challenge events. J of Geophys Res 111, A11S10.

Kletzing, C.A. et al. (2013). The Electric and Magnetic Field Instrument Suite and Integrated Science (EMFISIS) on RBSP. Space Sci Rev 179, 127-181.

Leimohn, M.W., Ridley, A.J., Gallagher, D.L., Ober, D.M., and Kozyra, J.U. (2004). Dependence of plasmaspheric morphology on the electric field description during the recovery phase of the 17 April 2002 magnetic storm. J of Geophys Res 109, A03209.

Lemaire, J.F., and Gringauz, K.I. (1998). The Earth's Plasmasphere. Cambridge University Press, New York.

Lyons, L.R., Thorn, R.M., Kennel, C.F. (1972). Pitch-angle diffusion of radiation belt electrons within the plasmasphere. J of Geophys Res 77, 19, 3455.

Maynard, N.C., and Chen, A.J. (1975). Isolated cold plasma regions: Observations and their relation to possible production mechanisms. J of Geophys Res 80, 1009.

Moldwin, M.B. et al. (2002). A new model of the location of the plasmapause: CRRES results. J of Geophys Res 107, A11, 1339-1348.

Nishida, A. (1966). Formation of plasmapause by the combined action of magnetospheric convection and plasma escape from the tail. J of Geophys Res 71, 23, 5669-5679.

O'Brien, T.P. and Moldwin, M.B. (2003). Empirical plasmapause models from magnetic indices. Geophys Res Letters 30, 4, 1152-1156

Wygant, J.R., et al. (2013). The Electric Field and Waves Instruments on the Radiation Belt Storm Probes Mission. Space Sci Rev 179, 183-220.

Rasmussen, C.E., Guiter, S.M., and Thomas, S.G. (1992) A two-dimensional model of the plasmasphere: refilling time constants. Planet Space Sci 41, 1, 35-43.

Richards, P.G., and Torr, D.G. (1985). Seasonal, Diurnal, and Solar Cyclical Variations of the Limiting H^+ Flux in the Earth's Topside Ionosphere. J of Geopphys Res 90, A6, 5216-5268

Singh, A.K., Singh, R.P., Siingh, D. (2011). State studies of Earth's plasmasphere: A review. Planet Space Sci 59, 810-834.

Stern, D.P. (1975). The motion of a proton in the equatorial magnetosphere. J of Geophys Res 80, 595.

Volland, H. (1973). A semi empirical model of large-scale magnetospheric electric fields. J of Geophys Res 78, 171.

Weimer, D.R. (2005). Improved ionospheric electrodynamic models and application to calculating Joule heating rates. J of Geophys Res 110, A05306.

Space-based Gamma Ray Burst Flash Spectrometer Development

Wade Duvall

Abstract

First detected in 1968, the cause of extragalactic gamma ray bursts (GRBs) is a mystery. A new approach to their detection may provide a new avenue of investigation. A multichannel gamma ray flash spectrometer has been designed to expand the dynamic range of typical GRB detectors. Unlike traditional spectrometers, this detector operates by measuring the energy deposited in each of the 18 channels of the detector array. Several proof of concept studies conducted by simulations of the array (using the Geant4 simulation package), as well as several calibrations and detector feasibility studies using consumer off the shelf CZT detectors will be shown.

Keywords: GRB, gamma ray burst, CZT, large band-gap semiconductor

1. Introduction

1.1. Gamma Ray Bursts (GRB)

Gamma ray bursts were first detected by several of the Vela satellites in 1968; reproduction shown in Fig. 1. These

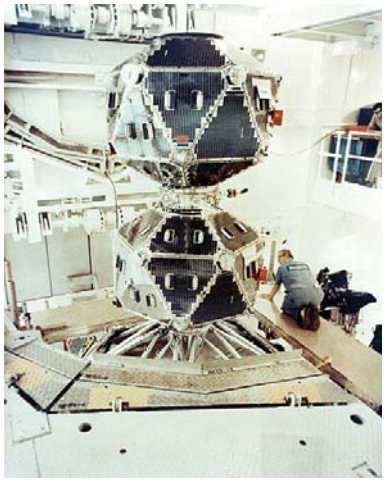

Figure 1: Vela satellite in clean room (NASA, 2003)

satellites were initially intended to detect x-rays generated from space-based nuclear tests to enforce the 1963 Partial Test Ban Treaty. The Vela satellites also had the secondary mission of studying space-based radiation that would be a potential background to the primary mission. Over the course of the mission, the Vela satellites detected several events that did not have a signature corresponding to space-based nuclear detonation. Using crude time of flight analysis, it was determined that the signal did not have terrestrial or solar origin (Klebesadel, 1973).

Today it is known that these bursts are extragalactic in origin. The mechanisms behind gamma ray bursts is still a mystery today, and no analytical model explaining all observed bursts exists. Gamma ray bursts are accompanied

Email address: wsduvall@vt.edu (Wade Duvall)

by an afterglow in many wavelengths of light from radio to x-ray. The afterglow is thought to be caused by Compton scattering as the gamma rays interact with matter. Many different theories exist for the exact cause of gamma ray bursts, but the leading theory is they are caused by ultra relativistic beaming. Relativistic beaming occurs when matter moves very close to the speed of light, causing most of the photons to be emitted in the direction of travel (Fishman, 1995) (Chen, 2013).

Even though no analytic model describes all gamma ray bursts, there is an empirically derived formula that seems to fit most GRB spectra. In 1993, David Band of Los Alamos National Laboratory published a paper introducing the Band function as shown in Fig. 2. This parameterization was used later to extract the spectrum of the burst.

$$N(E) = \begin{cases} E^{\alpha} exp(\frac{E}{E_0}) & \text{if } E \leq (\alpha - \beta)E_0 \\ [(\alpha - \beta)E_0]^{(\alpha-\beta)} E^{\beta} exp(\beta - \alpha) & \text{if } E > (\alpha - \beta)E_0 \end{cases} \quad (1)$$

where α is the low energy paramater, and β is the high energy paramater, E is the energy, and E_0 is the peak energy (Band, 1993).

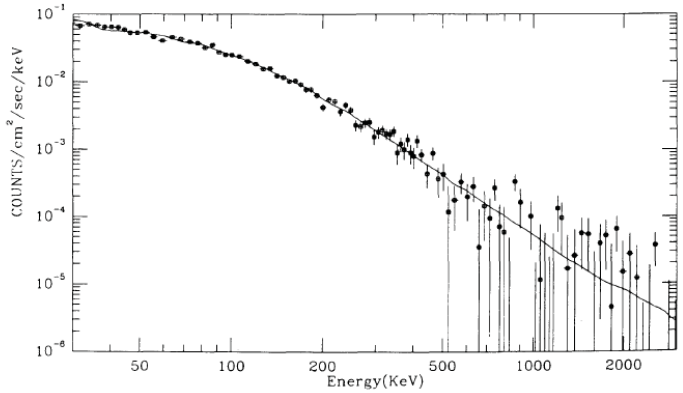

Figure 2: GRB 1B 911127 light curve with fitted Band function (Band, 1993)

1.2. Cadmium-zinc telluride (CZT)

Cadmium-zinc telluride is a semiconducting crystal made from an alloy of cadmium telluride (CdTe) and zinc telluride (ZnTe). The ratio of cadmium telluride to zinc telluride varies based on semiconductor design, but is usually made up of 80% - 96% cadmium telluride. CZT has many advantages over standard semiconductors. For example, a wide band gap of ~ 1.64 eV allows for larger detectors to operate at room temperature. Silicon has a band gap of 1.1 eV, which requires cooling to prevent thermal excitations in large detectors. In addition, CZT has a higher Z number and higher density than both silicon and germanium. The result is higher stopping power and a larger photopeak fraction. CZT has also been proven in space in several missions, including the gamma ray burst telescope Swift and the X-ray telescope NuSTAR. (Rana, 2009) (Gehrels, 2004) (Knoll, 2010)

However, detector grade CZT is difficult and costly to grow. The larger the detector dimensions, the more likely there will be defects in the crystal. Also, CZT has low charge collection compared to silicon, which reduces the energy resolution at higher incident energies. There are some new techniques which work around this problem, such as using a pixelated CZT detector. CZT is also susceptible to space charge effects which may induce nonlinearity in detector response. (Knoll, 2010)

1.3. Flash spectrometer design

For this project, a multichannel gamma ray flash spectrometer using 16 discrete CZT detectors, shown in Fig. 3a, and 2 silicon carbide (SiC) detectors was used; see Fig. 3b . The array of CZT detectors is 20 mm × 20mm. The CZT pieces are 2 mm thick and the SiC pieces are 1 mm thick. Each of the CZT detector channels has a 0.1 mm thick filter that is made of a different element (discussed later). One of the SiC detector channels has a filter made from 0.1 mm

(a) eV Products CZT detector

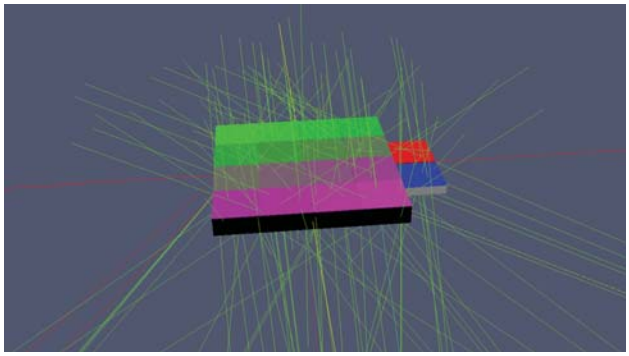

(b) Geant4 simulation of detector array

Figure 3

thick mylar and the the other detector has a filter made from 0.001 mm thick aluminum. The SiC detector channels helps increase low energy sensitivity (less than ~ 1 keV).

2. Methodology

2.1. Simulation

In order to study this detector concept, the Geant4 simulation package was used. The 16 CZT channels with filters and 2 SiC channels with filters, as shown in Fig. 3b, were implemented. The metals used for CZT filters were beryllium, carbon, aluminum, titanium, nickel, zirconium, silver, neodymium, terbium, tantalum, and lead. A variety of metals are used because they have different K-edge energies. This simulation was used to generate detector response matrices (DRM) which help in understanding detector operation in general, and are also crucial to the analysis algorithm. A DRM is simply the incident particle energy verses deposited energy. The averaged DRMs for all channels is shown in Fig. 4 (Agostinelli, 2003).

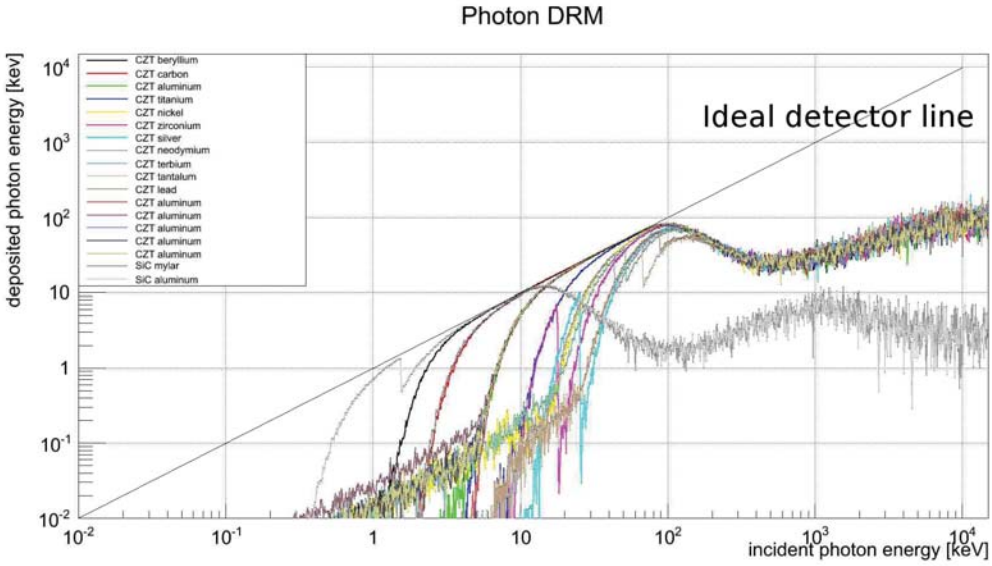

Figure 4: Geant4 simulation of detector array

2.2. Detector algorithm

The detector algorithm works by comparing the energy deposited in each channel against a lookup table generated using the parameterization of the light curve, in this case the Band function, and the DRM for each channel which is known from simulation. For each α and β in the Band function, the DRM is applied to the spectrum for each of the 18 channels, then the total energy is obtained. The total energy for each channel, along with α and β are then stored in the lookup table. When light hits the detector, α and β can be obtained by comparing the energy deposited to the energies in the lookup table using χ^2 minimization. An algorithm was written and tested using several different paramaterizations, including the Band fuction, and was successful at matching spectra.

2.3. Space weather background

Space is a high radiation environment, so a short study on the effects of space weather was conducted using SPENVIS. Most of the background energy deposition will come from electrons and protons depositing energy in the detector. Using Geant4, electron and proton DRMs were obtained. Using SPENVIS, fluxes for electrons and protons were calculated for the worst-case orbit, medium earth orbit (MEO), as shown in Fig. 5. Under normal conditions the flux of background particles at low earth orbit and geosynchronous orbit are orders of magnitude smaller than medium earth orbit.

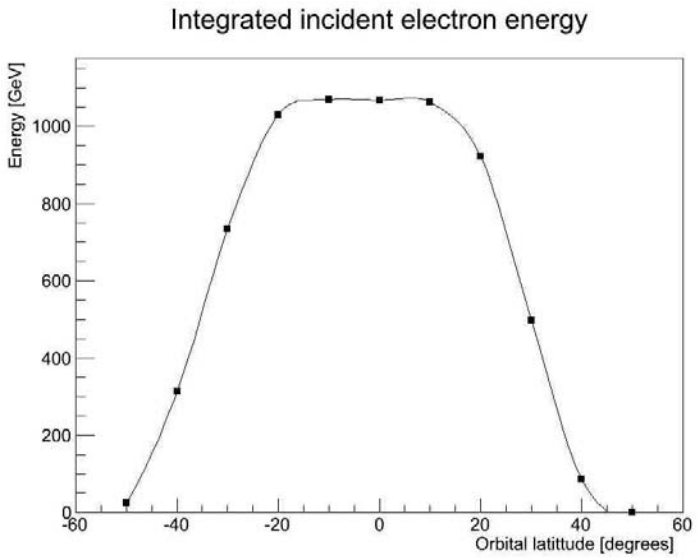

Figure 5: Integrated incident electron energy calculated from SPENVIS

By adding this incident energy to the estimated energy from a gamma ray burst and running it though the detector algorithm, it was discovered that when the background signal was on the order of the gamma ray burst signal, the algorithm would fail to find the correct parameters. Highly elliptical orbits (HEO), which are becoming more popular as space becomes more crowded, tranverse the Van Allen radiation belts. By studying MEO orbits a worse case signal to background was characterized (Agostinelli, 2003).

2.4. Experimental

To experimentally study the feasibility of implementing a small multichannel spectrometer, a small test DAQ was set up using an eV Products CZT detector, a low noise high voltage power supply, a shaping amplifier, and a CoolFET preamp. For actual data acquisition, a 14-bit pocket MCA was used. Several gamma sources were used: Na-22, Am-241, Th-228, Co-57, Co-60, Ba-133. MCA channel number verses energy was plotted to obtain the calibration curve, as shown in Fig. 6.

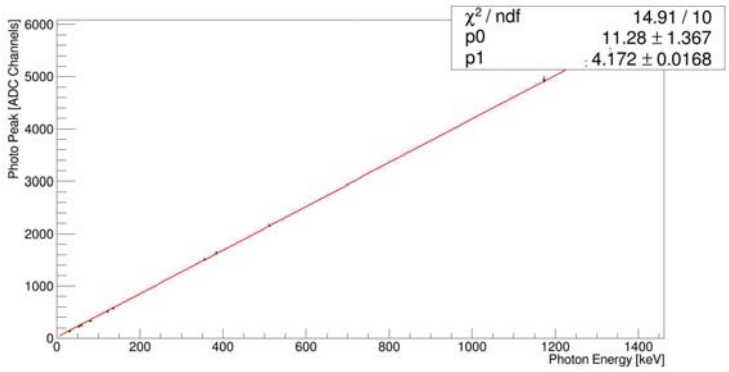

Figure 6: Calibration curve for CZT detector

Since CZT is known to have higher space charge and trapping effects than Si, we measure $\mu\tau$ which governs how charge in a semiconductor will behave. μ is the carrier mobility, which is related to the drift velocity in a given electric field in a semiconductor.

$$v_{drift} = \mu E \tag{2}$$

τ is the carrier lifetime, which is the average lifetime of an electron hole pair before becoming trapped. This parameter gives us the limit on how fast the detector array can be read out and how efficiently charge is collected. $\mu\tau$ is important to understand when designing the electronics chain as well (Knoll, 2010).

To study the $\mu\tau$ product of this particular CZT detector, the detector was placed in a vacuum chamber. High vacuum was applied ($\sim 10^{-6}$ torr) which allowed the detector to be bombarded with alpha particles. The alpha particles deposited all of their energy near the surface of the detector which forced the electron charge carriers to traverse the thickness of the detector before being collected. Next, by varying the bias voltage, the channel of the alpha peak was measured verses channel number and fit to

$$\frac{N_{ch}}{N_{ch_0}} = \frac{\mu\tau V}{d^2}\left[1 - exp\left(\frac{-d^2}{\mu\tau V}\right)\right] \tag{3}$$

as shown in Fig. 7a. Voltages were taken up to the operating voltage of 400 V. Fig. 7b shows an Am-241 spectrum with various escape and x-ray peaks.

3. Results

The results for $\mu\tau$ are shown in Fig. 7a and give a value of 6.909×10^{-4} cm^2/V. This is about an order of magnitude smaller than other detector grade CZT, and could result in reduced energy resolution and higher space charge. The detectors used were consumer grade CZT detectors, and not mission specific. A 400 V operating voltage, while achievable in space, can prove challenging. With larger $\mu\tau$, it would be possible to run CZT at lower voltages.

4. Conclusion

Given the proper low background flux orbit or an HEO where the flux is high only part of the time, a wide band-gap semiconductor flash spectrometer would extend the dynamic range of counting based GRB detectors. CZT has been space tested by several space missions and could be part of a GRB flash spectrometer in the future. Our results show that, given certain limitations, the conceptual detector is feasible and would be relatively insensitive to thermal excitations, and would reduce the size, weight, and power relative to current flash spectrometers.

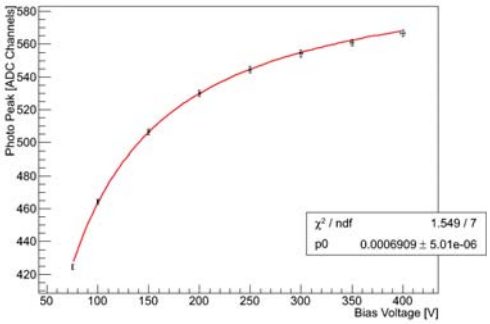

(a) $\mu\tau$ measurement, $\mu\tau = 6.909 \times 10^{-4}$

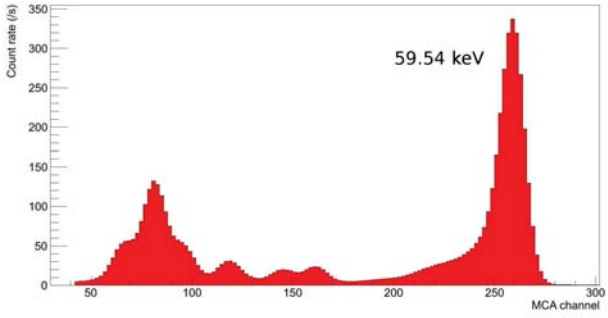

(b) Am-241 spectrum from CZT detector

Figure 7

References

Agostinelli, Allison, A., 2003. Geant4a simulation toolkit. Nuclear Instruments and Methods in Physics Research Section A 506, 250.

Band, Matteson, F., 1993. BATSE observations of gamma-ray bursts spectra. I. spectral diversity. Astrophysical Journal 413, 281.

Chen, H., 2013. Gamma-ray-burst beaming and gravitational-wave observations. Physical Review Letters 111, 181101.

Fishman, M., 1995. Observations of gamma-ray bursts of cosmic origin. Annual Review of Astronomy and Astrophysics 33, 415.

Gehrels, Chincarini, G., 2004. The Swift gamma-ray burst mission. Astrophysical Journal 611, 1005.

Klebesadel, Strong, O., 1973. Observations of gamma-ray bursts of cosmic origin. Astrophysical Journal 182, 85.

Knoll, G., 2010. Radiation Detection and Measurement. Wiley.

NASA, 2003. Vela-5a/b gallery.

Rana, Cook, H., 2009. Development of focal plane detectors for the nuclear spectroscopic telescope array (NuSTAR) mission. Proceedings of SPIE 7435.

An Event-Specific Inner Magnetosphere Density Model

John Haiducek, Greg Cunningham, Steve Morley, Weichao Tu

University of Michigan, Ann Arbor, MI and Los Alamos National Laboratory, Los Alamos, NM

Abstract

A new event-specific electron number density model for the inner magnetosphere has been constructed using data from the Van Allen Probes, in order to provide global electron densities to the Dynamic Radiation Environment Assimilation Model in 3 Dimensions (DREAM3D). This model fits several empirical models of the inner magnetosphere to the electron number density data from the Electric and Magnetic Field Instrument Suite and Integrated Science (EMFISIS) instruments of the Van Allen Probes, although the approach would work with other datasets. The fit is done separately for each satellite pass, so that the model accounts for changes in magnetospheric structure over time. Comparison with density measurements from the 10 Oct, 2012 geomagnetic storm show that the new model performs comparably to the model by Sheeley et al. which is currently used within DREAM3D, but this work points to improvements that could be made to construct a better model.

Keywords: Plasmasphere, plasmapause, Van Allen probes, plasma density

1. Introduction

The inner magnetosphere can be divided into two regions. The inner region is characterized by relatively high electron densities and is called the plasmasphere. Beyond this is the trough region, which is characterized by markedly lower electron densities. Plasma motion in both regions is characterized by an $\mathbf{E} \times \mathbf{B}$ drift. In the plasmasphere, the dominant field, called the "corotation electric field," points radially outward and drives the plasma counterclockwise in closed paths around the Earth. The dominant field in the trough, called the "convection electric field," points from the dawn to the dusk side of the magnetosphere and drives the plasma in a sunward direction. This sunward drift removes the plasma from the magnetosphere and accounts for the lower electron densities in the trough region [Chappell (1972)].

During storm times, the weakening of the magnetic field in the magnetosphere causes the plasmapause to suddenly move inward, leaving a population of dense plasma from the plasmasphere on open drift paths. The result is a plume of dense plasma which convects around the outside of the plasmasphere before finally escaping toward the sun on the dusk side, leaving behind a plasmasphere of reduced size [Chen and Wolf (1972)].

This project seeks to construct a model of electron number density (N_e) in the inner magnetosphere which captures changes in the inner magnetosphere over time as seen from in situ measurements. Data from the Electric Field Instrument Suite and Integrated Science (EMFISIS) instrument on the Van Allen Probes is used as the basis for this model, providing a means to identify the location of the plasmapause at various times and to characterize the density in both the plasmasphere and trough regions. EMFISIS measures electric fields with a sufficiently fast frequency response to identify the upper hybrid line, from which cold plasma density is obtained [Kletzing et al. (2014)].

The Van Allen Probes orbit the earth in elliptical, low-inclination orbits, with perigee occurring around 1.1 earth radii (R_e) and apogee around 5.8 R_e. As a result, they provide a good picture of the plasma density in the equatorial region but not in the higher latitudes. Their orbits are slightly different so that they pass through approximately the same locations for a given orbit but at different times, with one spacecraft overtaking the other every 75 days. [Mauk et al. (2013)]. During the time period of interest the spacecraft were located on the dawn side of the magnetosphere, so the model results presented here are based on data from that region.

Email address: jhaiduce@umich.edu (John Haiducek, Greg Cunningham, Steve Morley, Weichao Tu)

1.1. Motivation

The Dynamic Radiation Environment Assimilation Model in 3 Dimensions (DREAM3D) diffusion model requires an estimate of N_e in order to calculate diffusion coefficients, which it uses to calculate transport of high-energy electrons between various states and locations. Diffusion of high-energy electrons is then modeled on a grid according to the adiabatic invariants L, μ, and K Tu et al. (2013).

Currently within DREAM3D, N_e in the trough is obtained from an empirical model by Sheeley et al. (2001), while in the plasmasphere a model from Carpenter and Anderson (1992) is used. Both of these models are based on a fit to data provided by the Combined Radiation Release and Effects Satellite (CRRES). The fit to the CRRES data was done on the entire CRRES dataset. As a result, the Sheeley model provides a spatially varying expression for N_e, but does not include any mechanism for accounting for current conditions (although the Carpenter and Anderson (1992) plasmapause model does include an activity level dependence).

Sheeley et al. (2001) provides two density models, one for the plasmasphere and one for the trough. In both regions the density is expressed as a polynomial function of L value. Within the plasmasphere region, Sheeley et al. (2001) give the N_e as

$$n_p = 1390(3/L)^{4.83}, \tag{1}$$

while in the trough it is

$$n_t = 124(3/L)^{4.0} + 36 * (3/L)^{3.5} \cos[(LT - 7.7(3/L)^{2.0} + 12)\pi/12], \tag{2}$$

where LT is the local time in hours.

The transition between the plasmasphere region and the trough region is called the plasmapause. The DREAM3D code models the plasmapause location as circular (constant L), with its location L_{pp} dependent in Kp according to a function obtained by Carpenter and Anderson (1992).

$$L_{pp} = 5.6 - 0.46Kp_{max}, \tag{3}$$

where Kp_{max} is the maximum value of the Kp index from the previous 24 hours.

An initial examination of the October 2012 storm showed that the N_e measured by the EMFISIS instrument on one of the two Radiation Belt Storm Probe (RBSP) spacecraft, RBSP-A, frequently differed from the Sheeley et al. (2001) model by a factor of 2.5. To examine the sensitivity of the DREAM3D diffusion model to electron density, the electron density from the Sheeley et al. (2001) model was divided by 2.5 inside the DREAM3D code instead of being used directly. This resulted in a dramatic increase in phase space density. Figure 1 illustrates this, using a run of DREAM3D for the period 6-10 Oct 2012. This shows a cut through the grid with μ fixed at $1279MeV/G$ and K fixed at $0.115R_eG^{0.5}$. The top half of Figure 1 shows the result of running DREAM3D with its usual N_e input, while the bottom half shows the result of dividing those inputs by a factor of 2.5 before calculating the diffusion coefficients for DREAM3D. Increases in phase space density approaching two orders of magnitude can be seen in some places.

The strong sensitivity of the DREAM3D diffusion model to electron density provided a motivation to create an event-specific empirical density model, leading to the current effort to create a new model based on data from the Van Allen Probes.

2. Methodology

In order to create an event-specific plasma density model, a functional form was assumed which is derived from the Sheeley et al. (2001) density model, but the functional form from the Sheeley model is multiplied by an undetermined coefficient chosen to match current observations. Two undetermined coefficients were used, one for the plasmasphere and one for the trough region. This enables the modified model to better match current conditions, while retaining the local time dependence terms in from the Sheeley model.

The values for L and other RBSP ephemeris parameters are obtained from the RBSP MagEphem files provided by the RBSP-ECT team at `http://www.rbsp-ect.lanl.gov` [Spence et al. (2014)]. For L-shell, the 'Lsimple' dataset was used, which is defined as the geocentric distance from the point field line that is passing through the spacecraft intersects the equator to the point of minimum magnetic field.

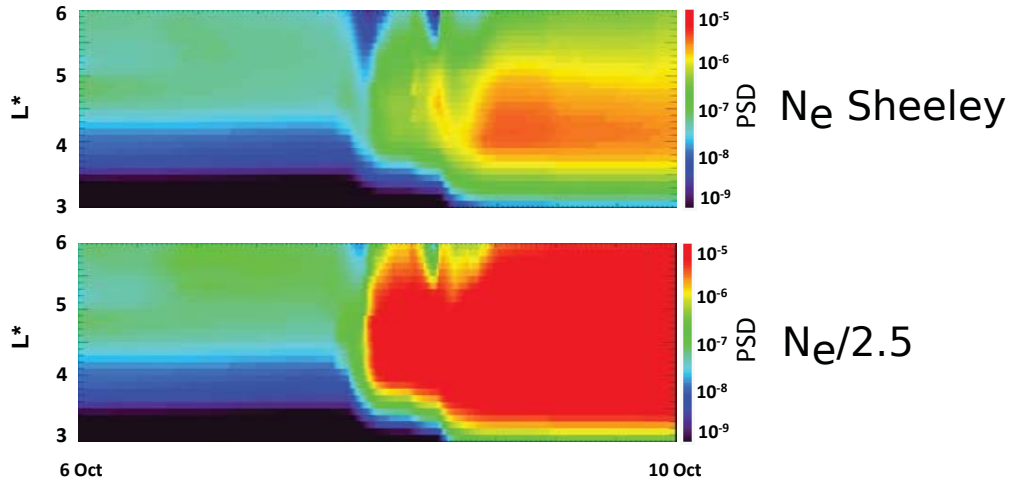

Figure 1: DREAM3D phase space density (PSD) during the period from 6-10 October. These plots show a slice with μ fixed at $1279 MeV/G$ and K fixed at $0.115 R_e G^{0.5}$. The upper plot shows the PSD using the Sheeley et al. (2001) and Carpenter and Anderson (1992) models for electron number density as described in the text, while the lower plot shows the result of dividing the electron number density by 2.5. This illustrates the large sensitivity of the PSD to plasma density.

Rather than assuming an abrupt transition across the plasmapause, a cubic interpolation function commonly known in the computer graphics community as 'smoothstep' (see Ebert et al. (2002)) was used to transition across the plasmapause. Two additional undetermined parameters, a plasmapause location L_{pp} and width δ_{pp}, were used to characterize the plasmapause at a given time. These parameters were used in combination with the smoothstep function to form a simple weight function to describe the plasmapause as a function of L:

$$w(L, L_{pp}, \delta_{pp}) = smoothstep(L_{pp} - \delta_{pp}/2, L_{pp} + \delta_{pp}/2). \tag{4}$$

This function was used in combination with the Sheeley expressions and their respective coefficients to form an expression for the plasma density in the plasmasphere, plasmapause, and trough:

$$n_e(L, LT) = s_p w(L_{pp}, \delta_{pp}) n_p(L) + s_t(1 - w(L_{pp}, \delta_{pp})) n_t(L, LT), \tag{5}$$

where s_p and s_t are the respective scaling factors for the plasmapause and trough. The four undetermined parameters (s_p, s_t, L_{pp}, and δ_{pp}) were obtained using a modified Levenberg-Marquardt algorithm[1]. Two fits were computed for each orbit of the RBSP-A spacecraft, one for the inbound pass and one for the outbound pass. Although the algorithm provides no guarantee of convergence, much less convergence to the correct values, it converged to a reasonable form for every satellite pass it was applied to as part of this effort, including some orbits where the plasmapause was at the outside of the RBSP orbit or was affected by dynamic features along the plasmapause boundary.

A representative result of this fitting process is shown in Figure 2. The left half of the figure shows N_e as a function of L-shell, with the RBSP-A measurements as dots and the model output as a line. Next to this graph is a plot of the orbital path during the same time period, superimposed on top of a picture of the model output for the equatorial plane. In the figure, the spacecraft's path does not quite reach perigee; this is because no density data is available from the EMFISIS instrument very close to perigee.

Rather than assuming the plasmapause to be circular, a local time dependent plasmapause model was used and its parameters adjusted to match the L_{pp} found by the fit. One option for this is the empirical model given in O'Brien and Moldwin (2003):

$$L_{pp} = -0.39\left[1 + 0.34\cos\left(\frac{2\pi}{12}(LT - 16.6)\right)\right]Q + 5.6\left[1 + 0.12\cos\left(\frac{2\pi}{24}(LT - 3)\right)\right], \tag{6}$$

[1] Specifically, the implementation used the leastsq provided by scipy, which is a wrapper for the LMDIF subroutine of MINPACK [Jones et al. (2001–)].

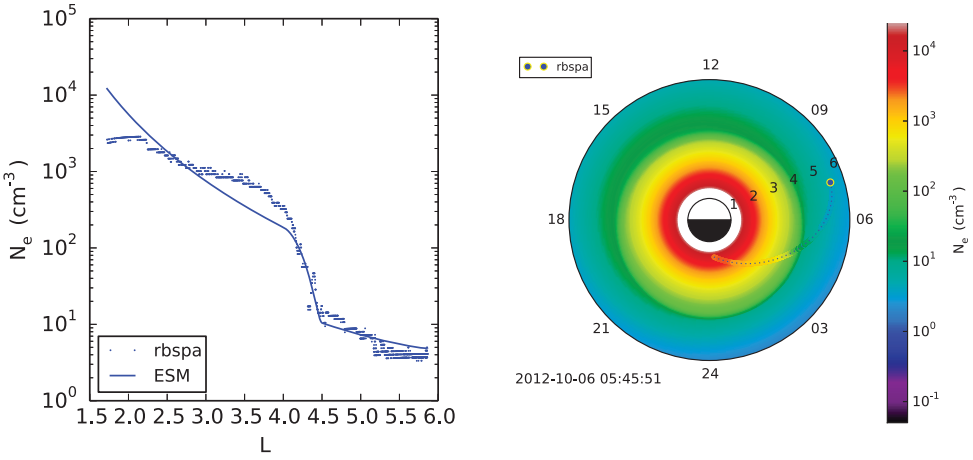

Figure 2: Example of the fitting process for one RBSP-A pass. This covers the time period 1:45:09-5:45:51 UTC on 6 October, 2012. The plot on the left shows the density measured by the EMFISIS instrument on RBSP-A, along with the fit to that data. The plot on the right shows the satellite path during this time period, along with the ESM model output for the equatorial region during this period. The blue dotted line shows the satellite's path. The colored line immediately under the satellite path corresponds to the EMFISIS density measurement at each point, while the colors elsewhere on the plot correspond to the density predicted by the model.

where Q represents the value of the Kp index. Depending on the activity level, this function may be nearly circular (as is the case in Figure 2, where the nearly circular plasmapause appears as an abrupt transition in number density in the right half of the figure), or it may result in a broad bulge on one side of the magnetosphere.

In order to maintain consistency with the fitted L_{pp} obtained from the RBSP satellite, the new model modifies the plasmapause model from O'Brien and Moldwin (2003) so that it matches the value of L_{pp} found by the fit process. This is done by re-defining Q to be the value that causes the O'Brien plasmapause model to match the observed plasmapause location, rather using the Kp index. To do this, Equation 6 was solved algebraically for Q, which gives:

$$Q = \frac{L_{pp} - 5.6\left(1 + 0.12\cos(\frac{2\pi}{24}(LT_{pp} - 3)\right)}{0.39\left(1 - 0.34\cos\left(\frac{2\pi}{24}(LT_{pp} - 16.6)\right)\right)}, \tag{7}$$

where LT_{pp} is the local time at which the spacecraft crossed the plasmapause. Using values of LT_{pp} and L_{pp} obtained from the fitting process described above, this expression gives the value of Q that will cause Equation 6 to match the observed plasmapause at the point where the satellite crossed the plasmapause, while retaining local time dependence elsewhere.

A theoretical plasmapause model can be formed by assuming that the plasmapause follows an equipotential line, as described in Lemaire et al. (1998) (among others), and also assuming that the convection electric field E_0 is constant and aligned perpendicular to the Sun-Earth line in the equatorial plane. This results in a plasmapause of the form

$$L_{pp} = \begin{cases} \frac{1-\sqrt{1-\sin\left(\frac{2\pi}{24}(LT-12)\right)}}{\sin\left(\frac{2\pi}{24}(LT-12)\right)}\sqrt{\frac{C_0 R_e}{E_0}}, & LT \bmod 12 \neq 0 \\ \frac{1}{2}\sqrt{\frac{C_0 R_e}{E_0}}, & LT \bmod 12 = 0, \end{cases} \tag{8}$$

where the corotation electric field C_0 is 92 kV and the the convection electric field E_0 is a free parameter (and assumed constant). As with the O'Brien and Moldwin (2003) plasmapause model, the model has only a single free parameter which can be solved for algebraically such that the equipotential L_{pp} matches the plasmapause location measured by the RBSP spacecraft at the location where the spacecraft crossed the plasmapause. The solution to this is:

$$E_0 = \begin{cases} \frac{C_0 R_e}{L_{pp}^2}\left(\frac{1-\sqrt{1-\sin\left(\frac{2\pi}{24}(LT-12)\right)}}{\sin\left(\frac{2\pi}{24}(LT-12)\right)}\right)^2, & LT \bmod 12 \neq 0 \\ \frac{C_0 R_e}{4L_{pp}^2}, & LT \bmod 12 = 0. \end{cases} \tag{9}$$

Local time variation in the plasmapause width was modeled by modifying an empirical formula from Gallagher et al. (2000):

$$\delta_{pp} = 0.036 \sin\left(\frac{2\pi}{24}(LT - 6)\right) + 0.14. \tag{10}$$

In order to match the observed plasmapause width at a given time, this formula was multiplied by a constant so that it produces the same plasmapause width as the value found by fitting the EMFISIS data from the current satellite pass:

$$\delta_{pp} = D_{pp}\left(0.2571 \sin\left(\frac{2\pi}{24}(LT - 6)\right) + 1\right), \tag{11}$$

where D_{pp} is a constant for each satellite pass. Rather than obtaining D_{pp} algebraically, the entire expression above was inserted into Equation 5 in place of L_{pp}, with D_{pp} replacing δ_{pp} as the free parameter. The effect of the local time dependent plasmapause width can be seen in the right half of Figure 2, in which the plasmapause appears as a sharp transition on the night side but gives way to a smoother transition on the day side.

Ozhogin et al. (2012) give an expression for N_e which includes latitude dependence:

$$N(L, \lambda) = N_{eq}(L)\left(1 + \gamma\frac{\lambda}{\lambda_{INV}}\right)\cos^{-\beta}\left(\frac{\pi}{2} \cdot \frac{\alpha\lambda}{\lambda_{INV}}\right), \tag{12}$$

where λ is the magnetic latitude and λ_{INV} the magnetic invariant latitude. α, β, and γ are fit coefficients, for which Ozhogin et al. (2012) found values of $\alpha = 1.081, \beta = 0.678$, and $\gamma = 0.297$. The new model uses these values as-is.

The fitting process described above necessarily discards any small-scale features in the data provided by EMFISIS. This provides the benefit of extracting useful information from the fit (especially the location and width of the plasmapause), and also makes it relatively easy to include local time dependence. To see whether discarding these features is worth the benefit of including local time dependence, an additional model was created which simply interpolates and smooths the EMFISIS data, assuming radial symmetry. This provided a means to test the importance of the information lost as a result of the fitting process. [2]

In order to assess the usefulness of the new model, henceforth called the event-specific model (ESM), the model was run for the period 6-9 October, 2012, using N_e from the RBSP-A spacecraft as input. Since the ESM is based on electron number density measurements from RBSP-A, measurements from four other spacecraft were used to assess its accuracy at locations away from the RBSP-A spacecraft. A natural choice for this is RBSP-B, because of its identical instrumentation. However, the relatively close proximity between RBSP-A and RBSP-B means that they often are passing through nearly the same locations only a short time apart from each other, and during the October, 2012 event both were generally on the dawn side of the inner magnetosphere. In order to assess the model's accuracy in locations far removed in local time, three of the THEMIS spacecraft were used. Electron number densities for the THEMIS spacecraft are derived from the spacecraft potential [Li et al. (2010)]. This introduces some inconsistency to the analysis because the method by which the number densities are measured by THEMIS is quite different from those available for RBSP. However, this was deemed preferable to analyzing the model's performance using only data taken from the two Van Allen Probes, given their closeness to one another. The accuracy of the THEMIS results is expected to be within a factor of two [Li, W., pers. comm., 2014], while the EMFISIS density data has an uncertainty of about 20% [de Pascuale, S., pers. comm., 2014]. Because both the Van Allen Probes and the THEMIS spacecraft are in low-inclination orbits, this leaves the latitude dependence of the model largely unconstrained and untested.

3. Results

As a test for the model, the time period of 6-10 October, 2012 was chosen. RBSP-A served as input to the ESM model. Data from RBSP-B, THEMIS-A, THEMIS-D, and THEMIS-E were used for comparison. Several variants

[2]The interpolation-based model was constructed using a cubic spline using the UnivariateSpline class of scipy. The order of the spline is configurable but defaults to cubic (cubic was used throughout this effort). Similarly the amount of smoothing is controlled by a smoothing factor *s*, which defaults to 0 (causing the spline to pass directly through all the data points) [Jones et al. (2001–)]. In this effort, default settings are used unless specified otherwise.

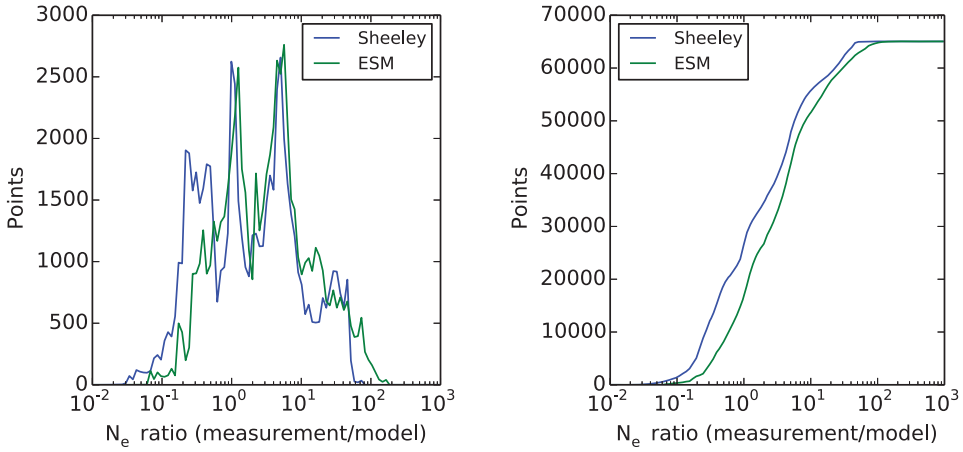

Figure 3: Comparison of the event-specific model (ESM, variant [1]) with the Sheeley model (variant [0]) for points covered by N_e datasets from THEMIS-A, D, and E and RBSP-B during the period 6-9 Oct 2012. The left hand plot shows the distribution of N_e(meas)/N_e(model) for all points; the right hand plot shows the corresponding cumulative distribution function (CDF).

Table 1: The model variations tested

Identifier	Density model	Plasmapause model
[0]	Sheeley et al. (2001)	Carpenter and Anderson (1992)
[1]	Sheeley et al. (2001) (modified)	O'Brien and Moldwin (2003) (modified)
[2]	Interpolated	None
[3]	Smoothed interpolated	None
[4]	Sheeley et al. (2001) (modified)	Equipotential
[5]	Sheeley et al. (2001) (modified)	Circular

of ESM (and also the Sheeley model) were evaluated at each point for which data had been collected at each of the spacecraft (except RBSP-A), and the ratio of the measurement to the model output taken. This ratio serves as the primary metric to indicate how closely the model agreed with each in situ measurement.

The complete list of model variants tested is in Table 1. The baseline ESM model (identified as [1]) uses the Sheeley density model modified in the manner described in the previous section, with the plasmapause modeled using O'Brien and Moldwin (2003), but with the geomagnetic index chosen such that the model reproduces the observed plasmapause location. Two interpolation-based models are tested. [2] uses cubic spline interpolation, while [3] uses cubic spline interpolation with a smoothing factor of 2×10^6. Finally, two additional variations were tried for the purpose of evaluating different plasmapause models. [4] is the baseline ESM but with an equipotential plasmapause model, while [5] is the baseline ESM with a circular plasmapause model (where the circle's radius is set to pass through the observed plasmapause location).

Since the original objective was to provide a replacement for the Sheeley model to be used in DREAM3D, the baseline model ESM model [1] was first compared with the Sheeley model [0]. These ratios were grouped into bins, and the resulting distribution plotted. Figure 3 shows the resulting distribution function and its corresponding cumulative distribution function (CDF). Values near 10^0 (or unity) indicate that the model agrees closely with the measurement. Values greater than unity indicate that the measurement value was greater than the model output, while values less than unity indicate that the measured value was less than the model output. Both distributions here appear similar, although the Sheeley model has a peak near 10^{-1} which is absent in the ESM analysis, and the ESM distribution is shifted slightly to the right, indicating a tendency to produce slightly greater values of N_e (for this event at least). The ESM appears to have a slightly broader peak around 10^0, and this may be interpreted as a slight improvement since the height of this peak is about the same as for the Sheeley model.

The ESM model ([1]) was next compared with two radially symmetric models (variants [2] and [3]; [2] consists

of cubic-spline interpolation in L-space while [3] also uses cubic-spline interpolation but with a smoothing factor of 2×10^6, see footnote in previous section) in the same manner as was done for the Sheeley model ([0]), and the results of this are shown in Figure 4. The radially symmetric model shows a long tail of points where the measured densities were orders of magnitude greater than predicted by the radially symmetric model. The addition of smoothing to the radially symmetric model produces a similar distribution as the version using interpolation only, except that the peak around 10^0 is broadened and shortened.

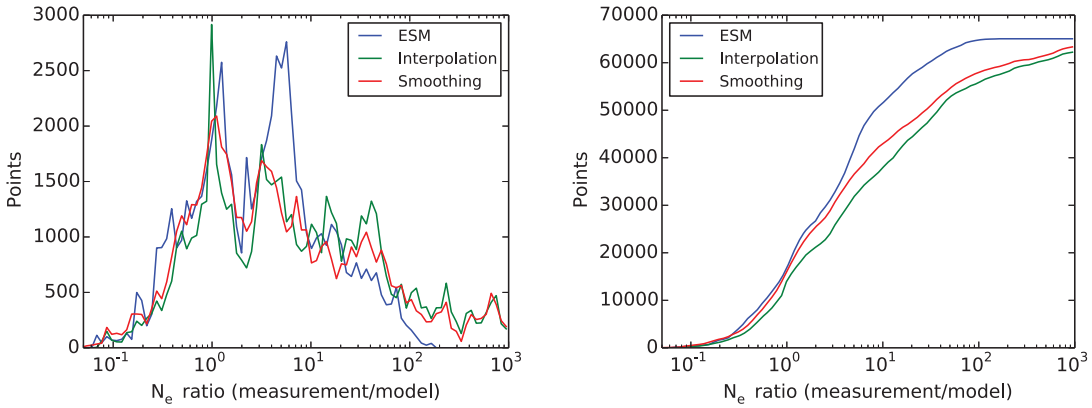

Figure 4: Comparison of the event-specific model (ESM) to a model which assumes radial symmetry. The radially symmetric model is shown with interpolation only (green curve, variant [2]) and with interpolation and smoothing (red curve, variant [2]). The plot to the left shows the distribution of N_e(measurement)/N_e(model), while the plot to the right shows the CDF of this distribution.

The three plasmapause models (O'Brien and Moldwin [1], equipotential ([4]), and circular ([5])), were also compared by taking the ratio of spacecraft measurements to their corresponding model outputs, with the distribution of this ratio shown in Figure 5. The equipotential model has a much different distribution in the wings with a few points diverging from the measurements by a factor of 10^3 or more. It shares the double-peak distribution seen with the O'Brien model, but the peak around 10^0 is significantly taller and broader. Using the circular plasmapause results in fewer points for which the model output falls near the spacecraft measurements, but its distribution otherwise looks similar to the O'Brien model.

Figure 6 uses the same metric (measurement value divided by model output) to assess the accuracy of the baseline ESM (variant [1]) at various radial distances from Earth, but here the ratios were plotted as a function of L-shell rather than as a histogram. These data come from the time period from 7:23 UTC on October 7th, 2012, to 2:35 UTC on October 8th. This time period corresponds to a single RBSP pass. Only a single RBSP pass is shown here because the model fits each pass individually, so that combining passes results in a discontinuity in the model output. This particular pass was chosen because RBSP-A data and THEMIS are available during this time, and because it is representative of the sensitivity of the model to the plasmapause location. In this case the model output is within an order of magnitude of the spacecraft measurements for most points. However, the plasma densities measured by THEMIS A exceed the model output by nearly two orders of magnitude between the model's plasmapause location and 0.5-0.7 earth radii beyond that point.

Figure 7 shows a summary of how the performance of the baseline model (variant [1]) compares in different spatial locations. Here, the ratio of measurement to model output was averaged over a number of bins in both L-shell and local time. The bins between 0 and 12 local time are mostly populated with data from the RBSP-B spacecraft, while the bins between 12 and 24 LT are mostly populated with data from the THEMIS spacecraft. A few points near 12 and 24 LT are populated with points from both THEMIS and RBSP-B. The points covered by RBSP-B tend to have an average ratio close to unity, indicating good agreement between model and measurement, while the points covered by the THEMIS spacecraft tend to have an average ratio significantly larger, indicating that the measured density was greater than that predicted by the model. A few bins between 1200 and 1500 LT have values significantly less than unity.

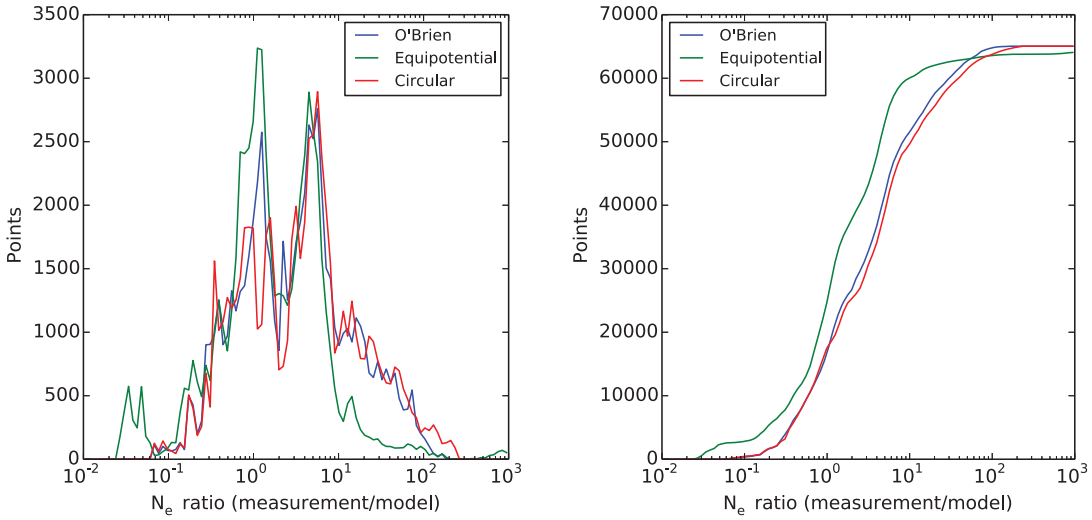

Figure 5: Performance comparison of three plasmapause models during the October 2012 storm. The model variants compared here are variants [1], [4], and [5]. The left plot shows the distribution of N_e(measurement)/N_e(model), while the plot to the right shows the CDF of this distribution.

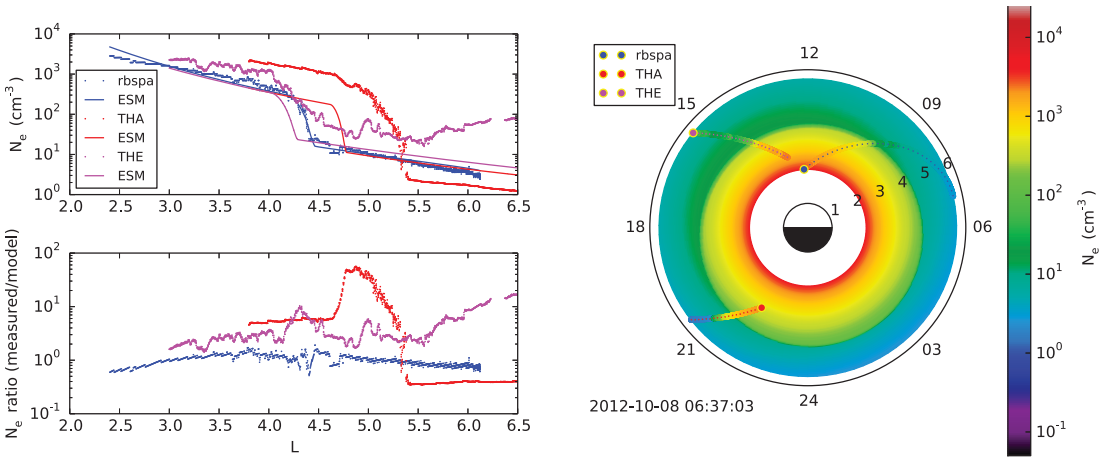

Figure 6: An illustration of the model's sensitivity to plasmapause location. The plot on the upper left shows electron number density predicted by the baseline ESM (variant [1]) compared with spacecraft measurements as a function of L-shell, for the time period 2:47:57-6:37:03 UTC on 8 Oct 2012. Each color corresponds to a spacecraft; dots indicate the measurements from the spacecraft while the line of the same color indicates the model output corresponding to that spacecraft. Here, THA and THE denote THEMIS-A and THEMIS-E, respectively. The plot on the lower left shows the ratio of model output to measurements during the same time period. This ratio reaches its largest value (almost 10^2) for THEMIS-A near the plasmapause, indicating that the model under-predicted the number density by that factor. The upper plot shows that this is mainly due to THEMIS-A crossing the plasmapause at a larger L than predicted by the model. The plot on the right shows the locations of the spacecraft during this time period.

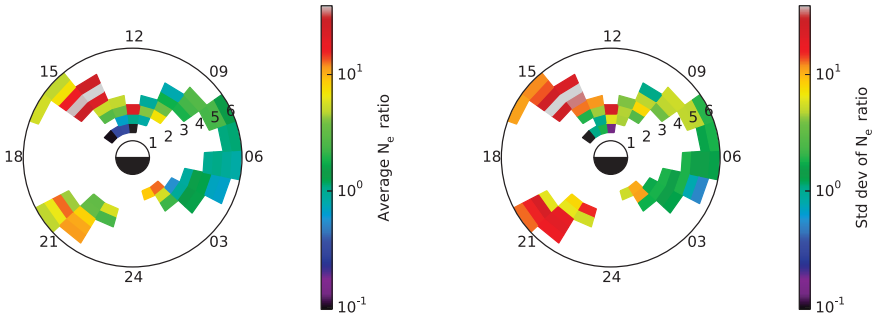

Figure 7: Density ratio (measurement vs. model) of the baseline model (variant [1]) as a function of radius and local time. The left side plot shows the average of this ratio for each bin in L and LT space, while the right side shows the standard deviation. The areas on the left (containing high averages and correspondingly high standard deviations) are mostly populated with THEMIS data, while the lower values on the right are mostly populated with RBSP-B data.

4. Discussion

The baseline ESM ([1]) appears at first glance not to offer a significant improvement over the Sheeley model ([0]). Figure 3 shows a broad peak between $1.2 - 1.4 \times 10^{-1}$ for the Sheeley model which is absent in the ESM distribution. This indicates a population of points for which the Sheeley model overpredicted the density, while the ESM did not. However, the overall width and shape of the distribution is similar for both models.

The local time dependence introduced by the baseline ESM appears to outweigh the loss of information that results from the fitting process. As seen in Figure 4, the ESM model (variant [1]) outperforms both the radially symmetric models (variants [2] and [3]). The benefit of local time dependence in the ESM appears to outweigh any loss of fidelity caused by smoothing out fine-scale features. Also, the addition of smoothing does not appear to significantly reduce the performance of the radially symmetric model. This probably means that the features being smoothed are essentially local in nature and not representative of the global structure.

Figures 5 and 6 show that the model can be very sensitive to the plasmapause location. This is expected, because the plasma density changes by two orders of magnitude across the plasmapause in some cases. During storms such as this one, the plasmasphere can develop features such as plumes which cannot be captured by an empirical model like the ESM. In such cases the usefulness of the model is not as great as during quieter periods. However, the relatively good performance of the equipotential model leaves open the possibility that better results might be obtained with some other plasmapause model.

Plumes tend to occur on the dusk side of the magnetosphere, which is where the THEMIS spacecraft were orbiting during this event. This is likely one of the factors contributing to the reduced accuracy of the model in the 12-24 LT period as seen in Figure 7. At least as important is the fact that the RBSP-B spacecraft was in close proximity to RBSP-A (on whose data the model was based), which may be sufficient alone to explain the higher accuracy in the 0-12 LT period. Another possible contributing factor is that the THEMIS densities are measured using a different (and less accurate) technique than the RBSP densities. In addition, the THEMIS spacecraft are operating on the dusk side where plumes are likely to be a factor.

5. Conclusion

Despite the ability to account for current conditions based on in situ measurements, the new ESM model appears not to offer significant improvement over the Sheeley model. However, in some cases the ESM provides a better result when an equipotential plasmapause model is used. Although the equipotential plasmapause model sometimes underpredicts the plasma density by a large factor, a new plasmapause model could probably constructed that addresses this problem.

Since this study was limited to a single event, it would be useful to attempt a similar study on other events, particularly ones for which the spacecraft locations are significantly different than was the case here. In doing so, a

more quantitative metric could be used to compare the models, such as the fraction of points for which the model output was within a particular factor of the corresponding measurement. In addition, more detailed analysis could be made of the several variations possible in the model (substitution of different plasmapause models, for instance), and of any spatial variation in the model's accuracy, particularly with respect to what fraction of the less-accurate points occur near the plasmapause. Some test of the latitude dependence of the model would also be beneficial.

An interesting modification to investigate here would be to use an interpolation method in conjunction with a deformation to account for the local time dependence of the plasmapause location. This would allow for preservation of some of the finer scale features while also utilizing a plasmapause model that incorporates local time dependence.

The greatest limitation of an empirical model such as this one is its inability to capture dynamics such as plumes. This might be overcome in part by using the ESM to construct an initial condition for a physics-based inner magnetosphere model. During quiet periods, when the inner magnetosphere is closer to its average conditions, the assumptions inherent in the ESM are likely to be more accurate, and this would provide a means of creating an initial condition that accounts for the state of the magnetosphere just prior to a specific event.

References

Carpenter, D.L., Anderson, R.R., 1992. An isee/whistler model of equatorial electron density in the magnetosphere. Journal of Geophysical Research: Space Physics 97, 1097–1108.

Chappell, C.R., 1972. Recent satellite measurements of the morphology and dynamics of the plasmasphere. Reviews of Geophysics 10, 951–979.

Chen, A., Wolf, R., 1972. Effects on the plasmasphere of a time-varying convection electric field. Planetary and Space Science 20, 483 – 509.

Ebert, D.S., Musgrave, F.K., Peachey, D., Perlin, K., Worley, S., 2002. Texturing and Modeling: A Procedural Approach. Morgan Kaufmann Publishers Inc., San Francisco, CA, USA. 3rd edition.

Gallagher, D.L., Craven, P.D., Comfort, R.H., 2000. Global core plasma model. Journal of Geophysical Research: Space Physics 105, 18819–18833.

Jones, E., Oliphant, T., Peterson, P., et al., 2001–. SciPy: Open source scientific tools for Python. [Online; accessed 2014-10-24].

Kletzing, C., Kurth, W., Acuna, M., MacDowall, R., Torbert, R., Averkamp, T., Bodet, D., Bounds, S., Chutter, M., Connerney, J., Crawford, D., Dolan, J., Dvorsky, R., Hospodarsky, G., Howard, J., Jordanova, V., Johnson, R., Kirchner, D., Mokrzycki, B., Needell, G., Odom, J., Mark, D., Pfaff, R., J., Phillips, J., Piker, C., Remington, S., Rowland, D., Santolik, O., Schnurr, R., Sheppard, D., Smith, C., Thorne, R., Tyler, J., 2014. The electric and magnetic field instrument suite and integrated science (emfisis) on rbsp, in: Fox, N., Burch, J. (Eds.), The Van Allen Probes Mission. Springer US, pp. 127–181.

Lemaire, J.F., Gringauz, K.I., Carpenter, D.L., Bassolo, V., 1998. Theoretical aspects related to the plasmasphere, in: The Earth's Plasmasphere. Cambridge University Press, pp. 221–309. Cambridge Books Online.

Li, W., Thorne, R.M., Bortnik, J., Nishimura, Y., Angelopoulos, V., Chen, L., McFadden, J.P., Bonnell, J.W., 2010. Global distributions of suprathermal electrons observed on themis and potential mechanisms for access into the plasmasphere. Journal of Geophysical Research: Space Physics 115.

Mauk, B., Fox, N., Kanekal, S., Kessel, R., Sibeck, D., Ukhorskiy, A., 2013. Science objectives and rationale for the radiation belt storm probes mission. Space Science Reviews 179, 3–27.

O'Brien, T.P., Moldwin, M.B., 2003. Empirical plasmapause models from magnetic indices. Geophysical Research Letters 30.

Ozhogin, P., Tu, J., Song, P., Reinisch, B.W., 2012. Field-aligned distribution of the plasmaspheric electron density: An empirical model derived from the image rpi measurements. Journal of Geophysical Research: Space Physics 117.

Sheeley, B.W., Moldwin, M.B., Rassoul, H.K., Anderson, R.R., 2001. An empirical plasmasphere and trough density model: Crres observations. Journal of Geophysical Research: Space Physics 106, 25631–25641.

Spence, H., Reeves, G., Baker, D., Blake, J., Bolton, M., Bourdarie, S., Chan, A., Claudepierre, S., Clemmons, J., Cravens, J., Elkington, S., Fennell, J., Friedel, R., Funsten, H., Goldstein, J., Green, J., Guthrie, A., Henderson, M., Horne, R., Hudson, M., Jahn, J.M., Jordanova, V., Kanekal, S., Klatt, B., Larsen, B., Li, X., MacDonald, E., Mann, I., Niehof, J., OBrien, T., Onsager, T., Salvaggio, D., Skoug, R., Smith, S., Suther, L., Thomsen, M., Thorne, R., 2014. Science goals and overview of the radiation belt storm probes (rbsp) energetic particle, composition, and thermal plasma (ect) suite on nasas van allen probes mission, in: Fox, N., Burch, J. (Eds.), The Van Allen Probes Mission. Springer US, pp. 311–336.

Tu, W., Cunningham, G.S., Chen, Y., Henderson, M.G., Camporeale, E., Reeves, G.D., 2013. Modeling radiation belt electron dynamics during gem challenge intervals with the dream3d diffusion model. Journal of Geophysical Research: Space Physics 118, 6197–6211.

Application of the DSMC Method in Modeling Earth's Rarefied Upper Atmosphere

William A. Hoey

The University of Texas at Austin, Austin, TX

Andrew C. Walker

Los Alamos National Laboratory, Los Alamos, NM 87545

Abstract

Improving the accuracy and robustness of simulations of Earth's upper atmosphere is a priority for satellite drag and space weather applications. The Direct Simulation Monte Carlo method is well-suited to modeling the dynamics of such rarefied and non-equilibrium regimes, where continuum techniques break down. Here, we apply DSMC in three-dimensional, transient, and self-consistent neutral density simulations of Earth's rarefied upper atmosphere.

An existing planetary-science code base, established in the modeling of the lunar and Ionian environs, is extended to reflect the physics of Earth's upper atmosphere. Comprehensive atmospheric simulations are computed in parallel on a domain extending from the mid-thermosphere, near the continuum-rarefied transition, through 1000 km altitude. The simulation code includes multi-species photo-chemistry, tracking of particle rotational and vibrational states, and non-equilibrium radiation. Substantial model development is demonstrated in application to the Earth's atmosphere, including the incorporation of lower-boundary conditions consistent with the NRLMSISE-00 semi-empirical model, ultraviolet radiation and photo-chemistry rates modeled with reference to space weather indices, and radiative absorption attenuated by integrated column density.

Comparisons with results drawn from the MSIS semi-empirical model and from indirect satellite mass density measurements are employed in benchmarking model accuracy. Avenues for further development include hybridization with continuum global circulation models in the mid-thermosphere, and the extension of the planetary code's magnetic field and charged-particle models to the Earth case.

Research supported by the Los Alamos Space Weather Summer School, LANL Institutional Computing, and the Institute of Geophysics, Planetary Physics, and Signatures (IGPPS) at LANL.

1. Introduction

The space weather and satellite operations communities employ a range of models in simulating thermospheric composition, density, and temperature; these models are imperfect in their application to that rarefied and non-equilibrium regime, in which improving the accuracy and robustness of predictive simulations is a priority. To that end, and in a novel extension of the IMPACT project, an existing planetary-science code base currently employed in the simulation of the rarefied lunar and Ionian environs has been modified to reflect the physics of Earth's upper atmosphere. In that model, presented herein, transient and self-consistent neutral density simulations are performed via the Direct Simulation Monte Carlo (DSMC) method. This method is the approach of choice for modeling a wide range of continuum-to-rarefied flows with mean free path comparable to characteristic flow length scale. In DSMC, the motions and collisions of representative molecules are computed. Multiple gas species, each having different numbers of rotational and vibrational degrees of freedom, are modeled, along with non-equilibrium radiation (for either transparent or partially opaque gases), high speed collisions, and photochemistry. Comprehensive atmospheric simulations are computed in parallel on one- and three-dimensional domains that span Earth's upper atmosphere, extending hundreds of kilometers vertically to the exobase. The emphasis of the Earth DSMC is on the incorporation of all relevant physics and the development of a predictive capability given appropriate boundary conditions: at the domain lower boundary such a model requires macroscopic atmospheric properties (e.g. species number densities and temperature) drawn from an established GCM. NRLMSISE-00, hereafter abbreviated to MSIS, is a semi-empirical model of atmospheric composition, temperature, and mass density that extends in applicability from the

Earth's surface to its exobase; it is the most recent in a series of Mass Spectrometer Incoherent Scatter Radar models that incorporate a diverse array of observed datasets. It is a widely used and familiar tool in the space weather and satellite operations communities. MSIS is publically available and, as an empirical model, its use is computationally cheap – therefore, MSIS can be directly linked to the planetary DSMC, and can be called to generate boundary conditions tens of millions of times in the course of a full-scale planetary simulation without difficulty.

1.1. Project Benchmarks.

A set of objectives were established at the project outset in order to direct Earth DSMC model development. The first such objective was to link the MSIS code to the planetary DSMC, and to modify the DSMC such that simulation particles could be generated on the lower boundary of a domain positioned above Earth's surface via a Maxwellian flux. This generation is informed by species number density and bulk temperature output from the MSIS model, which required conversion of the global simulation time in the DSMC to UTC, the conversion of code coordinates into geocentric latitude and longitude, tracking of local solar time, and the general overhaul of code parameters and species information to match the physics of the Earth system. The Earth DSMC model takes input of F10.7 and AP parameters, as well as a time in UTC and a domain in latitude, longitude, and altitude. It advances a simulation through time, at each step interfacing with MSIS on every cell on the lower boundary of the initially-empty domain, generating an atmosphere which rises, expands, and ultimately achieves a quasi-steady state that exhibits transient variation on a diurnal scale.

With atmospheric generation complete, the next objective was the introduction of a solar heating model, achieved largely through radiative absorption into the rotational states of trace species. Molecules able to accept such radiation are those with permanent electric dipoles, none of which are included in the MSIS atmosphere; species present in the mid-thermosphere and above with the necessary structure and composed of atoms in the MSIS system include NO, OH, and H_2O. In practice, solar heating was passed to the rotational states of representative molecules of these species at a rate attenuated by their atmospheric depth – the molecules then experienced rotational relaxation and potentially spontaneous photon emission while transferring their internal energy to the remainder of the atmosphere via collision. That process necessitated incorporation of models for solar shadow, for the attenuation of solar heating with atmospheric shielding, and for Monte Carlo photon transfer between molecules.

Further objectives included the incorporation of photochemistry for the Earth species, and the ability to toggle between rates for quiet and active sun cycle cases to match a simulation date. Photodissociation alters atmospheric chemistry, introducing energy into the translational modes of daughter species and serving as a secondary mechanism for atmospheric heating. Finally, satellite-tracking functions were developed to facilitate code comparison with mass-density observations from the CHAMP and GRACE satellite datasets.

2. Methodology

2.1. Development and application of the Earth DSMC model.

In application of the Direct Simulation Monte Carlo method, the motions and collisions of a number – here, $O[10^6$ to $10^9]$ – of representative molecules in a rarefied flow are computed, offering a probabilistic solution to the Boltzmann equation. In the context of the Earth simulation, these representative molecules are introduced as Maxwellian flux through the lower boundary, with species number densities and bulk temperatures along that boundary drawn from the semi-empirical MSISE-00 model. This process of surface flux creation occurs at the start of each time-step, and within each boundary cell. MSIS is queried at the boundary altitude, with cell-centered geocentric latitude and longitude at the local solar time. Geomagnetic and solar flux indices are set manually in these simulations and are not coupled to the simulation time; however, the DSMC is linked with code enabling the interpolation of such values from historic space weather datasets. The number of simulation particles generated for one species in a time step of length Δt may be calculated

$$\sqrt{\frac{k\,T}{2\,\pi\,m_s}}\left[\frac{n_s\,A\,\Delta t}{W}\right] \tag{1}$$

with k the Boltzmann constant, temperature T, species mass m_s, species number density n_s, surface cell area A, and weight ratio (that is, real-particles-per-simulation-particle) W. This is necessarily a real number, so generation of an integer count of particles requires sampling from a Poisson distribution. MKL and GSL library functions are

available, but Garcia presents a useful algorithm for DSMC applications that we employ here. Positions of fluxing particles are distributed uniform-random on the boundary surface, with velocities drawn from accept-reject sampling about the most probable molecular speed.

Photodissociation of sunlit molecules alters chemistry and introduces heat to the atmospheric column. Particles in sunlight are selected to photodissociate with probability calculated

$$P_i = 1 - \exp[-\Sigma_j^{N_i}(k_{i,j}\Delta t)] \quad (2)$$

in which N_i is the number of photoreactions available for species i, and $k_{i,j}$ is the rate of the j-th photoreaction of that species. When a molecule is photodissociated in the DSMC, it is broken apart into its daughter species, increasing the number of particles present in the simulation; its internal energy is directed into the relative translational motion of the products, as is the reaction's mean excess energy as given by Huebner. Product velocities are isotropically oriented. Both active and quiet sun cycle photochemistry data are included in the DSMC, as shown in Table 1.

Table 1: Unattenuated photodissociation rates and excess energies for selected upper-atmospheric species.

Reactant	Products	Reaction Rate (Active / Quiet) [s^{-1}]		Excess Energy (Active / Quiet) [eV]	
O_2	O + O	$6.78 * 10^{-6}$	$4.23 * 10^{-6}$	1.675	1.431
N_2	N + N	$1.56 * 10^{-6}$	$6.61 * 10^{-7}$	3.380	3.380
NO	N + O	$3.21 * 10^{-6}$	$2.20 * 10^{-6}$	2.720	1.840
OH	O + H	$3.35 * 10^{-5}$	$1.98 * 10^{-5}$	5.576	4.370
H_2O	OH + H	$1.76 * 10^{-5}$	$1.03 * 10^{-5}$	4.040	3.420

A primary mechanism for heat introduction into the simulation is through the absorption of solar infrared radiation into the rotational states of molecules with permanent electric dipole moments. Emission band strengths are calculated for such diatomics – NO and OH, for these simulations – from kinetic theory, and fit to observations in the literature for more complex molecules (e.g. H_2O). The rate of infrared emission is modeled with a power law in temperature, with exponent 2.0 for diatomics and linear triatomics. Absorption may occur as solar radiation penetrates the atmosphere or as radiation emitted spontaneously from cooling molecules is re-absorbed. The latter process is implemented via a photon Monte Carlo method. Total column density is integrated in an independent and comparatively coarse grid oriented parallel to incident sunlight, allowing for the attenuation of photo-dissociation and radiative absorption rates with atmospheric shielding, a technique demonstrated in Figure 1.

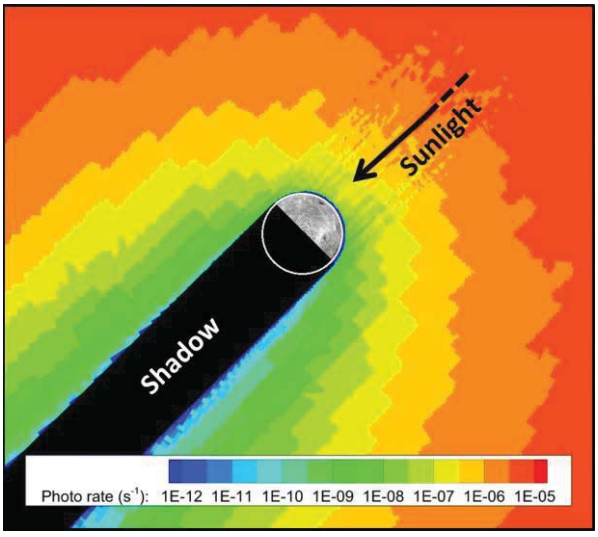

Figure 1: Attenuation of H_2O photodissociation rates through a cloud of neutral gas in the lunar environs[1].

The remainder of the DSMC method is straightforward to apply in this case – simulation particles are moved within the time step, passing between processors and interacting with domain boundaries if necessary – they are

[1] P. Prem, personal communication, June 2014.

indexed within the cell structure and may collide with one another within a cell. Particles are moved via the integration of their force equations in a predictor-corrector scheme; in this neutral-density simulation, forcing includes gravity but neglects E and B fields. Non-inertial forcing models are available in the planetary DSMC for the Io–Jupiter case, but were not adapted to the Earth—Moon system for this work.

In the DSMC method collisions are probabilistic, not deterministic, and may occur between sampled representative molecules within the domain's cells. A gas of sufficient rarefaction allows the treatment of solely binary collisions, in which the timescale for collision dynamics between two representative molecules is dwarfed by the mean time between collisions: these assumptions allow for particle collision and motion to be decoupled. In the Earth simulations collisions drive bulk motion and transfer energy between molecules, but do not induce chemistry – an Arrhenius mechanism for dissociative and recombinative reactions was considered, but its treatment ultimately deemed beyond the scope of this work. Lastly, representative molecules are sampled within cells (not necessarily of the same configuration as the collision cells) in calculating bulk atmospheric properties: these are the output densities, temperatures, and pressures ultimately compared against MSIS and the satellite datasets.

2.2. Treatment of the simulation domain.

Continuum models of fluid dynamics break down for gases of sufficient rarefaction, in which "gradients of the macroscopic variables become so steep that their scale length is of the same order as […] their *mean free path*" (Bird 2). More generally, the continuum conservation equations are only valid to the extent that shear stress and heat flux may be expressed in lower-order quantities. A useful ratio in expressing the level of rarefaction in a gas is the Knudsen number, which relates the mean free path λ to a flow characteristic length L,

$$Kn = \lambda / L. \tag{3}$$

This is expressed most clearly when L is a local characteristic length, relating density ρ to its spatial gradient as

$$L = \rho / (\partial \rho / \partial x). \tag{4}$$

Continuum assumptions begin to break down for Knudsen numbers above 0.1; the Boltzmann equation, which the DSMC is formulated to approximate, remains valid past this range. A Knudsen number may be calculated for a characteristic atmospheric simulation in which L is taken to be the scale height.

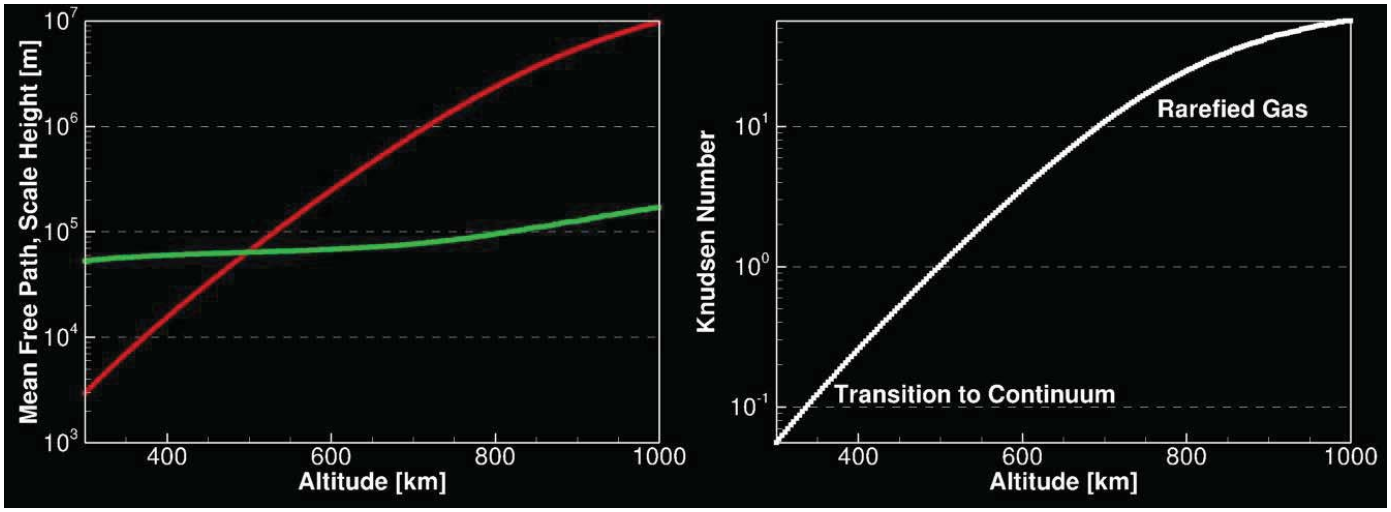

Figure 2: Mean free path (red) and scale height (green) at left; atmospheric Knudsen number at right.

Scale height is a macroscopic length scale, but the results for L as local characteristic length as expressed in (4) above are comparable. The simulation domain selection is motivated by the finding that the transition to continuum model validity occurs just above 300 km, while the transition to collisionless flow (at $Kn \sim 100$) occurs at 1000 km. As continuum GCMs are established below 300 km, and the particle-based DSMC method increases rapidly in computational expense with atmospheric density at lower altitudes, 300 km is employed as the lower boundary for the simulations discussed herein. A 1000 km upper boundary is selected for direct comparison against the MSIS model, which also terminates at that altitude. However, a 10000 km vacuum buffer cell is appended to the domain

top, in which particles move in purely ballistic trajectories and without collision sampling, to prevent non-physical escape. Particles that exit the domain top or bottom are deleted from the simulation: a vacuum boundary.

One-dimensional simulations are first considered – this bears the necessary caveat that DSMC simulations are not strictly one-dimensional in particle motion, as it is critical that representative molecules retain their three translational degrees of freedom. Instead, such simulations are performed in thin columns with periodic edge boundaries. As the only interface between the Earth DSMC model and the MSIS comes on the lower boundary surface, it is useful to compare temperature, number density, and molar fraction profiles against the MSIS output to determine how the complex physics of the DSMC simulation can replicate that empirical fit. Full-planet, three-dimensional simulations are next considered. A property of interest is the integrated column density, that is, the particle count per unit area taken from the lower boundary into the exosphere. It is in these three-dimensional simulations that satellite paths may be tracked through cells, and comparisons of mass-density made.

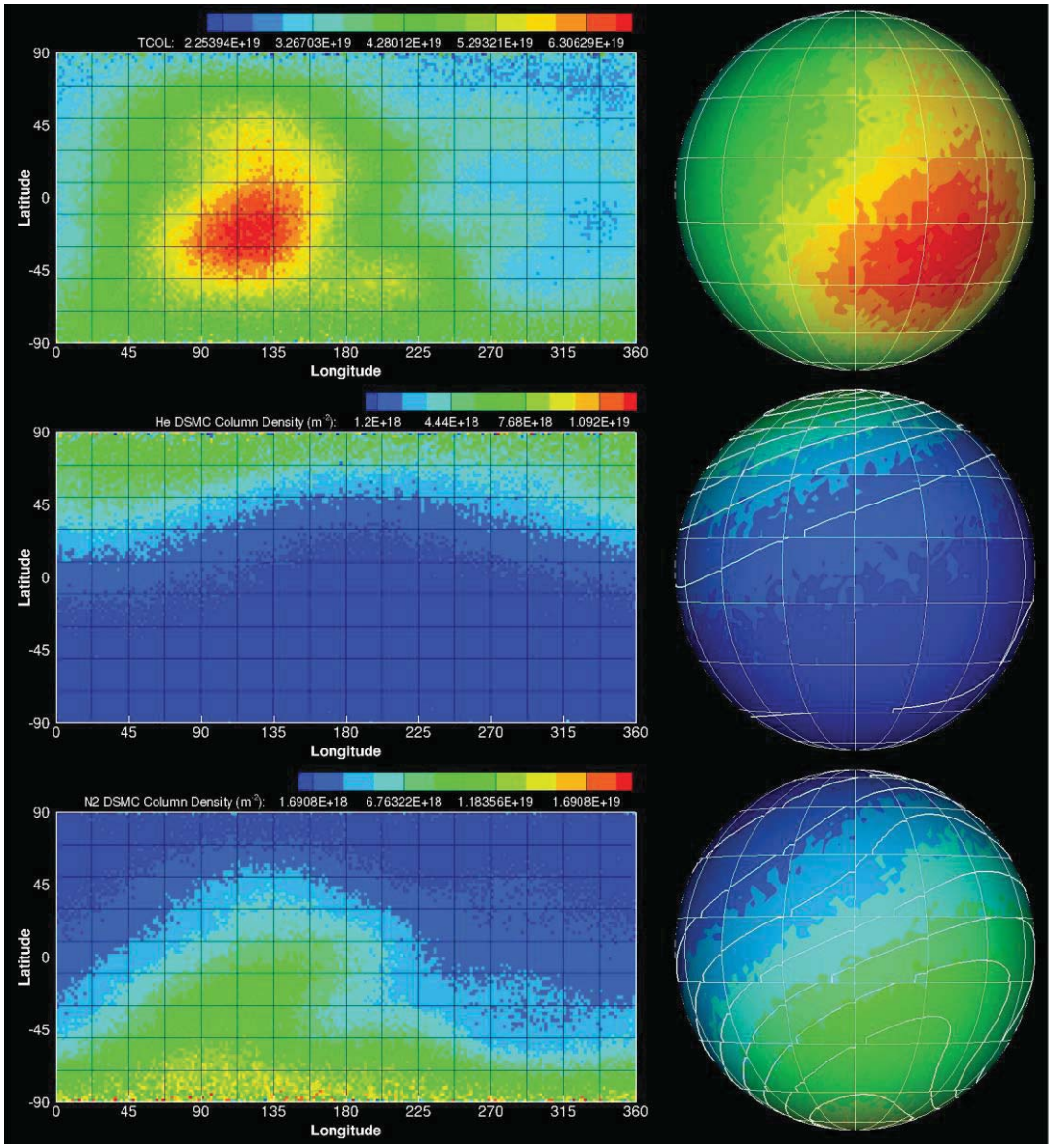

Figure 3: Full-planet atmospheric simulations demonstrating total (at top) and select species column densities. The figures at right are looking down on the subsolar point, presently at 90° longitude. Note the polar variance in He and N_2 species column densities, and their similarity to MSIS boundary number density in white contours on the globes. The visible grid in latitude and longitude also represents the surface boundaries of this 144 processor simulation.

3. Results

A one-dimensional simulation is performed in which the domain encompasses an equatorially-centered grid 3° on edge: latitudes from -1.5° to 1.5° and longitudes from 0.0° to 3.0° are considered. The simulation lower boundary is set to 300 km altitude, while the upper limit of the collisional domain is taken at 1000 km. After a period of equilibration (of duration 9300 s) at the outset of the calculation, during which the initially-empty domain is populated by flux across its lower boundary, time-averaged flow field properties are calculated between 17:15 and 17:25 LST. To ensure sufficient representative molecule populations at high altitudes, on the order of $3 * 10^5$ particles are employed per cell column. The MSIS species [N, O, N_2, O_2, He, and H, with Ar neglected at these altitudes] are generated from that model's density output, while the trace species NO, OH, and H_2O are generated to the order of their estimated concentrations: one part-per-thousand NO, and one part-per-million each OH and H_2O.

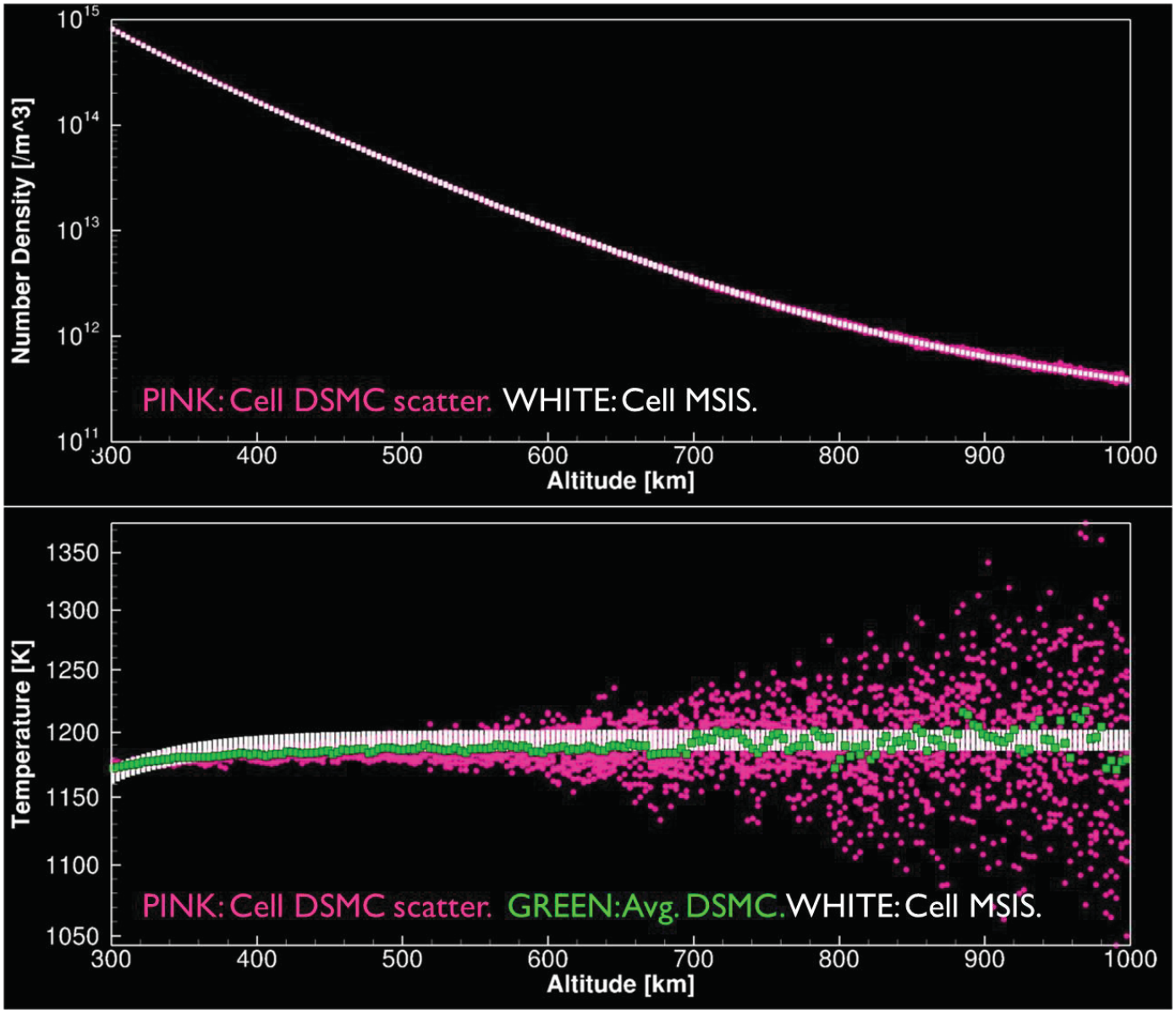

Figure 4: Cell-sampled total number density and temperature versus MSIS expectation. [600 s time-average.]

The DSMC number density profile, shown in the top portion of Figure 4 as pink scatter points of cell-sampled values versus the MSIS in white, demonstrates a close match: at 1000 km, the models agree to within 3 %. It is

important to note that these results are a natural outgrowth of the simulation physics – the DSMC only interfaces with MSIS during particle generation on the lower boundary. The DSMC temperature is noisy, even in the time-average, but a spatial average across the domain (shown in green) demonstrates the MSIS trend of near-constant temperature, including heating at the lower boundary that corresponds with radiative absorption of NO.

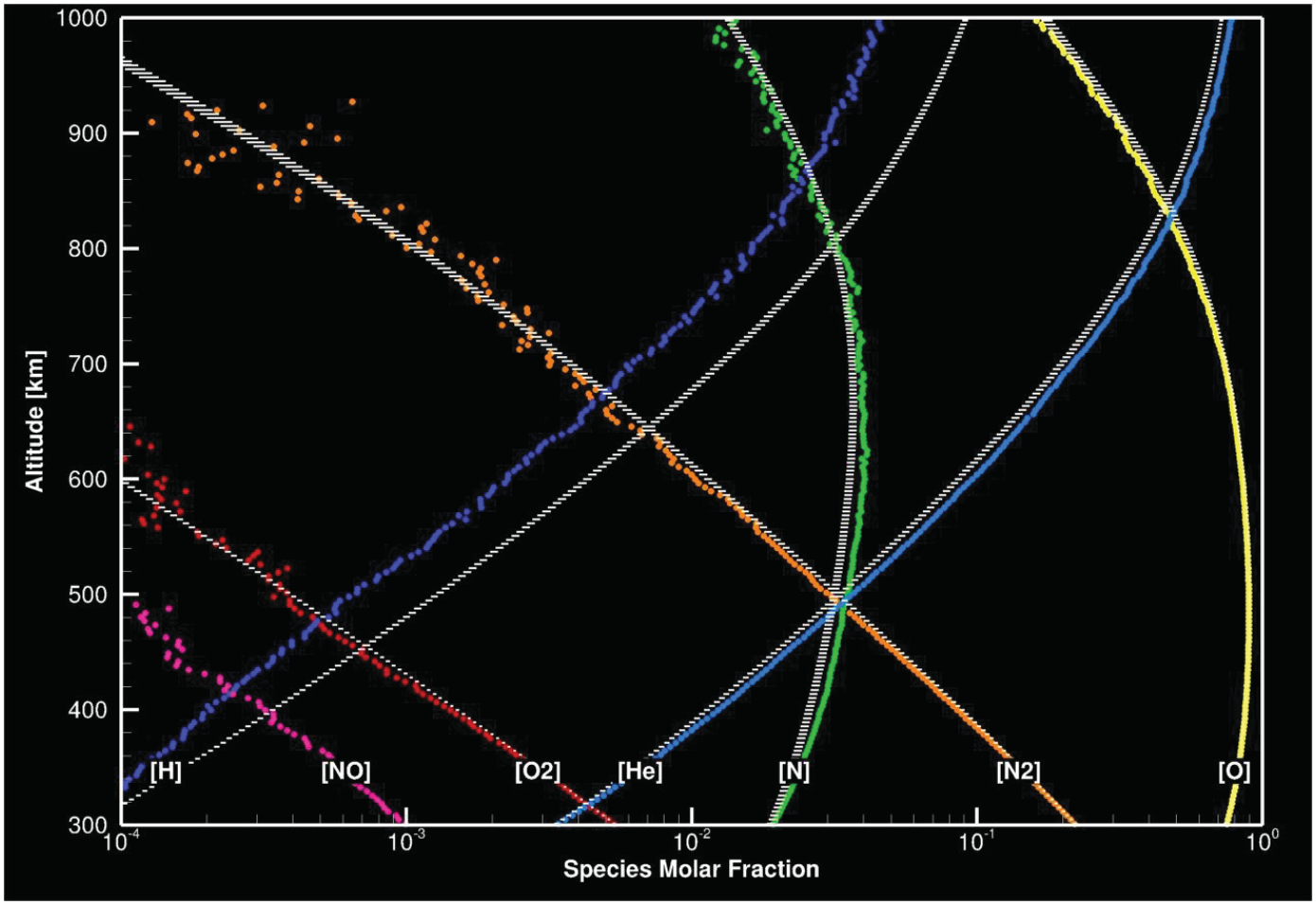

Figure 5: Cell-averaged species molar fractions versus MSIS expectation. [600 s time-average.]

Molar fractions trend closely in altitude with their corresponding MSIS profile and exhibit separate species scale heights, shown in Figure 5. A notable disagreement is monatomic hydrogen, comparatively underrepresented by the DSMC in this calculation: a consequence of non-physical escape. A vacuum boundary condition is enforced at the edge of the buffer cell (here, effectively 11000 km above the Earth's surface), which eliminates any particles that pass above the boundary – even if they have insufficient energy to escape Earth's gravity, and would ultimately fall back along their ballistic trajectories. This effect is only noticeable here for hydrogen, due to its low mass and consequently large species scale height, and is reparable by extending the vacuum buffer cell.

Three-dimensional, full-planet simulations were necessary for comparison against the CHAMP satellite dataset. For the case demonstrated in Figure 6, 09 Jan. 2005 was selected as a simulation date with anomalously low geomagnetic activity. Solar flux and geomagnetic indices were set according to their observed values on that date, with reference to the simulation time in UTC. The DSMC output was time-averaged in bins between CHAMP data-points, at roughly 50 s intervals. Satellite mass-density was compared against the value of the DSMC mass-density in the cell occupied by the satellite at a given point in time: this process could be refined in future work by averaging density among cell nearest-neighbors and weighting against the actual satellite position within its cell.

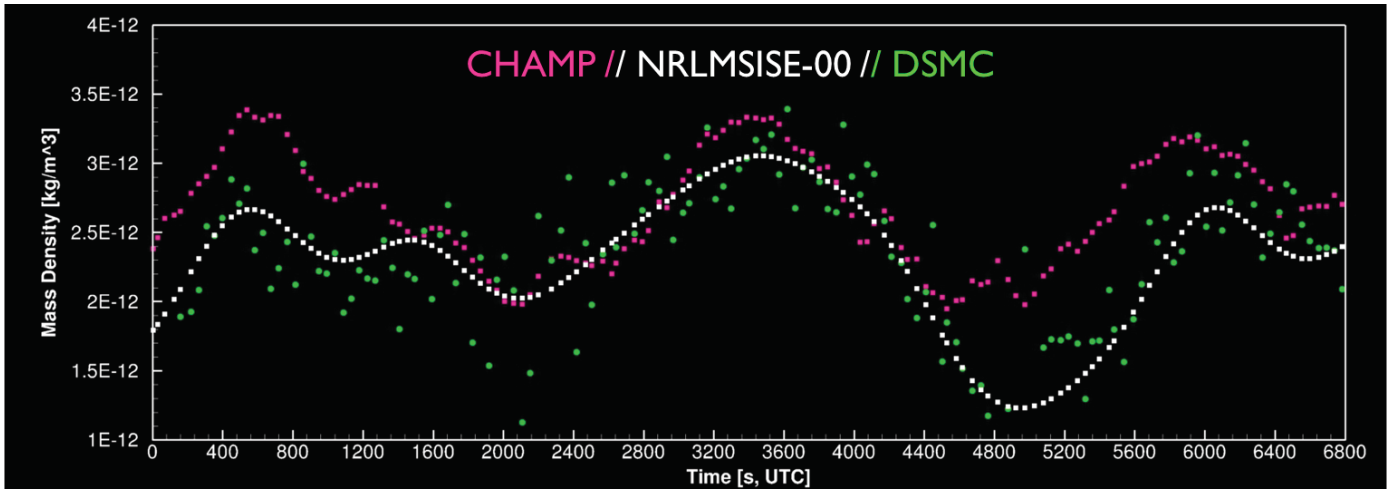

Figure 6: Comparison of CHAMP mass-density observation with MSIS and a DSMC calculation.

The DSMC mass-density values are shown to trend closely with the MSIS and CHAMP data-sets, although there is an evident bias toward the former when they disagree. This is unsurprising, as CHAMP operates here below 400 km, near the lower boundary informed in the DSMC by MSIS. Periods of high noise in the DSMC calculation (e.g. 1600 to 2400 s) correspond to the satellite passing over a polar region, an artifact of small cells in such regions.

4. Conclusions

A fully three-dimensional and transient model of the rarefied component of Earth's neutral atmosphere is presented. The DSMC method has many advantages in this domain: most notably, its comparatively low expense and high stability in the rarefied regime by comparison with continuum solutions, and the ease with which the method may be modified to include new physics. DSMC results demonstrate close agreement with the trends of MSIS throughout the atmosphere, in a natural consequence of the code physics and MSIS-informed creation on the lower boundary surface. Future work will include the comparison of wind patterns against observation, the addition of more sophisticated physics and chemistry models, and large-scale, direct comparison against other GCM datasets.

References

Belehaki, A., Stanislawska, I, and Lilensten, J., "An overview of ionosphere – thermosphere models available for space weather purposes", Space Science Review, Vol. 147, 271-313, 2009.

Bird, G. A. *Molecular Gas Dynamics and the Direct Simulation of Gas Flows*. Oxford University Press: New York, NY, 1994.

Garcia, A. L. and Wagner, W., "Generation of the Maxwellian inflow distribution", Journal of Chemical Physics, Vol. 217, 693–708, 2006.

Huang, T. and Hickey, M., "On the latitudinal variations of the non-periodic response of minor species induced by a dissipative gravity-wave packet in the MLT region", Journal of Atmospheric and Solar-Terrestrial Physics, Vol. 69, 741-757, 2007.

Huebner, W. F., Keady, J. J., and Lyon, S. P., "Solar photo rates for planetary atmospheres and atmospheric pollutants", Astrophysics and Space Science, Vol. 195, 1-294, 1992.

Moore, C. H., *Monte Carlo Simulation of the Jovian Plasma Torus Interaction with Io's Atmosphere and the Resultant Aurora during Eclipse* (Doctoral dissertation). The University of Texas at Austin, Department of Aerospace Engineering and Engineering Mechanics, 2011.

Ozawa, T. *Improved Chemistry Models for DSMC Simulations of Ionized Rarefied Hypersonic Flows* (Doctoral dissertation). The Pennsylvania State University, Department of Aerospace Engineering, 2007.

Picone, M., Hedin, A. E., and Drob, D., "NRLMSISE-00 empirical model of the atmosphere: Statistical comparisons and scientific issues", Journal of Geophysical Research, Vol. 107, No. A12, 1468-1483, 2002.

Rusch, D. W., Gerard, J., and Fesen, C. G., "The diurnal variation of NO, N(^{2}D), and ions in the thermosphere: A comparison of satellite measurements to a model", Journal of Geophysical Research, Vol. 96, No. A7, 11331-11339, 1991.

Vincenti, W. G. and Kruger, C. H. *Introduction to Physical Gas Dynamics*. John Wiley & Sons, Inc., 1965.

Global high-latitude conductivity modeling: New data and improved methods

Ryan McGranaghan

Aerospace Engineering Sciences, University of Colorado Boulder, Boulder, CO

Humberto Godinez

Los Alamos National Laboratory, T-5, Los Alamos, NM

Steve Morley

Los Alamos National Laboratory, ISR-1, Los Alamos, NM

Delores Knipp

High Altitude Observatory, National Center for Atmospheric Research, Boulder, CO

Aerospace Engineering Sciences, University of Colorado Boulder, Boulder, CO

Tomoko Matsuo

Cooperative Institute for Research in Environmental Sciences, Boulder, CO

Abstract

This work focuses on determining how effectively the upper atmosphere, as a medium, transmits the influence of an electric field into differential charge motion (current). This effect is called conductivity. Conductivity modulates height-specific energy deposition in the ionosphere and thermosphere. In most space-age applications this influence has been simplified to an equivalent behavior in a thin shell at ∼120 km, so the determination has traditionally been made for height-integrated conductivity (conductance) only. Further, several assumptions in past work have led to large representativeness error in conductance models that are still used in simulations of the global atmosphere. We present two primary results that represent significant improvements in conductivity modeling: 1) a first principles model for calculating height-dependent ionization and conductivity profiles and 2) empirical orthogonal function representation of the primary modes of variability for mid- and high-latitude Hall and Pedersen conductivities. These results represent a crucial improvement for atmospheric specification by enabling global height-specific views of how solar and magnetospheric energy influence the dynamics of the ionosphere and thermosphere, and how this energy then feeds back to the magnetosphere.

Keywords: conductivity, ionospheric electrodynamics, empirical orthogonal functions

1. Introduction

Atmospheric drag produces the dominant uncertainty in the orbital prediction for objects in lower and mid-Earth orbits (Marcos, 2006; Bowman et al., 2008a). The collision between the Iridium 33 and Cosmos 2251 spacecraft scattered hundreds of pieces of space debris into low Earth orbit (LEO) (Wang, 2010) and created an international awareness of the space debris problem. Currently, many thousands of objects reside in LEO and the potential for future collisions puts billions of dollars of space assets at risk. Collision prevention for the international space station,

Email addresses: ryan.mcgranaghan@colorado.edu (Ryan McGranaghan), hgodinez@lanl.gov (Humberto Godinez), smorley@lanl.gov (Steve Morley), delores.knipp@colorado.edu (Delores Knipp), tomoko.matsuo@noaa.gov (Tomoko Matsuo)

conjunction analysis, satellite lifetime estimates, space situational awareness, and reentry prediction are just a few of the critical applications for precise orbit determination and tracking. Neutral density uncertainties primarily determine errors in drag estimates. Specifying thermospheric neutral density between 100 and 1000 km remains a central focus of the space science and aerospace communities (Prölss, 2011).

Highly variable external drivers complicate the accurate prediction of drag forces on objects below 700 km. Continual attention since the 1970s has led to advancements in modeling this dynamic thermospheric state by a number of empirical models, including the Jacchia models and their derivatives (Bowman et al., 2008b), Mass Spectrometer and Incoherent Scattering relations (Picone et al., 2002), and the Air Force High Accuracy Satellite Drag Model (Storz et al., 2005; Marcos, 2006). Recently, studies of global thermospheric density using thermospheric and ionospheric general circulation models (GCMs) have provided significant capabilities in reproducing periodic variations in neutral mass density (Sutton et al., 2009; Qian and Solomon, 2012; Zhang et al., 2014). However, thermospheric modeling efforts are limited by current shortcomings in the reconstruction of the ionosphere and its coupling to the magnetosphere above. In this work, we address a key element enabling more accurate reconstructions: the ionospheric conductivity.

Ionospheric current systems, and their associated electrodynamics, not only intrinsically link the magnetosphere and ionosphere to neutral atmospheric circulation, but also couple the entire system from the solar wind through the base of the upper atmosphere (~80 km). A number of electrodynamic processes are driven by solar wind-magnetosphere-ionosphere interactions (Amm et al., 2008). The coupling between these regimes is largely controlled by a complex system of field-aligned currents linked by horizontal Hall and Pedersen currents. To truly understand these current systems, 3-D spatial and temporally evolving distributions of electrodynamic quantities are needed to solve the dynamics of the system, for which the salient equations (Eqs. 1 - 4) are fundamentally coupled as demonstrated by Vasyliunas (1970). Accurate specification of the ionospheric electrodynamic state is crucial. In any magnetosphere-ionosphere (MI) forecast algorithm two key parameters must be specified: Electric field and conductivity. These parameters are crucial elements of upper atmosphere General Circulation Models (GCMs).

The Thermosphere Ionosphere Electrodynamics General Circulation Model (TIEGCM) (Richmond et al., 1992) and the Global Ionosphere Thermosphere Model (GITM) (Ridley et al., 2006), have aided in interpreting observations and the verifying hypotheses about the state of the thermosphere arrived at from other means. These GCMs yield a large degree of qualitative agreement with observations, but also contain differences that may largely be due to uncertainties in the high-latitude energy inputs (Codrescu et al., 1995; **?**). Particularly, Joule heating, which is one of the main energy sources of the upper atmosphere, is a function of the electric field and its variability, as well as conductivity and its variability in the ionosphere. Fluctuations in these quantities occur on a variety of temporal and spatial scales and are extremely difficult to characterize, especially during substorm activity. Storm and substorm activity cause intensification of ionospheric currents, whose distributions largely determine redistribution of mass, energy, and momentum throughout the system. Characterizing these distributions and their relationship to the electric fields depends on knowledge of the Hall and Pedersen ionospheric conductivities. GCMs currently rely on statistical averages to quantify the electric field and conductivities. Statistical averages lead to an overly simplistic characterization of the ionospheric electrodynamic environment and what can amount to significant errors in the model output in general. Uncertainties and disagreement in the GCMs are exacerbated by poor knowledge of ionospheric conductivitities.

Accurate specification of the global ionospheric conductivity fields are thus vitally important, yet this is a very difficult problem due to uncertainties in the system and the available observations. We present two results that demonstrate significant progress toward more accurate specification: 1) a new model that calculates height-resolved ionization rate and conductivity profiles free of several assumptions that limited past efforts and 2) characterization of the principal modes of variability of the Pedersen and Hall conductances. The model is built on the framework of the GLobal AirglOW (GLOW) code (Solomon et al., 1988), a first-principles approach to ionosphere-thermosphere energy redistribution, but extended to include direct calculations of the ionospheric conductivities. We refer to this new model as GLOWcon, GLOW + conductivity. Further, accurate specification of the ionosphere depends on optimal statistical interpolation methods using sparse or irregular observations. Such methods are only truly optimal if accurate background error covariance matrices are used. By characterizing the primary modes of variability of the conductivities, we determine the necessary information for improved background error covariance matrix design that will directly contribute to more accurate ionospheric models.

This paper is laid out in the following manner: first, we briefly detail the current state of ionospheric electrodynamic modeling, including its limitations. Next we discuss the methodology, followed by a results section accompanied by discussion. We present concluding remarks, including plans for future work, in the final section.

2. Background and improvements

Figure 1 (from Lotko et al. (2014)) shows a motivating example of the importance of the ionospheric conductivity and its wide influence in the magnetosphere-ionosphere-thermosphere (MIT) system. The figure shows three columns, each with a different applied Hall conductance distribution (shown in color in the top row of the figure). The labels *Uniform*, *Causal-empirical*, and *Hall depletion* refer to the Hall conductivity distribution applied for that column and represent the only difference between simulations. The bottom row shows an equatorial cut from the results of a magnetohydrodynamic simulation of the magnetosphere (color shows the velocity magnitude and the white line is the magnetic reconnection x-line mapped along magnetic field lines). All plots are shown with the Sun off to the top of the figure and looking down on the northern hemisphere.

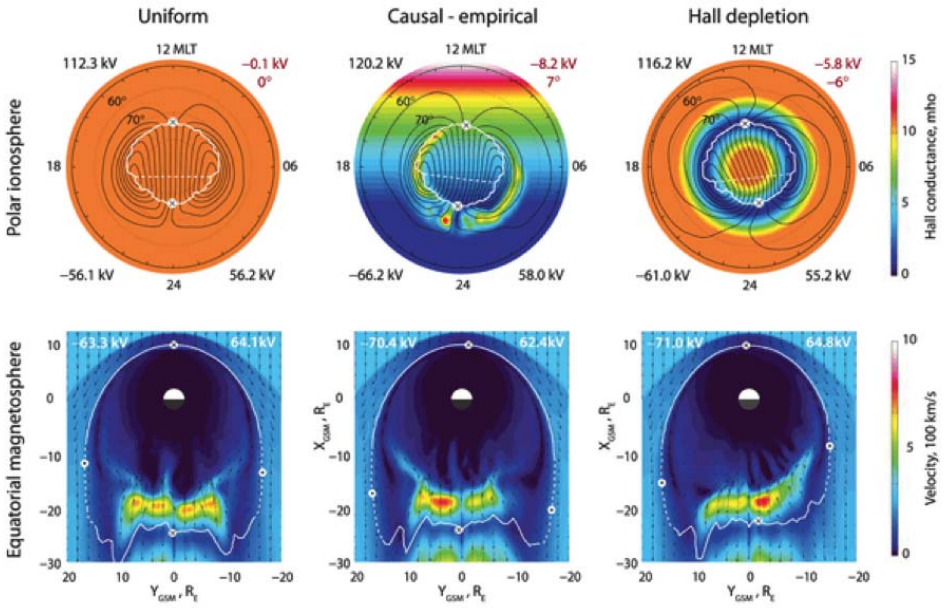

Figure 1: Reproduction of Figure 3 from Lotko et al. (2014) showing simulated ionospheric convection (8 kV contours) and Hall conductance distributions (color) on the top and the simulated equatorial magnetosphere with velocity vectors overlaid on the velocity magnitude in color. In the left and right panels, a uniform 5 S Pedersen conductance is applied, whereas the middle panel uses a causal value close to that shown for the Hall conductance. The white line in the top shows the magnetic x-line mapped along magnetic field lines from the magnetosphere and in the bottom it represents the $B_z = 0$ contour (magnetic reconnection x-line).

Clearly, the Hall conductance, which manifests deep in the ionosphere, drastically affects magnetospheric convection and even the locale of magnetic reconnection. The realistic Hall conductance distribution, middle panel, produces plasmasheet flows consistent with satellite observations and convection consistent with empirical patterns (Lotko et al., 2014).

The Assimilative Mapping of Ionospheric Electrodynamics (AMIE) procedure (Richmond and Kamide, 1988) has addressed and illuminated the outstanding issues of ionospheric electrodynamics. Both as a self-consistent model of the ionospheric electrodynamics and as input to the GCMs, AMIE has significantly contributed to knowledge of MIT linkages, and has been applied to MIT problems in wide measure. AMIE brings together diverse sets of remote and in-situ ionospheric observations in a Bayesian analysis scheme with the assumption of multivariate normal prior and observational errors to estimate electrodynamic quantity distributions (Richmond et al., 1988; Knipp, 1989; Richmond, 1992; Matsuo et al., 2005). AMIE, and similar procedures, calculate a solution for the electrostatic potential, Φ, from which the complete electrodynamic state of the ionosphere can be specified under certain simplifying assumptions using Maxwell's equations:

$$\mathbf{E} = -\nabla\Phi \tag{1}$$

$$\mathbf{J}_\perp = \bar{\bar{\Sigma}} \cdot \mathbf{E} \tag{2}$$

$$\mathbf{J}_\parallel = \nabla \cdot \mathbf{J}_\perp \tag{3}$$

$$\nabla \times \delta\mathbf{B} = \mu_0 \mathbf{J}, \tag{4}$$

where:

$\mathbf{E}$ = electric field
$\bar{\bar{\Sigma}}$ = conductance distribution (assumed given *a priori*)
$\mathbf{J}_\perp$ = horizontal currents
$\mathbf{J}_\parallel$ = field-aligned currents
$\mathbf{B}$ = magnetic field
μ_0 = permeability of free space.

The output of the AMIE procedure, usually mapped to 110 km, where ionospheric conductivity tends to maximize, can be used to supply the high-latitude input to the GCMs. AMIE relies on assumed knowledge of the ionospheric conductance and bases this knowledge on 2-D distributions created more than 25 years ago by Fuller-Rowell and Evans (1987). AMIE provides distributions of height-integrated conductivity (conductance) as a first step in the procedure, though the estimates are built on a formulation based on a Maxwellian auroral spectrum (Robinson et al., 1987). Particles incident on the topside ionosphere travel along magnetic field lines into the ionosphere where collisional processes allow them to deposit their energy in the form of excitation and ionization of ambient constituents and their momentum in the form of elastic collisions. Ionization causes an increase in the charged particle population and thus affects electrical conductivities. The modification of the ionosphere as a result is a function of the incident particles' spectral energy distributions.

Auroral particle precipitation has distinctive source regions such as the cusp, low-latitude boundary layer (LLBL), central plasma sheet (CPS), and boundary plasma sheet (BPS). The characteristics of precipitation across regions vary greatly (Hardy et al., 2008). Simply assuming a Maxwellian distribution to describe all high-latitude precipitation can introduce large errors in atmospheric specification. An important breakthrough for the space science community is the elimination of this base assumption, which we accomplish in this work.

2.1. Reducing the reliance on conductance and improving uncertainty estimates of conductivity

Traditionally, ionospheric conductivity modeling has been one dimensional (e.g. along a single radar beam) or two dimensional (from a system of ground magnetometers or satellite observations of particle precipitation) (Amm et al., 2008). However, with new observations and advanced techniques to process them, a 3-D picture of the ionospheric conductivity is attainable. We move toward this goal by using satellite observations with a first-principles model of energy redistribution in the atmosphere to create a 3-D characterization of the dominant modes of variability of the high-latitude conductivity. Though 3-D conductivity has been examined before (see, for example, Evans et al. (1977) and Kirkwood et al. (1988)), this work is unique in two respects: 1) we analyze global conductivity variations over an extended interval and 2) we model the height-resolved conductivity free of several assumptions used in these analyses previously. These assumptions that can be dropped include:

- an equivalent ionospheric current (2-D approximation) for the ionospheric current systems;
- a Maxwellian energy spectrum of precipitating particles; and
- proxies and/or indices of geomagnetic activity as substitutes to quantify ionospheric phenomena associated with currents.

We use direct observations of precipitating particles made by the Defense Meteorological Satellite Program (DMSP) F16, F17, and F18 satellites with the first-principles GLOW model of the ionization and energy redistribution (Solomon et al., 1988) to eliminate these assumptions and analyze the ionospheric conductivity. The global maps of conductivity variability presented here can be utilized to directly address the uncertainty in the GCMs and the outstanding issues in the AMIE procedure. This work, to our best knowledge, represents the first attempt to determine the primary modes of variability of ionospheric conductivity using first-principles modeling and directly-observed complete particle precipitation spectra.

2.2. Removing the Maxwellian assumption: Particle precipitation data set

Defense Meteorological Satellite Program (DMSP) spacecraft provide the primary data set for this work: The energy flux of charged particles precipitating into the upper atmosphere along satellite orbit tracks from the magnetosphere. This information is a useful measure of geomagnetic activity and energy dissipation (Hardy, 1985; Fuller-Rowell and Evans, 1987; Hardy et al., 2008; Newell, 2009; Emery et al., 2009). DMSP satellites are in polar orbits about the Earth at geocentric altitudes between 800-900 km with orbital periods of roughly 100 minutes (Rich et al., 1985). Each spacecraft is in a sun-synchronous orbit which guarantees a 360° precession of the orbital plane per year in inertial space.

Figure 2 shows the coverage of the F16, F17, and F18 spacecraft in the (a) northern hemisphere and (b) southern hemisphere in magnetic latitude and local time during 2010. There is broad local time coverage in both hemispheres due to the eccentricity, or offset, of the geomagnetic poles from the geographic poles (Hardy, 1984). The geomagnetic pole in the southern hemisphere has a larger eccentricity, which creates the hemispherical asymmetry in MLT coverage (Knipp et al., 2014).

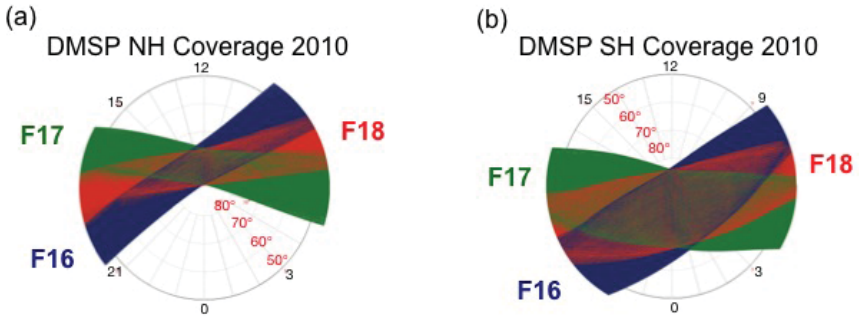

Figure 2: DMSP satellites F16 (blue), F17 (green), and F18 (red) orbital coverage in magnetic local time and magnetic latitude throughout 2010. Local noon is at the top of the figure. (a) Northern hemisphere and (b) southern hemisphere.

The DMSP F16, F17, and F18 spacecraft are outfitted with space environment monitors (the Precipitating Electron and Ion Spectrometer (SSJ/5)) that detect auroral electrons and ions with energies between 30 eV and 30 keV. The SSJ/5 instrument replaced the SSJ/4 instrument for DMSP satellites subsequent to F15. The DMSP detectors provide complete particle energy spectra so that no assumption about the distribution is necessary. Complete particle spectra are provided every second such that, given a lower latitude limit of 45° and a compilation duration of one year, ~8 million spectra per satellite per hemisphere are available. The electron differential energy fluxes directly measured by the SSJ/5 instrument drive the first-principles model in this work (i.e. no assumption about the spectral shape is made). We discuss the incorporation of these spectra into a first-principles model and our supporting methodology in the next section.

Recently, Matsuo et al. (submitted) adapted the AMIE procedure to incorporate large quantities of space-based magnetometer data to produce high latitude electrodynamic maps (see example in Knipp et al. (2014)). Further investigation by Matsuo and colleagues revealed discrepancies between AMIE results generated using ground- vs. space-based observations, and thus a pressing need to improve the height-dependent conductivity. Conductivity is

the key parameter that enables the assimilation of ground- and space-based data sets for consistent electrodynamics analyses. 2-D approximations of the conductivities are unable to produce the localized heating and ionospheric modification that influence this coupling of the upper atmospheric plasma and neutral environments. In this work we address several of the shortcomings in previous attempts to specify the ionospheric conductivity that links Earth's atmosphere to the magnetosphere.

3. Methodology

In this section, we focus on the methodology for a new means to address conductivity research. This new technique promotes significant improvement in high-latitude electrodynamic analysis. The methodology for this study is threefold, each tier addressing a limitation in the current state of conductivity modeling: 1) improved characterization of high-latitude particle precipitation and its combination with the effects of solar ionization, 2) creation of a height-dependent conductivity model, and 3) creation of a means to estimate the global distribution of conductivity and its variability.

3.1. Characterization of ionization sources

The first step in arriving at conductivity profiles requires an accurate characterization of the ionizing sources. The two primary sources are solar radiation and magnetospheric particle precipitation. The EUVAC (Richards et al., 1994) solar irradiance flux spectrum, along with the Hinteregger et al. (1981) spectrum in the 1.8-5.0 nm wavelength range, is adopted to model the solar radiation source and DMSP particle spectra polewards of 45° latitude handle the auroral source term. Subsequently, we address atmospheric particle transport, which is the second tier in our methodology.

3.2. Overcoming lack of direct observation of conductivity: GLobal AirglOW + Conductivity (GLOWcon) model

The GLobal AirglOW (GLOW) model (Solomon et al., 1988) handles the particle transport calculations and yields a description of the redistribution of the atmosphere according to the energy of the source terms, background atmosphere, and resulting chemistry. Appendix A details the atmospheric chemistry model used by GLOW in terms of the collision frequencies that govern the redistribution of energy, momentum, and mass. The equations therein can be used to determine the conductivity profiles given the ion and electron density profiles. Summarizing Appendix A:

$$\sigma_P = \frac{q_e}{B}\left[N_{O^+}\frac{r_{O^+}}{1+r_{O^+}^2} + N_{O_2^+}\frac{r_{O_2^+}}{1+r_{O_2^+}^2} + N_{NO^+}\frac{r_{NO^+}}{1+r_{NO^+}^2} + N_e\frac{r_e}{1+r_e^2}\right] \tag{5}$$

$$\sigma_H = \frac{q_e}{B}\left[-N_{O^+}\frac{1}{1+r_{O^+}^2} - N_{O_2^+}\frac{1}{1+r_{O_2^+}^2} - N_{NO^+}\frac{1}{1+r_{NO^+}^2} + N_e\frac{1}{1+r_e^2}\right], \tag{6}$$

where:

$$r_x = \frac{\text{collision frequency}}{\text{gyrofrequency}} = \frac{\nu_x}{\omega_x} \tag{7}$$

$$\omega_x = \frac{q_e B}{m_x}. \tag{8}$$

Thus, the conductivities are derived from more basic measurements (i.e. ionization and electron density profiles driven by solar and particle precipitation ionization sources). Nonetheless, we will refer to conductivities as observations in this report.

In the GLOW model, the electron transport calculations are performed using a two-stream approach in which upward and downward hemispherical fluxes are determined along a magnetic field line as a function of energy (Banks and Nagy, 1970; Nagy and Banks, 1970; Banks et al., 1974; Solomon et al., 1988). The dynamical effects of gravity, parallel electric fields, and magnetic field convergence are not considered, while collisions are given extensive treatment. Elastic collisions with O_2, O, and N_2, inelastic collisions driving ionization and excitation of these species, and

thermal excitement of the ambient electrons are included. All inelastic cross sections are approximated with analytical fitting functions, using the Jackman et al. (1977) work for ionization and secondary electron production and the Green and Stolarski (1972) work for excitation. Elastic cross sections were interpolated from tabulated values which reflect both experimental and theoretical data. A detailed account of revisions to the formula given in these works for the model is provided by Appendix A of Solomon et al. (1988). An energy grid spanning 0.25 eV - 49.0 keV in 190 bins is implemented to handle energy redistribution. Ionospheric conductivities are dependent on ionization from the sun and from particles precipitating into the auroral zone. The combined DMSP particle data and GLOW model fully cover these dependencies.The model that has been built on the framework of the GLOW code to calculate conductivity profiles is hereafter referred to as GLOWcon.

Figure 3 shows an example illustrating the primary input (Fig. 3(a)) and output (Figs. 3(b)-(c)) to the GLOWcon model for the purposes of this study. Figure 3(a) shows the total electron energy flux along the track of the F16 spacecraft in altitude adjusted corrected geomagnetic coordinates (AACGM) (Baker and Wing, 1989) for a ~3 minute window during solstice conditions on May 29, 2010. Figures 3(b) and (c) show the Pedersen and Hall conductivity profiles during the same window as calculated by GLOWcon. When the precipitation is absent or low, near the left side of the satellite track, the conductivities take on the more familiar stratified formation, focusing most of the intensity within the 100-120 km altitude range. However, when the precipitation is more substantial, typically when the satellite moves to magnetic latitudes poleward of 60°, the conductivity profiles show significant height gradients and expanded bands of high intensity at lower altitudes that reach well beyond the 100-120 km range.

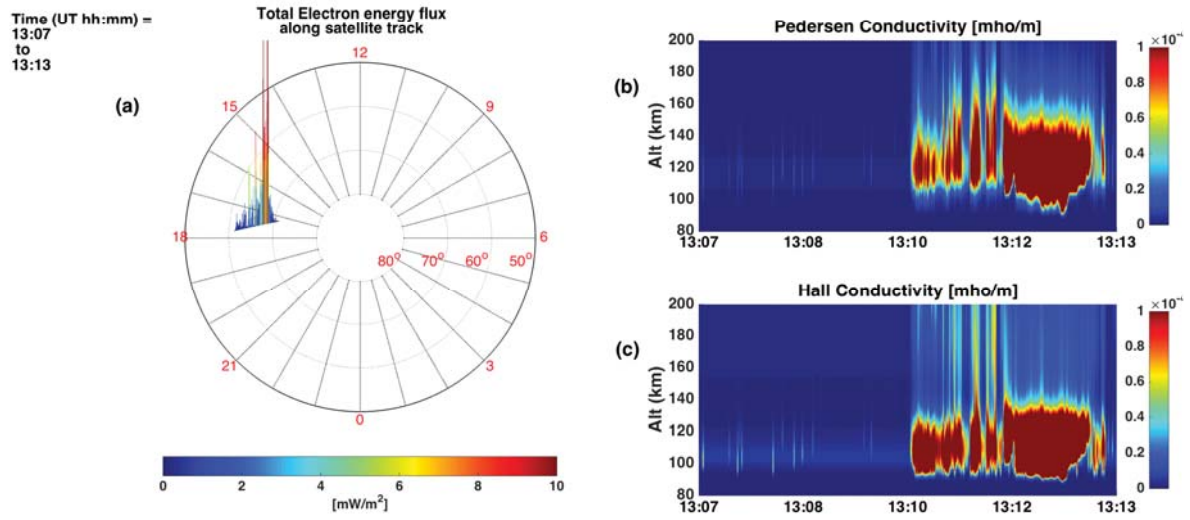

Figure 3: Primary input and output of the GLOWcon model for the purposes of this work shown graphically. On the left, total electron fluxes in mW/m^2 along the path of the DMSP F16 satellite during solstice conditions throughout the entire day of May 29, 2010. On the right, the output height-resolved conductivities, including Pedersen (top) and Hall (bottom) in mho/m between 80 and 200 km. A single ~ 200 s window is captured.

Although GLOWcon is able to represent the conductivity profiles along the DMSP satellite tracks, an estimation procedure is required to accurately and effectively 'spread' this information to characterize these parameters over the globe. This is the focus of the final tier of the methodology.

3.3. Spreading sparse information into a global picture: EOF creation

The primary objective of this work was to analyze the variability of Pedersen and Hall conductivities over the entire mid-to-high latitude ionosphere. In order to do so, we employ empirical orthogonal function (EOF) analysis as a means to estimate distributions of the conductivity variability given observations of the particle precipitation along

the satellite tracks of DMSP F16-F18. The method of EOF creation closely follows that originally developed for electrostatic potential by Matsuo et al. (2002). Extending the terminology therein to the current work, *conductivity variability* in the high-latitude ionosphere will be represented by:

$$\boldsymbol{\Sigma}' = \boldsymbol{\Sigma} - \bar{\boldsymbol{\Sigma}}, \tag{9}$$

where:

$\bar{\boldsymbol{\Sigma}}$ = mean conductivity field

$\boldsymbol{\Sigma}$ = observed conductivity field.

The EOF method applied in this work does not conform to the classical principal component analysis technique which carries out an eigenvalue decomposition on the variance-covariance matrix for a particular set of observations. Rather, in light of the sparsity of the DMSP satellite data, we estimate the principal components directly from 1-D conductivity calculations, and perform this process at discrete altitudes to ultimately prescribe principal components of conductivity in two dimensions at each altitude. The altitude resolution is variable, but between 80 and 200 km (the altitudes focused on in this work) it increases from 1 km between 80-110 km, 1.5 km between 110-116 km, 2 km between 116-150, and 3 km to the upper limit. The altitude grid was designed to reduce the representativeness error in the atmospheric air glow in each altitude band and to address numerical energy conservation issues that can occur in the two-stream code for insufficiently fine altitude grids (Solomon et al., 1988). The EOFs are calculated sequentially, with each successive principal mode derived orthogonally to the one prior. We transform the conductance data to log coordinates in order to reduce complications in the EOF estimation process that arise from the high-dimensionality of these variables. The final step in the process, then, is to back transform to linear coordinates for analysis and visualization.

A general description of the process is given first, and the full development follows in the rest of this subsection. The time-invariant background mean is first subtracted from the data to provide residual conductivities. The residual conductivities are then analyzed by performing a nonlinear regression fit to a functional form given by a chosen set of basis functions, separately scaled at each analysis time step. The first, or dominant, EOF is obtained by the first regression fit. Successive EOF modes are obtained by removing the effects of each previous EOF mode and performing a new regression fit in an orthogonal space to the previous EOF mode. In this way, the orthogonal direction exhibiting the highest variability left in the data is identified at each step.

The mean conductivity field must first be estimated and subtracted from the observations to yield residual conductivities. The mean field can be determined statistically or by the sample mean from some data set. We choose to remain consistent with Matsuo et al. (2002) in defining the EOFs:

$$\begin{aligned}\boldsymbol{\Sigma}'(\mathbf{r},t) = \alpha^{(1)}(t)\cdot\mathcal{EOF}^{(1)}(\mathbf{r}) + \ldots \\ \alpha^{(v)}(t)\cdot\mathcal{EOF}^{(v)}(\mathbf{r}) + \mathbf{e}'(\mathbf{r},t),\end{aligned} \tag{10}$$

where:

$\mathbf{r}$ = spatial position

$\alpha^{(v)}(t)$ = time-dependent coefficient of the vth $\mathcal{EOF}$

$\mathbf{e}'(\mathbf{r},t)$ = residual after removing the mean and sum of weighted $\mathcal{EOF}$s from $\boldsymbol{\Sigma}$.

The mean fields in this work are calculated via an expansion of the chosen bases to fit the DMSP data from the entirety of 2010.

We choose to fit the observations to the same basis functions used in the AMIE procedure. These basis functions are described by generalized Legendre functions at high latitudes with appropriate low-latitude extensions that satisfy a zero Laplacian requirement (Richmond and Kamide, 1988):

$$\Phi_i(\theta,\phi) = K_{1i}P_n^{|m|}(\cos\theta)\,f_m(\phi) \qquad \theta<\theta_0,\quad \theta>\pi-\theta_0 \tag{11}$$

$$= K_{2i}\left[\cot^m(\theta/2)+\tan^m(\theta/2)\right]f_m(\phi) \qquad \theta_0<\theta<\pi-\theta_0, \tag{12}$$

where:

$$f_m(\phi) = \sqrt{2}\cos m\phi \qquad m < 0 \tag{13}$$

$$= 1 \qquad m = 0 \tag{14}$$

$$= \sqrt{2}\sin m\phi \qquad m > 0, \tag{15}$$

and θ is the colatitude, θ_0 is the transition colatitude signifying the point beyond which the auroral high-latitude conductivity enhancement subsides, chosen as 45° in this study, ϕ is the longitude, and $K_{1i,2i}$ are normalizing constants.

The nonlinear regression analysis to determine each EOF is performed by minimizing the following cost function Matsuo et al. (2002):

$$L^{(v)} = \sum_j^J \sum_i^I \left[\mathbf{Y}_{ij}^{(v)} - \alpha_j^{(v)} \sum_k^N \beta_k^{(v)} \mathbf{X}_{kij} \right]^2, \tag{16}$$

where:

$\mathbf{Y}_{ij}^{(v)}$ = vector containing I residual observations at a location i on a satellite track j

$\alpha_j^{(v)}$ = weighting factor for track j

$\beta_j^{(v)}$ = regression coefficient

$\mathbf{X}_{kij}$ = kth basis function evaluated at location i on a satellite track j

N = number of basis functions chosen.

The typical scaling convention used in principal component analysis, $\sum \left(\beta_k^{(v)}\right)^2 = 1$, is applied to circumvent the non uniqueness of the analysis (the equations are still valid if a constant is multiplied throughout) along with a constraint to force orthogonality:

$$\sum \beta_k^{(v)} \beta_k^{(v-n)} = 0 \qquad n = 1, ..., v-1. \tag{17}$$

The EOF calculations can only be performed after a suitable mean field has been calculated and appropriately removed from the data. This corresponds to a minimizing linear regression on $L^{(0)}$ in Equation 16 with $\alpha_j^{(0)} = 1$ and the constraint on $\beta_k^{(0)}$ shown in Equation 17 lifted.

Throughout the course of 2010, each spacecraft completes roughly 5000 orbits and takes > 20,000 observations per day per hemisphere at latitudes poleward of 45°. However, the observations are carefully down-sampled for EOF calculations to reduce computation time. The down-sampling reduces the data from 1085 satellite days to 109 (one day from every ten is used). This is not believed to sacrifice accuracy because the DMSP orbit tracks are nearly repeating in geomagnetic coordinates and the down-sampled set contains equivalent information. Additionally, the data is averaged over contiguous 60 second intervals, and the mean observations location-tagged with the mean location in the interval. This is done to smooth the observations slightly, which is important for the estimation procedure when dealing with high-dimensional data such as these.

4. Results and Discussion

We present the results as follows: first, a case study during solstice conditions demonstrates the GLOWcon model; subsequently the first maps of the ionospheric conductivity variability are presented. These maps show height-integrated conductances for a concise presentation with the caveat that the process is easily extended to discrete altitudes to retain the 3-D conductivity information. Those results will be the focus of future work.

4.1. Case study: May 29, 2010

The electron particle precipitation and resulting ionization for an event during a solstice period with active geomagnetic conditions on May 29, 2010 is shown in Figure 4. In this figure all data is presented along the satellite track and organized by MLT. Figure 4(a) contains the total electron energy flux in mW/m^2 in the same manner described for Figure 3(a), (b) plots the average electron energy in eV, and (c) provides the electron impact ionization rates in cm^{-3} s^{-1}. Figures 4(b) and (c) are shown on log scales.

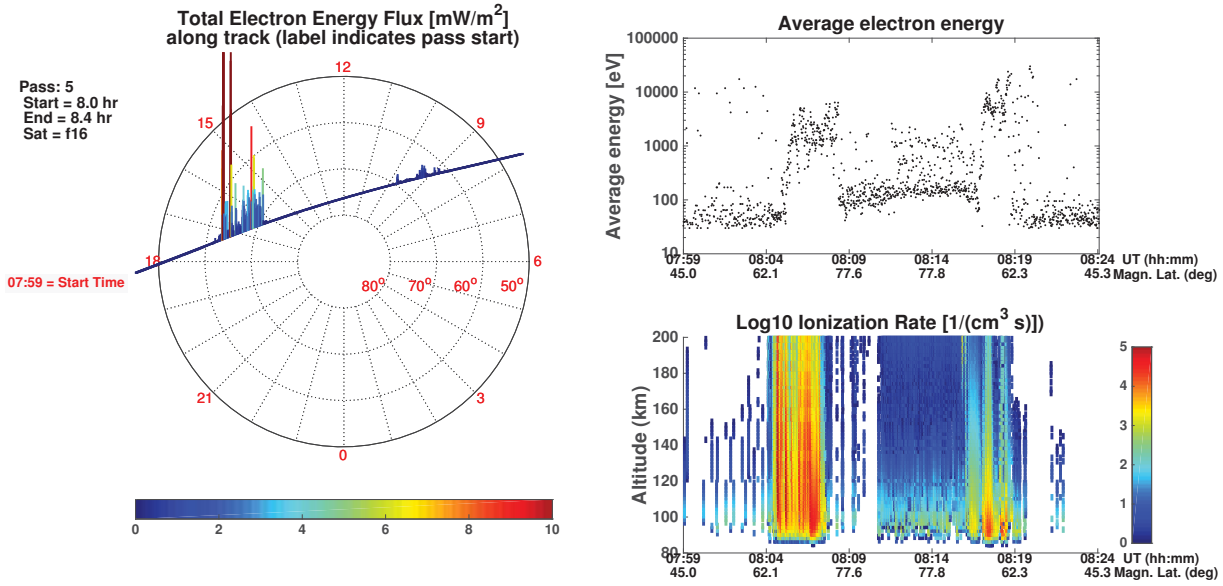

Figure 4: Characterization of the DMSP electron particle data and profiles of the ionization rate for an active solstice period (May 29, 2010). (a) Total electron energy flux in mW/m^2 shown along the DMSP F16 satellite path in geomagnetic latitude and local time coordinates, (b) average electron energies between 10 eV and 100 keV on log scale, and (c) electron impact ionization rates in cm^{-3} s^{-1} between 80 and 200 km altitude on log scale.

In Figure 4, the F16 spacecraft undergoes two auroral crossings, a dusk-side crossing and a pre-noon crossing, identified by locations where particle loss precipitation into the 80-200 km altitude band is significant. The first crossing, identified as the location of intense flux near 8.1 h UT, occurs between magnetic latitudes 62-72°. A visual inspection shows that the second crossing encounters nearly the same auroral bounds. The auroral zone is expanded, which is consistent with high activity represented by extremes in the Dst and auroral electrojet (AE) indices of ∼-85 nT and ∼1300 nT, respectively, for this event. However, the longitudinal extent of the auroral zone cannot be specified from such sparse information. Both auroral zone crossings yield electron precipitation with average energies above 1 keV, and the high-latitude precipitation between the two is relatively stable around 500 eV. The first auroral crossing has larger total energy flux and relatively high average energy and thus causes large ionization rates throughout the 80-200 km altitude range pictured in Figure 4(c). The second crossing shows lower total energy flux and higher average energy. This corresponds to smaller altitude-integrated ionization, but greater penetration of particles, focusing ionization at lower altitudes.

In both crossings, significant fine-scale structure is captured by the model. Both the dusk and pre-noon auroral crossings have small-scale peaks in the average energy data, and the model effectively shows these in the ionization rate profiles. The pre-noon auroral zone shows small bands of high ionization occurring discretely with small spatial separation. This is similar to what would be seen for an auroral streamer structure, though a claim that these structures are in fact auroral streamers cannot be substantiated without optical observations.

The penetration depth of particles allows a determination of where energy is deposited in the atmosphere and is therefore an important variable. GLOWcon calculates the height-resolved energy deposition profiles in the form of ionization rates using the direct data from the DMSP spacecraft as shown in these three figures. These profiles are used in combination with the National Research Laboratory Mass Spectrometer and Incoherent Scatter Radar Extended 2000 model (NRLMSISE-00), International Reference Ionosphere (IRI), and chemistry models to calculate conductivities. First, height-integrated conductances for this event will be compared with conductances calculated using the Robinson formulas (Robinson et al., 1987). Then, the conductivity profiles will be examined.

Figure 5 shows GLOWcon conductivity results integrated over 80-200 km altitude (blue points) overlaid on Robinson formula conductances (red points) for the (a) Pedersen and (b) Hall conductances as well as the (c) Hall-to-Pedersen conductance ratios. In these figures, no assumption on the incoming particle energy distributions is made for the GLOWcon output, but the inherent assumed Maxwellian distribution drives the Robinson conductances. Note that the vertical axes limits are different among the three plots. This is done to support discussion that follows.

The GLOWcon results include background conductances due to solar radiation. The background Pedersen conductance level is ~1-10 S and that of the Hall conductance is ~1-5 S. Both background levels increase toward the end of the satellite track as the F16 spacecraft enters locations of smaller solar zenith angle, or more vertical radiation incidence on the portion of the atmosphere being measured. This background increase is evident in all figures, even pronounced on Figure 5(c) where the larger effects of solar radiation on the Pedersen conductances are evident and the smaller vertical scale makes the background more apparent. There is no significant baseline in the Hall conductance because photoionization tends to occur at altitudes above where Hall conductances typically maximize due to the relatively low energy of incident photons when compared with precipitating magnetospheric particles. Additionally, the Hall conductances are plotted with a scale a factor of 2.5 larger than the Pedersen conductances. Corresponding backgrounds are not present in the Robinson results because those equations do not include solar contributions. Despite this, comparisons with the Robinson-generated ratio are still valid and illuminating.

The high activity contributes to poor agreement between the GLOWcon and Robinson results, where discrepancies in both conductances follow similar patterns. As activity increases and solar influences become more important the Robinson results become less realistic, often exceeding 200% error when measured against GLOWcon results. As the F16 satellite encounters smaller solar zenith angles, the background conductances exceed those predicted by the Robinson formulas. Additionally, in both auroral regions (first and second crossings at ~61.1-70.8 and ~70.1-60.3 magnetic latitudes, respectively) the Robinson formulas underestimate the conductances compared to GLOWcon.

The Hall-to-Pedersen conductance ratio isolates the conductance-modifying effect of precipitating electrons because the source density and temperature effects present in the Hall or Pedersen conductance calculations alone are canceled out when the ratio is formed Robinson et al. (1985). The electrons are charge carriers in the ionosphere and where they deposit their energy: 1) depends on their incident energy and 2) determines ionization profiles and thus conductivity and current distributions. High energy precipitation penetrates to low altitudes (<~110 km), where the Hall current systems are predominant. Lower energy precipitation causes ionization at altitudes where the Pedersen currents predominate (<~110-140 km). Hence, with a large Hall-to-Pedersen ratio, energy deposition and ionization is expected deeper in the atmosphere, and a small ratio signifies reduced penetration levels. Thus, the ratio is a measure of the ionospheric altitude at which currents are predominantly flowing. Figure 5(c) emphasizes that the solar ionization component has an important effect on the conductance ratio, acting as a background. If we ignore that background and assume a solar conductance model could accurately account for it, there are still issues with the Robinson results. For instance, the nonphysical heightened variability in the Robinson-generated ratios, particularly between the auroral crossings and into the morning sector auroral crossing (universal times 8.2-8.4 hrs), demonstrates degradation of performance as activity increases.

The shortcomings of the Robinson formulas in Figure 5 demonstrate that significant errors can be introduced if simplistic models of the conductance are used. Namely, diminishing accuracy with increasing activity, underestimation of auroral zone and polar cap conductances, and inability to capture fine-scale conductance changes. The capabilities of GLOWcon with respect to height-resolved conductivities are demonstrated next.

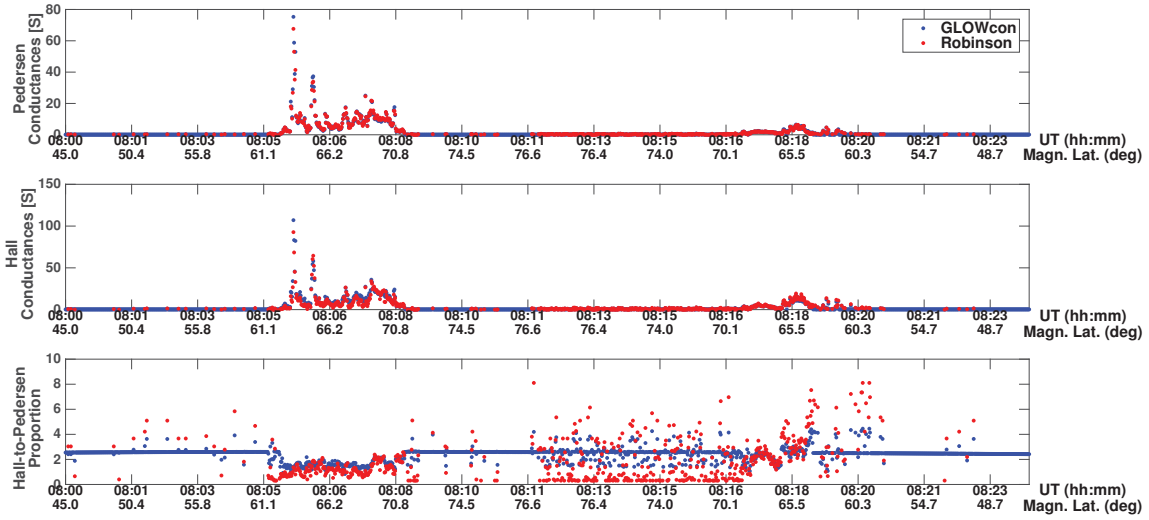

Figure 5: GLOWcon and Robinson formulas conductance comparisons for the solstice May 29, 2010 period. (a) Pedersen conductance, (b) Hall conductance, and (c) Hall-to-Pedersen conductance ratio.

Figure 6 shows the (a) photo- and (b) electron impact ionization rate profiles and the (c) Pedersen and (d) Hall conductivity profiles as output by the GLOWcon model for this event. This figure allows us to visually isolate the effect the electron impact ionization on the Pedersen and Hall conductivities. Clearly, Figure 6(c) and (d) demonstrate that the height gradients are significant. During periods of reduced particle precipitation away from the auroral zone crossings, the conductivities are reasonably stratified with the highest intensity around 110 km altitude, however throughout magnetic latitudes poleward of roughly 70° the intensities are significant in a much wider altitude band. In the auroral zones, the high average energies and higher total flux contributes to columns of significant conductivities over nearly the entire range of E-region altitudes.

During the solstice pass in Figure 6, the solar radiation contribution to the ionization is significant and increases as the DMSP F16 satellite occupies areas of smaller solar zenith angles as shown in Figure 6(a). The most intense photoionization is to the far left of the figure where the local time and latitude combine to yield smaller zenith angles. As a result, the conductivity profiles have a clear background of ~0.001 mho/m imposed over altitudes of 100-160 km in the Pedersen conductivity and 90-130 km in Hall conductivity. The initial auroral zone crossing, on the right hand side of each subfigure in Figure 6, contained a high total energy flux of electrons. This is manifested as enhanced electron impact ionization rates throughout the E-region, intense Hall conductivities between 90-130 km, and intense Pedersen conductivities between 100-140 km. Both Hall and Pedersen conductivities also experience more modest, yet potentially significant, enhancements throughout the E-region. The second auroral zone crossing in the pre-noon sector was not quite as intense, but had a similar effect on the conductivities regardless. The background conductivities also increase in this region due to the increased photoionization. This is indicated by a broadening of the altitude bands that reach the 0.001 mho/m level.

4.2. Northern hemisphere maps of conductance variability

The results shown so far have represented information limited to a satellite path where the observations were taken. Effectively spreading these sparse observations over the globe to obtain a full characterization of the ionospheric conductivity has not yet been discussed. We move into this discussion in this subsection.

Figures 7 and 8 show the mean and first five EOFs in terms of the 2010 northern hemisphere Hall and Pedersen conductances (integrated over the altitude range 80-200 km), respectively. The mean field in both cases captures the general auroral zone structure, and both patterns exhibit a peak in the dusk - pre-midnight sector which is consistent

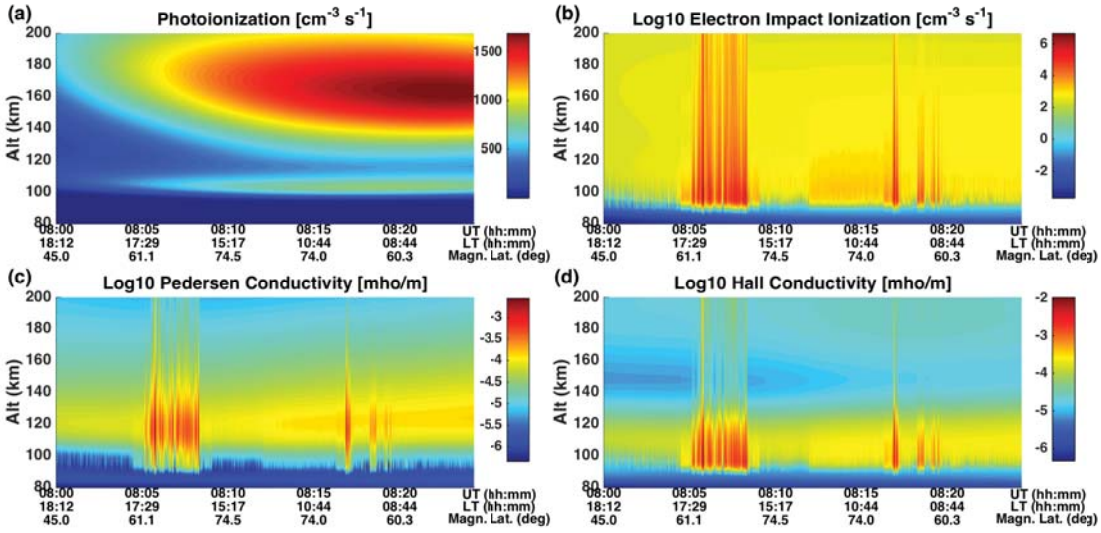

Figure 6: GLOWcon products for the solstice May 29, 2010 period. The products are: (a) photoionization rate, (b) $\log_{10}$ electron impact ionization rate, (c) $\log_{10}$ Pedersen conductivity, and (d) $\log_{10}$Hall conductivity.

with the asymmetry in ionospheric convection (stronger dusk-side convection cell). Lotko et al. (2014) discuss this stronger dusk-side convection in support of the larger plasmasheet velocities shown in the middle panel of their Figure 3 (reproduced in this paper as Figure 1). Recall that the mean is removed from the data prior to estimation of the EOFs.

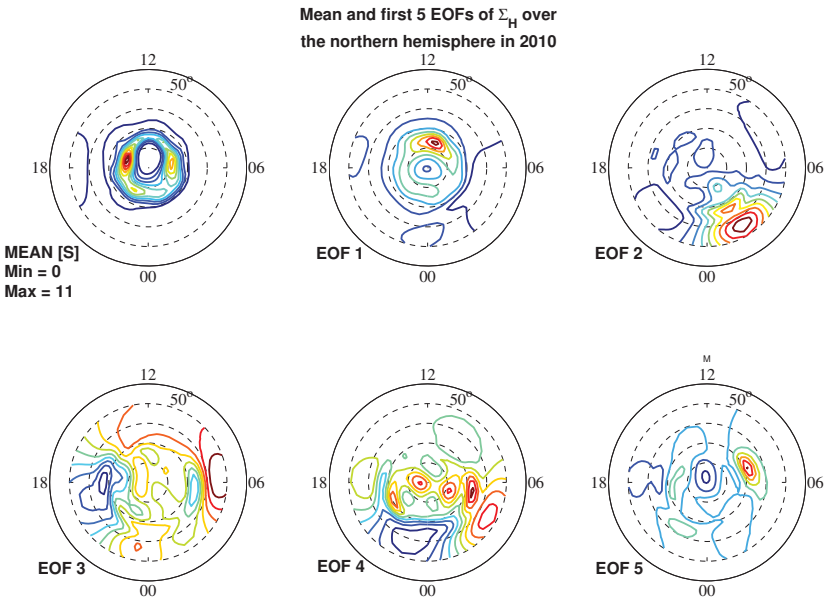

Figure 7: The mean and first 5 EOFs for the Hall conductance in the northern hemisphere in 2010 obtained using nonlinear regression on the DMSP F16, F17, and F18 data. The plot cutoff is 50° and the outer solid ring is 40° for each polar plot.

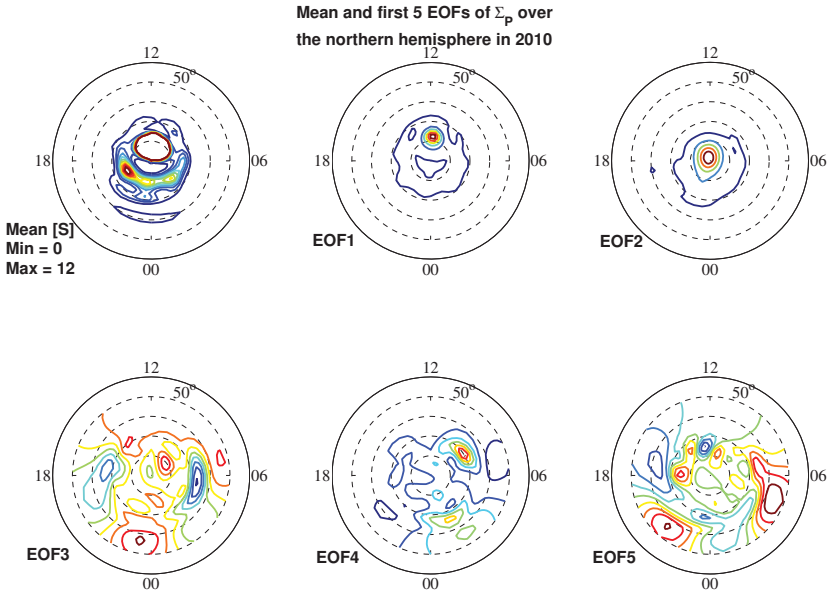

Figure 8: The mean and first 5 EOFs for the Pedersen conductance in the northern hemisphere in 2010 obtained using nonlinear regression on the DMSP F16, F17, and F18 data. The plot cutoff is 50° and the outer solid ring is at 40° for each polar plot.

The first and second modes of variability also describe relatively clear geophysical structures. The first EOF shows a signature of cusp precipitation for both conductances, but the Hall conductance also has a prominent auroral zone encircling all local times. The asymmetry in the Pedersen and Hall conductance patterns is apparent in the second EOF. Primarily, the different sensitivities to the characteristic energies of the precipitating particles is demonstrated. The Hall conductance has a stronger dependence on the characteristic energy and thus this mode shows a pattern consistent with high-energy particles precipitating into an expanded auroral zone in the post-midnight sector that is typical of high-activity periods. On the other hand, the second mode of variability for the Pedersen conductance shows a signature of lower characteristic energy polar rain particles.

The next three EOFs capture increasingly smaller percentages of the total variation (see Figures 9 and 10 below) and, though there are geophysical features present, the spatial structures are smaller and their effects on the large-scale ionospheric phenomena are more difficult to describe.

Figures 9 and 10 show the contribution to the total squared Hall and Pedersen conductances by the mean and first 10 EOFs, respectively. Roughly a third of the total variability is captured in the first 10 EOFs. This represents a somewhat smaller percentage than expected, which is evidence of the high-dimensionality of the Pedersen and Hall conductance observations. We discuss several avenues of future work below that could improve the percentage variations that the estimation process captures.

Any difficulty in estimating the mean patterns will also affect the accuracy of the EOF estimation that follows. Therefore, obtaining accurate mean patterns is important with this technique. We have identified two takeaways from the early EOF estimation work that are extremely important to future work: 1) further constraining the estimation using additional observations and 2) applying regularization techniques with *a priori* conductivity information.

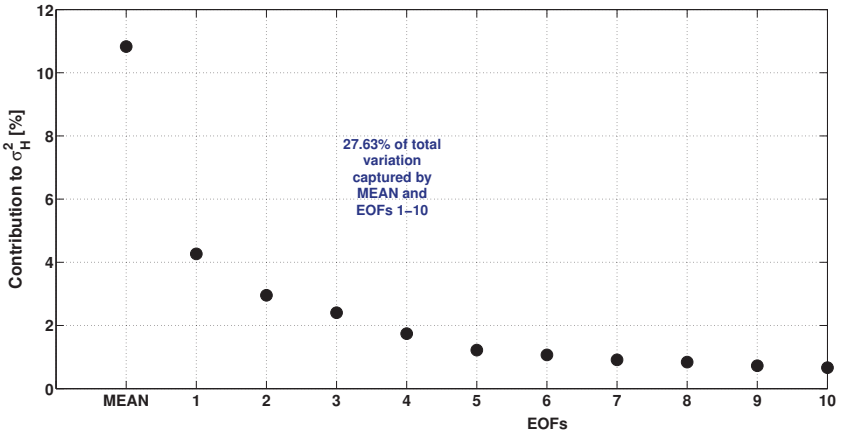

Figure 9: Contribution to the total squared Hall conductance in the northern hemisphere of the mean and EOFs 1-10.

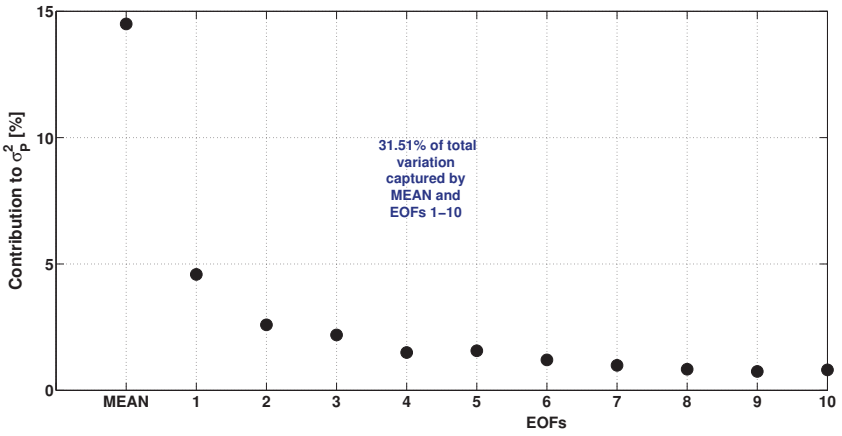

Figure 10: Contribution to the total squared Hall conductance in the northern hemisphere of the mean and EOFs 1-10.

Figure 2 attests that the coverage afforded by the DMSP F16, F17, and F18 has significant gaps in a global sense. Primarily, there are swaths surrounding noon and midnight that are simply unobserved and the estimation procedure is thus unconstrained in these regions. In future attempts to describe the global conductivities, we will incorporate DMSP observations from the F6 through F9 spacecraft. The F7/F9 spacecraft covered a roughly 1100-2300 local time regime, and the F6/F8 spacecraft orbit largely on the antisunward side of the dawn-dusk meridian, following roughly 1900-0500 local time paths. Observations from these four additional spacecraft will largely fill in the observational gaps left by the F16-F18 constellation.

Another approach to the data coverage issue is to introduce *a priori* particle precipitation information using available statistical maps as further constraining information. Particle precipitation maps could be transformed into conductivity 'observations' using the GLOWcon model and then serve as background fields for regularization of the estimation process. These maps have been created based on several different data sources, with a variety of assumptions, and have progressed in sophistication over multiple decades (Hardy, 1985; Newell et al., 2001; Newell,

2009; Newell et al., 2010; McIntosh and Anderson, forthcoming) and are thus widely available. Similar maps of the height-integrated conductances exist (the most notable being Fuller-Rowell and Evans (1987)), but we are interested in preserving the height-resolved quantities which precludes the use of these conductance models directly.

5. Conclusions and Future Work

We have presented the first results from a model capable of producing height-resolved conductivities from direct particle precipitation measurements by the DMSP satellites. The model was built of the framework of the GLobal AirglOW (GLOW) model, reformulated to directly ingest satellite particle precipitation information and to output height-resolved conductivities. This new model is called GLOWcon.

We demonstrated the capabilities of the GLOWcon model for a high activity event during a solstice period. GLOWcon was able to capture the energy deposition from the highly variable precipitation measured by the DMSP F16 satellite for this event. Further, we showed the success of the model in resolving the intense height gradients and fine scale structuring generated. Finally, the GLOWcon conductances were compared with those calculated via the Robinson formulas. GLOWcon values consistently reproduced accurate Hall and Pedersen conductances, whereas the Robinson conductances were increasingly nonphysical as activity rose, particularly when total electron flux rose well above 1 keV.

We also showed the first attempt to capture global conductivity variability in EOF maps. These were presented as height-integrated conductances in the northern hemisphere, though we note that this process is applicable to discrete altitudes to maintain height dependency and has already been extended to the southern hemisphere (not shown). The EOF analysis was able to reconstruct major geophysical features and capture a third of the total variability for both Pedersen and Hall conductances. Possible explanations for the relatively low percentage of variability described by these maps include fitting issues caused by incomplete coverage and the high dimensionality inherent in conductivity data. These outstanding issues were discussed and avenues to address them detailed in Section 4.

Overall, this work represents an important step for ionospheric electrodynamics analysis. The GLOWcon model is capable of producing Hall and Pedersen conductivities free of the primary assumptions that limited past work in this field. This will be a valuable tool for the community moving forward and will be used to create the first global height-specific views of how solar and magnetospheric energy influence the dynamics of the ionosphere and thermosphere, and how this energy feeds back to the magnetosphere.

6. Acknowledgements

We acknowledge the Los Alamos National Laboratory's space weather summer school program, through which a vast majority of this work was completed. The LANL HPC group was instrumental in assisting with issues related to the high performing computing aspect of this study. Humberto Godinez and Steve Morley, my mentors during the space weather summer school. Misa Cowee, the coordinator of the summer school. Stan Solomon for his support in using the GLOW code. Rob Redmon for his work in preparing and providing the DMSP satellite data and advising on its use. Liam Kilcommons for providing general coding tools. NSF Award No. DGE 1144083.

Appendix A. GLOW atmospheric chemistry calculations

The atmospheric chemistry for the purposes of conductivity calculations can be described by collision frequencies. The frequencies used in the GLOW model are obtained from Schunk and Nagy (2009):

$$\frac{1}{N_{O_2}}\nu_{O_2^+-O_2} = 2.59\times10^{-11}\sqrt{\frac{T_i+T_e}{2}}\left[1-0.73\log_{10}\sqrt{\frac{T_i+T_e}{2}}\right]^2$$
$$\frac{1}{N_{O_2}}\nu_{O^+-O_2} = 6.64\times10^{-10}$$
$$\frac{1}{N_{O_2}}\nu_{NO^+-O_2} = 4.27\times10^{-10}$$
$$\frac{1}{N_{O}}\nu_{O^+-O} = 3.67\times10^{-11}\sqrt{\frac{T_i+T_e}{2}}\left[1-0.064\log_{10}\sqrt{\frac{T_i+T_e}{2}}\right]^2 f_{cor}$$
$$\frac{1}{N_{O}}\nu_{NO^+-O} = 2.44\times10^{-10}$$
$$\frac{1}{N_{O}}\nu_{O_2^+-O} = 2.31\times10^{-10}$$
$$\frac{1}{N_{N_2}}\nu_{O_2^+-N_2} = 4.13\times10^{-10}$$
$$\frac{1}{N_{N_2}}\nu_{NO^+-N_2} = 4.34\times10^{-10}$$
$$\frac{1}{N_{N_2}}\nu_{O^+-N_2} = 6.82\times10^{-10},$$

where the temperature dependent terms denote resonant reactions, and the constants denote non-resonant reactions. The term f_{cor} has a default value of 1.5 and is representative of the Burnside correction (Burnside et al., 1987) for the $O^+ - O$ reaction. This term was empirically determined to improve agreement between general circulation models and observed winds and electron densities (Nicolls et al., 2006). The collision frequencies can then be found in units of [Hz]:

$$\nu_{O_2^+} = \nu_{O_2^+-O_2} + \nu_{O_2^+-O} + \nu_{O_2^+-N_2}$$
$$\nu_{O^+} = \nu_{O^+-O_2} + \nu_{O^+-O} + \nu_{O^+-N_2}$$
$$\nu_{NO^+} = \nu_{NO^+-O_2} + \nu_{NO^+-O} + \nu_{NO^+-N_2}$$
$$\nu_{en} = 2.33\times10^{-11}N_{N_2}T_e\left(1-1.21\times10^{-4}T_e\right) + 1.82\times10^{-10}N_{O_2}\sqrt{T_e}\left(1+3.6\times10^{-2}\sqrt{T_e}\right) + 8.9\times10^{-11}N_O\sqrt{T_e}\left(1+5.7\times10^{-2}\sqrt{T_e}\right).$$

References

Amm, O., Aruliah, A., Buchert, S.C., Fujii, R., Gjerloev, J.W., Ieda, A., Matsuo, T., Stolle, C., Vanhamäki, H., Yoshikawa, A., 2008. Towards understanding the electrodynamics of the 3-dimensional high-latitude ionosphere: Present and future. Annales Geophysicae 26, 3913–3932.

Baker, K.B., Wing, S., 1989. A new magnetic coordinate system for conjugate studies at high latitudes. Journal of Geophysical Research: Space Physics 94, 9139–9143.

Banks, P.M., Chappell, C.R., Nagy, A.F., 1974. A new model for the interaction of auroral electrons with the atmosphere: Spectral degradation, backscatter, optical emission, and ionization. Journal of Geophysical Research 79, 1459–1470.

Banks, P.M., Nagy, A.F., 1970. Concerning the influence of elastic scattering upon photoelectron transport and escape. Journal of Geophysical Research 75, 1902–1910.

Bowman, B., Tobiska, K., Marcos, F., Huang, C., Lin, C., Burke, W., 2008a. A new empirical thermospheric density model, JB2008 using new solar and geomagnetic indices, in: Proceedings of the American Institute of Aerodynamics and Astronautics, Air Force Space Command. AIAA.

Bowman, B.R., Tobiska, W.K., Marcos, F.A., Huang, C.Y., Lin, C.S., Burke, W.J., 2008b. A new empirical thermospheric density model, JB2008 using new solar and geomagnetic indices, in: Proceedings of the American Institute of Aerodynamics and Astronautics, Air Force Space Command. AIAA.

Burnside, R.G., Tepley, C.A., Wickwar, V.B., 1987. The O(+)-O collision cross-section - Can it be inferred from aeronomical measurements? Annales Geophysicae .

Codrescu, M.V., Fuller-Rowell, T.J., Foster, J.C., 1995. On the importance of e-field variability for joule heating in the high-latitude thermosphere. Geophysical Research Letters 22, 2393–2396.

Emery, B., Richardson, I., Evans, D., Rich, F., 2009. Solar wind structure sources and periodicities of auroral electron power over three solar cycles. Journal of Atmospheric and Solar-Terrestrial Physics 71, 1157–1175.

Evans, D.S., Maynard, N.C., Trim, J., Jacobsen, T., Egeland, A., 1977. Auroral vector electric field and particle comparisons, 2, electrodynamics of an arc. Journal of Geophysical Research 82, 2235–2249.

Fuller-Rowell, T.J., Evans, D.S., 1987. Height-integrated pedersen and hall conductivity patterns inferred from the tiros-noaa satellite data. Journal of Geophysical Research: Space Physics 92, 7606–7618.

Green, A., Stolarski, R., 1972. Analytic models of electron impact excitation cross sections. Journal of Atmospheric and Terrestrial Physics 34, 1703 – 1717.

Hardy, D., 1984. Precipitating Electron and Ion Detectors (SSJ/4) for the Block 5D/flights 6-10 DMSP Satellites: Calibration and Data Presentation. Air Force Geophysics Laboratory, United States Air Force.

Hardy, D., 1985. A statistical model of auroral electron precipitation. Journal of Geophysical Research 90, 4229–4248.

Hardy, D.A., Holeman, E.G., Burke, W.J., Gentile, L.C., Bounar, K.H., 2008. Probability distributions of electron precipitation at high magnetic latitudes. Journal of Geophysical Research: Space Physics 113, n/a–n/a.

Hinteregger, H.E., Fukui, K., Gilson, B.R., 1981. Observational, reference and model data on solar EUV, from measurements on AE-E. Geophysical Research Letters 8, 1147–1150.

Jackman, C.H., Garvey, R.H., Green, A.E.S., 1977. Electron impact on atmospheric gases, I. updated cross sections. Journal of Geophysical Research 82, 5081–5090.

Kirkwood, S., Opgenoorth, H., Murphree, J., 1988. Ionospheric conductivities, electric fields and currents associated with auroral substorms measured by the {EISCAT} radar. Planetary and Space Science 36, 1359 – 1380.

Knipp, D.J., 1989. Quantifying and reducing uncertainty in the assimilative mapping of ionospheric electrodynamics. Ph.D. thesis. UCLA via Air Force Institute of Tech Wright-Patterson Air Force Base.

Knipp, D.J., Matsuo, T., Kilcommons, L., Richmond, A., Anderson, B., Korth, H., Redmon, R., Mero, B., Parrish, N., 2014. Comparison of magnetic perturbation data from leo satellite constellations: Statistics of dmsp and ampere. Space Weather 12, 2–23.

Lotko, W., Smith, R.H., Zhang, B., Ouellette, J.E., Brambles, O.J., Lyon, J.G., 2014. Ionospheric control of magnetotail reconnection. Science 345, 184–187. http://www.sciencemag.org/content/345/6193/184.full.pdf.

Marcos, F.A., 2006. Accuracy of earth's thermospheric neutral density models, in: AIAA (Ed.), In Proceedings of the AIAA/AAS Astrodynamics Specialist Conference and Exhibit, Air Force Research Laboratory.

Matsuo, T., Knipp, D.J., Richmond, A.D., Kilcommons, L., Anderson, B.J., submitted. Inverse procedure for high-latitude ionospheric electrodynamics: Analysis of satellite-borne magnetometer data. Journal of Geophysical Research Manuscript submitted for publication.

Matsuo, T., Richmond, A.D., Lu, G., 2005. Optimal interpolation analysis of high-latitude ionospheric electrodynamics using empirical orthogonal functions: Estimation of dominant modes of variability and temporal scales of large-scale electric fields. Journal of Geophysical Research: Space Physics 110, n/a–n/a.

Matsuo, T., Richmond, A.D., Nychka, D.W., 2002. Modes of high-latitude electric field variability derived from DE-2 measurements: Empirical orthogonal function (EOF) analysis. Geophysical Research Letters 29, 11–1–11–4.

McIntosh, R., Anderson, P., forthcoming. Maps of precipitating electron spectra characterized by Maxwellian, Lorentzian, and Ellison-Ramaty distributions. Journal of Geophysical Research .

Nagy, A.F., Banks, P.M., 1970. Photoelectron fluxes in the ionosphere. Journal of Geophysical Research 75, 6260–6270.

Newell, P.T., 2009. Diffuse, monoenergetic, and broadband aurora: The global precipitation budget. Journal of Geophysical Research: Space Physics 114, n/a–n/a.

Newell, P.T., Liou, K., Sotirelis, T., Meng, C.I., 2001. Auroral precipitation power during substorms: A Polar UV imager-based superposed epoch analysis. Journal of Geophysical Research: Space Physics 106, 28885–28896.

Newell, P.T., Sotirelis, T., Wing, S., 2010. Seasonal variations in diffuse, monoenergetic, and broadband aurora. Journal of Geophysical Research: Space Physics 115, n/a–n/a.

Nicolls, M.J., Aponte, N., Gonzlez, S.A., Sulzer, M.P., Oliver, W.L., 2006. Daytime F region ion energy balance at Arecibo for moderate to high solar flux conditions. Journal of Geophysical Research: Space Physics 111, n/a–n/a.

Picone, J.M., Hedin, A.E., Drob, D.P., Aikin, A.C., 2002. NRLMSISE-00 empirical model of the atmosphere: Statistical comparisons and scientific issues. Journal of Geophysical Research: Space Physics 107, SIA 15–1–SIA 15–16.

Prölss, G.W., 2011. Density perturbations in the upper atmosphere caused by the dissipation of solar wind energy. Surveys in Geophysics 32, 101–195.

Qian, L., Solomon, S.C., 2012. Thermospheric density: An overview of temporal and spatial variations. Space Sci. Rev. 168, 147–173.

Rich, F.J., Hardy, D.D., Gussenhoven, M.S., 1985. Enhanced ionosphere-magnetosphere data from the DMSP satellites. Eos, Transactions American Geophysical Union 66, 513–514.

Richards, P.G., Fennelly, J.A., Torr, D.G., 1994. EUVAC: A solar EUV Flux Model for aeronomic calculations. Journal of Geophysical Research: Space Physics 99, 8981–8992.

Richmond, A., 1992. Assimilative mapping of ionospheric electrodynamics. Advances in Space Research 12, 59 – 68.

Richmond, A.D., Kamide, Y., 1988. Mapping electrodynamic features of the high-latitude ionosphere from localized observations: Technique. Journal of Geophysical Research: Space Physics 93, 5741–5759.

Richmond, A.D., Kamide, Y., Ahn, B.H., Akasofu, S.I., Alcaydé, D., Blanc, M., de la Beaujardiére, O., Evans, D.S., Foster, J.C., Friis Christensen, E., Fuller Rowell, T.J., Holt, J.M., Knipp, D., Kroehl, H.W., Lepping, R.P., Pellinen, R.J., Senior, C., Zaitzev, A.N., 1988. Mapping electrodynamic features of the high-latitude ionosphere from localized observations: Combined incoherent-scatter radar and magnetometer measurements for january 1819, 1984. Journal of Geophysical Research: Space Physics 93, 5760–5776.

Richmond, A.D., Ridley, E.C., Roble, R.G., 1992. A thermosphere/ionosphere general circulation model with coupled electrodynamics. Geophysical Research Letters 19, 601–604.

Ridley, A., Deng, Y., Tth, G., 2006. The global ionosphere thermosphere model. Journal of Atmospheric and Solar-Terrestrial Physics 68, 839 – 864.

Robinson, R.M., Vondrak, R.R., Miller, K., Dabbs, T., Hardy, D., 1987. On calculating ionospheric conductances from the flux and energy of precipitating electrons. Journal of Geophysical Research: Space Physics 92, 2565–2569.

Robinson, R.M., Vondrak, R.R., Potemra, T.A., 1985. Auroral zone conductivities within the field-aligned current sheets. Journal of Geophysical Research: Space Physics 90, 9688–9696.

Schunk, R., Nagy, A., 2009. Ionospheres: Physics, Plasma Physics, and Chemistry. Cambridge Atmospheric and Space Science Series, Cambridge University Press.

Solomon, S.C., Hays, P.B., Abreu, V.J., 1988. The auroral 6300 emission: Observations and modeling. Journal of Geophysical Research: Space Physics 93, 9867–9882.

Storz, M.F., Bowman, B.R., Branson, M.J.I., Casali, S.J., Tobiska, W.K., 2005. High accuracy satellite drag model (HASDM). Advances in Space Research 36, 2497 – 2505. Space Weather .

Sutton, E.K., Forbes, J.M., Knipp, D.J., 2009. Rapid response of the thermosphere to variations in joule heating. Journal of Geophysical Research: Space Physics 114, n/a–n/a.

Vasyliunas, V., 1970. Mathematical models of magnetospheric convection and its coupling to the ionosphere, in: McCormac, B. (Ed.), Particles and Fields in the Magnetosphere. Springer Netherlands. volume 17 of *Astrophysics and Space Science Library*, pp. 60–71.

Wang, T., 2010. Analysis of debris from the collision of the Cosmos 2251 and the Iridium 33 satellites. Science & Global Security 18, 87–118. `http://scienceandglobalsecurity.org/archive/sgs18tingwang.pdf`.

Zhang, J.T., Forbes, J.M., Zhang, C.H., Doornbos, E., Bruinsma, S.L., 2014. Lunar tide contribution to thermosphere weather. Space Weather 12, 538–551.

A Particle-in-Cell Study of Dipole Model for Radiation Belt Dynamics

Ivy Bo Peng

KTH Royal Institute of Technology, Sweden

Delzanno, Gian Luca

Los Alamos National Laboratory, New Mexico, US

Jordanova, Vania Koleva

Los Alamos National Laboratory, New Mexico, US

Yu, Yiqun

Los Alamos National Laboratory, New Mexico, US

Stefano Markidis

KTH Royal Institute of Technology, Sweden

Abstract

In this summer school project, we studied the formation of Earth's Radiation Belts using Particle-in-Cell (PIC) method. We first established the performance benchmark of our highly-parallel implicit PIC code, iPIC3D (Markidis et al., 2010), by conducting convergence tests of whilster anisotropy instability at low electron β (Gary et al., 2011). To study the dynamics of Radiation Belts, we implemented the dipole model (Öztürk, 2012) of Earth's magnetic field for the initialization of simulation. During the simulation, we implemented procedure to slowly ramp up the magnitude of magnetic field for each particles to allow relaxation from non-equilibrium status to equilibrium status. We implemented sub-cycling technique for Particle Mover to correctly simulate the movement of particles. We also implemented post-processing procedures to visualise and to analyse the simulation results. We carried out the three dimensional simulations on Mustang supercomputer using 4096 processes and $128 \times 128 \times 128$ cells with 3,3554,432 particles. The data of particles and fields information is captured during simulation for post-processing. We used a small simulation domain due to the nature of exploration of this project. From the visualisation of the particle densities, it is clear to see that the simulation first went through expanding stage then shrinking stage before reaching equilibrium stage. The equilibrium status, once reached, could be used as the initial status for future large scale simulation of Radiation Belts dynamics. To prepare for future simulation on large supercomputer, we also performed scaling test and profiling on Mustang to identified the load imbalance on processes, which need to be addressed before proceeding to exascale simulations.

Keywords: large simulation, radiation belt, particle-in-cell, implicit PIC, HPC

1. Introduction

Van Allen Radiation Belts shield Earth from energetic particles. High energetic particles could still pass through the radiation belts and enter the atmosphere of Earth, bringing impact to our daily life. Thus the dynamics of radiation belts are of significance to the safety of spacecraft, communication system and the astronauts. Radiation Belts

Email addresses: bopeng@kth.se (Ivy Bo Peng), delzanno@lanl.gov (Delzanno, Gian Luca), vania@lanl.gov (Jordanova, Vania Koleva), yiqun@lanl.gov (Yu, Yiqun), markidis@kth.se@kth.se (Stefano Markidis)

are known as layers of plasma held by the Earth's magnetic field around the planet. There are usually two layers of Radiation Belts: the outer layer has radius of approximately of (3 -10) radius of Earth and the inner layer has radius of approximately (0.2 - 2) radius of Earth. In this project, we studied the formation of these radiation belts to reach an equilibrium status from non-equilibrium initial status to facilitate future simulations.

Computer simulations on supercomputers are used to model the dynamics of the radiation belts and to predict the critical impacts. (Lapenta et al., 2013). Fully kinetic Particle-in-cell model is often used for simulation of plasma, where plasma particles are mimicked by computational particles moving in a self-consistent electromagnetic field. However, the explicit PIC method is subject to some numerical stability constraints, such as so-called finite grid instability, which restrict the grid space to be of the order of or smaller than Debye length λ_D (Markidis et al., 2010). Due to the large scale of Earth's radiation belts, the explicit PIC is no longer feasible for such simulation. In our summer project, we used implicit PIC code, iPIC3D, to explore the setup and formation of radiation belts.

iPIC3D is an Implicit Particle-in-Cell code for the simulation of plasma. Implicit scheme such as the implicit moment method (Mason, 1981) is implemented in the code so that time step and grid size larger than that of explicit PIC method are allowed. Due to the advantage of implicit PIC, we can start exploring the simulation of domain size 6 RE, where RE is the radius of Earth. In previous works, similar dipole set up has been used to study lunar magnetic anomalies (Deca et al., 2014). Several simplified models of dipole set up could also be found in Ref(bell1984nonlinear, tao2013importance). In our summer project, we set up the dipole model according to the model describe in (Öztürk, 2012).

We benchmarked the performance the new version of our iPIC3D code, which uses hybrid programming models of MPI and OpenMPI, as the first phase of our summer project. We conduct convergence test of whistler anisotropy Instability at low electron β (Gary et al., 2011). The simulations were carried on Mustang supercomputer in Los Alamos National Laboratory, with increasing resolution parameters. Three values of β are used in each round of these simulations. Parallel and oblique propagation pattern were observed. The growth rate of the instability approximates the theoretical estimation as the resolution increases.

The next phase of our project is to explore how to reach equilibrium status from non-equilibrium status in a dipole model setup for radiation belts in iPIC3D. This is the preliminary step for the future simulation of dynamics of radiation belts. We start the simulation from unstable non-equilibrium status with magnetic field in dipole model (Öztürk, 2012) and particles initialized following classic Maxwellian distribution. By extracting the location of ion and electrons, we identified two layers of particles surrounding Earth after reaching the equilibrium status. From the visualisation of the captured data of particles, we identified three phases for the simulation to reach equilibrium status: the expansion stage, during which the electron is much faster than ion, moving to the surface of the Earth, creating sheath that results in electric field; the electric field from sheath starts to decelerate particles, which leads to the next phase: shrinking phase. When both field and particles reach the equilibrium status, the system remained stable status with minimal changes for the rest of the simulation.

The rest of the report organises as follows: the second section gives a brief description of Particle-in-cell method and iPIC3D code. Dipole setup, sub-cycling of particles and simulation parameters are introduced in the third section. We will present the results of simulation in section four with a following discussion. We will conclude our report in section five as well future works.

2. Particle-in-Cell Method and iPIC3D code

Computer simulations facilitate large scale simulation of Earth system on supercomputers of thousands and even millions of cores (Birdsall and Langdon, 2004). Particle-in-cell method simulate the interaction of particle to grid and interpolate from particle to grid (Hockney and Eastwood, 1988). In our work, we use a massively parallel Particle-in-Cell code, iPIC3D (Markidis et al., 2010), to simulate the dynamics of Earth's radiation belts.

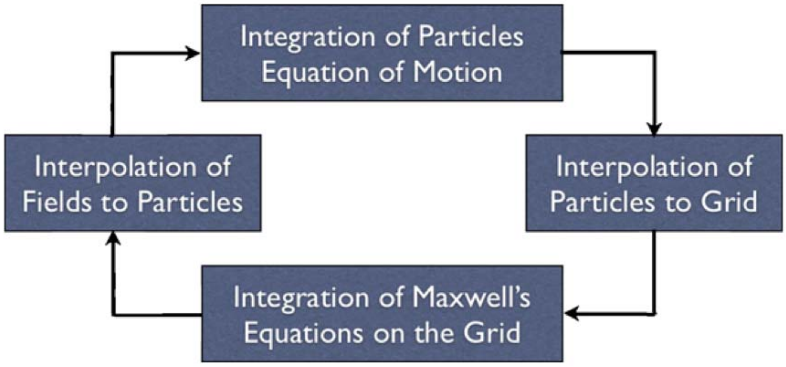

Figure 1: At each computational cycle, four major steps are carried out: the velocity and location of each particle are updated, the current and charge density are interpolated to the mesh grid and Maxwell equations are solved.

There are two main directions in solving Vlasov-Maxwell system: direct approaches such as finite difference method and Particle-in-cell (PIC) method that simulates the interaction between particles and field through grid. In PIC method, a reduced number of computational particles are used to mimic real plasma particles and to sample distribution function. Depending on the numerical scheme used, there are explicit and implicit PIC method. The explicit PIC method is subject to some numerical stability constraints, such as so-called finite grid instability, which restrict the grid space to be of the order of or smaller than Debye length λ_D (Markidis et al., 2010). Due to the large scale of Earth's radiation belts, the explicit PIC is no longer feasible for such simulation. In our summer project, we used implicit PIC code, iPIC3D, to explore the setup and formation of radiation belts. In iPIC3D, each computational particle has different weight for the reconstruction of the statistical distribution and is moved by Newton's equation of motion. The implicit momentum scheme implemented in iPIC3D, evaluates charge density ρ and current density J at the future time level (n+1) and (n+1/2) respectively for solving the Maxwell's equation. Details of the equations can be found in (Markidis et al., 2010).

A typical diagram in Figure 1 shows the four major steps in each computational cycle in PIC model. At each computational cycle, the velocity and location of each particle are updated, the current and charge density are interpolated to the mesh grid and Maxwell equations are solved. Large parallel computer systems are used to carry out the simulation so that the computation load is divided among processes. Each process only calculates a sub-domain of the simulation box. Extensive communications among the processes are required for halo exchange of field values defined on the mesh and for communicating particles exiting a sub-domain.

3. Dipole Setup and Simulation Parameter

3.1. Initialisation of the Magnetic Dipole

We follow the dipole model described in (Öztürk, 2012) to set up magnetic field during the initialisation of the simulation. The equation is reproduced in Eq. 1.

$$\mathbf{B_{dip}} = -\frac{B_0 R_e^3}{r^5}[3xz\hat{x} + 3yz\hat{y} + (2z^2 - x^2 - y^2)\hat{z}]. \tag{1}$$

3.2. Ramp up the Magnetic Dipole during simulation

The simulation starts from non-equilibrium status. The key to reach equilibrium status is to allow particles have sufficient time to relax. As a result, instead of applying the magnetic field fully at the initialisation, we slowly ramp up the magnetic field in the first two hundred cycles of simulations. In each computational cycle, the magnetic field for each particles will add in an external magnetic field of magnitude proportional to the current number of cycles,

i.e. $(magnetic\_field + (\frac{Current\_No\_of\_Cycles}{200}) \times external\_magnetic\_field)$. The ramp up will stop after saturation, in our simulation, we chose hundred cycles to ramp up the field.

3.3. Sub-cycling of Particle Mover

The Earth radiation belts are a large scale system, where electric and magnetic field evolve slowly in the simulation, i.e. the magnitude of electric field and magnetic field vary little in each time step. Particles, on the other hand, have much larger magnitude of velocity, which means the location of particles could vary much in one time step. If we keep the time step in very small value, the simulation process will take very long time to observe evolution. Our strategy is to use sub-cycling technique for particle movement in each cycle. Recall that the location and velocity of each particle are governed by the equation of motion in Eq. 2

$$\begin{cases} \dfrac{d\mathbf{x}_p}{dt} = \mathbf{v}_p \\ \dfrac{d(m_s\gamma\mathbf{v}_p)}{dt} = q_s\left(\mathbf{E}_p + \dfrac{\mathbf{v}_p}{c} \times \mathbf{B}_p\right), \end{cases} \tag{2}$$

We implement two sub-cycles for ion and ten sub-cycles for electron. As a result, in each time step in the simulation, ion will be moved two times with the time step for each move reduced to $dt/2$. Similarly, electron will be moved ten times with the time step for each move reduced to $dt/10$.

3.4. Simulation parameters

Due to the nature of exploration of our project, we chose a small domain size for simulation. For the simulation of radiation belts, the simulation box has size of $6.0d_i \times 6.0d_i \times 6.0d_i$, where the center of the dipole is positioned at $(3.0d_i, 3.0d_i, 3.0d_i)$, with assumption of zero magnetic field inside radius of $0.5d_e$. The number of cells used is $128 \times 128 \times 128$ and the total number of particles used is $3,3554,432$ for two species: ion and electron. To speed up the simulation and reduce the computation cost, we use an unrealistic mass ratio between ion and electron: 25 to 1, instead of the real value 1836 to 1. We use equal thermal velocity in 3 directions (x, y, z) for electron: $Vth_e = 0.045 \times c$ and for ion, $Vth_e = 0.0063 \times c$, where c is the speed of light in vacuum. In the simulation, we normalize the speed of light to be 1. We ran the simulation on 4096 processes on Mustang with periodic boundary conditions for both field and particles.

4. Simulation Results and Discussion

In this summer school project, two simulations have been carried on the new iPIC3D code: benchmark test and formation of radiation belts. Three sets of parameters, with increasing resolution, were used to simulate whistler anisotropy instability at low electron β (Gary et al., 2011). Convergence to the theoretical estimate was observed with increase resolution. The results of the simulations are present in Figure 2.

The focus of our summer project is to explore how to reach an equilibrium status from non-equilibrium initial status in a dipole model setup with particles initialised by Maxwellian distribution of velocity and uniform distribution of location. This step is the preliminary step for the future study of dynamics in Earth's radiation belts. The initial distribution of particles is not consistent with the field, causing the system in non-equilibrium status. Particles then start to relax to equilibrium status. The formation of radiation belts was observed in the simulation and present below.

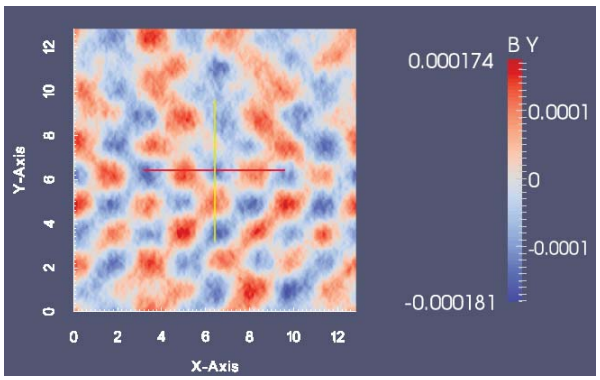

(a) oblique propagation of whistler wave

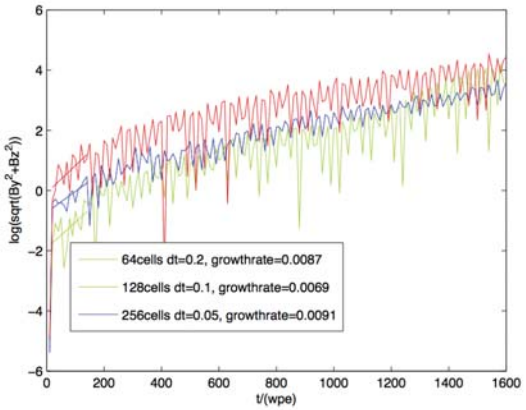

(b) Growth rate of instability

Figure 2: The simulation results of convergence test, whistler anisotropy instability at low electron β. Figure 2a shows whistler wave formation as effect of the instability. Two initial anisotropy simulations are present here: parallel and oblique propagation of whistler wave. Figure 3b shows The growth rate converges to the linear theory prediction with finer resolution.

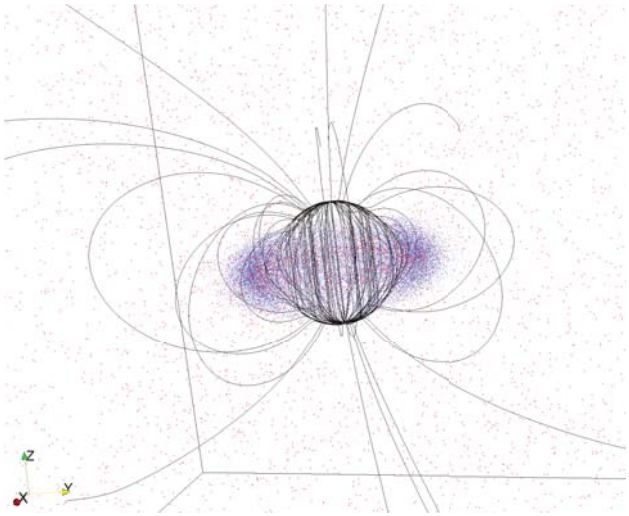

(a) Formation of Radiation Belts with iPIC3D

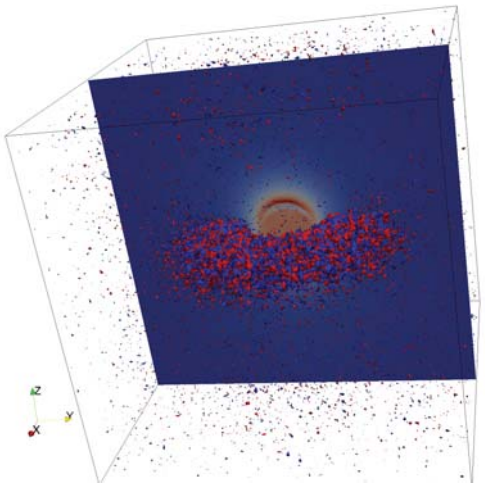

(b) Isosurface of the charge density

Figure 3: The simulation results of Earth radiation belts on 4096 processes with 128^3 cells and 3.4×10^7 super-particles. Figure 3a shows the Earth magnetic field lines as the black lines, electrons as blue points and ions as red points. Figure 3b shows the Earth magnetic field density in slice, isosurface of the electron density in blue and the ion density in red. Similar perspectives are used for both figures. It is visible that two belts formed around the Earth.

We capture the data of field and particle information at high frequency to visualise the formation process. We identified three phases during the relaxation process. At the early stage of the simulation, since the velocity of electrons is much faster than ion, electron moved to the surface of the Earth, creating plasma sheath. This stage is clearly visible as the expansion of particle belts from Figure 4a to Figure 4b. As a result of electric field created by sheath, which in turn decelerate particles, the particles belts start to shrink. This stage can be clearly visualise in from Figure 4b to Figure 4c. The interaction of particles and field continued and reached an equilibrium status, which remained until the end of the simulation. Figure 4d is taken at a much later time than Figure 4c in the simulation. It is clear that

minimal changes are observed and particles are trapped inside the Earth's dipole field, creating plasma belts.

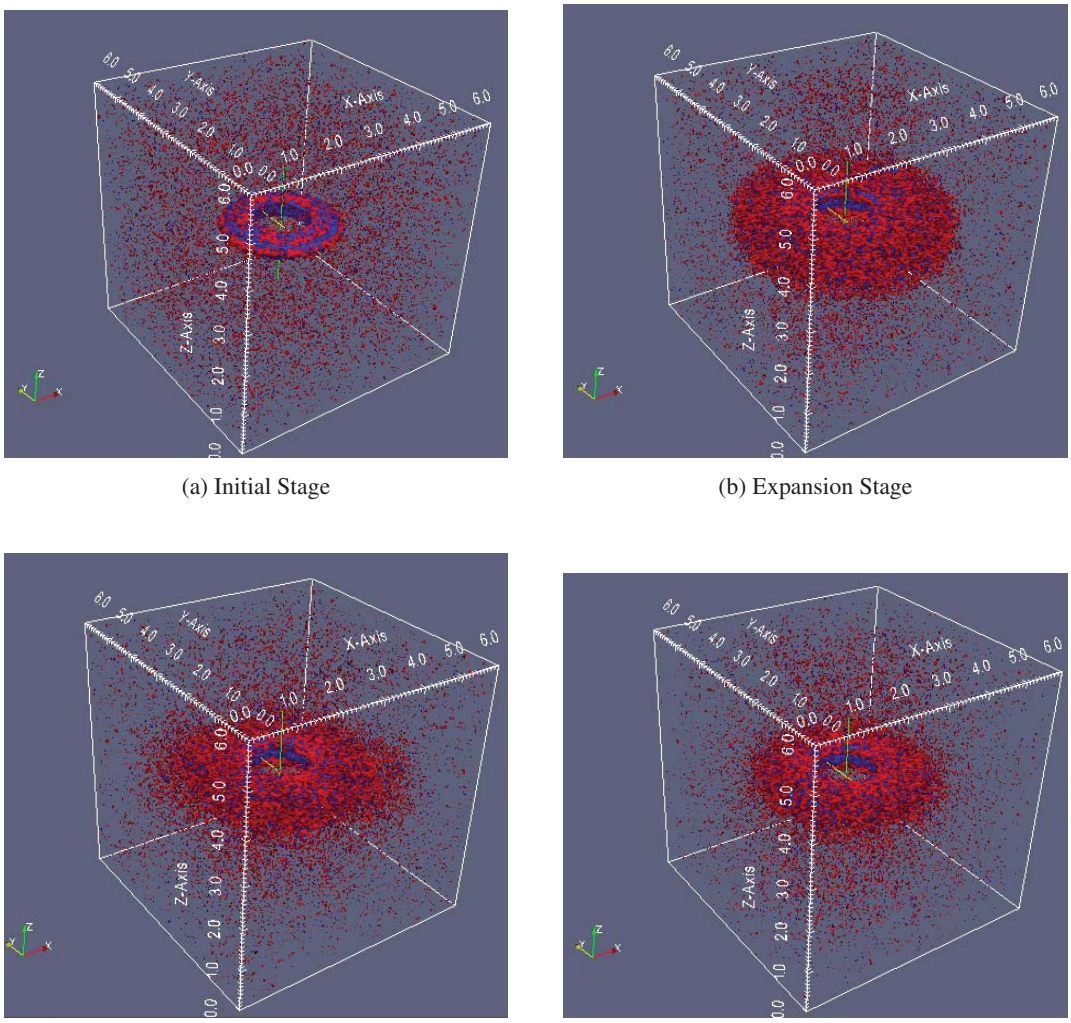

(a) Initial Stage

(b) Expansion Stage

(c) Shrinking Stage

(d) Stable Stage

Figure 4: Three phases during the relaxation process of the system from non-equilibrium status to equilibrium status were observed. Figure 4a to Figure 4b show the expansion of particle betts. Figure 4b to Figure 4c show the shrinking of particle betts. Figure 4c to Figure 4d show the system has reached equilibrium status.

To better locate the particle belts, we also extract high energetic particles after the system reached equilibrium status. From the plots present below, it is clear that radiation belts of ion and electrons formed around Earth and stayed stable for the rest of the simulation.

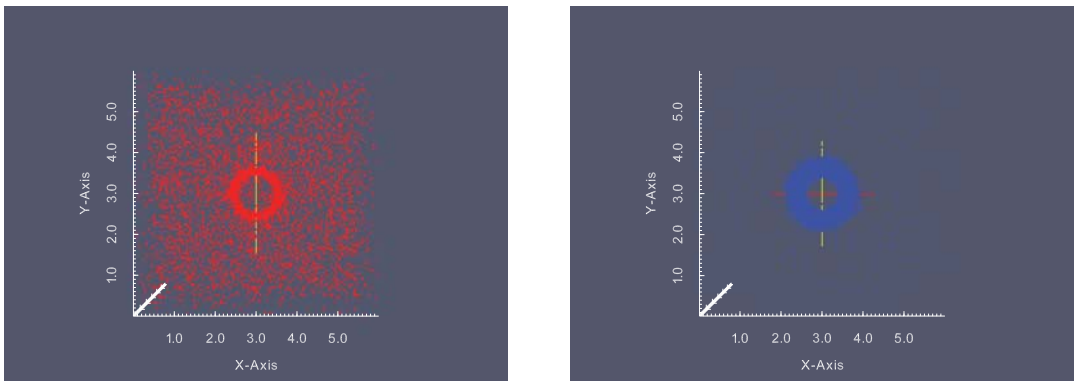

(a) Distribution of Ion in equilibrium status

(b) Distribution of Particle in equilibrium status

Figure 5: Figure 5a shows ions in red points, a belt around the Earth is visible. Figure 5b shows ions in blue points, a belt around the Earth is visible. It is also visible that the ion spreads more evenly over the whole simulation box, while electron is more concentrated around the Earth.

This project is mainly to explore the possible set up of system that could be used for initial condition of future simulations. We start from a small domain and with constraints summarised below. We observed the formation of particle belts and relaxed the system to equilibrium status, however, for more realistic large simulation in the future, the below constrains need to be addressed.

1. The goal of the work is to start from a non-equilibrium set up of dipole model and relax to equilibrium status.
2. A very small system is used while full simulation requires a much larger system.
3. Unrealistic mass ratio (1:25 rather than 1:1836) between electron and ion is used to speed the simulation.
4. Classic particle mover with sub-cycling is used while particles faster than then 10% of speed light exit. Relativistic mover needs to be implemented.
5. Load unbalance (shown in Figure 6) needs to be addressed before full simulation.

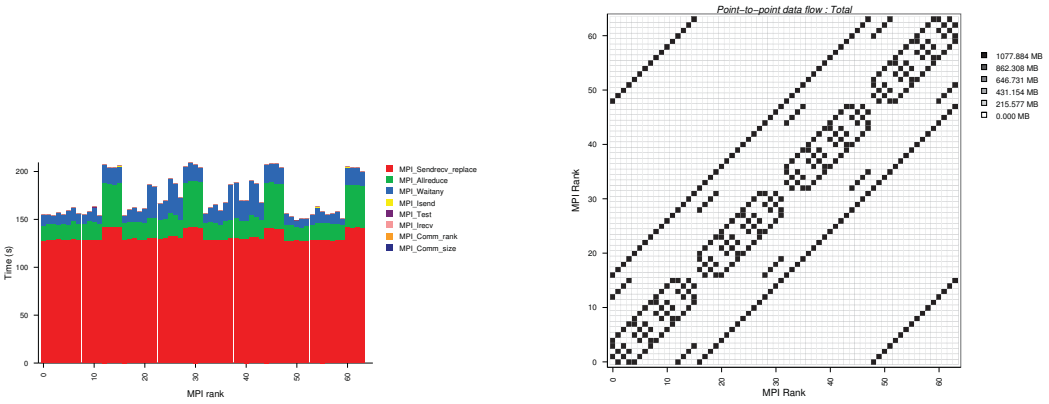

(a) Distribution of time spent on each process

(b) Data flow between processes

Figure 6: Figure 6a shows the distribution of time spent by each process. Load unbalance is visible as some processes spent significant larger amount of time for MPI_Allreduce operation. Figure 6b shows the data flow between processes.

5. Conclusion

We completed our project in two phases. First, we performed convergence test of our new version of implicit PIC code, by simulating whistler anisotropy instability at low electron β (Gary et al., 2011). After the performance benchmark has been established, we proceed to the second phase to explore how to reach an equilibrium status in dipole set. We first implemented the dipole model to initialise the Earth's magnetic field for the dynamics of radiation belts. We also implemented the procedure in particle mover to slowly ramp up the magnitude of magnetic field on each particles in the first 200 cycles. We implemented sub-cycling technique to correctly move the particles in each cycle, where ion has 2 sub-cycles and electron has 10 sub-cycles in each computational cycle. Simulations of radiation belts were carried on Mustang supercomputer. We observed the formation of particles belts and the relaxation from non-equilibrium status to equilibrium status. We also profiled and analysed the performance of the new iPIC3D code. Constrains of the current simulation are also discussed. In the future we will simulate larger systems with higher particle mass ration and also look into open boundary conditions.

References

Birdsall, C.K., Langdon, A.B., 2004. Plasma physics via computer simulation. CRC Press.

Deca, J., Divin, A., Lapenta, G., Lembège, B., Markidis, S., Horanyi, M., 2014. Electromagnetic particle-in-cell simulations of the solar wind interaction with lunar magnetic anomalies. Physical review letters 112, 151102.

Forum, M.P.I., 2012. MPI: A Message-Passing Interface Standard Version 3.0. Chapter author for Collective Communication, Process Topologies, and One Sided Communications.

Gary, S.P., Liu, K., Winske, D., 2011. Whistler anisotropy instability at low electron β: Particle-in-cell simulations. Physics of Plasmas (1994-present) 18, 082902.

Hockney, R.W., Eastwood, J.W., 1988. Computer simulation using particles. CRC Press.

Lapenta, G., Markidis, S., Poedts, S., Vucinic, D., 2013. Space weather prediction and exascale computing. Computing in Science & Engineering 15, 68–76.

Markidis, S., Lapenta, G., Rizwan-uddin, 2010. Multi-scale simulations of plasma with iPIC3D. Mathematics and Computers in Simulation 80, 1509 – 1519.

Mason, R.J., 1981. Implicit moment particle simulation of plasmas. Journal of Computational Physics 41, 233–244.

OpenMP Architecture Review Board, 2013. OpenMP application program interface.

Öztürk, M.K., 2012. Trajectories of charged particles trapped in earth?s magnetic field. American Journal of Physics 80, 420–428.

Influence of ionospheric conductivity on the magnetospheric dynamics

Shreedevi P.R.

Space Physics Laboratory, VSSC, ISRO, Trivandrum, India 695022

Yiqun Yu, Vania Jordanova

Los Alamos National Laboratory, Los Alamos, NM 87545.

Abstract

This study examines the influence of ionospheric conductivity on the magnetospheric dynamics for the geomagnetic storm event triggered at 06:00 UT on March 17, 2013 (Dst ~ -130nT). Three simulations were performed with different ionospheric conductances using the SWMF which couples a global MHD code (BATS-R-US) to the RAM-SCB model for the inner magnetosphere and the ionospheric potential solver. The solutions are investigated in comparison with the observations from satellite measurements as well as empirical models. The preliminary results illustrate that the inclusion of solar EUV conductance gives rise to an asymmetry in the dawn-dusk potential thereby forcing the field-aligned currents to close on the dayside. The pressure distribution in the magnetosphere responds to this forcing and shows high correlation with the Dst indices simulated at the main phase of the storm. The model reproduces the magnetic field in the inner magnetosphere for all the three simulations.

Keywords: ionosphere, magnetosphere, geomagnetic storm

1. Introduction

One of the important factors that determine the global state of the magnetosphere is the ionospheric conductivity. The conducting ionosphere enables the closing of field-aligned currents thereby allowing magnetospheric convection and the exchange of energy and momentum between the neutral and ionized gases to occur. The interaction of the solar wind and the IMF with the magnetosphere results in the generation of region-1 current system which flow at high latitudes. Pressure gradients in the inner magnetosphere give rise to the region-2 current system which lies equatorward of the region-1 current system.

Ionospheric conductivities arise due to the absorption of solar EUV by the neutral species present in the upper atmosphere thus creating photoelectrons (e.g., Torr et al., 1979). They are also dependent on the solar zenith angle and the composition of the neutral atmosphere between a given point and the sun. The perpendicular conductivity is low in the region above ~150km because there are very few collisons between ions, electrons and neutrals. In the region between 100 to 150km, the electrons tied to the magnetic field create a Hall current due to the EXB drift while the diverted ion motion due to ion-neutral collisions create the Pederson current. In the high latitudes, particle precipitation is an important contributor to the conductivities (e.g., Galand et al., 2001). The auroral particle precipitaion can be related to the Hall and Pederson conductivities (Robinson et al., 1987) which in turn are related to the ground-based magnetometer measurements (Ahn et al., 1983) . There are various conductance models which highlight the importance of solar radiation and particle precipitation in producing ionospheric conductivities.

The influence of ionosphere on the magnetospheric configuration is currently an area of much interest mainly because of its implications to space weather phenomena. In order to determine how the ionospheric conductivity controls the magnetospheric dynamics, we require satellite measurements for different ionospheric conductances from the same region of the magnetosphere while we have very similar solar wind conditions. This is practically very difficult to fulfil. A number of studies have been done using global MHD codes to determine what effects the ionosphere has on the magnetosphere (e.g., Fedder and Lyon, 1987; Ridley et al., 2004) . Using a global magnetohydrodynamic(MHD)

code, Fedder and Lyon (1987) showed that the magnetosphere is neither a current nor a voltage generator. Ridley et al. (2004) continued the work by Fedder and Lyon (1987) and showed that in the case of both larger and smaller values of conductance the steady-state magnetosphere is neither a current nor a voltage generator.

This study will examine the dependence of magnetospheric dynamics on the ionospheric conductance. We use the SWMF(Space Weather Modelling Framework) (Toth et al., 2005) which is an unified self-consistent model that allows for a comprehensive investigation of the processes happening in the global magnetosphere, inner magnetosphere and the ionosphere during the chosen geomagnetic storm event. The aim of this project is to run several simulations for studying the influence of the ionospheric conductances on the magnetospheric dynamics during the severe storm(Dst ~ -130 nT) that started on 06:00 UT of March 17, 2013. For this purpose, we have run 3 global simulations with different ionospheric conductances. The results from these simulations are compared with the satellite measurements and the field-aligned currents(FACs) and electric potential obtained from the Weimer model.

2. Methodology

We ran global simulations of the solar wind-magnetosphere-ionosphere interaction for the geomagnetic storm triggered on March 17, 2013 by coupling several first-principle physics-based models including a global MHD code Block-Adaptive Tree Solar-Wind Roe Upwind Scheme(BATS-R-US) (Powell et al., 1999) , a kinetic ring current model RAM-SCB (e.g., Jordanova et al., 2006; Zaharia et al., 2006) , and an ionospheric electrodynamics solver (Ridley et al., 2004) . The schematic representation of the couping framework between these models is shown in Figure 1.

The global MHD code is coupled to the ionospheric electrodynamics solver at an altitude of 100km. The FACs computed at 3.5 R_E of the BATS-R-US code are mapped to the ionosphere at an altitude of 100km. The ionospheric electric potential computed using the FACs and ionospheric conductance are mapped to the inner boundary of the MHD code(i.e., 2.5 R_E) to obtain the EXB convection velocity which is used as the inner boundary condition in the MHD code. The ionospheric conductance used in the potential solver includes solar generated conductance which is dependent on the solar zenith angle and F10.7, nightside conductance caused by star light and galactic sources and auroral conductance that is associated with particle precipitation. The auroral conductance is specified through an empirical relationship with FACs which was derived using the assimilative mapping of ionospheric electrodynamics(AMIE) technique (Richmond and Y. Kamide, 1988).

The kinetic Ring current Atmosphere interactions Model(RAM) along with a 3-D Euler-potential based plasma equilibrium code is coupled by RAM-SCB code that models the kinetic physics of charged particles inside 6.5 R_E in the inner magnetosphere. The MHD code and the ionospheric potential solver are also coupled with the RAM-SCB code. The 3-D equilibrium code uses the plasma pressure produced by the RAM ring current distribution to calculate the force balanced magnetic field which is again coupled back to RAM. The pressure and density corrections obtained from the RAM-SCB code is used by the BATS-R-US code thereby modifying the global magnetospheric configuration and current systems. In turn, the kinetic model receives density and characteristic temperature at 6.5 R_E from the MHD code which is updated every 5 minutes and is used by the RAM-SCB code as the plasma sheet source boundary condition.

The 3-D equilibrium code gets the magnetic field boundary condition from an empirical model T-89. In regular intervals of 10 seconds, the electric potential obtained from the ionospheric potential solver is mapped onto the inner magnetosphere from which the electric field needed in RAM is derived. In this way a self consistent electric field drives the ring current model along with its self-consistent magnetic field.

Each simulation was run for 24 hours. The upstream boundary conditions obtained from the satellite measurements were used to run the BATS-R-US code. Our first simulation has a constant Hall and Pederson conductance in the ionosphere. The second simulation uses a conductance model including contributions from extreme ultraviolet(EUV) and night side conductances along with an artificially depleted conductance in a band centered on the magnetic pole. The final simulation uses a more realistic conductance model, including contributions from ionization induced by extreme ultraviolet(EUV) radiation, starlight and galactic sources and polar cap conductance.

3. Results

For the geomagnetic storm triggered on March 17, 2013 at 06:00 UT, global simulations were run with three types conductance models using the SWMF, the results of which are described below.

Type 1: Constant Hall and Pederson conductance

The simulated FACs and electric potential in the northern hemisphere with constant Hall and Pederson conductance during the quite period at 06:00 UT and during the storm main phase at 09:10 UT are shown in Figure 2. In row(a), before the sudden storm commencement at 06:00 UT, a weak region-1 current system is seen on the dawnside whereas the region-2 current system is seen to be very little. During the main phase of the storm at 09:10 UT, both the region-1 and region-2 current systems are intensified and expand equatorward. The reason for this can be understood by examining the flow patterns in the inner magnetosphere displayed in Figure 3. It is evident that the pressure gradients associated with the region-2 current system is not large during the quite time at 06:00 UT whereas at 09:10 UT there is a large enhancement in the ring current pressure gradient which leads to intensification of the region-2 current system. The electric potential exhibits the classical two-cell pattern as can be seen in row(b). It is clearly seen that the electric potential cell expands to lower latitudes during the disturbed period. This is because of the penetration of convection electric field to the sub-auroral latitudes.

Type 2: Solar EUV, Nightside conductance and a depleted auroral oval

Figure 4 shows results of the simulation including contributions from solar EUV and the nightside 'starlight conductance'. In addition to this an artificially depleted conductance is specified by scaling the FACs in such a way that their latitudinal strength varies exponentially from the center of the oval at each longitude. Row(a) shows the variation in Hall conductance at 06:00 UT (quite time) and 09:10 UT (storm main phase) respectively. It is clearly seen that during the main phase of the storm (09:10 UT) there is an enhancement in the hall conductivity with the maximum value at the center of the auroral band. The Pederson conductivity shown in row(b) also shows a similar trend. This enhancement in conductances during the disturbed period is because of the increased particle precipitaion. Row(c) displays the FACs for the quiet and disturbed periods. It is clearly observed that the FACs intensify and expand equatorward which is due to the pressure build-up in the equatorial plane of the magnetosphere as shown in Figure 5. The electric potential displayed in row(d) also exhibits the typical two-cell pattern as was in the type 1 case. It can be seen that the field-aligned currents in this case flow primarily on the dayside, while the potential is confined to the nightside. The dayside conductance has a higher magnitude which leads to stronger FACs and a lower potential while the reverse happens in the case of nightside conductance.

Type 3: Solar EUV, Nightside conductance and Polar cap conductance

Figure 6 shows the Hall and Pederson conductances, FACs and electric potential simulated using contributions from solar EUV radiation, Nightside conductance and Polar cap conductance. Row(a) and row(b) displays the Hall and Pederson conductance at 06:00 UT and 09:10 UT. It is clearly seen that the Hall and Pederson conductances increase during the main phase of the storm owing to the increase in particle precipitation. The FACs shown in row(c) and the electric potential cell shown in row(d) are both seen to intensify and expand equatorward in response to the disturbance. The potential cell also extends into the postmidnight region with the flow reversal in the Harang reversal region. Figure 7 shows the pressure gradients in the equatorial plane of the magnetosphere. It is clear that the large pressure gradients in the 2-6 R_E region of the inner magnetosphere leads to enhancement of the region-2 current system during the main phase of the storm.

Comparison with observations

Figure 8 shows the FACs and electric potential obtained from the Weimer model. The results obtained from the simulation using the type 3 conductance model is in close agreement with that obtained from the Weimer model. Figure 9 displays the observed Dst index in comparison with the simulated Dst indices for all the three cases calculated using the Dessler-Parker-Sckopke relation (Dessler and Parker, 1959; Sckopke, 1966) based on the ring current energy

density at 6.5 R_E. The variations in the simulated Dst indices shows good correlation with the pressure variations in the inner magnetosphere which clearly indicates that the plasma injected into the inner magnetosphere after reconnection is an important source for the intensification of ring current. The observed Dst index agrees well with the Dst index simulated using the type 3 conductance model which represents the realistic case. Figure 10 and Figure 11 show the simulated z-component of the magnetic field in comparison with the actual measurements of the GOES and RBSP satellites for the same period. The magnetic field measured from the RBSPa and RBSPb satellites is well in agreement with the results from all the three simulations. The magnetic field measured by the GOES satellites also show a good correlation with the simulations run using type 2 and type 3 conductance models till around 14:00 UT. The observed discrepancy in the simulated z-component of magnetic field during the later period will be investigated in our future work.

4. Conclusion

The influence of ionospheric conductivities on the magnetospheric dynamics during the severe geomagnetic storm triggered on March 17, 2013 has been studied using the SWMF. The ionospheric convection patterns obtained from the simulations have been compared with the results from the Weimer model which is an empirical model.

While the conductances were assumed to be constant globally the convection pattern was found to be quasi-symmetric across the noon-midnight meridian whereas when the day-to-night gradient in conductance was introduced in the simulation the potential cell was pushed to the nightside and the FACs flow on the dayside in response to the increased conductivity on the dayside. For the type 1 conductance model the ring current pressure gradients are distributed in the equatorial magnetosphere unlike the westward flow of ring current in the type 2 and type 3 case. In all the three simulations the Dst indices show high correlation with the plasma pressure gradients in the inner magnetosphere which is well represented by the RAM-SCB model. The capability of including the satellite trajectory in the SWMF allows for comparison of simulated magnetic field along the trajectories of the satellites with actual measurements. The simulated magnetic field is also in agreement with the measurements from the RBSP satellites in all the cases which indicates that the self consistent treatment of magnetic field in the RAM-SCB model is highly suitable.

This work highlights the role of global conductance patterns in modulating the dynamic magnetosphere-ionosphere system. Future work will focus on the study of the influence of ionospheric conductance on various magnetospheric processes like reconnection, flow patterns and flux injections in order to quantify what effects the ionosphere has on the magnetosphere.

References

Ahn, B.H., Robinson, R., Kamide, Y., Akasofu, S.I., 1983. Electric conductivities, electric fields and auroral particle energy injection rate in the auroral ionosphere and their empirical relations to horizontal magnetic disturbances. Planet.Space Sci., 31, 641.

Dessler, A.J., Parker, E.N., 1959. Hydromagnetic theory of magnetic storms. J.Geophys.Res., 64, 2239.

Fedder, J., Lyon, J., 1987. The solar wind-magnetosphere-ionosphere current-voltage relationship. Geophys.Res.Lett., 14, 880.

Galand, M., Fuller-Rowell, T., Codrescu, M., 2001. Response of the upper atmosphere to auroral protons. J.Geophys.Res., 106, 127.

Jordanova, V.K., Zaharia, S., Welling, D.T., 2006. Comparative study of the ring current development using empirical,dipolar and self-consistent magnetic field simulations. J.Geophys.Res., 115, A00J11.

Powell, K.G., P.L. Roe, T.J. Linde, T.I. Gombosi, D.L.D. Zeeuw, 1999. A solution-adaptive upwind scheme for ideal magnetohydrodynamics. J.Comp.Phys., 154, 284.

Richmond, A.D., Y. Kamide, 1988. Mapping electrodynamic features of the high-latitude ionosphere from localized observations: Technique. J.Geophys.Res., 93(A6), 5741–5759.

Ridley, A.J., T.I.Gombosi, D.L.DeZeeuw, 2004. Ionospheric control of the magnetosphere: conductance. Ann.Geophys., 22, 567.

Robinson, R., Vondrak, R., Miller, K., Dabbs, T., Hardy, D., 1987. On calculating ionospheric conductances from the flux and energy of precipitating electrons. J.Geophys.Res., 92, 2565.

Sckopke, N., 1966. A general relation between the energy of trapped particles and the disturbance field near the Earth. J.Geophys.Res., 71, 3125.

Torr, D., Torr, M., Brinton, H., Brace, L., Spencer, N., Hedin, A., Hanson, W., Hoffman, J., Nier, A., Walker, J., Rusch, D., 1979. An experimental and theoritical study of the mean diurnal variation of O^+,NO^+,0_2^+, and N_2^+ ions in the midlatitude F_1 layer of the ionosphere. J.Geophys.Res., 84, 3360.

Toth, G., Igor V. Sokolov, T.I. Gombosi, David.R.Chesney, C.Robert Clauer, D.L.D Zeeuw, Kenneth C.Hansen, Kevin J.Kane, Ward B.Manchester, Robert C.Oehmke, K., Aaron J.Ridley, Ilia I.Roussev, Quentin F.Stout, Ovsei Volberg, 2005. Space Weather Modeling Framework: A new tool for the space science community. J.Geophys.Res., 110, A12226.

Zaharia, S., Jordanova, V.K., Themsen, M.F., Reeves, G.D., 2006. Self-consistent modeling of magnetic fields and plasmas in the inner magnetosphere. J.Geophys.Res., 111, A11S14.

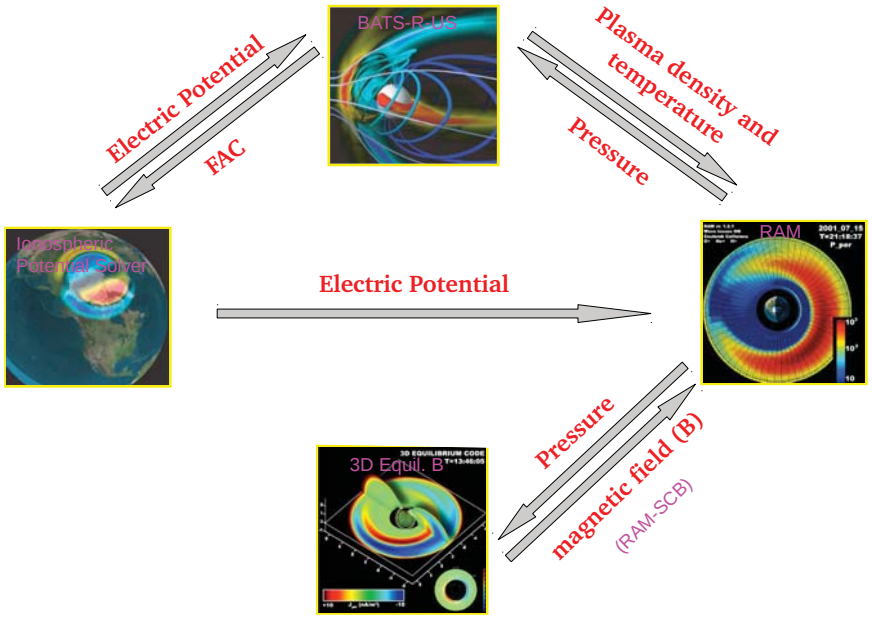

Figure 1: The Space Weather Modeling Framework(SWMF) and its coupling between the various physics based models

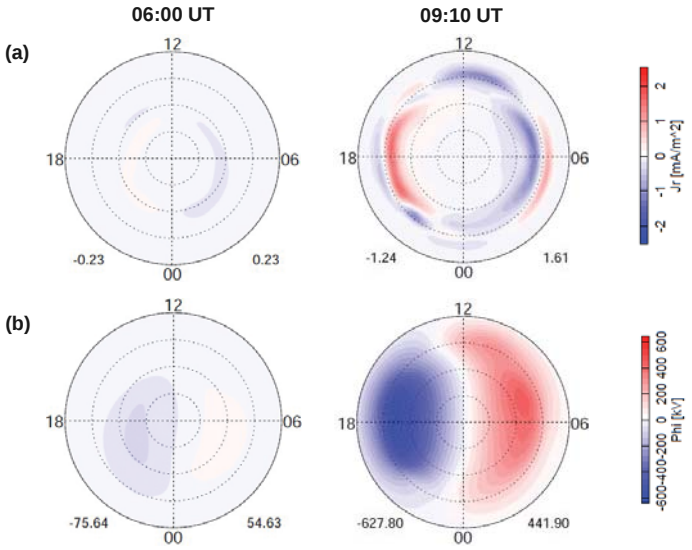

Figure 2: Results of simulation using type 1 conductance model at 06:00 UT(quite time) and 09:10 UT(storm main phase): (a)field-aligned currents(red indicates upward current system and blue indicates downward current system),(b) Electric potential.The maximum and minimum values are shown below each plot to the right and left, respectively.

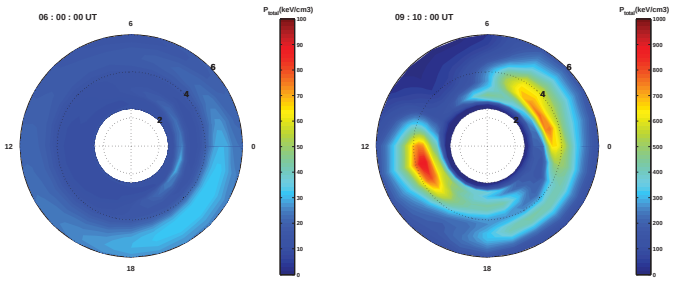

Figure 3: Simulated pressure gradients in the inner magnetosphere (2-6 R_E) at 06:00 UT (quite time) and 09:10 UT (storm main phase) using the type 1 conductance model.

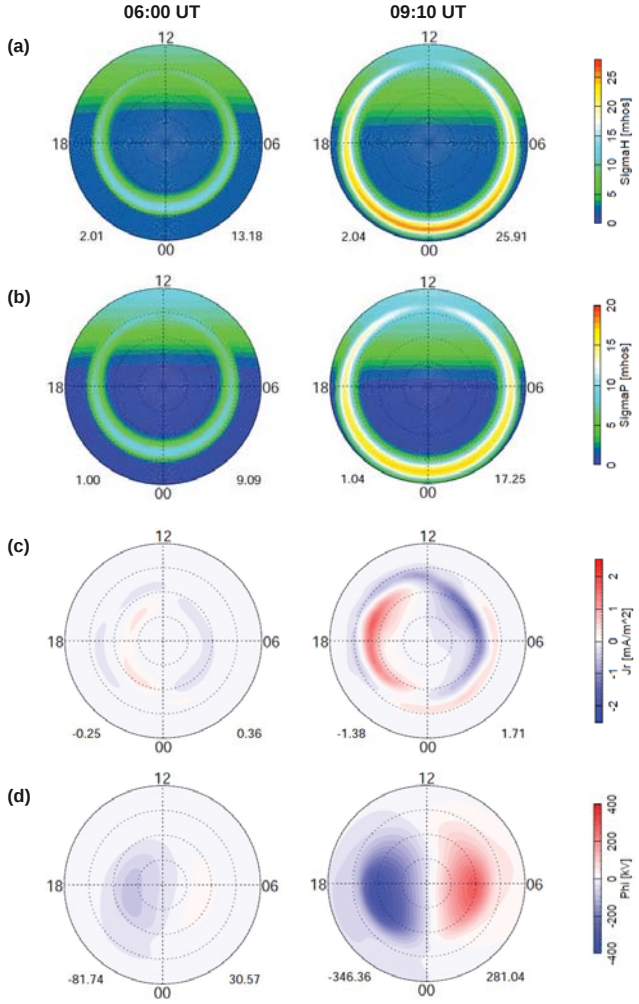

Figure 4: Results of simulation using Type 2 conductance model at 06:00 UT(quite time) and 09:10 UT(storm main phase): (a)Hall coductance,(b)Pederson conductance,(c)field-aligned currents(red indicates upward current system and blue indicates downward current system),(b) Electric potential.The maximum and minimum values are shown below each plot to the right and left, respectively.

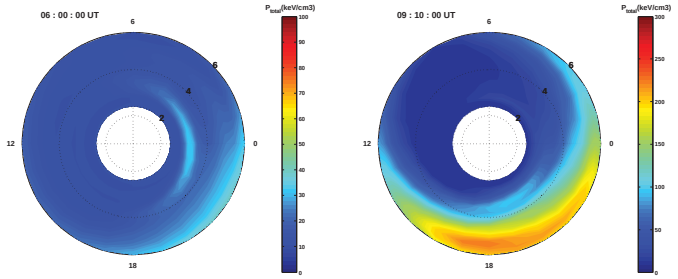

Figure 5: Simulated pressure gradients in the inner magnetosphere (2-6 R_E) at 06:00 UT (quite time) and 09:10 UT (storm main phase) using the type 2 conductance model.

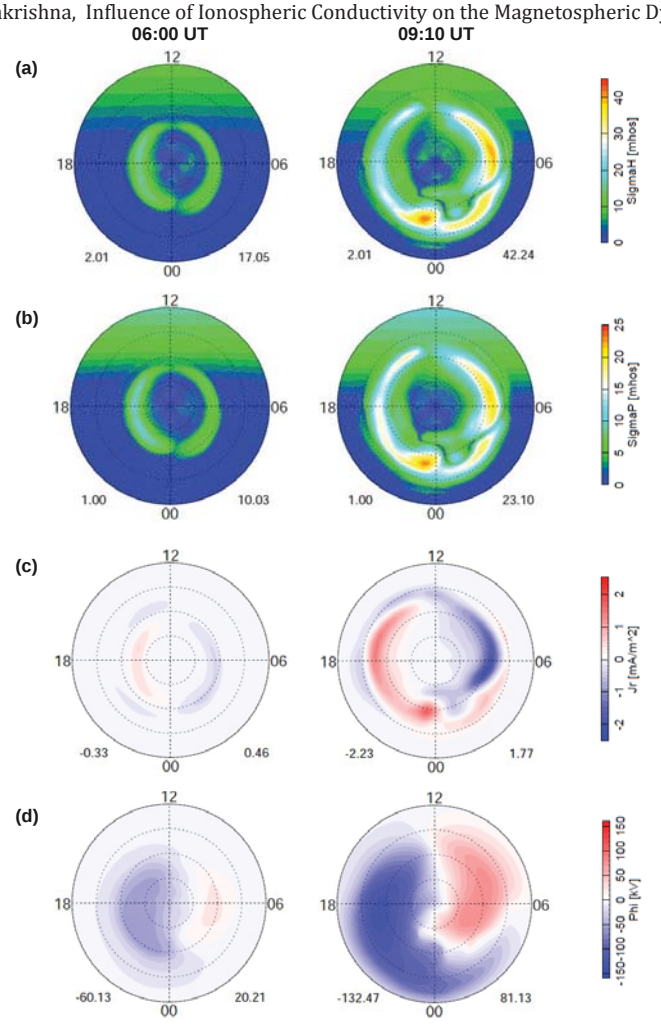

Figure 6: Results of simulation using Type 3 conductance model at 06:00 UT(quite time) and 09:10 UT(storm main phase):(a)Hall coductance,(b)Pederson conductance,(c)field-aligned currents(red indicates upward current system and blue indicates downward current system),(b) Electric potential.The maximum and minimum values are shown below each plot to the right and left, respectively.

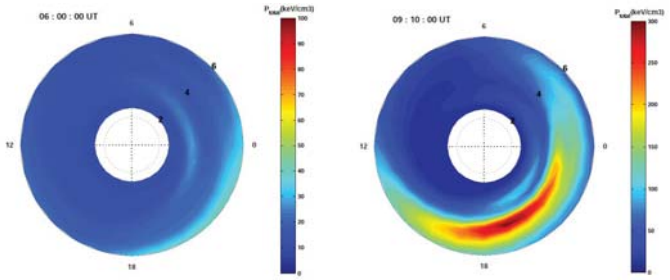

Figure 7: Simulated pressure gradients in the inner magnetosphere (2-6 R_E) at 06:00 UT (quite time) and 09:10 UT (storm main phase) using the type 3 conductance model.

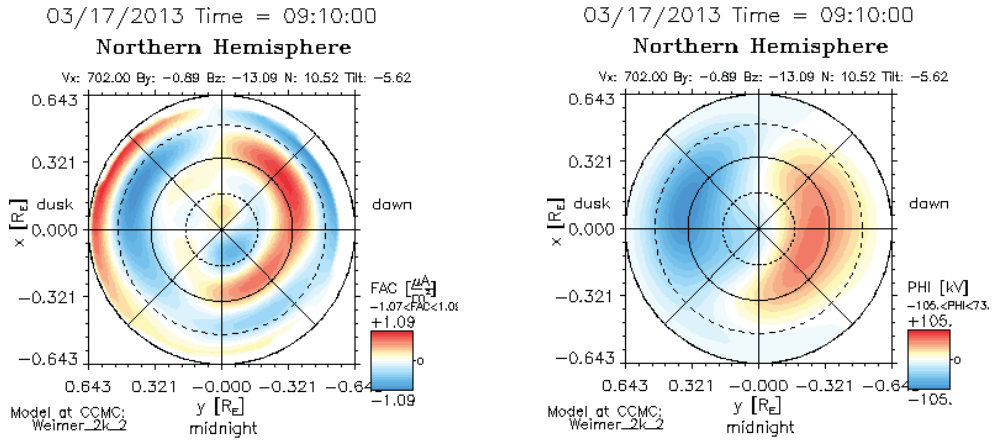

Figure 8: Field-aligned currents and electric potential at 09:10 UT (storm main phase) obtained from the Weimer model.

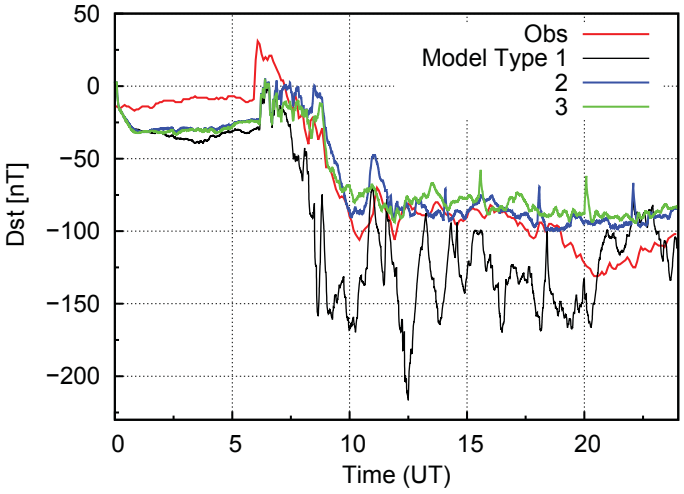

Figure 9: Comparison of the simulated Dst index using type 1 (black), type 2 (blue) and type 3 (green) conductance models with the observed SYM-H index (red).

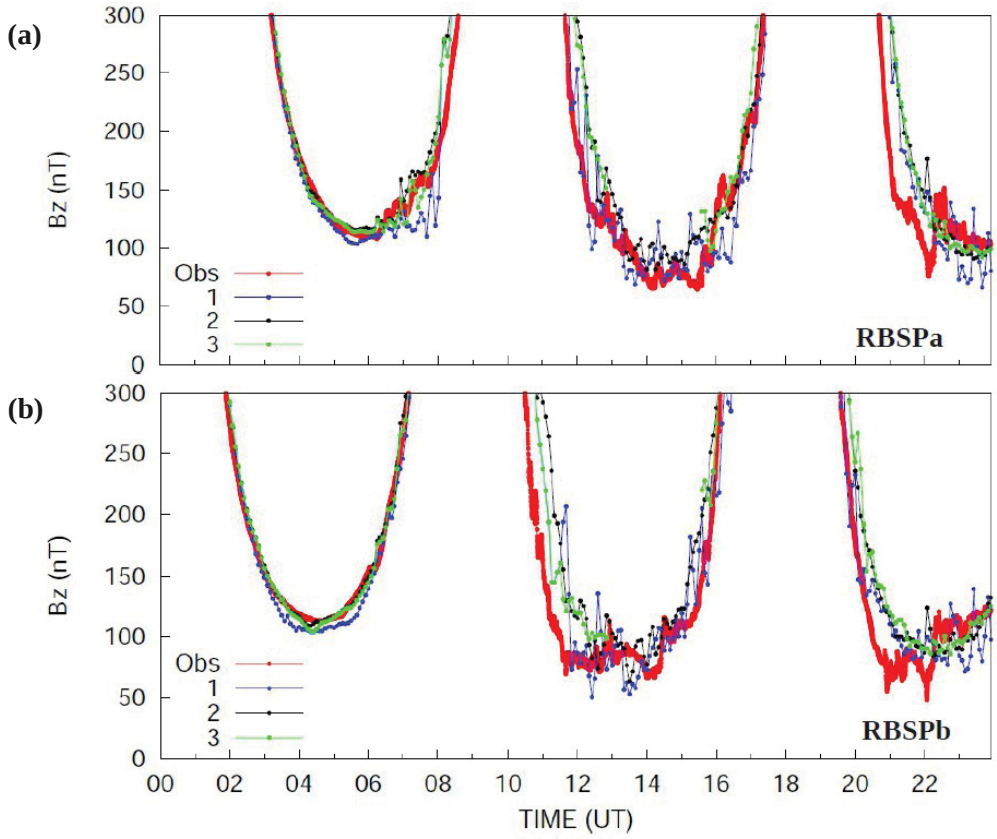

Figure 10: Comparison of insitu measurements (red) from RBSPa and RBSPb satellites with B_z component of magnetic field simulated using type 1 (blue), type 2 (black) and type 3 (green) conductance models.

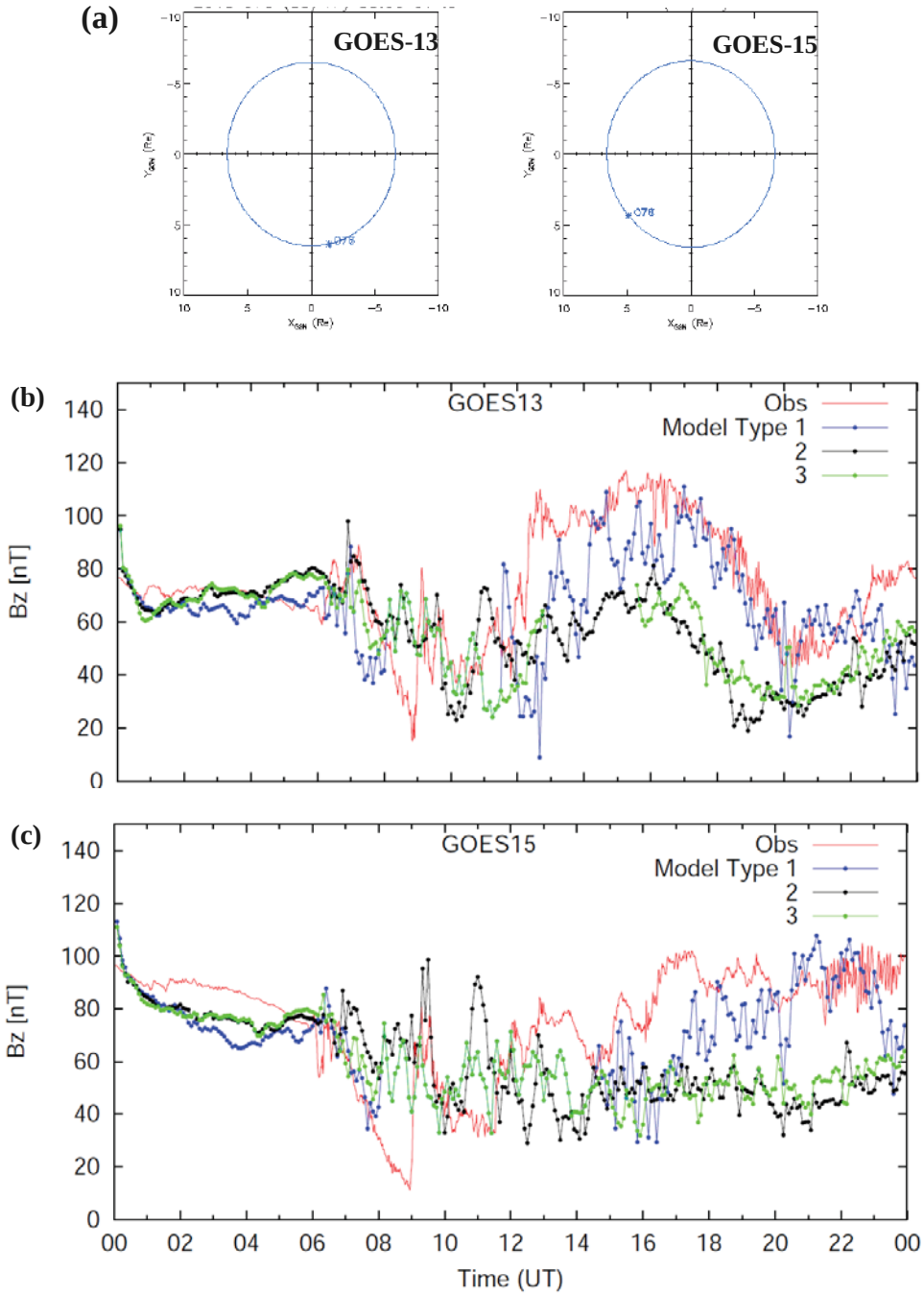

Figure 11: (a)The orbit of GOES-13 and GOES-15 satellites in the GSM XY plane. (b)Comparison of insitu measurements (red) from GOES-13 and GOES-15 satellites with B_z component of magnetic field simulated using type 1 (blue), type 2 (black) and type 3 (green) conductance models.

Global Thermospheric Density Response to a Geomagnetic Storms

Padmashri Suresh

Utah State University, Logan, UT 84321

Andrew Walker

Los Alamos National Laboratory, Los Alamos, NM 87545

Humberto Godinez

Los Alamos National Laboratory, Los Alamos, NM 87545

Richard Linares

Los Alamos National Laboratory, Los Alamos, NM 87545

Abstract

Thermosphere density measurements have led to an improved understanding of the global state of the upper atmosphere since the advent of using accelerometer data from satellites for deriving densities. With the availability of a global picture of the upper atmosphere from these satellites measurements, the atmospheric response to various episodic and periodic solar and geomagnetic events has recently been studied in great detail. This has led to large improvements in now-casting of the thermosphere state through various physics and empirical atmospheric models. However, forecasting the accurate state of the upper atmosphere, especially during geomagnetic storms, is currently not possible with these models. With the increasing satellite populace in near Earth space, such forecasting is highly essential to determine accurate orbits and continue space operations.

The Los Alamos National Lab (LANL) project, Integrated Modeling of Perturbations in Atmospheres for Conjunction Tracking (IMPACT), is a step forward in this direction, by harnessing the power of the physics based models and global satellites measurements, by employing data assimilation techniques. One of the key steps for employing data assimilation techniques is to establish and quantify the uncertainty of the physics and empirical models in contrast to the true state measured by the satellites. In this paper, we present a case study of geomagnetic storm conditions as replicated by the empirical and physics based models, in order to ascertain their behavior in comparison to the corresponding satellite measurements. We also present a framework which will aid in extending such a comparison to a statistical scale that could be potentially used to calibrate the integrated data assimilation model under storm conditions.

Keywords: orbital drag, thermosphere density, space weather

1. Introduction

The growing number of space faring nations in the world has led to the overpopulation of near Earth space with satellites and debris growing at an increasingly alarming rate. It has been speculated that orbital collisions will get more frequent, and, between now and 2030, it could possibly reach a runaway environment. This catastrophic scenario referred to as Kessler syndrome has been touted to potentially destroy our assets in near-Earth space, resulting in a debris cloud that could make space itself inaccessible. In today's era of space-technology-reliant society, such a scenario will have devastating impacts on all aspects of our life, making it a top priority for the space community to tackle this problem as quickly and as effectively as possible [Koeller et al.,2013.a]. Preventing the Kessler Syndrome would require an innovative, ground breaking, orbital dynamics framework that could perform

accurate orbit propagation, and conjunction analysis with detailed uncertainty quantification to address the space debris and collision avoidance problem.
The Los Alamos National Lab (LANL) project, Integrated Modeling of Perturbations in Atmospheres for Conjunction Tracking (IMPACT), was conceptualized with the goal of developing such an integrated modeling system that would address the current needs in space debris and conjunction analysis for resident space objects (RSO) [Koeller et al.,2013.a, Koeller et al.,2013.b]. The project will provide an integrated solution combining physics-based density modeling of the upper atmosphere, satellite drag forecasting and conjunction analysis with non-Gaussian uncertainty quantification. A key element in improving satellite orbital predictions will be the correct specification of the space environment. This is especially important during space weather conditions since the biggest uncertainty in accurate LEO prediction is modeling drag due to density changes arising from space weather events. Although, there are numerous empirical and physics models that can estimate the current state variables of the upper atmosphere to a fairly large extent owing to the availability of global satellite measurements, they fail to accurately replicate the upper atmosphere during space weather events. Also, these models do not have forecasting capabilities.

IMPACT provides closure to all of these outstanding problems by creating a modeling system using data assimilation techniques based on ensemble Kalman filters which harnesses the power of satellite measurements in a physics based model. Hence this integrated system is not only able to forecast the LEO space environment but also better replicate the LEO space environment during space weather events.

A key step in creating this system will be to compare the global behavior of the physics based model under various storm conditions and to ascertain their associated deviation from true density values as measured by the satellites. This is necessary in-order to calibrate the data integrated physics based model and to understand any uncertainties arising from assumptions and physical representations that are used in constructing the physics models. In this paper, we perform such a comparison of GITM, the primary physics based model that is used in the IMPACT framework, with respect to the true atmospheric density given by the CHAMP and GRACE satellites. We also compare TIEGCM, which is a physics based model, and, NRLMSIS-00, an empirical model to compare how the primary physics model used in IMPACT compares to other frequently used physics and empirical models.

This comparison study aims to specifically answer the following questions:

1) How do the magnitude response of the models to a geomagnetic storm compare with that of true magnitude response as calculated from satellite measurements of the density?
2) What are the time scales of the storm response of the models and how do they compare to that of the time response measured by the satellite density data?

This work presented here was carried out for a single storm scenario but owing the usefulness of this study, a framework which could extend such a study to a statistical scale is also presented for future use.

In the following section, we present the data set and methodology used to compute the storm response

2. Data Presentation

The Challenging Mini-satellite Payload (CHAMP) satellite was launched into an almost circular, near polar orbit with an inclination of 87.28° and a period of ~93 days [Reigber et al.,2002]. It carried out simultaneous measurements of many thermospheric and ionospheric parameters, one of which was thermospheric total mass density. The twin satellites, Gravity Recovery And Climate Experiment Orbit (GRACE) A and B satellites, are an almost circular, polar orbits with an inclination of 89 ° and have an orbital period of ~ 95 minutes [Tapley et al., 2004]. The CHAMP and GRACE satellites, since their launch in 2002, have continuously provided pole-to-pole coverage of the upper atmosphere between 400-550Km at four local times across the globe. The neutral densities derived from accelerometer data of the CHAMP and GRACE satellites, as described by Sutton [2007] has been used in this study.

The empirical model, US Naval Research Laboratory Mass Spectrometer and Incoherent Scatter Radar (NRLMSISE-00), was developed by the US Naval Research Laboratory [Picone et al., 2002] and provides an excellent climatological description of the Earth's atmosphere. It calculates density and temperature of the neutrals

upwards of 90Km. It has been often used for atmospheric drag calculations and uses daily F10.7, a 81-day average F10.7 , Kp and Ap indices for solar and geomagnetic proxies respectively.

The physics model, Thermosphere-Ionosphere-Electrodynamics General Circulation Model (TIE-GCM), developed by the National Center for Atmospheric Research (NCAR), is a non-linear 3D representation of the coupled thermosphere-ionosphere system [Richmond, 1992]. The model solves the three-dimensional momentum, energy and continuity equations for neutral and ion species at each time step, using a semi-implicit, fourth-order, centered finite difference scheme on each pressure surface in a staggered vertical grid. The model uses daily F10.7, a 81-day average F10.7 value, and Kp Index and hemispheric power index and the lower boundary conditions are provided by the Global Scale Wave Model (GSWM).

Global Ionosphere Thermosphere Model (GITM), the primary physics model used by IMPACT, is another global thermosphere and ionosphere model that solves the full Navier-Stokes equations for density, velocity, and temperature for neutral and charged components [Ridley et al., 2006]. GITM uses F10.7, the hemispheric power index (HPI), interplanetary magnetic field (IMF) data and solar wind velocity as solar and geomagnetic inputs. GITM inherently allows for non-hydrostatic solutions to develop which allows for realistic dynamics in the auroral zones. This is the main difference between GITM and the hydrostatic solution of TIE-GCM.

3. Data Analysis

The thermosphere density structure if given by the modulation of the zonal mean density by various periodic processes like seasonal and local time variations. In addition to this, there is an additional deposition of energy and momentum during the episodic geomagnetic activity during space weather events, which alter the thermosphere mean structure from its quiet time structure. In this paper, it is the alteration of the thermosphere mean structure by this geomagnetic activity, we are interested in understanding. In particular, we are interested in understanding what the increase in the density structure globally and how long does the space weather events induced density changes take to propagate globally.

To obtain the magnitude response, we simply have to subtract the quiet day density values from the active/storm day in order to obtain the thermosphere response to the space weather event. However we need to choose the active and quiet day such that they have the same local time and season. This needs to be done to prevent aliasing from local time and seasonal tidal structures. The satellites used in this study, CHAMP and GRACE precesses in local time slowly, making it easier to satisfy this condition of ensuring that the measurements behave like they are synoptic. The time response can be obtained by calculating the cross-correlation of the magnitude response to a storm index like Kp or Ap and obtaining the time delay. In this study we have taken the orbit averaged data of the satellites and hence the responses calculated in this work are global responses or latitude independent responses.

We were particularly interested in studying a geomagnetic storm during the solar minimum since most of the model and data comparison studies that have been carried out so far have been for solar maximum conditions. For our case study, we chose the Oct 11th 2008 storm. It was a moderate storm with a maximum Kp Index of 6. Also, this was preceded by a quiet day (October 10 2008) ensuring the local time and F10.7 and seasonal effects do not alias into the satellite data and thus can be easily used to calculate storm responses. We present the geomagnetic data and the solar data for the storm and quiet day under study in Figure.1.

Note that, in this study, we have assumed periods with $Kp<3$ as quiet times and $Kp>3$ and $Kp<5$ as active and $Kp>4$ as storm periods. The orbit averaged density data from GRACE and the model computed density values along its trajectory of the two satellites are presented in Figures 2. The calculated magnitude response for GRACE, CHAMP and the time response are presented in Figures 3 and 4 along with all the 3 models along both of their trajectories. The percentage time and magnitude responses are presented in Figures 5 and 6.

Although this study was conducted for a single storm, it would be highly beneficial to extend this to a statistical scale to truly understand the biases and deviations that could be expected from the models in comparison to the actual storm time atmosphere behavior. This would be essential to ensure accurate forecasting of storm conditions by the data assimilated physics model defined by the IMPACT framework.

To carry out such a study, we need to define a framework which can isolate the non-storm effects like local time (longitudinal) and seasonal modulations in the density that might result due to the asynoptic nature of satellite measurements.

In order to define such a framework, we separate all the geo-magnetically quiet times in a year and perform a Lomb-Scargle periodogram to look for dominant tidal activity. We then perform calculate the magnitude and phase of the dominant tides and now subtract them from the entire year to isolate the response to geomagnetic activity alone.

We performed a Lomb Scargle periodogram for 2003 density data that is shown in Figure 7 and the resulting periodogram for the quiet times only is shown in Figure 8. The residues from fitting the amplitudes and phases calculated form the dominant tidal activity resulting from non-geomagnetic activity is shown in Figure 9. The resulting response to geomagnetic activity alone is presented in Figure 10.

4. Conclusions

The study of storm response using CHAMP and GRACE has been carried out extensively in the recent past. Significant progress has been made in understanding the storm time behavior [E. K. Sutton. 2005, E.K. Sutton 2006, Liu et. al. 2010, Liu et. al, 2011, J. Lei 2011]. In spite of this, the physics based models which have forecasting capabilities built into them need tremendous amount of work in improving storm time behavior. Statistical studies become important in such cases which would decipher the missing physics and fine tune the physics based models to better replicate the storm time atmosphere.

In this paper, we performed a case study to see how the primary physics model, GITM, used in project IMPACT fared against other models and data during a storm. It was seen that both of the physics based and the empirical models underestimate the storm time response, although, they replicate the time scales of the response closely. In order to isolate the reason for the models not being able to replicate the actual magnitude response of the atmosphere to storm energy deposition, we would need to study multiple storms and find the source causing the under estimation of energy. Therefore a methodology for performing such a study was developed and presented here.

By carrying out such a study, we would be able to build on the vast heritage of already existing case studied of the storm time atmosphere and better train our physics models to now-cast and forecast both storm time and quiet time atmospheric behavior.

References

J. Koeller et al, IMPACT - Integrated Modeling of Perturbations in Atmospheres for Conjunction Tracking, LA-UR-13-26931, AMOS Conference, 2013-09-10/2013-09-13 (Wailea, Maui, Hawaii, United States), Report Web Issued: 2013-09-05

J. Koeller et al, IMPACT - Integrated Modeling of Perturbations in Atmospheres for Conjunction Tracking, LA-UR-13-22686. Space Weather Week, 2013-04-16/2013-04-19 (Boulder, Colorado, United States)

Reigber, C ., Luhr, H ., and Schwintz er, P., CHAMP Mission Status, Advances in Space Research, V ol. 30, N o. 2, pp. 129-134.

Tapley, B. D., S. Bettadpur, M. Watkins, and C. Reigber (2004), The gravity recovery and climate experiment: Mission overview and early results, Geophys. Res. Lett., 31, L09607, doi:10.1029/2004GL019920.

Picone, J. M., A. E. Hedin, D. P. Drob, and A. C. Aikin (2002), NRLMSISE-00 empirical model of the atmosphere: Statistical comparisons and scientific issues, J. Geophys. Res., 107(A12), 1468, doi:10.1029/2002JA009430.

E.K. Sutton, R.S. Nerem, J.M. Forbes, Density and Winds in the Thermosphere Deduced from Accelerometer Data, Journal of Spacecraft and Rockets. 44 (2007) 1210–1219.

A.J. Ridley, Y. Deng, G. Toth, The global ionosphere–thermosphere model, Journal of Atmospheric and Solar-Terrestrial Physics. 68 (2006) 839–864.

E. K. Sutton, J. M. Forbes, and R. S. Nerem. Global thermospheric neutral density and wind response to the severe 2003 geomagnetic storms from CHAMP accelerometer data. J. Geophys. Res., 110:9, 2005. doi: 10.1029/2004JA010985.

E. K. Sutton, J. M. Forbes, R. S. Nerem, and T. N. Woods. Neutral density response to the solar flares of October and November, 2003. Geophys. Res. Lett., 33:22101, November 2006. doi: 10.1029/2006GL027737.

Jiuhou Lei, Guangming Chen, Jiyao Xu and Xiankang Dou, Impact of Solar Forcing on Thermospheric Densities and Spacecraft Orbits from CHAMP and GRACE, Geodetic Sciences - Observations, Modeling and Applications, Chapter 7, http://dx.doi.org/10.5772/56599

R. Liu, H. L¨uhr, E. Doornbos, and S.-Y. Ma, Thermospheric mass density variations during geomagnetic storms and a prediction model based on the merging electric field, Ann. Geophys., 28, 1633–1645, 2010, doi:10.5194/angeo-28-1633-2010

R. Liu, S.-Y. Ma, and H. L¨uhr, Predicting storm-time thermospheric mass density variations at CHAMP and GRACE altitudes, Ann. Geophys., 29, 443–453, 2011,doi:10.5194/angeo-29-443-2011

Bruinsma, S., Forbes, J. M., Nerem, R. S., and Zhang,X.: Thermospheric density response to the 20-21 November 2003 solar and geomagnetic storm from CHAMP and GRACE accelerometer data. J. Geophys. Res., 111, A06303, doi:10.1029/2005JA011284, 2006.
Lei, J., Thayer, J. P., Wang, W., and McPherron, R. L.: Impact of CIR storms on thermosphere density variability during the solar minimum of 2008, Solar Phys., in press, doi:10.1007/s11207-010-9563-y, 2010b.

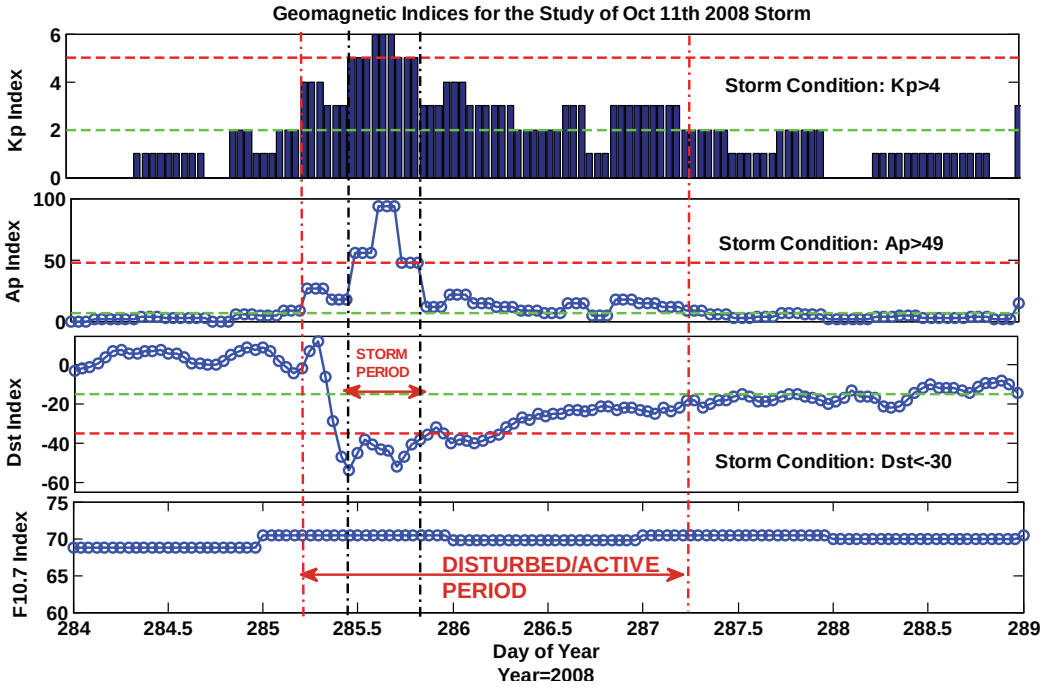

Figure 1. Geomagnetic and solar Indices representing the storm period under study.

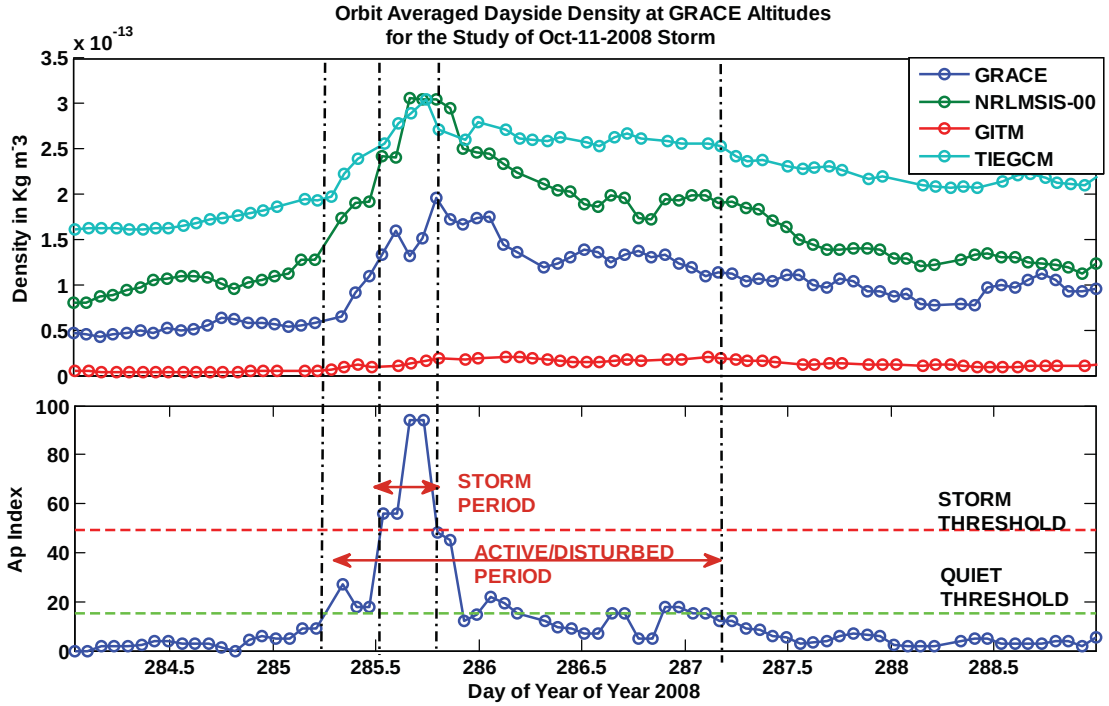

Figure 2. Orbit averaged GRACE satellite data and the model data along GRACE trajectory.

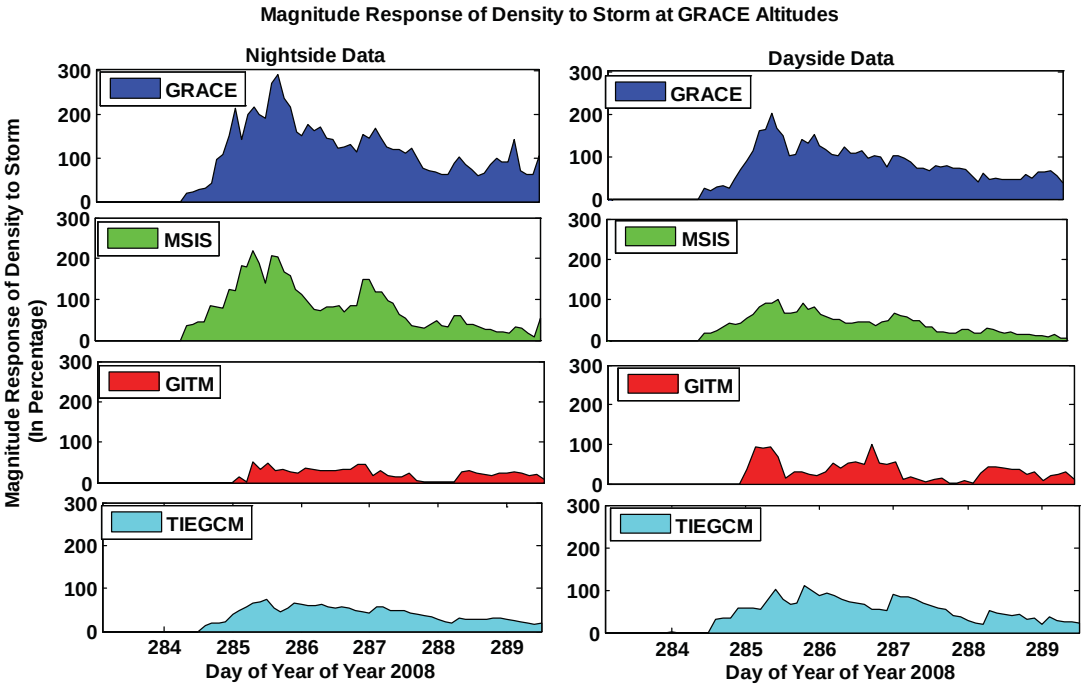

Figure 3. Time Response for the Oct. 11 2008 storm period

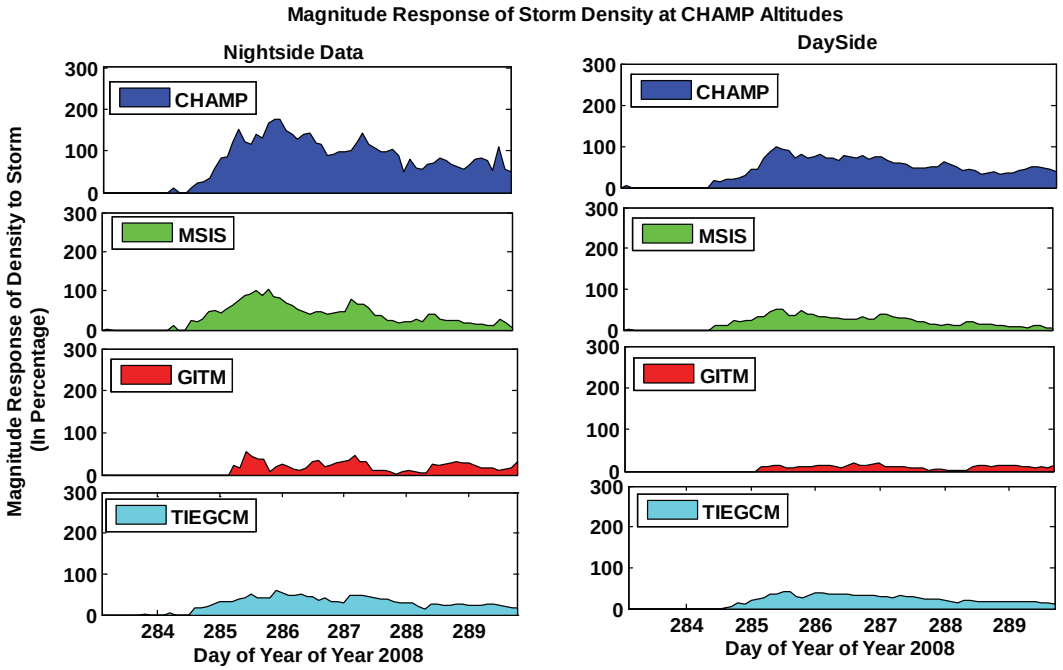

Figure 4. Magnitude Response for the Oct. 11 2008 storm period

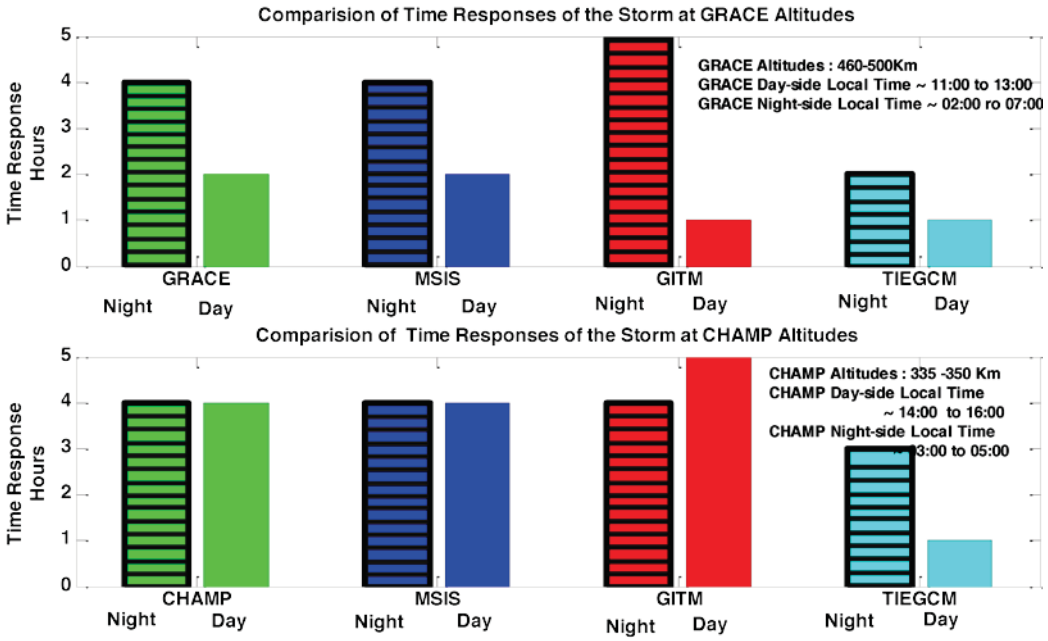

Figure 5. Comparison of the time response of the model and satellite data for the Oct. 11 2008 storm period

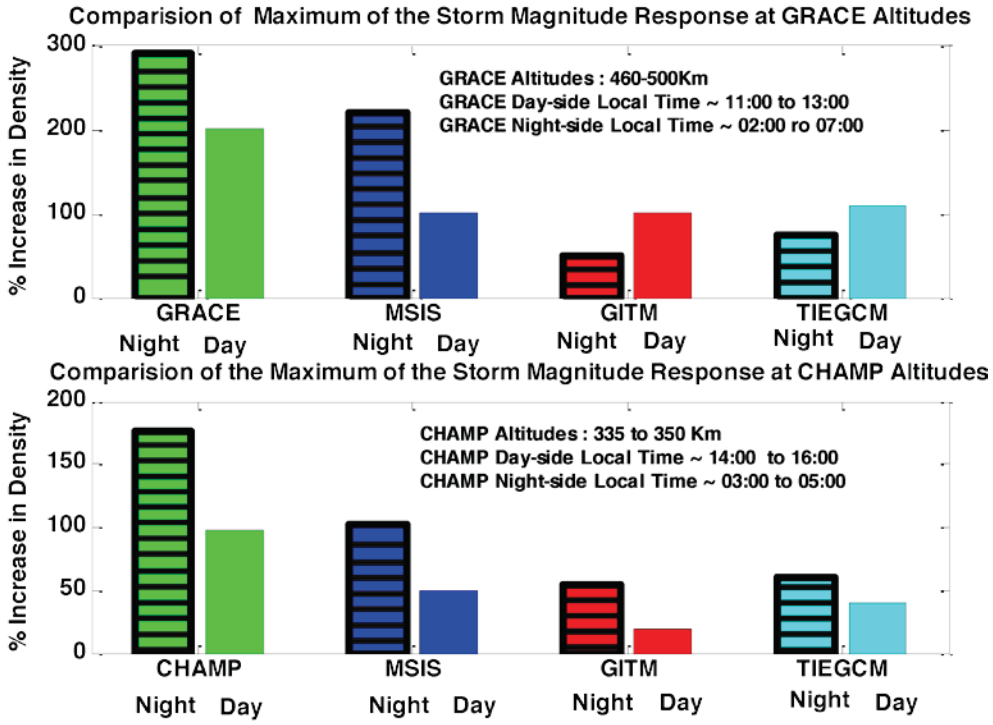

Figure 6. Comparison of the magnitude response of the model and satellite data for the Oct. 11 2008 storm period

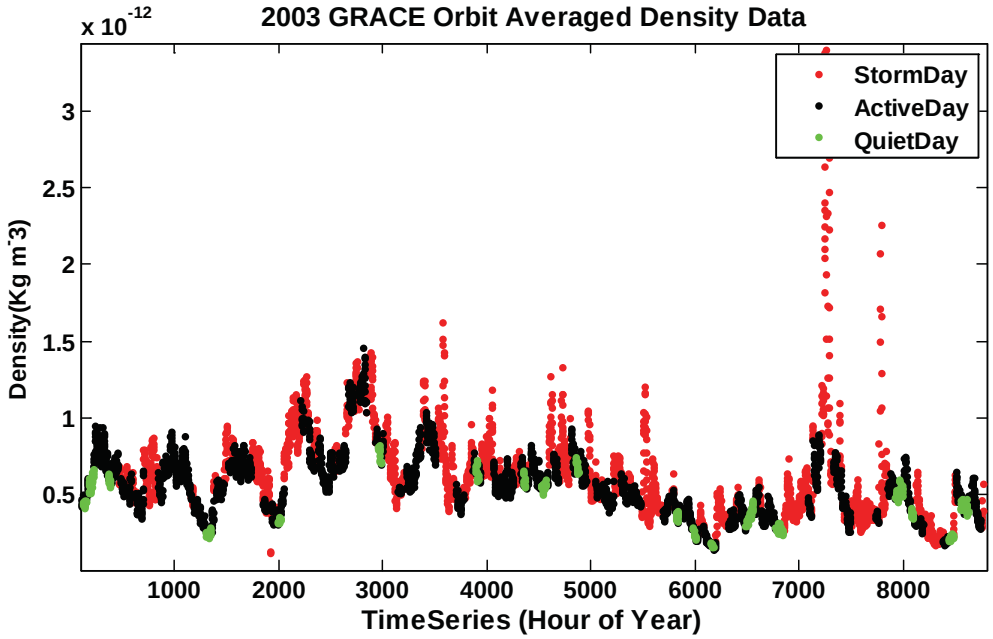

Figure 7. 2003 density data represented in terms of geomagnetic activity.

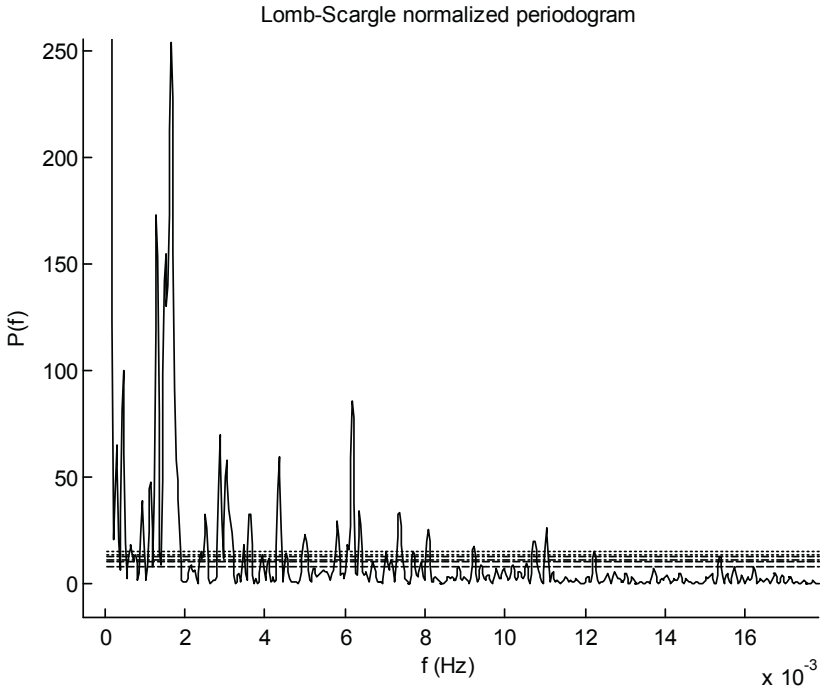

Figure 8. Lomb Scargle periodogram of the 2003 quiet time data

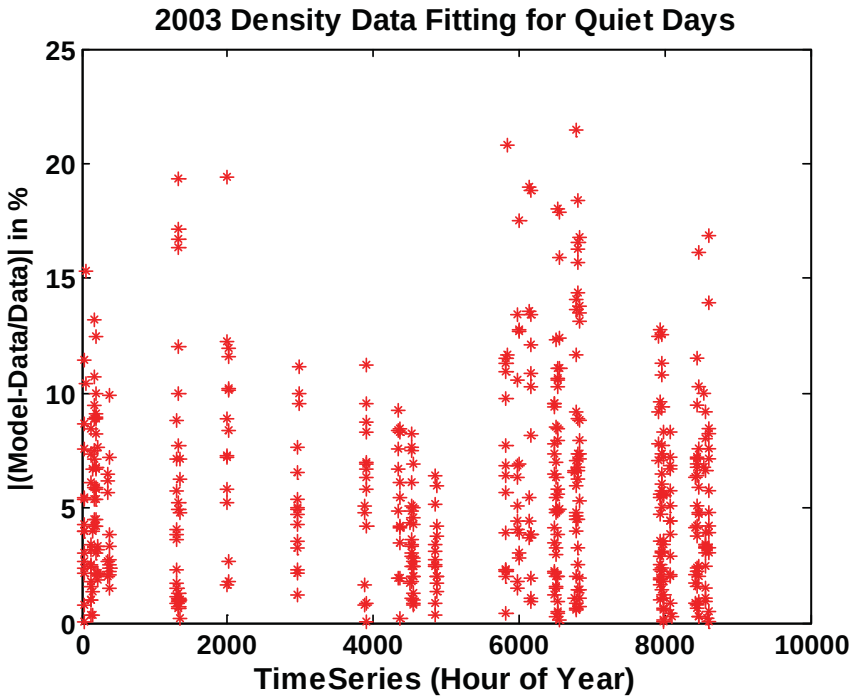

Figure 9. Residue from regression analysis using significant modes calculated from Lomb Scargle periodogram.

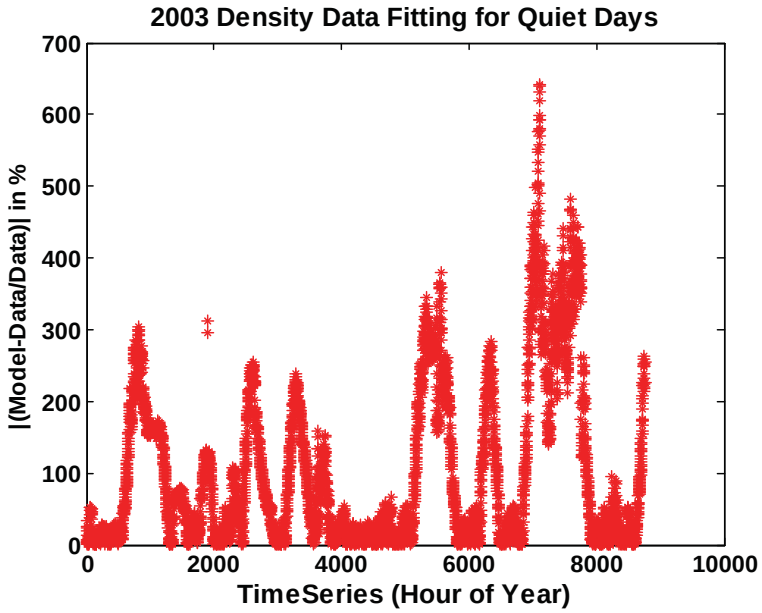

Figure 10. Geomagnetic activity density reponse for 2003/

An accurate scheme to evaluate the linear dispersion relation for magnetized plasmas with arbitrary parallel distribution functions.

Tim Waters

Department of Physics & Astronomy, University of Nevada Las Vegas, Las Vegas, NV

Xiangrong Fu

Los Alamos National Laboratory, Los Alamos, NM

Abstract

The collisionless plasmas that comprise the solar wind and occupy the earth's magnetosphere have long been observed to have nonthermal components. Locally, it is a good approximation to model these plasmas under the assumptions that they are homogenous and embedded in a uniform magnetic field. There is a well known procedure to obtain the linear dispersion relation (LDR) for such plasmas, which allows for nonthermal velocity distributions. Unfortunately, due to the difficulty of solving this general LDR, most studies to date have instead assumed that the velocity distributions are Maxwellian or Maxwellian-like. Recently, a new method was developed to accurately evaluate a 'generalized plasma dispersion function' and it was shown to be effective at solving the Langmuir LDR for arbitrary distribution functions. Here we apply this method to build a scheme for evaluating the LDR for a warm magnetized plasma, allowing for arbitrary distribution functions parallel to the magnetic field. This scheme does not use the Padé approximation and is shown to be very accurate. We speculate that this scheme can be successfully combined with a novel root finding method that eliminates the need for a starting guess, and can hopefully lead to a powerful new dispersion solver.

Keywords: plasmas, dispersion relations

1. Introduction

The observed abundance and important dynamical role of plasma waves were central topics of this summer school. Perturbations in a finite temperature plasma can give rise to enhanced or damped fluctuations which can dynamically influence the plasma and its environment. Plasma instabilities can arise if one or more components of the plasma possesses free energy in the form of a nonthermal velocity distribution function (VDF). As an example, electrons in the solar wind are subject to an electron/electron beam instability, as they are observed to be comprised of separate populations, with $\sim$ 10% consisting of an isotropic 'halo' component and an even higher energy anisotropic tail component known as the 'strahl' that are well modeled by so-called 'Kappa' distributions (e.g., Marsch 2006).

A basic starting point in investigating the dependence of the properties of the plasma (i.e., its density, temperature, and magnetic field strength and orientation) on the individual VDFs is the linear dispersion relation (LDR) that governs the types of waves or oscillations the collisionless plasma can support. Despite the fact that the procedure to obtain the LDR for warm magnetized plasmas is well laid out (e.g., Stix 1992), most studies of plasma waves treat each VDF as a linear combination of individual Maxwellian distributions. To better understand what modes can be excited in actual space environments, it is important to develop a dispersion solver capable of handling general VDFs.

The principal difficulty in treating a general VDF is the evaluation of the generalized plasma dispersion function

$$Z(\zeta) = \int_{\mathcal{L}} \frac{F(\mathrm{v})}{\mathrm{v} - \zeta}\, d\mathrm{v}, \tag{1}$$

Email addresses: waterst3@unlv.nevada.edu (Tim Waters), xrfu@lanl.gov (Xiangrong Fu)

where $F(\mathrm{v})$ is an arbitrary input function that normally depends on both the VDF and its derivative, while $\mathcal{L}$ is the Landau contour that must pass below the pole at $\mathrm{v} = \zeta$, which physically represents the (Doppler-shifted) phase velocity of the wave. The presence of a pole leads to the famous effect of Landau damping for electrostatic plasma LDRs. The discovery of Landau damping first required viewing $F(\mathrm{v})$ as a function of a complex variable v in order to employ the tools of residue calculus to properly handle the contour integration around the pole (Landau 1946). If $F(\mathrm{v})$ is further supposed to be an entire function (i.e. free of singularities for all finite values of v, which is almost always the case), then $Z(\zeta)$ will also be an entire function of ζ once its analytic continuation into the full complex plane is made explicit:

$$Z(\zeta) = \begin{cases} \displaystyle\int_{-\infty}^{\infty} \frac{F(\mathrm{v})}{\mathrm{v}-\zeta} d\mathrm{v}, & \mathrm{Im}(\zeta) > 0, \quad (2a) \\ \displaystyle PV \int_{-\infty}^{\infty} \frac{F(\mathrm{v})}{\mathrm{v}-\zeta} d\mathrm{v} + \pi i f(\zeta), & \mathrm{Im}(\zeta) = 0, \quad (2b) \\ \displaystyle\int_{-\infty}^{\infty} \frac{F(\mathrm{v})}{\mathrm{v}-\zeta} d\mathrm{v} + 2\pi i f(\zeta), & \mathrm{Im}(\zeta) < 0. \quad (2c) \end{cases}$$

Here, PV denotes the principal value of the integral, so the middle integral is by definition the Hilbert transform of $\pi F(\mathrm{v})$, and the domain of integration of each of these integrals is along the real axis. For the special case of a one-dimensional Maxwellian distribution, $F(\mathrm{v}) = \exp(-\mathrm{v}^2)/\sqrt{\pi}$, the well-known plasma dispersion function $Z_p(\zeta)$ is obtained. Its properties are well documented (Fried & Conte 1961), and efficient open-source algorithms exist to evaluate it for any value of ζ (e.g., S. Johnson's Fadeeva Package[1]). However, the singularity in these integrals have thwarted most attempts to reliably and efficiently evaluate $Z(\zeta)$ for arbitrary input functions $F(\mathrm{v})$.

A recent breakthrough was made by Xie (2013), who exploited methods developed by Weideman (1994, 1995) to avoid the singularity altogether. The basic idea is to expand the function $F(\mathrm{v})$ using an orthogonal basis set that is a manipulated form of a Fourier series, which allows the expansion coefficients to be easily and efficiently evaluated using a fast fourier transform (FFT). Each term in the series can be integrated analytically by again invoking residue calculus, i.e. by evaluating each integral in equation (2) over a closed contour in the complex plane consisting of the real axis plus a semi-circular arc extending to infinity. The power of this technique lies in the fact that the integral over the semi-circular arc can be shown to vanish, independently of the VDF, on account of the basis functions, allowing the integrals in equation (2) to be replaced by infinite analytic sums. In the case of the complex error function (which is simply related to $Z_p(\zeta)$), Weideman (1994) demonstrated that this scheme has excellent convergence properties when truncating the sums. For instance, he obtained 12 digits of accuracy with just 32 terms. Weideman (1995) extended this approach to compute the Hilbert transform of arbitrary functions. Xie (2013) adopted the algorithm from Weideman (1995) to compute the Hilbert transform in equation (2), and he further generalized the approach taken by Weideman (1994) to compute $Z(\zeta)$ for the cases $\mathrm{Im}(\zeta) > 0$ and $\mathrm{Im}(\zeta) < 0$.

Xie (2013) applied this scheme to solve the LDR for Langmuir waves, which describe the electrostatic longitudinal oscillations of a finite temperature, homogenous, non-relativistic plasma. The present work is aimed at applying this scheme to such a plasma that is also threaded by a uniform magnetic field, in which case both electrostatic and electromagnetic waves arise from the LDR. Adding a uniform magnetic field immensely complicates the LDR, due to both the anisotropy it causes (so that susceptibility tensors must be calculated) and because the principle and higher harmonic resonances of particles gyrating about the magnetic field results in an infinite sum of Bessel functions. Nevertheless, it will be shown that extending Xie's scheme to warm plasmas is quite straight forward and does not require use of the Padé approximation, which is known to sometimes give rise to spurious instabilities (Rönnmark 1982; see also Tjulin et al. 2000).

This report is organized as follows. In the §2, we write down the LDR for warm plasmas. In §3, we describe how to extend Xie's scheme to evaluate this LDR. In §4, we summarize our results, concentrating on a simple measure to assess the accuracy and efficiency of this scheme. Finally, in §5, we present our conclusions and plans for future work.

[1] `http://ab-initio.mit.edu/wiki/index.php/Faddeeva_Package`

2. Warm plasma linear dispersion relation

Here we provide the LDR from §10-7 of Stix (1992) in a dimensionless form suitable for numerical implementation. We adhere to Stix's notation as much as possible, so our dimensionless variables, defined in Table 1, typically have the same symbols as the dimensional quantities from Stix (1992). This LDR, which we denote as $D(\omega)$, assumes that the VDF perpendicular to the magnetic field is a non-relativistic Maxwellian, but it allows for an arbitrary (albeit still non-relativistic) parallel VDF. It was derived assuming field quantities that oscillate as $\exp(i\mathbf{k}\cdot\mathbf{r} - i\omega t)$.

Quantity	Symbol	Definition
wave frequency	ω	$\omega/(k\mathrm{v}_1)$
plasma frequency	ω_p	$\omega_p/(k\mathrm{v}_1)$
cyclotron frequency	Ω	$\Omega/(k\mathrm{v}_1)$
thermal velocity ($\perp$ to $\mathbf{B}$)	$\mathrm{v}_\perp$	$w_\perp/\mathrm{v}_1$
parallel velocity	z	$\mathrm{v}_\parallel/\mathrm{v}_1$
parallel VDF	$f(z)$	$\mathrm{v}_1\, h(\mathrm{v}_\parallel)$
input function of A_n's	$F(z)$	$\mathrm{v}_1\, H(\mathrm{v}_\parallel)$
dimensionless A_n	A_n	$k\mathrm{v}_1 A_n$
dimensionless B_n	B_n	kB_n
dimensionless $\mathbf{Y}_n$	$\mathbf{Y}_n$	$k\mathrm{v}_1\mathbf{Y}_n$

Table 1: **Definition of dimensionless quantities**
The quantities in the middle column are the dimensionless ones used here. They are defined in terms of the *dimensional* quantities in the right column (often involving the same symbol) from Stix (1992). Here, $\mathbf{B} = B_0\hat{\mathbf{z}}$ refers to the uniform background magnetic field, v_1 is an unspecified characteristic unit for velocity, and k is the magnitude of the wave vector $\mathbf{k}$.

Explicitly, $D(\omega)$ is given by the following determinant involving components of the dielectric tensor ϵ, the angle θ that the wave vector makes with respect to the uniform background magnetic field (which is aligned with the z-axis), and the magnitude of the index of refraction $n_r = (c/\mathrm{v}_1)/\omega$, where c is the speed of light:

$$D(\omega) \equiv \begin{vmatrix} \epsilon_{xx} - n_r^2\cos^2\theta & \epsilon_{xy} & \epsilon_{xz} + n_r^2\sin\theta\cos\theta \\ \epsilon_{yx} & \epsilon_{yy} - n_r^2 & \epsilon_{yz} \\ \epsilon_{zx} + n_r^2\sin\theta\cos\theta & \epsilon_{zy} & \epsilon_{zz} - n_r^2\sin^2\theta \end{vmatrix} = 0. \tag{3}$$

This form for $D(\omega)$ assumes that the coordinate system is chosen so that $\mathbf{k}$ lies in the $x-z$ plane, which can be done without loss of generality. The dielectric tensor is composed of the individual susceptibilities of the constituent plasma species, denoted by χ_s:

$$\epsilon = \mathbf{1} + \sum_s \chi_s. \tag{4}$$

Each susceptibility tensor is given by

$$\chi_s = \left(\frac{\omega_p^2}{\omega}\right)\left[\frac{\langle z\rangle}{\mathrm{v}_\perp^2\cos\theta}\hat{\mathbf{e}}_\parallel\hat{\mathbf{e}}_\parallel + e^{-\lambda}\sum_{n=-\infty}^{\infty}\mathbf{Y}_n(\lambda)\right], \tag{5}$$

with

$$\mathbf{Y}_n(\lambda) = \begin{bmatrix} n^2 I_n A_n/\lambda & -in(I_n - I_n')A_n & nI_n B_n\sin\theta/(\lambda\,\Omega) \\ in(I_n - I_n')A_n & [n^2 I_n/\lambda + 2\lambda(I_n - I_n')]A_n & i(I_n - I_n')B_n\sin\theta/\Omega \\ nI_n B_n\sin\theta/(\lambda\,\Omega) & -i(I_n - I_n')B_n\sin\theta/\Omega & I_n(\omega - n\Omega)B_n/\mathrm{v}_\perp^2 \end{bmatrix}. \tag{6}$$

Here $I_n = I_n(\lambda) \equiv i^{-n}J_n(i\lambda)$ are modified Bessel functions with argument $\lambda = (\mathrm{v}_\perp\sin\theta/\Omega)^2$, and $I_n' = dI_n/d\lambda$. The quantity B_n can be written in terms of $A_n = A_n(\zeta_n)$, which is an integral of the same type as $Z(\zeta)$:

$$A_n = -\frac{1}{\cos\theta}\int_{\mathcal{L}}\frac{F(z)\,dz}{z-\zeta_n}; \tag{7}$$

$$B_n = \frac{1}{\cos\theta} - \frac{\langle z\rangle}{\omega} + \zeta_n A_n. \tag{8}$$

In these relations, $\zeta_n = (\omega - n\Omega)/\cos\theta$; it is both frequency and species-dependent. The input function $F(z)$ is related to the VDF $f(z)$ and its derivative $f'(z) = df(z)/dz$:

$$F(z) = -\left(1 - \frac{z\cos\theta}{\omega}\right) f(z) + \frac{\mathrm{v}_\perp^2 \cos\theta}{\omega} f'(z). \tag{9}$$

In equation (8), the quantity $\langle z\rangle$ is the average velocity, $\langle z\rangle = \int_{-\infty}^{\infty} z\, f(z)\, dz$. Using this definition, it is straight forward to show that ϵ_{zz} reduces to the Langmuir LDR for $\theta = 0$ and $n = 0$. The simplest benchmark of the warm plasma LDR is therefore the recovery of the solutions to the Langmuir LDR, which in our units is

$$1 - \omega_p^2 \int_{\mathcal{L}} \frac{f'(z)\, dz}{z - \omega} = 0. \tag{10}$$

The warm plasma LDR depends on $1+(3+N_\parallel)S$ parameters, where $N_\parallel$ denotes the number of parameters associated with the parallel VDF $f(z)$ and S is the total number of plasma species. The species-independent parameter is θ, while two of the species-dependent parameters are ω_p and Ω. Since each species can have a different perpendicular Maxwellian VDF and a different arbitrary parallel VDF $f(z)$, the remaining $(1+N_\parallel)S$ parameters are the perpendicular Maxwellian thermal velocity $\mathrm{v}_\perp$ and the parameters specifying the parallel VDF. The most common non-Maxwellian distributions, e.g. the Kappa distributions, have $N_\parallel = 2$.

3. Scheme to evaluate the dispersion relation

As described in the introduction, the scheme presented in Xie (2013) is an algorithm to evaluate the integral in equation (10). The main difference that arises when extending this scheme to evaluate equation (7) is that the input function $F(z)$ given by equation (9) is frequency dependent, whereas $f(z)$ is frequency independent. While this presents no complications in terms of the applicability of this scheme, it imposes a substantial increase in computational expense when actually solving $D(\omega)$ for ω. The reason, of course, is because the scheme for evaluating $D(\omega)$ has to be paired with a root finding algorithm that necessarily samples many different values of ω in the process of converging to the actual root. Since $F(z)$ will change with each of these samplings, S new FFTs will have to be computed with every evaluation of $D(\omega)$, in contrast to the root finding process to solve equation (10), in which the same S FFTs can be reused for different ω.

Applied to the warm plasma LDR, Xie's generalization of the schemes developed by Weideman (1994, 1995) can by summarized as the following 2-step procedure:

1. For each species, use an FFT to evaluate the expansion coefficients a_m, based on the formal expansion

$$F(z) = \lim_{N\to\infty} \sum_{m=-N}^{N} W(z) a_m(z) \rho_m(z), \tag{11}$$

where $W(z)$ is a weight function and $\rho_m(z)$ are the basis functions. When the pole at ζ_n lies on the real line, $\rho_m(z) = (L + iz)^m/(L - iz)^{m+1}$ and $W(z) = 1$, while $\rho_m(z) = [(L + iz)/(L - iz)]^m$ and $W(z) = 1/(L^2 + z^2)$ when the pole is off the real line. Here the parameter L controls the convergence rate when truncating the sum from $m = -N$ to $m = N$. As discussed by Weideman (1995), L likely has an optimal value that in general depends on N, but the truncated sum will still converge for other fixed values of L. Weideman (1995) was able to determine an optimal value of $L = 2^{-1/4}N^{1/2}$ for the case $F(z) = e^{-z^2}$, which will likely suffice for arbitrary input functions. Note that the basis functions can be casted in Fourier form by letting $z = L\tan(\phi/2)$ so that $(L+iz)/(L-iz) = e^{i\phi}$; this is what makes it possible to use an FFT to determine the a_m's.

2. Evaluate each A_n using the truncated version of the following exact expansion

$$-A_n(\zeta) = \lim_{N\to\infty} \begin{cases} \dfrac{2\pi i}{L^2+\zeta^2} \displaystyle\sum_{m=1}^{N} a_m \left(\frac{L+i\zeta}{L-i\zeta}\right)^m + \frac{\pi i a_0}{L(L-i\zeta)}, & \mathrm{Im}(\zeta) > 0; \quad (12a) \\ \dfrac{2\pi i}{L-i\zeta} \displaystyle\sum_{m=0}^{N} a_m \left(\frac{L+i\zeta}{L-i\zeta}\right)^m, & \mathrm{Im}(\zeta) = 0; \quad (12b) \\ \dfrac{2\pi i}{L^2+\zeta^2} \displaystyle\sum_{m=1}^{N} a_m \left(\frac{L-i\zeta}{L+i\zeta}\right)^m + \frac{\pi i a_0}{L(L+i\zeta)} + 2\pi i F(\zeta), & \mathrm{Im}(\zeta) < 0. \quad (12c) \end{cases}$$

Here we have omitted the subscript 'n' on $\zeta_n = (\omega - n\Omega)/\cos\theta$ for simplicity of notation.

All that remains is to evaluate the infinite sums in equation (5) involving products of the modified Bessel functions with A_n and B_n. The sums naturally separate into two distinct types: those involving $I_n(\lambda)$ and those involving $I_n'(\lambda)$. The former sums can be expressed as

$$\sum_{n=-\infty}^{\infty} a_n I_n = a_0 I_0 + \lim_{N_B\to\infty} \sum_{n=1}^{N_B} (a_n + a_{-n}) I_n, \quad (13)$$

where the second form, which follows from the fact that $I_n = I_{-n}$, is computationally advantageous. Our scheme is based on truncating this sum at a finite N_B. Using the properties $I_n' = (I_{n-1} + I_{n+1})/2$ for integer $n \neq 0$ and $I_0' = I_1$, the second type of sum can be expressed as

$$\sum_{n=-\infty}^{\infty} a_n I_n' = \frac{1}{2} \lim_{N_B\to\infty} \left[(a_{-1} + a_1) I_0 + (a_{-(N_B-1)} + a_{N_B-1}) I_{N_B} + (a_{-N_B} + a_{N_B}) I_{N_B+1} + \sum_{n=1}^{N_B-1} (a_{-(n+1)} + a_{-(n-1)} + a_{n-1} + a_{n+1}) I_n \right]. \quad (14)$$

When truncating this sum at $N_B = 0$, it is to be understood that only the I_{N_B+1} term is nonzero, so that this expression correctly gives $a_0 I_1$. Also, when $N_B = 1$ the final summation term is zero, correctly giving $a_0 I_1 + a_1(I_0 + I_2)$. Finally, note from equation (6) that a_n takes on the values A_n, nA_n, $n^2 A_n$, B_n, and nB_n for sums involving I_n, and A_n, nA_n, B_n, and nB_n for sums involving I_n'.

This completes the presentation of our scheme to evaluate $D(\omega)$. Both the efficiency and accuracy of this scheme depends on how fast the truncated versions of the above sums converge to the limiting sums, which we now address.

4. Results

We have implemented this scheme to evaluate $D(\omega)$ in python using a wrapper to FFTW[2], and we plan to make the code public once it is fully benchmarked. Thus far, we have reproduced the results of Xie (2013) by verifying that our own implementation to evaluate equation (10) produces identical output to the MATLAB program included with Xie's paper. We also paired Xie's evaluation scheme with a root finder to solve equation (10) and reproduce Figure 3.7 out of Gary (1993), which is an example of an electron/electron beam instability. Here we will use the "bump-on-tail" distribution function that gives rise to this instability to assess the speed of the full scheme, and its dependence on N in equation (12) and N_B in equations (13-14).

The bump-on-tail distribution can be implemented as one VDF or as separate drifting Maxwellian distributions for both the 'core' and the 'beam' electrons, as shown in Figure 1. When applying the trapezoid rule to calculate the FFT, it can be shown that the truncation of equation (12) at N leads to a sampling of the input function $F(z)$ with $M = 4N$ values. This sampling is not linear in $z = L\tan(\phi/2)$, but rather it is linear in ϕ. Hence, $F(z)$ will be sampled less densely at large velocities, which is generally advantageous. Figure 1 shows the excellent agreement between the sampled points and the reconstructed input function based on the sum in equation (11) truncated at $N = 64$. The

[2] http://www.fftw.org/

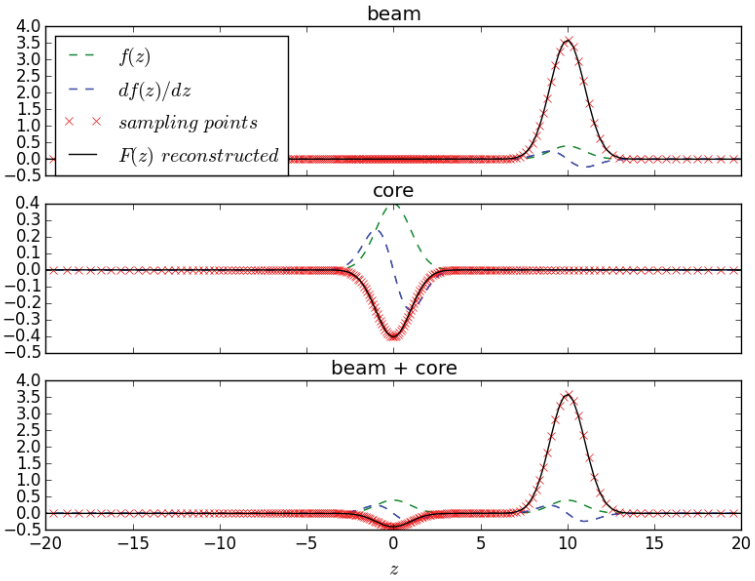

Figure 1: **Reconstructing $F(z)$ based on individual or combined distributions.** The top and middle panels show how $F(z)$ is sampled and reconstructed based on the individual beam and core components of a bump-on-tail distribution. Our scheme can equally well use the combined distribution as shown in the bottom panel. Here z is velocity measured in units of $\mathrm{v}_1 = \mathrm{v}_{\perp,core} = \mathrm{v}_{\perp,beam}$, which makes the VDF $f(z) = \exp(-(z - z_0)^2/2)/(2\pi)^{1/2}$. We use $z_{0,beam} = 10$, which gives $z_{0,core} \approx -0.01$ when the ratio of core to beam is 10^3. $F(z)$ is defined by equation (9) with $\omega = 1$ and $\theta = 0$; the black curve is $F(z)$ reconstructed from the expansion in equation (11).

parameters needed to fully specify a Langmuir LDR model are given in the caption in Figure 1 and will be used in what follows.

While $N = 64$ is sufficient to accurately resolve $F(z)$, it is important to show that Xie's scheme to evaluate $A_n(\zeta)$ converges to a unique value as N increases. A simple quantitative measure of this convergence is a weighted percent difference:

$$\text{weighted \%-difference} = \frac{|X\Delta X| + |Y\Delta Y|}{|X| + |Y|}, \tag{15}$$

where ΔX and ΔY are ordinary percent differences, e.g. $\Delta X = 100\%(X|_{N_1} - X|_{N_2})/(X|_{N_1} + X|_{N_2})/2$. In the bottom left panel of Figure 2 we plot the weighted %-difference of the Langmuir LDR (which recall is ϵ_{zz} for $\theta = 0$ and $n = 0$) in order to show the convergence behavior of $A_0(\zeta)$ for each of the three sums given in equation (12). For example, the leftmost value shows that $A_0(\zeta)$ evaluated at $N_1 = 16$ differs from $A_0(\zeta)$ evaluated at $N_2 = 32$ by only 0.01%. We chose values of $\zeta = 1.0$ and $1.0 \pm 0.1i$ to demonstrate that the three sums have identical convergence properties as $\mathrm{Im}(\zeta) \to 0$. Because $|A_0(\zeta)| < 10^2$ for these values, the weighted percent differences correspond to machine precision for $N \geq 256$, thereby confirming the accuracy of Xie's scheme. Moreover, $N = 256$ should be the default value for this scheme since $A_0(\zeta)$ becomes fully converged, and since the cost to evaluate $N = 256$ is not substantially greater than $N = 64$, as the top left panel shows. Similar results to these are obtained for $A_n(\zeta)$ with $n \neq 0$.

The bottom right panel shows the same convergence measure applied to $D(\omega)$, this time varying the number of terms used in the sum of modified Bessel functions. To fully specify a model for the warm plasma LDR, values for θ and Ω are needed in addition to those given in the caption of Figure 1. The colors in Figure 2 represent different choices for θ, i.e. orientations between $\mathbf{B}$ and $\mathbf{k}$: nearly parallel ($\theta = 5°$, red line), nearly perpendicular ($\theta = 85°$, blue line), and oblique ($\theta = 45°$, black line). Meanwhile, the line styles distinguish different choices for Ω: dashed-dotted, solid, and dashed lines are for Ω equal to 0.2, 1.0, and 10.0, respectively. It is clear that $D(\omega)$ converges, implying that our scheme can reach any desired accuracy. However, the convergence is very sensitive to the value $\lambda = (\mathrm{v}_\perp/\Omega)\sin\theta$, so N_B will need to be chosen to meet the accuracy requirements.

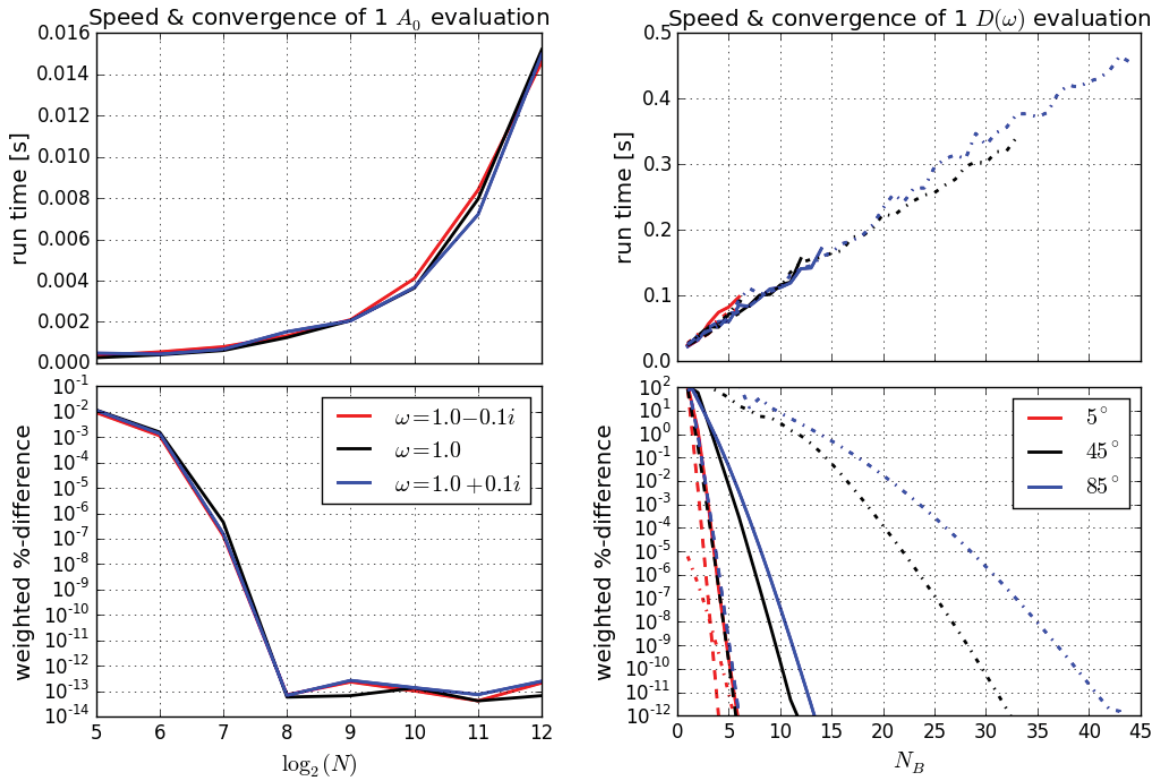

Figure 2: **Top panels**: CPU time in seconds to evaluate the Langmuir LDR (left panel) and the warm plasma LDR (right panel) on a Macbook Air 1.8 GHz Intel i7 processor. **Bottom panels**: The weighted %-differences defined by equation (15). The left panel measures the convergence of the three sums in equation (12), while the right panel measures the convergence of the sums involving modified Bessel functions in equations (13-14). Here the dashed-dotted, solid, and dashed lines are for Ω equal to 0.2, 1.0, and 10.0, corresponding to $\lambda = 5\sin\theta$, $\sin\theta$ and $0.1\sin\theta$, respectively.

That this λ-dependence is a generic feature of sums involving modified Bessel functions can be demonstrated quite simply using the identity $\sum_{n=-\infty}^{\infty} I_n(\lambda) = e^{\lambda}$. Figure 3 shows an ordinary percent difference of the quantity $\sum_{n=-N_B}^{N_B} I_n(\lambda)$, i.e. an approximation whose limiting sum is e^{λ}. It demonstrates that the qualitative behavior of $D(w)$ shown in Figure 2 is independent of the choice of input function $F(z)$ and input parameters. It also implies that our scheme will be become very costly for large λ.

All of the computational expense is in the evaluation of the $\mathbf{Y}_n(\lambda)$'s. Since our scheme amounts to computing a finite number of $\mathbf{Y}_n(\lambda)$'s, we expect the execution time to increase linearly with the number of $\mathbf{Y}_n(\lambda)$'s computed, i.e. to be linear in the quantity N_B. The top right panel in Figure 2 shows the run time for one evaluation of $D(\omega)$ as a function of N_B. The curves show a linear trend as expected; we terminate each one once a weighted percent difference of $10^{-12}\%$ has been reached. These evaluations were carried out for $N = 256$, and one evaluation of the Langmuir LDR takes $\sim$ 0.5ms according to the top left panel. Evaluation of the warm plasma LDR can exceed this amount by more than two orders of magnitude, depending on the desired accuracy and the magnitude of λ.

5. Conclusions and Future Work

We have presented a scheme to evaluate the warm plasma LDR that is based on finite truncations of two exact series expansions, one for A_n and one for sums involving modified Bessel functions. The results presented here validated the truncation of these sums. While this scheme can in principle achieve arbitrary accuracies, the efficiency

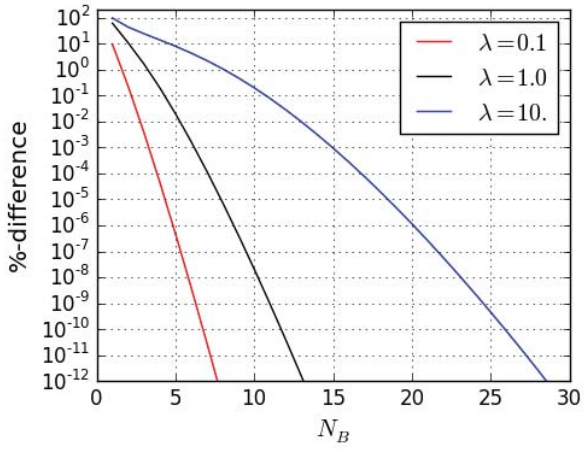

Figure 3: Percent differences associated with the approximation $e^{\lambda} = \sum_{n=-N_B}^{N_B} I_n(\lambda)$, which is an identity in the limit $N_B \to \infty$. This plot shows that the behavior of the weighted %-differences of $D(\omega)$ in the bottom right panel of Figure 2 is a generic feature of sums involving modified Bessel functions.

of this scheme can differ by orders of magnitude depending on the value of the argument to the modified Bessel functions, λ. Physically, a large λ can be realized as a high frequency wave, and such small scale waves will be highly damped in general and therefore not very interesting. Less commonly, however, for wave frequencies less than the cyclotron frequency, λ represents the spread in wave phases that is seen by the gyrating particles. The cold plasma approximation demands that this spread is small, and hence a necessary condition for this approximation is $\lambda < 1$. In other words, very warm plasmas will have $\lambda > 1$, and we showed this to be the most computationally expensive regime.

The overall efficiency of this scheme to evaluate $D(\omega)$ can only be determined when it is coupled to a root finder to actually solve $D(\omega)$ for all of its roots. We can provide an estimate based on our experience solving the simpler Langmuir LDR, equation (10), which requires $\sim 3 \times 10^3$ evaluations to produce a curve of ω vs. $k_{\|}$ showing the electron-beam instability. If this instability is studied with the warm plasma LDR with $\lambda \approx 5$, Figure 2 shows that it takes $\sim$ 500ms to evaluate $D(\omega)$ once. Hence, 3×10^3 evaluations requires 25 minutes of $D(\omega)$ evaluations when $N_B \sim 50$ terms are required. In the small λ regime (i.e. for longitudinal oscillations or for small scale waves), the runtime will likely be under 1 minute.

Future work is required to fully benchmark this scheme against existing codes such as WHAMP (Rönnmark 1982). Ideally, the considerations involving λ can be implemented automatically, so that the user can specify a desired accuracy and N_B will be appropriately calculated.

The main focus of our future work is to automate the root finding process, which is notoriously tricky for two-dimensional problems such as ours (where both $\mathrm{Re}[D(\omega)] = 0$ and $\mathrm{Im}[D(\omega)] = 0$ must be solved). We note here that an alternative scheme to solve $D(\omega)$, one that uses an eigenvalue approach instead of a root finding algorithm, was recently put forth by Xie (2014). However, this approach uses the Padé approximation, which we want to avoid. A promising traditional root finding approach appears to be the public code cZero, based on the recent work of Johnson & Tucker (2009). The idea here is to exploit the fact that $D(\omega)$ is an analytic complex function, so that the winding theorem in complex function theory allows for the determination of the number of zeros inside any closed contour in the complex plane. By tiling the desired domain in the complex plane with triangles, cZero computes the winding number around each triangle to systematically close in on all of the isolated roots. It is completely analogous to one-dimensional bracketing and bisection (Press et al. 1992), which is guaranteed to find all roots for one-dimensional problems. This code, coupled with our scheme to evaluate $D(\omega)$, has the potential to automate the entire solution process, so that the properties (i.e. wave modes and corresponding growth rates) of warm plasmas with arbitrary VDFs can be easily and reliably calculated.

References

Fried, B. D. and Conte, S. D., *The Plasma Dispersion Function*, Academic Press, New York and London (1961)
Gary, S.P. *Theory of Space Plasma Microinstabilities*, Cambridge U. Press, New York (1993)
Johnson, T., Tucker, W., Math. Comput. 228, 418 (2009)
Landau, L., J. Phys., 10, No 1, 25 (1946).
Marsch, E., Living Rev. Solar Phys, 3, 1. (2006) `http://www.livingreviews.org/lrsp-2006-1`
Press, W. H., Flannery, B. P., Teukolsky, S. A., *Numerical Recipes in C*, Cambridge U. Press, New York (1992)
Robinson, P. A., J. Comp. Phys., 88, 381 (1990).
Rönnmark, K., J. *WHAMP- Waves in Homogenous, Anisotropic, Multicomponent Plasmas*, KGI Report 179, Kiruna Geophysical Institute (1982)
Stix, T. H., *Waves in Plasmas*, American Institute of Physics New York (1992)
Tjulin, A., Eriksson, A. I., and André M., J. Plasma Physics 64, part 3, 287 (2000)
Weideman, J. A. C., SIAM J. Numer. Anal. 31, 1497 (1994)
Weideman, J. A. C., Math. Comput. 64, 745 (1995)
Xie, H., Physics of Plasmas 20, 092125 (2013)
Xie, H.-s., & Xiao, Y. (2014), arXiv:1410.2678

A 3-Parameter 4-Plasma Categorization Scheme for the Solar Wind: Plasma Occurrence Rates at Earth over Four Solar Cycles

Fei Xu

Physics Department, Nanjing University of Information Science & Technology, Nanjing China

CSPAR, University of Alabama, Huntsville, Alabama USA

Joseph E. Borovsky

AOSS, University of Michigan, Ann Arbor, Michigan USA

Physics Department, Lancaster University, Lancaster, Lancashire UK

Center for Space Plasma Physics, Space Science Institute, Boulder, Colorado USA

Abstract

A new 3-parameter scheme is developed to categorize the solar wind plasma at 1 AU into 4 types: coronal-hole-origin plasma, streamer-belt-origin plasma, sector-reversal-region plasma, and ejecta. The three parameters are the proton specific entropy $S_p = T_p/n_p^{2/3}$, the proton Alfvén speed v_A, and the proton temperature T_p compared with a velocity-dependent expected temperature. Four measurements are needed to apply the scheme: the proton number density n_p, the proton temperature T_p, the magnetic-field strength B, and the solar-wind speed v_{sw}. The scheme is tested and is found to be more accurate than existing categorization schemes. The categorization scheme is applied to the 1963-2013 OMNI2 data set spanning 4 solar cycles and to the 1998-2008 ACE data set. The statistical properties of the 4 types of plasma are examined. The sector-reversal-region plasma is found to have statistically low alpha-to-proton density ratios and high Alfvén Mach numbers. The statistical relations between the proton and alpha-particle specific entropies and oxygen and carbon charge-state density ratios S_p, S_α, O^{7+}/O^{6+}, and C^{6+}/C^{5+} from ACE are examined for the four types of plasma: the patterns observed imply a connection between sector-reversal-region plasma and ejecta and a connection between streamer-belt-origin plasma and coronal-hole-origin plasma. Plasma occurrence rates are examined and solar-cycle patterns are found for ejecta, for coronal-hole-origin plasma, and for sector-reversal-region plasma. A paper with full results and detailed methodology of this project are accepted by JGR Space physics and the DOI of the paper is: 10.1002/2014JA020412.

Keywords: solar wind source, solar cycle, streamer belt, coronal holes, ejecta

1. Introduction

A 4-plasma categorization scheme at 1 AU will be developed based on measurements of the solar-wind proton density and temperature, the solar-wind speed, and the solar-wind magnetic-field strength. An advantage of the new categorization scheme is that it does not rely upon heavy-ion measurements.

1.1. The Plasma Types in the Solar Wind

It is generally accepted that there are three major types of solar wind plasma, coronal-hole-origin plasma, streamer-belt-origin plasma, and ejecta. Ejecta are associated with solar transients such as coronal mass ejections [cf. *Richardson et al.*, 2000; *Zhao et al.*, 2009]. In this report streamer-belt plasma will be divided further into two subgroups [cf. *Antonucci et al.*, 2005; *Schwenn*, 2006; *Susino et al.*, 2008]: (a) streamer-belt plasma and (b) sector-reversal regions.

Coronal-hole-origin plasma is sometimes referred to as the fast solar wind; it originates from the interaction of open field lines with the low-lying closed loops on the floor of a coronal hole [*Sheeley et al.*, 1976; *Cranmer*, 2009] (see Figure 1). Streamer-belt-origin plasma is sometimes referred to as the slow solar wind. Where it originates is of some controversy (see Figure 1); streamer-belt plasma is believed to come from either (a) the interchange reconnection of open magnetic field lines with closed streamer-belt field lines [*Fisk et al.*, 1999; *Subramanian et al.*, 2010] or (b) the edge of a coronal hole near a streamer belt [*Wang and Sheeley*, 1990; *Arge et al.*, 2003], or (c) from corridors of coronal hole penetrating into streamer-belt regions of the solar surface [*Antiochos et al.*, 2011; *Crooker et al.*, 2012]. The sector-reversal-region plasma is likely emitted from the tops of helmet streamers [*Gosling et al.*, 1981; *Susino et al.*, 2008; *Suess et al.*, 2009; *Foullon et al.*, 2011] (see Figure 1).

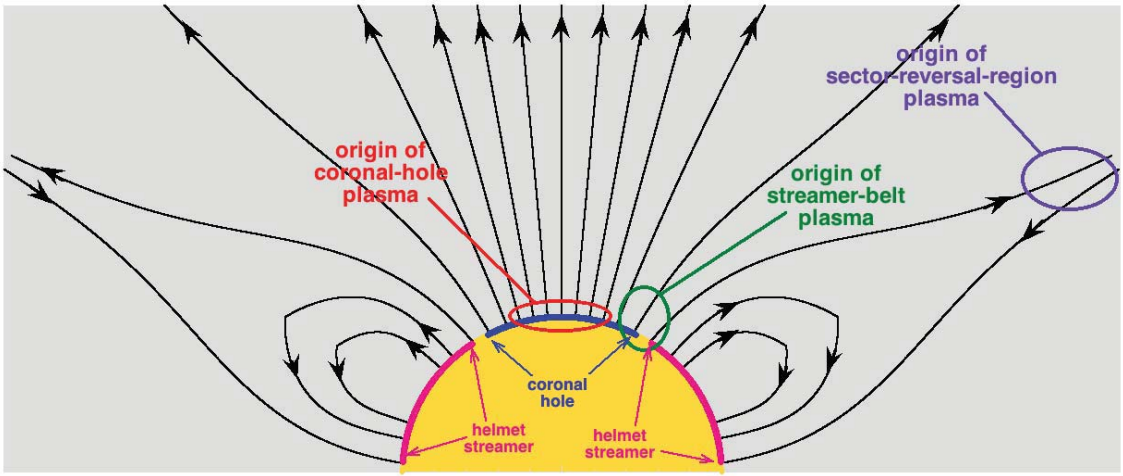

Figure 1. A sketch of the Sun (yellow) with a coronal hole surrounded by two helmet streamers (green labels). The source locations of three types of plasma are indicated with the circles: coronal-hole-origin plasma (red), sector-reversal-region plasma (purple), and streamer-belt-origin plasma (blue). The streamer-belt plasma may come from the edge of the coronal hole near the streamer belt and/or interchange reconnection between open flux and the closed loops of the streamer belt and/or from corridors of open flux penetrating into the streamer belt.

There are statistical differences between coronal-hole-origin plasma and streamer-belt-origin plasma. Coronal-hole-origin plasma tends to be homogeneous whereas streamer-belt-origin plasma is highly structured [*Bame et al.*, 1977; *Borovsky*, 2012a]; coronal-hole-origin plasma is dominated by outward-Alfvénic fluctuations whereas streamer-belt-origin plasma is not very Alfvénic [*Luttrell and Richter*, 1988; *Schwenn*, 1990; *Borovsky and Denton*, 2010a]. Coronal-hole plasma is characterized by an alpha-proton field-aligned relative drift at up to the local proton Alfvén speed [*Marsch et al.*, 1982], with such alpha-proton relative streaming typically absent in streamer-belt-origin plasma [*Hirshberg et al.*, 1974; *Asbridge et al.*, 1976]. Coronal-hole plasma exhibits a statistical non-adiabatic heating of the protons with distance from the Sun in the inner heliosphere [*Hellinger et al.*, 2011; *Borovsky and Gary*, 2014]; the protons of streamer-belt-origin plasma are closer to adiabatic [*Eyni and Steinitz*, 1978; *Freeman and Lopez*, 1985]. The Fourier spectra of the magnetic-field fluctuations, the velocity fluctuations, and the

Elsasser variables show statistical differences between the two types of plasma [*Tu and Marsch*, 1995; *Borovsky*, 2012a]. Current sheets in coronal-hole plasma are co-located with velocity shears [*Borovsky*, 2012b]; current sheets in streamer-belt plasma are co-located with plasma boundaries [*Borovsky*, 2012c]. A preliminary examination finds that the turbulence upstream and downstream of interplanetary shocks differs when the shock is in coronal-hole-origin plasma versus streamer-belt-origin plasma. Almost any study done of the solar wind needs to be organized by the origin of the solar-wind plasma.

Intervals of streamer-belt plasma in the data time series can be categorized as either helmet streamers or pseudostreamers. Helmet streamers form at the Sun when a loop arcade separates two coronal holes of opposite magnetic polarity [*Pneuman*, 1968; *Rusin et al.*, 2010]. Pseudostreamers form when two like-signed coronal holes are separated by a pair of loop arcades [*Wang et al.*, 2007; *Riley and Luhmann*, 2012]. A helmet-streamer interval is identified at 1 AU as an interval of streamer-belt plasma separating two coronal-hole plasma regions with opposite magnetic polarity; a pseudostreamer interval is identified at 1 AU as an interval of streamer-belt plasma separating two coronal-hole regions with the same magnetic polarity [*Borovsky and Denton*, 2013]. Within a helmet-streamer interval there is one sector reversal (which can be multiply structured [*Crooker et al.*, 1993, 2004a; *Blanco et al.*, 2006 *Foullon et al.*, 2009]). Within a pseudostreamer interval there is thought to be zero sector reversals, but one cannot rule out pseudostreamer intervals with an even number of sector reversals [cf. *Wang et al.*, 2007; *Panasenco and Velli*, 2013].

As will be seen, around the sector reversal of a helmet streamer there is an interval of plasma that has very low proton specific entropy, high number densities, either an absence of an electron strahl or a very intermittent electron strahl, and typically a very low velocity. These intervals of distinct plasma will be cataloged as “sector-reversal regions”. A sector-reversal region can include a heliospheric plasma sheet, which is a high-density region surrounding the heliospheric current sheet itself [*Winterhalter et al.*, 1994; *Crooker et al.*, 2004b]; or it can include a sector reversal without high density and/or high-density intervals outside of the sector reversal. Pseudostreamer intervals without sector reversals do not have this sector-reversal-region type of plasma in them [see also *Neugebauer et al.*, 2004; *Wang et al.*, 2012].

The other major category of solar-wind plasma is ejecta, also denoted as “interplanetary coronal mass ejections” (ICMEs). Ejecta include magnetic clouds, which are large well-defined closed-field-line structures (both magnetic foot points on the Sun). Ejecta also include smaller closed-loop structures. The ejecta originate as streamer-belt or active-region magnetic structures that were disconnected and ejected by large-scale reconnections in the corona. Unlike plasmas that are steadily emitted from the Sun, the magnetic fields in impulsively-emitted ejecta do not follow the Parker spiral [*Borovsky*, 2010]. Whereas steadily-emitted solar wind expands in the two directions transverse to radial as it advects from the Sun, impulsive ejecta can expand in all three directions as they propagate outward [*Klein and Burlaga*, 1982; *Poomvises et al.*, 2010]. This overexpansion results (usually) in anomalously low plasma temperatures at 1 AU for ejecta [*Gosling et al.*, 1973; *Elliott et al.*, 2005]. The closed-loop structures can often be detected by bi-directional electron strahls (indicating both magnetic footpoints on the Sun) [*Gosling et al.*, 1987; *Richardson and Cane*, 2010]. There are a number of additional signatures of ejecta [cf. *Neugebauer and Goldstein*, 1997; *Lepping et al.*, 2005; *Zurbuchen and Richardson*, 2006].

1.2. Why Categorization of the Solar Wind Is Important

A categorization of the solar wind into its four types of plasma is desirable for a number of reasons. From the above discussion, it is clear that the properties of the four types of solar wind differ considerably. Hence, when for example making a statistical study of solar wind parameters, the interpretation of the results can be clarified by dividing the solar wind measurements according to the type of solar wind in which they were observed.

Through the different phases of the solar cycle the occurrence rates at Earth of the various types of solar-wind plasma systematically change [*Intriligator*, 1974; *Bame et al.*, 1976; *Zhao et al.*, 2009; *D’Amicis et al.*, 2011; *Richardson and Cane*, 2012; *Lepri et al.*, 2013]. Recent studies have reported a solar-cycle variation in the manner by which the solar wind drives the Earth [*Nakai and Kamide*, 1999; *Nagatsuma*, 2006; *McPherron et al.*, 2009, 2013; *Burke*, 2011]. Any variation in the solar-wind driving of the Earth with solar cycle should really be caused by a difference in the solar-wind driving with plasma type. This root cause has never been investigated.

Further, to use in situ solar-wind measurements to diagnose physical processes ongoing at the Sun and to infer the properties of the solar wind at the Sun [*Mariani et al.*, 1983; *Thieme et al.*, 1988, 1989, 1990; *Matthaeus et al.*, 2007; *Borovsky*, 2008; *Zastenker et al.*, 2014], those solar-wind measurements must be sorted according to the origin of the solar-wind plasma.

1.3. Existing Solar-Wind Categorization Schemes

If the solar-wind plasma is categorized, it is usually simply separated into "fast wind" or "slow wind" according to the speed of the wind [e.g. *Arya and Freeman*, 1991; *Tu and Marsch*, 1995; *Feldman et al.*, 2005; *Yordanova et al.*, 2009; *Bruno and Carbone*, 2013]. This roughly separates the plasma into coronal-hole versus streamer-belt origin (see Section 3.1), except (a) when there are compressions or rarefactions, (b) when coronal holes are small and the speed at Earth is not fast, or (c) when ejecta are present. This velocity scheme also does not separate out sector-reversal-region plasma.

Many schemes have been developed to identify and separate ejecta (ICMEs and magnetic clouds). These may focus on anomalously low proton temperatures [*Gosling et al.*, 1973; *Richardson and Cane*, 1995; *Elliott et al.*, 2005], on low levels of magnetic-field fluctuations [*Lepping et al.*, 2005], or on the presence of a bi-directional electron strahl [*Gosling et al.*,1987; *Skoug et al.*, 2000]. *Richardson and Cane* [2010] (see also *Cane and Richardson* [2003]) produced an extensive list of ejecta intervals at Earth based on the combination of proton temperature, O^{7+}/O^{6+} density ratio, electron strahl, magnetic-field structure, and energetic-particle measurements. A catalog of magnetic clouds at Earth [e.g. *Lepping et al.*, 2005] based on plasma beta and magnetic-field structure has been produced and a catalog of ICMEs at Earth [*Jian et al.*, 2006] based on the total pressure, the proton temperature, the alpha-to-proton density ratio, the magnetic-field structure, and the presence of bi-directional electron streaming has been produced.

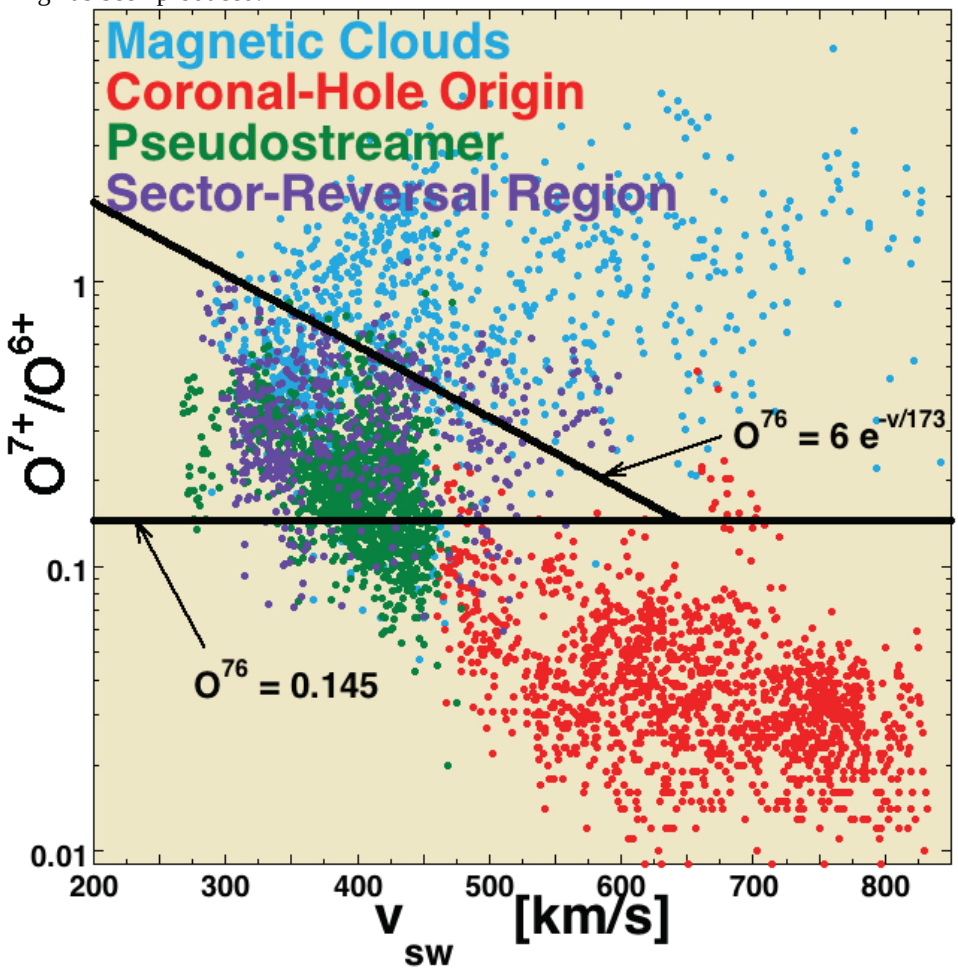

Figure 2. Hourly-averaged values of solar-wind data are plotted for 4 collections of wind types: unperturbed coronal-hole-origin wind (red), pseudostreamers (streamer-belt-origin wind, green), sector-reversal regions (purple), and the Lepping magnetic clouds (blue). The 4 known types of wind are plotted in the *Zhao et al.* [2009] O^{7+}/O^{6+}-versus-v_{sw} scheme (black curves). In the *Zhao et al.* [2009] scheme the top domain is ejecta, the lower domain is coronal-hole-origin plasma, and the middle domain is non-coronal-hole-origin plasma.

Zhao et al. [2009] (see also *Zurbuchen et al.* [2002] and *von Steiger et al.* [2010]) constructed an algorithm to categorize the 1998-2008 ACE solar-wind data set into coronal-hole-origin plasma, non-coronal-hole-origin plasma (streamer-belt origin), and ejecta based on the O^{7+}/O^{6+} density ratio and the wind speed. In Figure 2 the Zhao et al. O^{7+}/O^{6+}-versus-v_{sw} scheme is applied to four collections of plasma in the solar wind: a collection of unperturbed coronal-hole wind (red), a collection of pseudostreamer wind [*Borovsky and Denton*, 2013] (green), a collection of regions around sector reversals where the electron strahl becomes intermittent (purple), and the collection of Lepping magnetic clouds [*Lepping et al.*, 2005] http://wind.gsfc.nasa.gov/mfi/mag_cloud_pub1.html (green). (These collections are described further in Section 2.1.) As can be seen, the *Zhao et al.* O^{7+}/O^{6+}-versus-v_{sw} categorization scheme does a good job of separating the distinct types of solar wind in the 4 collections of events. Note that a drawback to using the Zhao et al. scheme is that O^{7+}/O^{6+} measurements are not generally available in solar-wind data sets, i.e. most solar-wind spacecraft do not carry ion-composition instrumentation.

Another plasma categorization scheme recently used [*Borovsky and Denton*, 2014] focuses on the parameter P_{type} (plasma type)

$$P_{type} = \log(S_p) + \log(S_\alpha) - \log(O^{7+}/O^{6+}) - \log(C^{6+}/C^{5+}) \quad (1)$$

where $S_p = T_p/n_p^{2/3}$ is the proton specific entropy of the solar wind, $S_\alpha = T_\alpha/n_\alpha^{2/3}$ is the alpha-particle specific entropy of the solar wind, and where O^{7+}/O^{6+} and C^{6+}/C^{5+} are the oxygen and carbon charge-state number-density ratios in the solar wind. The parameter P_{type} does a better job of separating coronal-hole-origin plasma from streamer-belt-origin plasma than O^{7+}/O^{6+} does (see Section 3.1), however, the parameters needed to evaluate P_{type} are not available in all solar-wind data sets.

The Genesis spacecraft had an onboard solar-wind-classification algorithm [*Neugebauer et al.*, 2003; *Reisenfeld et al.*, 2003] that used measurements of the alpha-to-proton density ratio, the strength of bi-directional electron strahl, the proton temperature, and the solar-wind speed. The algorithm used not only the measurements, but also the time history of measurements and the time history of the occurrence of interplanetary shocks.

1.4. The Present Work

In this report a 3-parameter algebraic algorithm to categorize the solar wind at 1 AU will be developed and tested. The three parameters are the proton specific entropy S_p, the proton Alfvén speed v_A, and the ratio of an "expected" temperature T_{exp} to the measured proton temperature T_p, where the expected temperature is determined as a function of the solar-wind speed v_{sw} by fitting non-ejecta plasma in T_p-versus-v_{sw} space. To implement the categorization scheme four solar-wind measurements are needed: the proton number density n_p, the proton temperature T_p, the wind speed v_{sw}, and the magnetic-field strength B. The categorization scheme will not be based on heavy-ion measurements.

This manuscript is organized as follows. In Section 2 the development of the 3-parameter 4-plasma categorization scheme for the solar wind is described. In Section 3 the categorization scheme is applied to the1963-2013 OMNI2 data set and the properties of the 4 types of plasmas are investigated. Using the categorized 1963-2013 OMNI2 data set, the occurrence rates of the 4 types of solar-wind plasma are examined over 4 solar cycles in Section 4. Section 5 contains a summary of the findings and Section 6 contains discussions about the sector-reversal-region plasma and about future research.

2. Results

We develop a new categorization scheme and the findings made using that scheme are summarized in the five subsections that follow.

2.1. The Categorization Scheme

An new algebraic scheme was developed to categorize the solar wind plasma into four types: coronal-hole-origin plasma, streamer-belt-origin plasma, sector-reversal-region plasma, and ejecta. The scheme uses 3 solar-wind parameters: (1) the proton specific entropy $S_p = T_p/n_p^{2/3}$, (2) the proton Alfvén speed $v_A = B/(4\pi m_p n_p)^{1/2}$, and (3) the ratio of the measured proton temperature T_p compared with the velocity-dependent expected temperature for the solar-wind speed $T_{exp} = (v_{sw}/258)^{3.113}$. To evaluate those three parameters measurements are needed of four solar-wind quantities: the proton number density n_p, the proton temperature T_p, the magnetic-field strength B, and the solar-wind speed v_{sw}.

The 3-parameter categorization scheme is versatile in that (1) it does not require measurements of the heavy-ion charge states of the solar wind and (2) it does not require looking at the time history of the solar wind nor at the recent occurrences of solar-wind events.

The categorization scheme was developed by using collections of solar-wind plasma of known types, such as (a) unperturbed coronal-hole plasma from constant-velocity high-speed streams, (b) published magnetic clouds, and (c) collected pseudostreamers.. The scheme was tested against those known collections of plasma and found to be very satisfactory. The scheme was tested against an existing 2-parameter scheme and found to be an improvement.

The common categorization of the solar wind into fast wind and slow wind was compared with the categorization by the 3-parameter scheme. Ejecta contamination is always a problem for fast-wind/slow-wind categorization. A selection of "fast wind" is found to result in a collection of mostly coronal-hole-origin plasma (with ejecta): a selection of "slow wind" is found to result in a mix of streamer-belt-origin plasma, sector-reversal-region plasma, and coronal-hole-origin plasma (with ejecta).

2.2. The Fourth Plasma Type: Sector-Reversal-Region Plasma

The usual streamer-belt-plasma category was split into two categories: streamer-belt-origin plasma and sector-reversal-region plasma. The candidate population for sector-reversal-region plasma was identified only by the properties of the electron strahl around sector reversals. The values of S_p, v_A, and T_{exp}/T_p for that candidate population were then used to define a region in S_p-v_A-T_{exp}/T_p parameter space that would be categorized as sector-reversal-region plasma. Examining the data points in OMNI2 that are categorized as sector-reversal-region plasma by their S_p-v_A-T_{exp}/T_p values, it is found that those regions indeed reside around magnetic sector reversals.

A statistical examination of the solar wind that is categorized as sector-reversal-region plasma finds that sector-reversal-region plasma has very low values of the α/p density ratio and sector-reversal-region plasma is likely to be the cores of helmet streamers: such plasma types were suggested by *Bavassano et al.* [1997] (stalks of coronal streamers) and by Wang et al., [2000] (dynamic streamers). Sector-reversal-region plasma has anomalously high Alfvén Mach numbers and the Kp index of the Earth is typically quite low when sector-reversal-region plasma is passing. The relationship between C^{6+}/C^{5+} and O^{7+}/O^{6+} for sector-reversal-region plasmas resembles that of magnetic clouds.

The fraction of the total-streamer-belt plasma that is sector-reversal-region plasma is maximum at solar minimum and minimum at solar maximum. Some suggested reasons why this might be so are given in the manuscript.

2.3. Properties of the Plasma Types

The statistical properties of the categorized plasmas were examined. Ejecta was found to have low values of the Alfvén Mach number M_A, low values of the proton beta β_p, and low values of the normalized amplitude of the magnetic-field fluctuations $\delta B/B$. The amplitude $\delta B/B$ was largest on average in coronal-hole-origin plasma, but it was only 10's of per cent larger than in streamer-belt-origin plasma and sector-reversal-region plasma. Sector-reversal-region plasma has very low values of α/p and high Alfvén Mach numbers. The large deviations of the solar-wind magnetic-field direction out of the ecliptic plane occur predominantly in ejecta and sector-reversal-region plasma.

2.4. Relations between S_p, S_α, O^{7+}/O^{6+}, and C^{6+}/C^{5+}

The correlations between the four parameters S_p, S_α, O^{7+}/O^{6+}, and C^{6+}/C^{5+} were examined for the four types of solar-wind plasma. Six mathematical relations between the four parameters are found: each of these mathematical relations holds for some of the four plasmas. The $S_\alpha \leftrightarrow S_p$ formula holds for all four types of plasma. The $O^{7+}/O^{6+} \leftrightarrow S_p$ and $O^{7+}/O^{6+} \leftrightarrow S_\alpha$ formulas hold for coronal-hole-origin plasma, streamer-belt-origin plasma, and sector-reversal-region plasma; they do not hold for ejecta. The $C^{6+}/C^{5+} \leftrightarrow S_p$, the $C^{6+}/C^{5+} \leftrightarrow S_\alpha$, and the $C^{6+}/C^{5+} \leftrightarrow O^{7+}/O^{6+}$ formulas hold for coronal-hole-origin plasma and streamer-belt-origin plasma; they do not hold for ejecta or for sector-reversal-region plasma. In plots of C^{6+}/C^{5+} versus O^{7+}/O^{6+}, points that are categorized as ejecta fall into two populations, one population that tracks the C^{6+}/C^{5+}-versus-O^{7+}/O^{6+} relationship of streamer-belt plasma and coronal-hole plasma and one population that tracks the C^{6+}/C^{5+}-versus-O^{7+}/O^{6+} pattern of magnetic clouds and sector-reversal regions. From these $C^{6+}/C^{5+} \leftrightarrow O^{7+}/O^{6+}$ relations it is speculated (1) that the birth mechanisms of coronal-

hole-origin plasma and of streamer-belt-origin plasma may be very similar to each other and (2) that the birth mechanisms of magnetic-cloud-type ejecta and of sector-reversal-region plasma may be very similar to each other.

2.5. Occurrence Rates at Earth

The well-known relations (1) that ejecta occurs most prevalently at solar maximum and rarely at solar minimum and (2) that coronal-hole-origin plasma occurs most prevalently during the declining phase and less prevalently during the ascending phase were both seen.

A strong correlation between the occurrence rate of ejecta and the sunspot number is seen. A modest anticorrelation between the sunspot number and the occurrence rate of sector-reversal-region plasma is seen.

The 3-parameter categorization scheme finds solar minimum to be a mix of streamer-belt-origin plasma, sector-reversal-region plasma, and coronal-hole-origin plasma; this is contrary to an earlier categorization scheme which has coronal-hole-origin plasma dominating at solar minimum.

3. Discussion and Future Studies

No plasma categorization scheme will be exact, owing to our lack of knowledge about the exact origins of solar wind from the Sun. However, the 3-parameter categorization scheme developed in this report is quite accurate when used to categorize known intervals of solar wind plasma, such as (a) unperturbed coronal-hole plasma from constant-velocity high-speed streams, (b) published magnetic clouds, and (c) collected pseudostreamers.

In this report a fourth solar-wind-plasma category has been defined: sector-reversal-region plasma. This is in addition to the three standard categories of solar-wind plasma: ejecta, coronal-hole-origin plasma, and streamer-belt-origin plasma. The parent population of the sector-reversal-region plasma is the "strahl confusion zones" around magnetic sector reversals. The sector-reversal-region plasma appears to be a definite, different type of plasma from the other three types. It is found to have low alpha-to-proton density ratios and higher-than-average Alfvén Mach numbers. It has statistical relations between C^{6+}/C^{5+} and S_p and between C^{6+}/C^{5+} and O^{7+}/O^{6+} that differ from the relations in coronal-hole-origin plasma and streamer-belt-origin plasma, more like the relations in magnetic clouds. This could be indicative of a birth mechanism for sector-reversal-region plasma that is related to the birth mechanism of magnetic-cloud-type ejecta. Future analysis of this sector-reversal-region plasma (such as a analysis of spectral indices, Alfvénicity, magnetic structure, and discontinuities) will be interesting.

This analysis also indicates that there are two populations of ejecta plasmas: a population with magnetic-cloud-like patterns of C^{6+}/C^{5+}-versus-O^{7+}/O^{6+} and a population with coronal-hole- and streamer-belt-like patterns of C^{6+}/C^{5+}-versus-O^{7+}/O^{6+}. A future investigation of these two ejecta populations is called for.

For future research there are numerous solar-wind studies that can be clarified by separating the solar-wind data into the four different types of plasma.

We have a rudimentary knowledge about the differences in the properties of turbulence (spectral slopes, Alfvénicities, correlation lengths) in different types of solar-wind plasma; this knowledge could be greatly improved by regularly separating solar-wind data into the different plasma categories and separating the turbulence studies into those plasma categories. Similarly our knowledge of the current sheets and pressure-balanced structures in the solar wind could be improved by separating studies into the appropriate types of solar-wind plasma. The origin of several types of solar-wind structures such as magnetic holes, ortho-Parker-spiral intervals, and non-ecliptic magnetic-field intervals are not known; information about these may be gained by statistically studying these intervals versus the types of plasma in which they occur.

Particle distribution functions and strahl properties also could be better organized versus the types of plasmas in which the observations are made. This is particularly true for the solar-wind core-halo electron distributions, where very little information exists as functions of the type of plasma.

To sort out systematic differences in the properties of the turbulence around shocks, interplanetary-shock data analysis needs to be sorted according to the type of plasma through which the shock propagates.

Connecting (a) the categorization of the plasma at 1 AU into 4 types with (b) model-based outward mappings of the solar wind from solar magnetograms to the Earth [e.g. *Arge et al*, 2004, *Owens et al.*, 2005] would provide information about what types of regions on the Sun give rise to the 4 types of plasma, and would conversely provide feedback to the mapping techniques about the origin of solar-wind types at the Sun.

A more-detailed study of the occurrence rates of the 4 plasmas and the properties of the 4 plasmas may help to answer questions such as [*Georgieva et al.*, 2006, 2012, 2013]: Are all solar cycles the same? Have there been long-

term variations in the occurrence rates of solar-wind plasmas reaching the Earth? Does this give rise to long-term variations in the magnetosphere-ionosphere-atmosphere system?

Studying the manner in which the solar wind drives the Earth's magnetosphere separately for the four types of solar-wind plasma may shed light on whether or not reported differences in the driving of the Earth during the different phases of the solar cycle are simply caused by different mixes in the occurrence fractions of the 4 types of plasma during the different solar-cycle phases.

Finally, a needed task for the future is a generalization of this 3-parameter 4-plasma categorization scheme for use closer to the Sun than 1 AU. Understanding existing and future r < 1 AU data sets is critical to gaining an understanding of the origins and evolutions of solar-wind features that reach the Earth.

A paper [*Xu and Borovsky*, 2015]with detailed methodology and full results of this project has been accepted by JGR Space Physics.

Acknowledgements. The authors thank Mick Denton, Gang Li, Ruth Skoug, John Steinberg, and Michelle Thomsen for helpful conversations. FX wishes to thank the Los Alamos National Laboratory for a Vela Fellowship while attending the Los Alamos Space Weather Summer School. This work was supported at the Space Science Institute by the NSF Solar-Terrestrial Program, the NASA Magnetospheric Guest Investigators program, and the NASA Heliophysics LWS Program; at the University of Michigan by the NASA Geospace SR&T Program; and at Lancaster University by Science and Technology Funding Council Grant ST/I000801/1. The hourly-averaged OMNI2 measurements and the ACE measurements used in this paper are available from NASA data-server websites (http://omniweb.gsfc.nasa.gov/form/dx1.html and http://cdaweb.gsfc.nasa.gov/istp_public/).

References

Antiochos, S. K., Z. Mikic, V. S. Titov, R. Lionello, and J. A. Linker, A model for the sources of the slow solar wind, Astrophys. J., 731, 112, 2011.

Antonucci, E., L. Abbo, and M. A. Dodero, Slow wind and magnetic topology I the solar minimum corona in 1996-1997, Astron. Astrophys., 435, 699, 2005.

Arge, C.N., D. Odstrcil, V.J. Pizzo, and L.R. Mayer, Improved method for specifying solar wind speed near the sun, AIP Conf. Proc., 679, 190, 2003.

Arge, C.N., J.G. Luhmann, D. Odstrcil, C.J. Schrijver, and Y. Li, Stream structure and coronal sources of the solar wind during the May 12th, 1997 CME,J. Atmos. Solar-Terr. Phys., 66, 1295, 2004.

Arya, S., and J. W. Freeman, Estimates of solar wind velocity gradients between 0.3 and 1 AU based on velocity probability distributions from Helios 1 at perihelion and aphelion, J. Geophys. Res., 96, 14183, 1991.

Asbridge, J. R., S. J. Bame, W. C. Feldman, and M. D. Montgomery, Helium and hydrogen velocity differences in the solar wind, J. Geophys. Res., 81, 2719, 1976.

Bame, S. J., J. R. Asbridge, W. C. Feldman, and J. T. Gosling, Solar cycle evolution of high-speed solar wind streams, Astrophys. J., 207, 977, 1976.

Bame, S. J., J. R. Asbridge, W. C. Feldman, and J. T. Gosling, Evidence for a structure-free state at high solar wind speeds, J. Geophys. Res., 82, 1487, 1977.

Blanco, J. J., J. Rodriquez-Pacheco, M. A. Hidalgo, and J. Sequeiros, Analysis of the heliospheric current sheet fine structure: Single or multiple currents sheets, J. Atmos. Solar-Terr. Phys., 68, 2173, 2006.

Borovsky, J. E., The flux-tube texture of the solar wind: Strands of the magnetic carpet at 1 AU?, J. Geophys. Res., 113, A08110, 2008.

Borovsky, J. E., On the variations of the solar-wind magnetic field about the Parker-spiral direction, J. Geophys. Res., 115, A09101, 2010.

Borovsky, The velocity and magnetic-field fluctuations of the solar wind at 1 AU: Statistical analysis of Fourier spectra and correlations with plasma properties, J. Geophys. Res., 117, A05104, 2012a.

Borovsky, J. E., The effect of sudden wind shear on the Earth's magnetosphere: Statistics of wind-shear events and CCMC simulations of magnetotail disconnections, J. Geophys. Res., 117, A06224, 2012b.

Borovsky, J. E., Looking for evidence of mixing in the solar wind from 0.31 to 0.98 AU, J. Geophys. Res., 117, A06107, 2012c.

Borovsky, J. E., Physics based solar-wind driver functions for the magnetosphere: Combining the reconnection-coupled MHD generator with the viscous interaction, J. Geophys. Res., 118, 7119, 2013.

Borovsky, J. E., and M. H. Denton, The differences between CME-driven storms and CIR-driven storms, J. Geophys. Res., 111, A07S08, 2006.

Borovsky, J. E., and M. H. Denton, Electron loss rates from the outer electron radiation belt caused by the filling of the outer plasmasphere: The calm before the storm, J. Geophys. Res., 114, A11203, 2009.

Borovsky, J. E., and M. H. Denton, Solar-wind turbulence and shear: A superposed-epoch analysis of corotating interaction regions at 1 AU, J. Geophys. Res., 115, A10101, 2010a.

Borovsky, J. E., and M. H. Denton, On the Heating of the Outer Radiation Belt to Produce High Fluxes of Relativistic Electrons: Measured Heating Rates for High-Speed-Stream-Driven Storms, J. Geophys. Res., 115, A12206, 2010b.

Borovsky, J. E., and M. H. Denton, The magnetic field at geosynchronous orbit during high-speed-stream-driven storms: Connections to the solar wind, the plasma sheet, and the outer electron radiation belt, J. Geophys. Res., 115, A08217, 2010c.

Borovsky, J. E., and M. H. Denton, The differences between storms driven by helmet-streamer CIRs and storms driven by pseudostreamer CIRs, J. Geophys. Res., 118, doi:10.1002/jgra.50524, 2013.

Borovsky, J. E., and M. H. Denton, Exploring the cross-correlations and autocorrelations of the ULF indices and incorporating the ULF indices into the systems science of the solar-wind-driven magnetosphere, J. Geophys. Res., 119, 4307, 2014.
Borovsky, J. E., and S. P. Gary, How important are the alpha-proton relative drift and the electron heat flux for the proton heating of the solar wind in the inner heliosphere?, J. Geophys. Res., 119, doi:10.1002/2014JA019758, 2014.
Borovsky, J. E., and J. T. Steinberg, The freestream turbulence effect in solar-wind/magnetosphere coupling: Analysis through the solar cycle and for various types of solar wind, in Recurrent Magnetic Storms: Cororating Solar Wind Streams, pg. 59, American Geophysical Union, 2006.
Bruno, R., and V. Carbone, The solar wind as a turbulence laboratory, Living Rev. Solar Phys. 10, 2, http://www.livingreview.org/lrsp-2013-2, 2013.
Burke, W. J., Solar cycle dependence of solar wind energy coupling to the thermosphere, J. Geophys. Res., 116, A06302, 2011.
Cane, H. V., and I. G. Richardson, Interplanetary coronal mass ejections in the near-Earth solar wind during 1996-2002, J. Geophys. Res., 108, 1156, 2003.
Cranmer, S. R., Coronal holes, Living Rev. Solar Phys., 6, 3, 2009.
Crooker, N. U., and R. L. McPherron, Coincidence of composition and speed boundaries in the slow solar wind, J. Geophys. Res., 117, A09104, 2012.
Crooker, N. U., G. L. Siscoe, S. Shodhan, D. F. Webb, J. T. Gosling, and E. J. Smith, Multiple heliospheric current sheets and coronal streamer belt dynamics, J. Geophys. Res., 98, 9371, 1993.
Crooker, N. U., S. W. Hahler, D. E. Larson, and R. P. Lin, Large-scale magnetic field inversions at sector boundaries, J. Geophys. Res., 109, a03108, 2004a.
Crooker, N. U., C.-L. Huang, S. M. Lamassa, D. E. Larson, S. W. Kahler, and H. E. Spence, Heliospheric plasma sheets, J. Geophys. Res., 109, A03107, 2004b.
D'Amicis, R., R. Bruno, and B. Bavassano, Response of the geomagnetic activity to solar wind turbulence during solar cycle 23, J. Atmos. Solar-Terr. Phys., 73, 653, 2011.
Elliott, H. A., D. J. McComas, N. A. Schwadron, J. T. Gosling, R. M. Skoug, G. Gloeckler, and T. H. Zurbuchen, An improved expected temperature formula for identifying ICMEs, J. Geophys. Res., 110, A04103, 2005.
Eyni, M., and R. Steinitz, Cooling of slow solar wind protons from the Helios 1 experiment, J. Geophys. Res., 83, 4387, 1978.
Feldman, U., E. Landi, and N. A. Schwadron, On the sources of fast and slow solar wind, J. Geophys. Res., 110, A07109, 2005.
Fisk, L. A., T. H. Zurbuchen, and N. A. Schwadron, Coronal magnetic field: Consequences of large-scale motion, Astrophys. J., 521, 868, 1999.
Foullon, C. B. Lavraud, N. C. Wardle, C. J. Owen, H. Kucharek, A. N. Fazakerley, D E. Larson, E. Lucek, J. G. Luhmann, A. Opitz, J.-A. Sauvaud, and R. M. Skoug, The apparent layered structure of the heliospheric current sheet: Multi-spacecraft observations, Solar Phys., 259, 389, 2009.
Foullon, C., B. Lavraud, J. G. Luhmann, C. J. Farrugia, A. Retino, K. D. C. Simunac, N. C. Wardle, A. B. Galvin, H. Kucharek, C. J. Owen, M. Popecki, A. Otitz, and J.-A. Sauvaud, Plasmoid releases in the heliospheric current sheet and associated coronal hole boundary layer evolution, Astrophys. J., 737, 1, 2011.
Freeman, J. W., and R. E. Lopez, The cold solar wind, J. Geophys. Res., 90, 9885, 1985.
Georgieva, K., B. Kirov, and E. Gavruseva, Geoeffectiveness of different solar drivers, and long-term variations of the correlation between sunspot and geomagnetic activity, Phys. Chem. Earth, 21, 81, 2006.
Georgieva, K., B. Kirov, P. Koucka Knizova, Z., Mosna, B. Kouba, and Y. Asenovska, Solar influences on atmospheric circulation, J. Atmos. Solar-Terr. Phys., 90-91, 15, 2012.
Georgieva, K., B. Kirov, and Y. A. Nagovitsyn, Long-term variations of solar magnetic fields derived from geomagnetic data, Geom. Aeron., 53, 852, 2013.
Gosling, J. T., V. Pizzo, and S. J. Bame, Anomalously low proton temperatures in the solar wind following interplanetary shock waves -- Evidence for magnetic bottles, J. Geophys. Res., 78, 2001, 1973.
Gosling, J. T., G. Borrini, J. R. Asbridge, S. J. Bame, W. C. Feldman, and R. T. Hansen, Coronal streamers in the solar wind at 1 AU, J. Geophys. Res., 86, 5438, 1981.
Gosling, J. T., D. N. Baker, S. J. Bame, W. C. Feldman, R. D. Zwickl, and E. J. Smith, Bidirectional solar wind electron heat flux events, J. Geophys. Res., 92, 8519, 1987.
Hellinger, P., L. Matteini, S., Stverak, P. M. Travnicek, and E. Marsch, Heating and cooling of protons in the fast solar wind between 0.3 and 1 AU: Helios revisited, J. Geophys. Res., 116, A09105, 2011.
Hirshberg, J., J. R. Asbridge, and D. E. Robbins, The helium component of solar wind velocity streams, J. Geophys. Res., 79, 934, 1974.
Intriligator, D. S., Evidence of solar-cycle variations in the solar wind, Astrophys. J., 188, L23, 1974.
Jian, L., C. T. Russell, J. G. Luhmann, and R. M. Skoug, Properties of interplanetary coronal mass ejections at one AU during 1995-2004, Solar Phys., 239, 393, 2006.
Klein, L. W., and L. F. Burlaga, Interplanetary magnetic clouds at 1 AU, J. Geophys. Res., 87, 613, 1982.
Lepping, R. P., C.-C. Wu, and D. B. Berdichevsky, Automatic identification of magnetic cloud-like regions at 1 AU: occurrence rate and other properties, Ann. Geophys., 23, 2687, 2005.
Lepri, S. T., E. Landi, and T. H. Zurbuchen, Solar wind heavy ions over Solar Cycle 23: ACE/SWICS measurements, Astrophys. J., 768, 94, 2013.
Luttrell, A. H., and A. K. Richter, The role of Alfvénic fluctuations in mhd turbulence evolution between 0.3 and 1 AU, in Proceedings of the Sixth International Solar Wind Conference, V. J. Pizzo, T. E. Holzer, and D. G. Sime (eds.), pg. 335, NCAR TN-306, 1988.
Mariani, F., B. Bavassano, and U. Villante, A statistical study of MHD discontinuities in the inner solar system: Helios 1 and 2, Solar Phys., 83, 349, 1983.
Marsch, E., K.-H. Muhlhauser, H. Rosenbauer, R. Schwenn, and F. M. Neubauear, Solar wind helium ions: Observations of the Helios solar probes between 0.3 and 1 AU, J. Geophys. Res., 87, 35, 1982.
Matthaeus, W. H., B. Breech, P. Dmitruk, A. Bemporad, G. Poletto, M. Velli, and M. Romoli, Density and magnetic field signatures of interplanetary 1/f noise, Astrophys. J., 657, L121, 2007.
McPherron, R. L., L. Kepko, T. I. Pulkkinen, T. S. Hsu, J. W. Weygand, and L. F. Bargatze, Changes in the response of the AL index with solar cycle and epoch within a corotating interaction region, Ann. Geophys., 27, 3165, 2009.
McPherron, R. L., D. N. Baker, T. I. Pulkkinen, T.-S. Hsu, J. Kissinger, and X. Chu, Changes in solar wind-magnetosphere coupling with solar cycle, season, and time relative to stream interfaces, J. Atmos. Solar-Terr. Phys., 99, 1, 2013.

Nagatsuma, T., Diurnal, semiannual, and solar cycle variations of solar wind-magnetosphere-ionosphere coupling, J. Geophys. Res., 111, A09202, 2006.
Nakai, H., and Y. Kamide, Solar cycle variations in the storm-substorm relationship, J. Geophys. Res., 104, 22695, 1999.
Neugebauer, M., R. Goldstein, and B. E. Goldstein, Features observed in the trailing regions of interplanetary clouds from coronal mass ejections, J. Geophys. Res., 102, 19743, 1997.
Neugebauer, M., J. T. Steinberg, R. L. Tokar, B. L. Barraclough, E. E. Dors, R. C. Weins, D. E. Gingerich, D. Luckey, and D. B. Whiteaker, Genesis on-board determination of the solar wind flow regime, Space Sci. Rev., 105, 661, 2003.
Neugebauer, M., P. C. Liewer, B. E. Goldstein, X. Zhou, and J. T. Steinberg, Solar wind stream interaction regions without sector boundaries, J. Geophys. Res., 109, A10102, 2004.
Owens, M. J., C. N. Arge, H. E. Spence, A. Pembroke, An event-based approach to validating solar wind speed predictions: High speed enhancements in the Wang-Sheeley-Arge model, J. Geophys. Res., 110, A12105, 2005.
Panasenco, O., and M. Velli, Coronal pseudostreamers: Source of fast or slow solar wind?, AIP Conf. Proc., 1539, 50, 2013.
Pneuman, G. W., Some general properties of helmeted coronal structures, Solar Phys., 3, 578, 1968.
Poomvises, W., J. Zhang, and O. Olmedo, Coronal mass ejection propagation and expansion in three-dimensional space in the heliosphere based on STEREO/SECCHI observations, Astrophys. J. Lett., 717, L159, 2010.
Reisenfeld, D. B., J. T. Steinberg, B. L. Barraclough, E. E. Dors, R. C. Weins, M. Neugebauer, A. Reinard, and T. Zurbuchen, Comparison of the Genesis solar wind regime algorithm results with solar wind composition observed by ACE, Amer. Phys. Soc. Conf. Proc., 679, 632, 2003.
Richardson, I. G., and H. V. Cane, Regions of abnormally low proton temperature in the solar wind (1965-1991) and their association with ejecta, J. Geophys. Res., 100, 23397, 1995.
Richardson, I. G., and H. V. Cane, Near-Earth interplanetary coronal mass ejections during solar cycle 23 (1996-2009): Catalog and summary of properties, Solar Phys., 264, 189, 2010.
Richardson, I. G., and H. V. Cane, Near-earth solar wind flows and related geomagnetic activity during more than four solar cycles (1963-2011), J. Space Weather Space Clim., 2, A02, 2012.
Riley, P., and J. G. Luhmann, Interplanetary signatures of unipolar streamers and the origin of the slow solar wind, Solar Phys., 277, 355, 2012.
Rusin, V., M. Druckmuller, P. Aniol, M. Minarovjech, M. Saniga, Z. Mikic, J. A. Linker, R. Lionello, P. Riley, and V. S. Titov, Comparing eclipse observations of the 2008 August 1 solar coronal with an MHD model prediction, Astron. Astrophys., 513, A45, 2010.
Schwenn, R., Large scale structure of the interplanetary medium, in Physics of the Inner Heliosphere I, R. Schwenn and E. Marsch (eds.), pg. 99, Springer-Verlag, Berlin, 1990.
Schwenn, Solar wind sources and their variations over the solar cycle, Space Sci. Rev., 124, 51, 2006.
Sheeley, Jr., N. R., J. W. Harvey, and W. C. Feldman, Coronal holes, solar wind streams, and recurrent geomagnetic disturbances: 1973-1976, Solar Phys., 49, 271, 1976.
Skoug, R. M., W. C. Feldman, J. T. Gosling, D. J. McComas, and C. W. Smith, Solar wind electron characteristics inside and outside coronal mass ejections, J. Geophys. Res., 105, 23069, 2000.
Subramanian, S., M. S. Madjarska, and J. G. Doyle, Coronal hole boundaries evolution at small scales II. XRT view. Can small-scale outflows at CHBs be a source of the slow solar wind?, Astron. Astrophys., 516, A50, 2010.
Suess, S. T., Y.-K. Ko, R. Von Steiger, and R. L. Moore, Quiescent current sheets in the solar wind and origins of slow wind, J. Geophys. Res., 114, A04103, 2009.
Susino, R., R. Ventura, D. Spadaro, A. Vourlidas, and E. Landi, Physical parameters along the boundaries of a mid-latitude streamer and its adjacent regions, Astron. Astrophys., 488, 303, 2008.
Thieme, K. M., E. Marsch, and R. Schwenn, Relationship between structures in the solar wind and their source regions in the corona, in Proceedings of the Sixth International Solar Wind Conference, Vol. I, V. J. Pizzo, T. Holzer, and D. G. Sime (eds.) pg. 317, Technical Note NCAR/TN-306+Proc, National Center for Atmospheric Research, Boulder, 1988.
Thieme, K. M., R. Schwenn, and E. Marsch, Are structures in high-speed streams signatures of coronal fine structures?, Adv. Space Res., 9(4), 127, 1989.
Thieme, K. M., E. Marsch, and R. Schwenn, Spatial structures in high-speed streams as signatures of fine structures in coronal holes, Ann. Geophys., 8, 713, 1990.
Tu, C.-Y., and E. Marsch, MHD structures, waves and turbulence in the solar wind, Space Sci. Rev., 73, 1, 1995.
Wang, Y.-M., and N. R. Sheeley, Jr., Solar wind speed and coronal flux-tube expansion, Astrophys. J., 355, 726, 1990.
Wang, Y.-M., J. B. Biersteker, N. R. Sheeley, Jr., S. Koutchmy, J. Mouette, and M. Druckmuller, The solar eclipse of 2006 and the origin of raylike features in the white-light corona, Astrophys. J., 660, 882, 2007.
Wang, Y.-M., R. Grappin, E. Robbecht, and N. R. Sheeley, Jr., On the nature of the solar wind from coronal pseudostreamers, Astrophys. J., 749, 182, 2012.
Winterhalter, D., E. J. Smith, M. E. Burton, N. Murphy, and D. J. McComas, The heliospheric plasma sheet, J. Geophys. Res., 99, 6667, 1994.
Xu, F., and J. E. Borovsky, A new four-plasma categorization scheme for the solar wind, J. Geophys. Res. Space Physics, 120, doi: 10.1002/2014JA020412.
Yordanova, E., A. Balogh, A. Noullez, and R. von Steiger, Turbulence and intermittency in the heliospheric magnetic field in fast and slow solar wind, J. Geophys. Res. 114, A08101, 2009.
Zastenker, G. N., I. V. Koloskova, M. O. Riazantseva, A. S. Yurasov, J. Safrankova, Z. Nemecek, L. Prech, and P. Cagas, Observation of fast variations of the helium-ion abundance in the solar wind, Cosmic Res., 52, 25,, 2014.
Zhao, L., T. H. Zurbuchen, and L. A. Fisk, Global distribution of the solar wind during solar cycle 23: ACE observations, Geophys. Res. Lett., 36, L14104, 2009.
Zurbuchen, T. H., and I. G. Richardson, In-situ solar wind and magnetic field signatures of interplanetary coronal mass ejections, Space Sci. Rev., 123, 31, 2006.
Zurbuchen, T. H., L. A. Fisk, G. Gloeckler, and R. von Steiger, The solar wind composition throughout the solar cycle: A continuum of dynamic states, Geophys. Res. Lett., 29, 1352, 2002.

Relativistic electron pitch angle distribution in the Earth's radiation belt

Hong Zhao

Laboratory for Atmospheric and Space Physics and Department of Aerospace Engineering Sciences, University of Colorado at Boulder, Boulder, CO 80302

Reiner Friedel, Yue Chen

Los Alamos National Laboratory, Los Alamos, NM 87545

Abstract

Using data from Energetic Particle, Composition, and Thermal Plasma (ECT) suite onboard Van Allen Probes, a statistical survey of relativistic electron pitch angle distribution (PAD) is performed. By fitting relativistic electron PADs to Legendre polynomials, an empirical model of PADs as a function of L, MLT, electron energy, and geomagnetic activity is developed and some intriguing results are found. Comparing the averaged PADs at different L and MLT during quiet times, the drift-shell-splitting effect can be clearly seen; however, during storm times, the drift-shell-splitting effect appears less significant for MeV electrons, which is possible due to the wave-particle interaction and/or the changes of magnetic field configuration and electron flux radial gradient. During quiet times, we find a dawn-dusk asymmetry of MeV electron PADs, and the averaged PADs for higher energy electrons are much steeper than those of lower energy electrons at dusk sector. For 10s of keV electrons, the region with highly steep PADs is found to be constrained to low L, and as the geomagnetic activity increases, the region with highly steep PADs shrinks. It suggests the presence and effectiveness of plasmaspheric hiss wave scattering inside the plasmasphere.

Keywords: radiation belt electrons, pitch angle distribution, wave-particle interaction

1. Introduction

The relativistic electron pitch angle distribution (PAD) is an important characteristic of radiation belt electrons, which can give information on source and loss processes in a specific region. Many previous studies have focused on the characteristics and evolution of electron PADs in the outer radiation belt [e.g., West et al., 1973; Gannon et al., 2007; Chen et al., 2014] and also some studies have focused on those in the slot region and inner belt [e.g., Lyons and Williams, 1975a, 1975b; Zhao et al., 2014a, 2014b].

Typical PADs in the radiation belt include normal "pancake" PADs, butterfly PADs and flattop PADs (Figure 1). The normal distribution is the most general type of PADs in the outer belt, for which the electron flux peaks at 90° pitch angle and smoothly decreases toward the field-aligned directions. The normal pitch angle distribution is thought to form as a result of the loss to the atmosphere combining with pitch angle diffusion. Inward radial diffusion can also cause the flux peak around 90° due to the conservation of the first two adiabatic invariants. When an electron transports inward, the perpendicular momentum increases more than the parallel component, thus the equatorial pitch angle of electron increase and a more 90°-peaked PAD forms [e.g., Schultz and Lanzerotti, 1974]. The butterfly pitch angle distribution has a minimum flux around 90° pitch angle and a maximum flux near 40°. It is thought to be caused by the drift-shell-splitting effect combined with magnetopause shadowing or strong negative radial flux gradient [e.g., Sibeck et al., 1987; Selesnick and Blake, 2002]. Horne et al. [2005] have also suggested that chorus wave heating could cause butterfly distribution by preferentially heating off-equator electrons. For the flattop pitch angle distribution the electron flux does not vary much for a relatively wide PA range. It can be a

transition between the normal distribution and butterfly distribution, or can be due to strong wave-particle interactions [Horne et al., 2003].

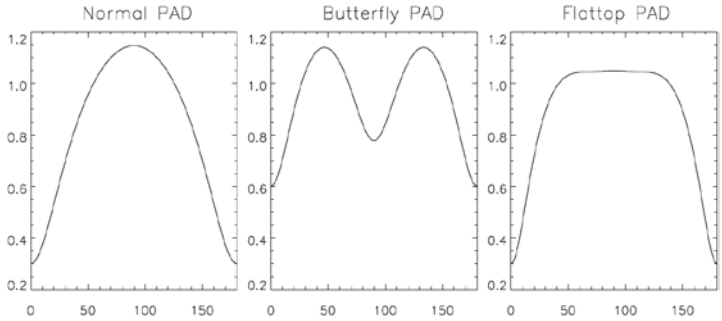

Figure 1. Examples of (left) Normal, (middle) butterfly, and (right) flattop pitch angle distributions.

Apart from these three types of PADs, other PAD types, e.g., cigar, cap, and 90°-minimum PADs (Figure 2), were also found in specific regions as results of different physical processes. For 10s - 100s keV electrons, cigar pitch angle distributions with flux peaking along the direction of local magnetic field were found in the outer radiation belt. It is thought to be related to the tail-like stretching of the night side magnetic field prior to substorms and thus was suggested as an indicator of likely substorm onset [Baker et al., 1978]. The cap PAD (also called head-and-shoulder PAD) has a bump around 90° on top of a normal distribution [e.g., Lyons and Williams, 1975a; Sibeck et al., 1987]. It is found to be present in the outer belt as well as slot region. Lyons and Williams [1975a] showed comparisons between observations and modelling of wave-particle interaction and the agreement between the two suggests that the cap distribution forms as a result of pitch angle scattering caused by the plasmaspheric whistler mode waves in the slot region. However, Sibeck et al. [1987] investigated the cap PAD in the outer belt and suggested that it can be caused by a combination of the drift-shell-splitting effect and a substorm injection or a sudden magnetospheric compression. Recently, Zhao et al. [2014a] reported a new type of PADs of 100s keV electrons in the inner belt and slot region using the observation from Van Allen Probes. This PAD type, called "90°-minimum PAD" here, shows as a Gaussian distribution with a small bite out around 90°. It is generally present in the inner belt and occurs in the slot region during storm time. The 90°-minimum PAD is distinct from the butterfly distribution by location – there is no drift shell splitting effect in the highly dipolar inner belt region - and the maximum flux of 90°-minimum PAD is generally near 70° while butterfly PADs usually has a maximum flux near 40°. The mechanism of the formation of this type of PADs still remains unknown.

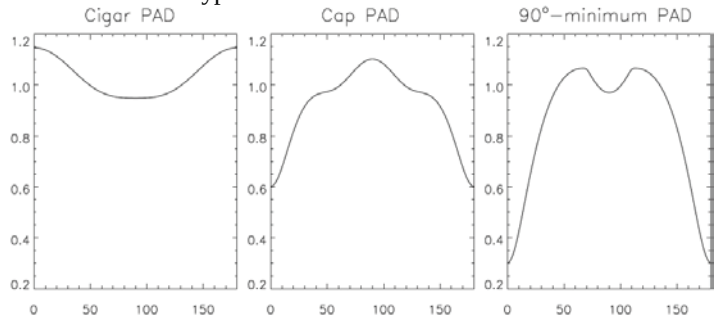

Figure 2. Examples of (left) cigar PAD, (middle) cap PAD, and (right) 90°-minimum PAD.

The electron pitch angle distribution reflects the effects of different physical processes and the competition between them in a specific region. Understanding the evolution of pitch angle distributions can contribute to identifying and understanding of those processes. In this report, using the pitch-angle-resolved electron flux data from Van Allen Probes, we show statistical pictures of electron equatorial PADs as a function of electron energy, L shell, MLT, and geomagnetic activity. Following the method used by Chen et al. [2014], we use Legendre polynomials to fit directional fluxes observed near the magnetic equator using data from Van Allen Probes, and calculate the median and standard deviation of the coefficients. The averaged PADs at different L, MLT, and geomagnetic activity of different energy electrons are compared and some interesting results are found.

2. Data

In this study, pitch-angle-resolved electron flux data from Energetic Particle, Composition, and Thermal Plasma (ECT) suite [Spence et al., 2013] onboard Van Allen Probes are used. The Van Allen Probes, launched on 30 Aug 2012, operate in an elliptical orbit with an inclination of 10° and altitude of ~600 km × 5.8 Re [Kessel et al., 2013]. Since our goal is to investigate the equatorial PADs in the outer radiation belt, we only use data when Van Allen Probes are near the magnetic equator with magnetic latitude < 10°, and propagate the electron PADs to the magnetic equator using T89D magnetic field model [Tsyganenko, 1989]. With the spin axis approximately pointing to the Sun, the spacecraft is spinning with a period of ~12s, which provides good pitch angle coverage during most times and thus provides an ideal data set for pitch angle distribution studies. Since the background subtraction has not yet been done for ECT data, in order to make sure the PADs used in this study are valid, we only include the PADs with counts significantly greater than the background level.

The RBSP-ECT suite consists of three instruments: the Helium Oxygen Proton Electron (HOPE) mass spectrometer, the Magnetic Electron Ion Spectrometer (MagEIS), and the Relativistic Electron Proton Telescope (REPT). MagEIS [Blake et al., 2013] provides high-resolution energetic electron flux measurement with energy range of ~35 – 4000 keV. It contains four independent magnetic electron spectrometers on each spacecraft, one low energy spectrometer (LOW), two medium energy spectrometers (M75 and M35) and a high energy spectrometer (HIGH). The low unit, high unit, and one of the medium units (M75) are mounted with the field of view centered at 75° to the spin axis, while the field of view of another medium unit (M35) is centered at 35° to provide larger PA coverage. In this study, we mainly use the pitch-angle-resolved electron flux data from LOW, M75, and HIGH units of MagEIS (with energy from ~35 keV – 2 MeV). The data are averaged into time bins of 1 min and PA bins of 10°. Only PADs with total square root of counts greater than 50 are used. REPT [Baker et al., 2013] provides high-quality measurement of relativistic electrons with energy from ~ 2 MeV to ~20 MeV. However, since the counts for ultra-relativistic electrons are too low to show clear PADs, only data for electrons with energy from 2 MeV to 3.6 MeV are used in this study. The data are also averaged into 1-min bins and 10° PA bins, and only PADs with total counts greater than 100 are included.

3. Methodology

To construct a statistical model for relativistic electron PADs, the PADs need to be quantified. One way to quantify the PADs is fitting PADs to Legendre polynomials. The electron PADs can be expressed as

$$j(\alpha) = \sum_{n=0}^{\infty} C_n P_n[\cos(\alpha)]$$

where $j(\alpha)$ is the flux of electrons with pitch angle α, $P_n[\cos(\alpha)]$ is the nth-degree Legendre polynomial, and C_n is the corresponding coefficient. The coefficient of each Legendre polynomial can be calculated using the orthogonal property:

$$C_n = \frac{2n+1}{2}\int_0^{\pi} j(\alpha) P_n[\cos(\alpha)]\sin(\alpha)d\alpha$$

The coefficients derived using this equation are then normalized as

$$c_n = \frac{C_n}{C_0}$$

Here C_0 is the actual directionally averaged flux.

Any PAD can be fully represented by a whole set of Legendre polynomials. However, in a statistical model we can only keep finite number of coefficients and the number of coefficients should be kept as small as possible. Based on the previous study [Chen et al., 2014], C_n decreases quickly with increasing n, and including the Legendre polynomials up to 6th-degree is enough to reproduce most observed PADs. Thus we fit measured PADs to a summation of 0th to 6th degree Legendre polynomials. In addition, the electron PADs in the radiation belt are expected to be symmetric with respect to 90° pitch angle. In this study, to give a full coverage on all pitch angles, we average PADs in bins of 10° PA and force them to be symmetric. Since only even-th degree Legendre polynomials are symmetric, we expect $c_n$with odd n to be 0. Thus in our statistical model, only the statistics of c_2, c_4, and c_6 are considered.

The accuracy of our model strongly depends on the accuracy of the fitting results, so we use the PADs that can be well represented by the Legendre polynomials to construct the statistical model. Only good fits with root-mean-square-deviation (RMSD)

$$RMSD = \sqrt{\frac{\sum_n (log(\hat{j}) - log(j))^2}{n}} < 0.05$$

are included in the statistics, where j is the measured flux and $\hat{j}$ is the fitting results. According to our results, most fits are valid. For example, for REPT E=2 MeV electrons, only 10% fits are rejected due to poor fitting. This also validates our fitting method. On the other hand, it is essential to make sure the fitting results represent the real PADs, so only PADs with full PA coverage have been included. PADs with no data points within high PA range [80°, 100°] or low PA range [0°, 20°]/[160°, 180°] are excluded from the statistics.

Example fits of normal, butterfly, and flattop PADs are shown in Figure 3, along with the coefficients c_0 - c_6 and RMSD of each fit. The RMSD overall is very small, showing good fitting results. All coefficients with odd n are 0, which is expected as we impose symmetry of PADs, and this also validates our fitting method. As shown in Figure 3, normal PADs usually have large negative c_2 with near zero c_4, and butterfly PADs have large negative c_4 with negligible c_2, while flattop PADs are combinations of these two types, for which c_2 and c_4 are both negative.

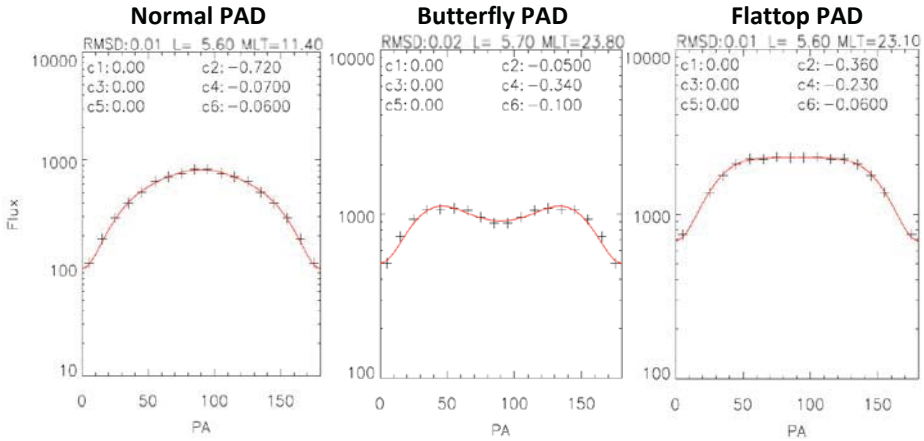

Figure 3. Example fits of normal, butterfly, and flattop PADs. Black dots are data and red curves are fitting results using Legendre polynomials. The RMSD for each fit is shown on the top of each panel, and the coefficients of Legendre polynomials are shown in each panel as well.

Based on this fitting method, a statistical relativistic electron equatorial PAD model is constructed as a function of L, MLT, geomagnetic activity and electron energy. The model includes 26 L bins from L=1 to L=6 with $\Delta L = 0.2$ and 12 MLT bins with $\Delta MLT = 2$. Note that for ~MeV and more energetic electrons our model only includes L shells down to L=3, since in the slot region and inner belt the fluxes of these electrons are usually too low to show clear PAD pattern. The geomagnetic activity, represented by the geomagnetic indices Dst and Kp, is divided into three levels. The data of ~ 35 keV – 2 MeV electrons from MagEIS and 2 MeV – 3.6 MeV electrons from REPT are used to construct the model. The medians and standard deviations of c_2, c_4 and c_6 are derived and recorded in each L and MLT bin for electrons with a specific energy under a specific geomagnetic condition. The averaged PADs are also generated using medians of c_2, c_4 and c_6 at each L shell, MLT, geomagnetic activity level for electrons with a specific energy.

4. Results

Using the method described in section 3, we construct a statistical model for electron PADs as a function of L, MLT, geomagnetic activity, and electron energy using data from Van Allen Probes. In this section, we will show the medians of these coefficients and averaged PADs as well as their dependence on L, MLT, geomagnetic activity and electron energy. Some interesting results are shown and discussed.

4.1. The dependence of relativistic electron pitch angle distributions on L, MLT, and geomagnetic activity

Model results for E ~ 740 keV electrons during quiet time (Dst > -20 nT, top panels) and active time (-20 nT > Dst > -50 nT, bottom panels) are shown in Figure 4 using data from MagEIS. The day-night asymmetry can clearly be seen from Figure 4. The coefficient c_2 is more negative at dayside and c_4 is more negative at nightside, indicating PADs strongly peak at 90° at dayside while butterfly distributions are generally present at nightside at higher L shells. Also, the coefficients show the expected dawn-dusk symmetry, which also validates our model results. Figure

5 shows the averaged PADs at L=5, 5.5, and 5.8 at different MLT, while the results during quiet times are shown in black curves and those during storm time are shown in red curves. Comparing the averaged PADs at different MLT, the butterfly PADs are present at MLT=0 at L=5.5 and 5.8 during quiet times while at MLT=12 the PADs are strongly peaked at 90°. This asymmetry is expected from the drift-shell-splitting effect resulting from asymmetric magnetic field. However, during active times, the drift-shell-splitting effect appears less significant. Also, comparing the results during quiet times and active times, the PADs are steeper at all MLTs during storm times. These phenomena have also been reported by Chen et al. [2014] using data from CRRES, Polar, and LANL-97A. They could be due to the strong wave-particle interactions during active times. The existence of extra sources of electrons with high pitch angles or losses of low pitch angle electrons during storm times could produce a steeper PAD and thus alter the PADs governed by drift-shell-splitting effect during quiet times. This could also be caused by the magnetic field configuration changes and/or the electron flux radial gradient changes during active times.

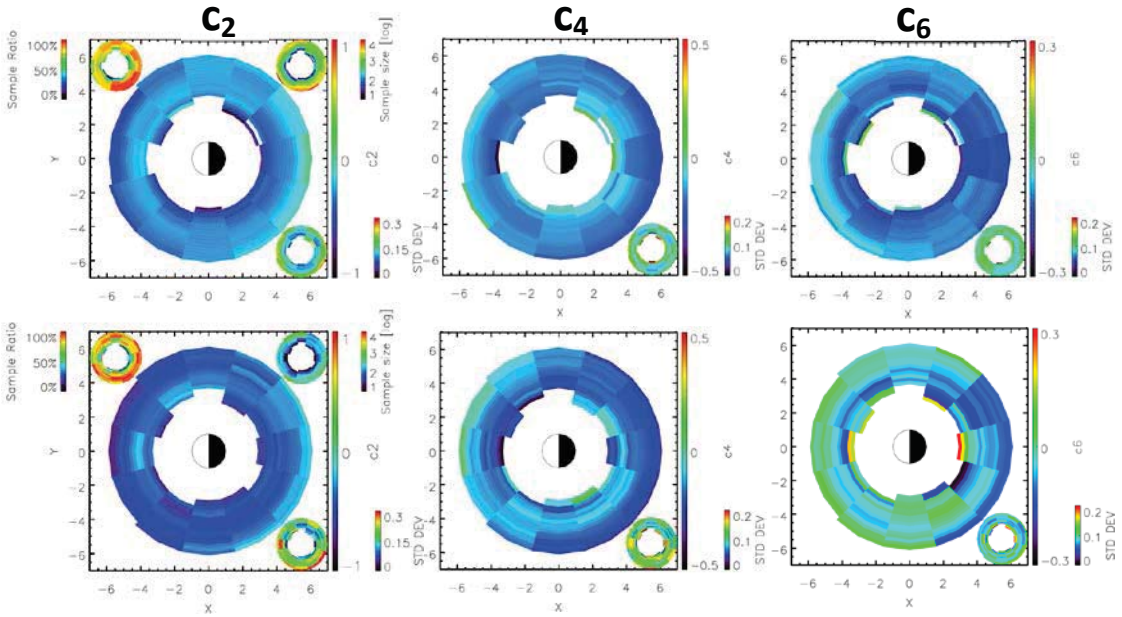

Figure 4. Medians of (left) c_2, (middle) c_4, and (right) c_6 as a function of L and MLT for E ~ 740 keV electrons during quiet times (Dst > -20 nT, top panels) and disturbed times (-20 nT > Dst > -50 nT, bottom panels). The ratios of good fits to total PADs are shown on the top left corner of left panels, and the sample sizes are shown on the top right corner. The standard deviation in each bin is also shown in the bottom right corner of each panel.

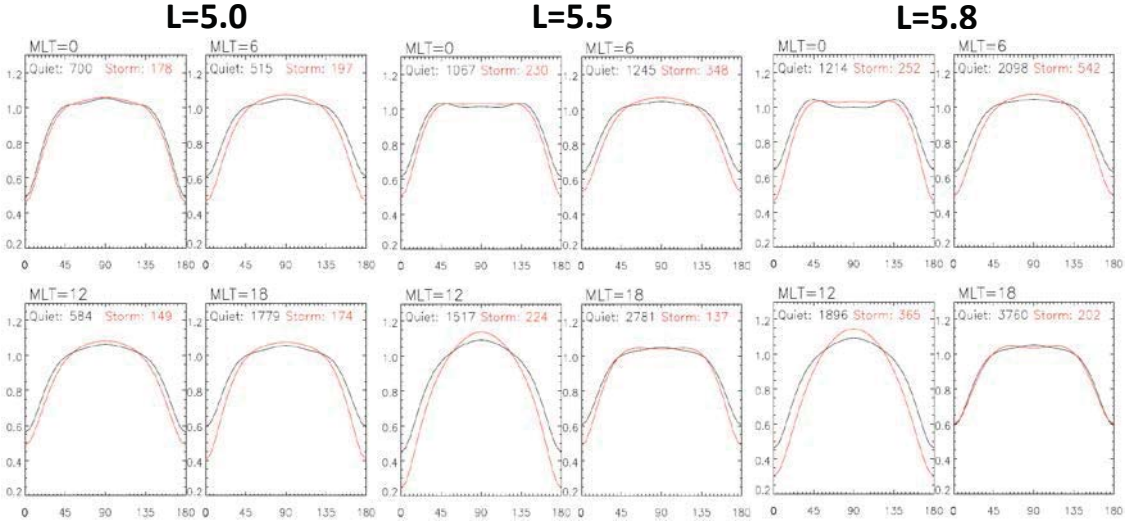

Figure 5. The averaged PADs of ~ 740 keV electrons at L= (left) 5.0, (middle) 5.5 and (right) 5.8 at different MLT.

4.2. The dependence of relativistic electron pitch angle distributions on electron energy

The dependence of relativistic electron PADs on energy is also investigated using data from REPT. Figure 6 shows the comparison of model results between 2 MeV (top panels) and 3.6 MeV (bottom panels) electrons during quiet times (Dst > -20 nT). The day-night asymmetry is still very clear, indicating the drift-shell-splitting effect. However, a surprising result is the presence of a dawn-dusk asymmetry. The coefficient c_2 is more negative at duskside while c_4 is more negative at dawnside, indicating that PADs are more anisotropic at dusk than at dawn. The plots of averaged PADs of electrons with E=2, 2.3, 2.85 and 3.6 MeV at L=3.5, 4.5 and 5.5 at different MLTs (Figure 7) confirm this point. At three L shells shown in Figure 7, the asymmetry of PADs between dawn and dusk can be clearly seen for electrons with different energies. Comparing to PADs at dawnside, PADs at duskside are much steeper and this trend is more significant for electrons with higher energies. At L=3.5, the averaged PADs of electrons with different energies are very similar; at L=4.5, the dispersion of PADs of electrons with different energies occurs at all MLTs except MLT=6; while at L=5.5, the PADs of electrons with different energies also show significant differences at noon and dusk. The differences in PADs at dawn and dusk sectors could be an indicator of the presence of EMIC waves, which are mostly present at dusk sector and plumes of plasmasphere. EMIC waves can cause losses of MeV and more energetic electrons with low pitch angles through pitch-angle scattering, and for electrons with higher energies the wave-particle interaction can occur at higher pitch angles [e.g., Li et al., 2007].

However, it is hard to determine if this dawn-dusk asymmetry is physically real or is just caused by sampling since the Van Allen Probes were at different local time sectors at different times. We investigate this by considering plots (Figure 8) of flux ratios of 90° pitch angle to 25° pitch angle for electrons with energy of 2 MeV and 3.6 MeV as a function of L and time from Sep 2012 to July 2014. Spin-averaged fluxes of 2 MeV electrons are also shown along with the corresponding position of the apogee of Van Allen Probes during this time period. It is clear that along with the electron flux variations, the ratios between 90° PA and 25° PA electron fluxes for 2 MeV and 3.6 MeV electrons varied accordingly, while the flux ratios of 3.6 MeV electrons are higher than 2 MeV electrons during these variations, indicating steeper PADs for 3.6 MeV electrons than 2 MeV electrons. At the beginning of mission, Van Allen Probes were at dawn sector, during which time only a few intense storms occurred. However, as the Van Allen Probes moved into the dusk sector, geomagnetic storms occurred more often, as did the changes of flux ratios of relativistic electrons with different PAs. Thus the averaged PADs in dusk sector highly peaked at 90°, while in dawn sector the averaged PADs are more isotropic. It is possible that the dawn-dusk asymmetry in relativistic electron PADs results from different events occurred at different times. However, we still cannot rule out the possibility of EMIC wave scattering. Detailed further work is needed to distinguish between the two scenarios.

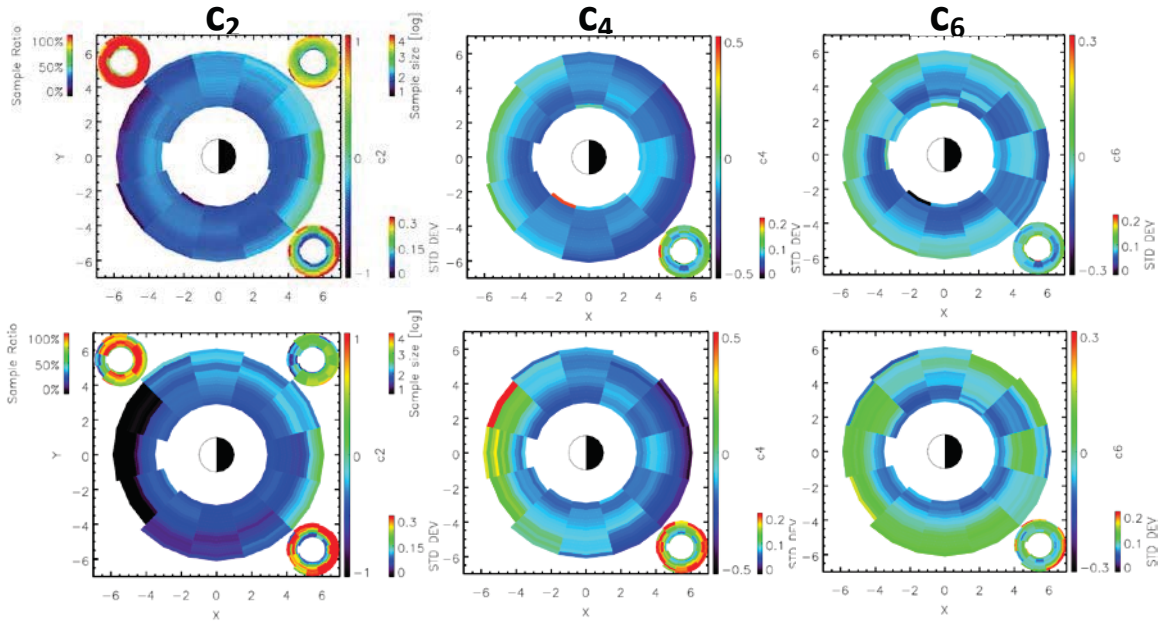

Figure 6. Medians of (left) c_2, (middle) c_4, and (right) c_6 as a function of L and MLT for E= (top panels) 2 MeV and (right panels) 3.6 MeV electrons during quiet times (Dst > -20 nT). Figure formats are the same with Figure 4.

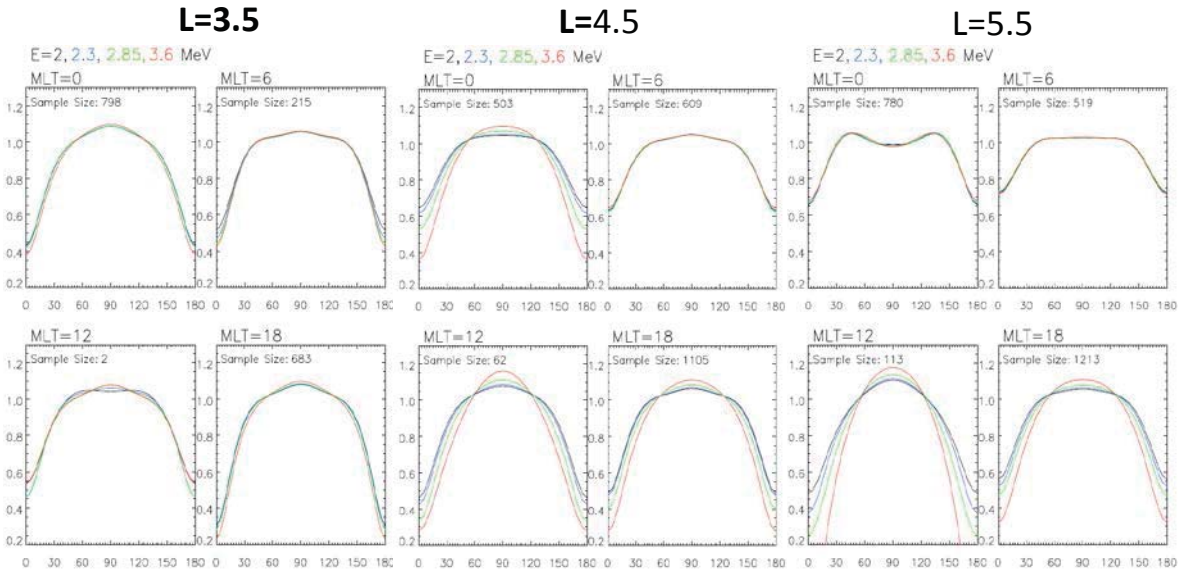

Figure 7. The averaged PADs of E=2 MeV (black curves), 2.3 MeV (blue curves), 2.85 MeV (green curves) and 3.6 MeV (red curves) electrons at L= (left) 3.5, (middle) 4.5 and (right) 5.5 at different MLT during quiet times (Dst > -20 nT).

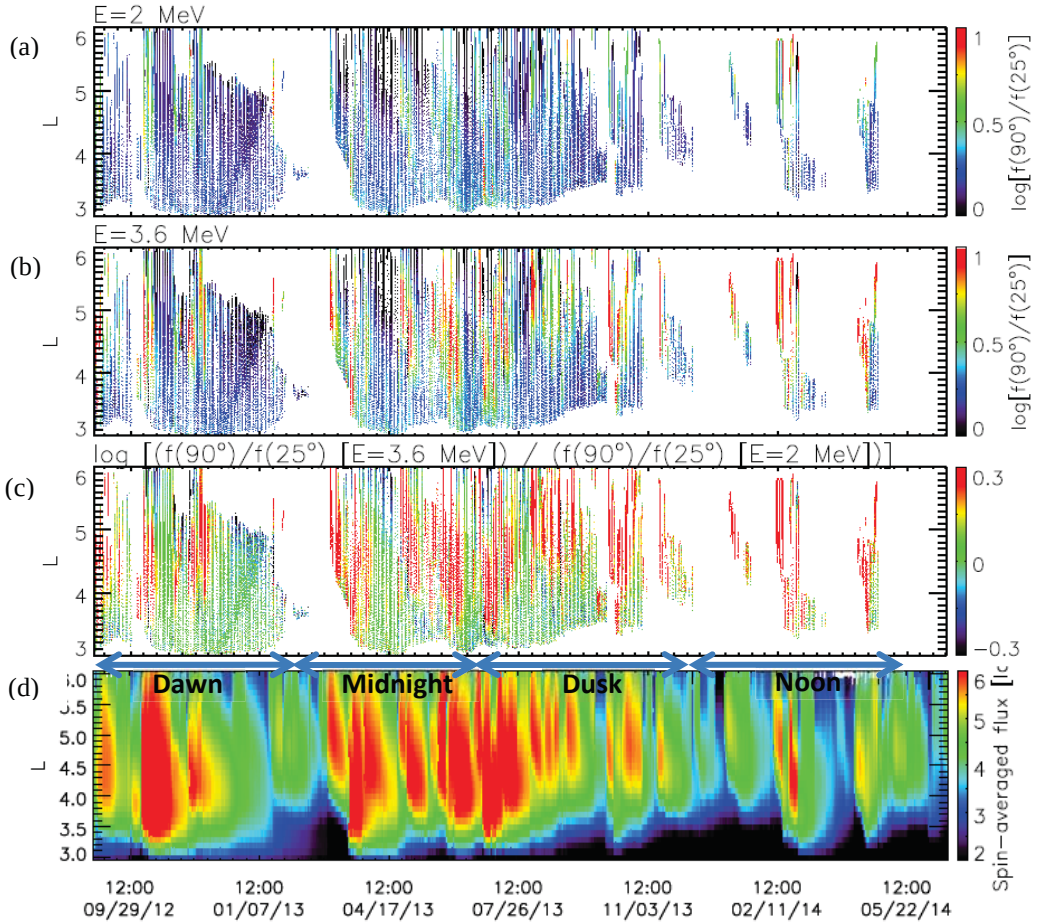

Figure 8. The flux ratio of electrons with pitch angle of 90° to 25° for (a) 2 MeV and (b) 3.6 MeV electrons, (c) the ratio between the two, and (d) spin-averaged flux of 2 MeV electrons.

4.3. Pitch angle distributions of 10s of keV electrons under different geomagnetic activities

The pitch angle distributions of MeV electrons have attracted a lot of attention. However, the pitch angle distribution of electrons with lower energies, e.g., 10s of keV, received little attention in the past mainly due to limited availability of good quality data. The MagEIS instrument provides pitch-angle-resolved data for electrons with energy down to ~ 35 keV, which give us a good opportunity to study the PADs of 10s of keV electrons and construct a statistical PAD model with a wider energy range. Figure 9 shows the model results for ~ 35 keV electrons under low (Kp ≤ 1+, left panels), medium (1+ < Kp ≤ 3+, middle panels), and high (Kp > 3+, right panels) activities respectively. During quiet times with Kp ≤ 1+, inside L~5 the coefficient c_2 is much more negative while c_4 and c_6 are almost zero, indicating highly 90°-peaked PADs. As the geomagnetic activity gets more intense, the region where c_2 is highly negative shrinks to lower L shells. The highly anisotropic PADs at lower L shells are likely to be caused by the plasmaspheric hiss waves which are generally present inside the plasmasphere. The plasmaspheric hiss waves are very effective for electrons with relatively lower energies [e.g., Abel and Thorne, 1998]. As the geomagnetic activity gets more intense, the enhanced convection electric field brings charged particles to dayside through E×B drift and shrinks the plasmasphere, thus the region with highly 90°-peaked PADs are also confined to lower L regions.

In addition, the HOPE instrument onboard Van Allen Probes provides pitch-angle-resolved fluxes of plasma ions and electrons from eV to 10s of keV energy range. With HOPE data, detailed PADs of electrons with even lower energies can be revealed and the effect of plasmaspheric hiss waves and convection electric field can be further investigated. Thus we plan future work on keV electron PADs using data from HOPE.

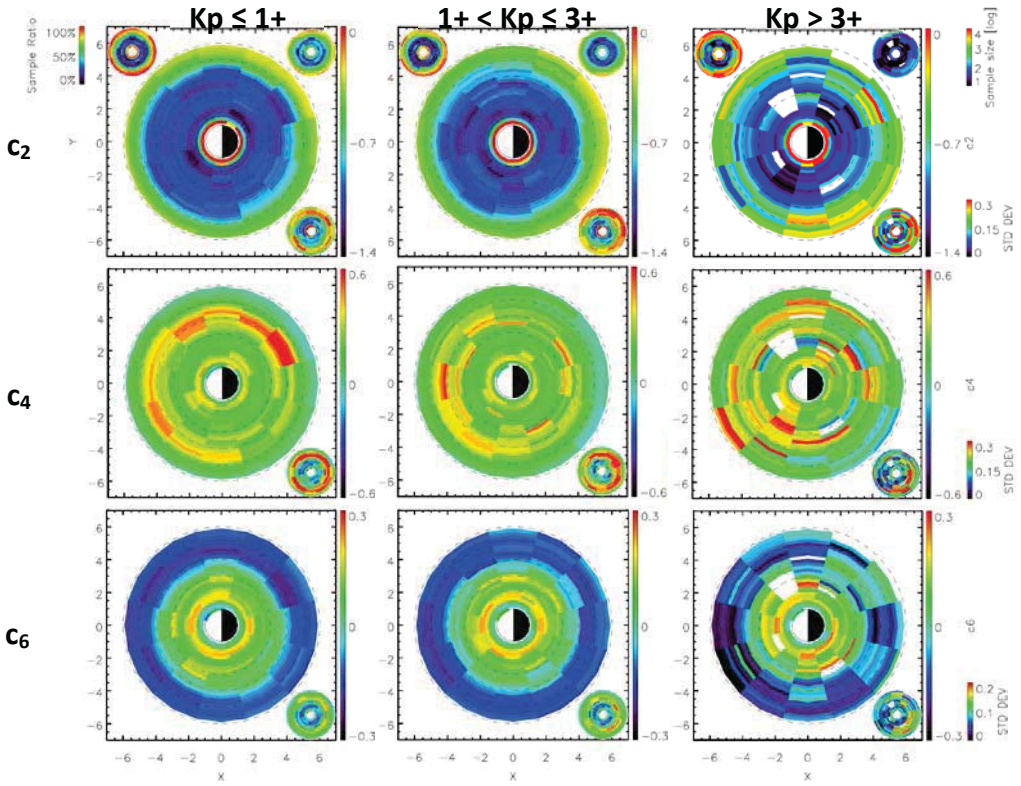

Figure 9. Medians of (top) c_2, (middle) c_4, and (bottom) c_6 as a function of L and MLT for E ~ 35 keV electrons under low (Kp ≤ 1+, left), medium (1+ < Kp ≤ 3+, middle), and high (Kp > 3+, right) activities.

5. Conclusions

We perform a statistical study of relativistic electron pitch angle distribution using data from ECT suite onboard Van Allen Probes. An empirical model of radiation belt electron pitch angle distribution as a function of L, MLT, electron energy, and geomagnetic activity was developed. The averaged PADs at different L, MLT, geomagnetic activity, and of different energy electrons are compared producing some surprising results that can be summarized as follows:

1) Comparing the averaged PADs at different MLT during quiet times, the highly 90°-peaked PADs and butterfly PADs can be clearly seen at noon and midnight respectively at higher L shells, which indicates that the drift-shell-splitting effect governs the relativistic electron PADs during quiet times. However, during storm times the drift-shell-splitting effect appears less significant for MeV electrons and the PADs of MeV electrons become steeper at all MLTs. These are possibly due to the wave-particle interaction, but also could be caused by the changes of magnetic field configuration and/or electron flux radial gradient.

2) For MeV electrons, the dawn-dusk asymmetry in PADs can be clearly seen during quiet times: the averaged PADs at dusk sector are steeper than those at dawn sector, and the differences become more significant for higher energy electrons. One possible explanation is the pitch angle scattering caused by EMIC waves, which exist at the dusk sector and plasmasphere plumes and are more effective for higher energy electrons. However, it is also possible that the Van Allen Probes were at different local time sectors at different time, which causes the statistical differences in PADs. Future work is still needed to reveal the physics behind it.

3) For 10s of keV electrons, the region with highly peaked PADs is found to be constrained to lower L shells, and during active times this region shrinks. This is consistent with pitch angle scattering caused by plasmaspheric hiss waves which only exist inside the plasmasphere.

References

Abel, B. and R. M. Thorne (1998), Electron Scattering Loss in Earth's Inner Magnetosphere 1. Dominant Physical Processes, J. Geophys. Res., 103(A2), 2385-2396.

Baker, D. N., P. R. Higbie, E. W. Hones Jr., and R. D. Belian (1978), High-resolution energetic particle measurements at 6.6 Re 3. Low-energy electron anisotropies and short-term substorm predictions, J. Geophys. Res., 83 (A10), 4863-4868, doi:10.1029/JA083iA10p04863.

Baker, D. N., et al. (2013), The Relativistic Electron-Proton Telescope (REPT) Instrument on Board the Radiation Belt Storm Probes (RBSP) Spacecraft: Characterization of Earth's Radiation Belt High-Energy Particle Populations, Space Science Reviews, doi:10.1007/s11214-012-9950-9.

Blake, J. B., et al. (2013), The magnetic electron ion spectrometer (MagEIS) instruments aboard the radiation belt storm probes (RBSP) spacecraft, Space Sci. Rev., doi:10.1007/s11214-013-9991-8.

Chen, Y., R. H. W. Friedel, M. G. Henderson, S. G. Claudepierre, S. K. Morley, and H. Spence (2014), REPAD: An empirical model of pitch angle distributions for energetic electrons in the Earth's outer radiation belt, J. Geophys. Res. Space Physics, 119, 1693–1708, doi:10.1002/2013JA019431.

Funsten, H. O., et al. (2013), Helium, Oxygen, Proton, and Electron (HOPE) Mass Spectrometer for the Radiation Belt Storm Probes Mission, Space Sci. Rev., doi:10.1007/s11214-013-9968-7.

Gannon, J. L., X. Li, and D. Heynderickx (2007), Pitch angle distribution analysis of radiation belt electrons based on Combined Release and Radiation Effects Satellite Medium Electrons A data, J. Geophys. Res., 112, A05212, doi:10.1029/2005JA011565.

Horne, R. B., N. P. Meredith, R. M. Thorne, D. Heynderickx, R. H. A. Iles, and R. R. Anderson (2003), Evolution of energetic electron pitch angle distributions during storm time electron acceleration to megaelectronvolt energies, J. Geophys. Res., 108(A1), 1016, doi:10.1029/2001JA009165.

Horne, R. B., R. M. Thorne, S. A. Glauert, J. M. Albert, N. P. Meredith, and R. R. Anderson (2005), Timescale for radiation belt electron acceleration by whistler mode chorus waves, J. Geophys. Res., 110, A03225, doi:10.1029/2004JA010811.

Kessel, R. L., N. J. Fox, and M. Weiss (2013), The Radiation Belt Storm Probes (RBSP) and space weather, Space Sci. Rev., 179(1-4), 531–543, doi:10.1007/s11214-012-9953-6.

Li, W., Y. Y. Shprits, and R. M. Thorne (2007), Dynamic evolution of energetic outer zone electrons due to wave-particle interactions during storms, J. Geophys. Res., 112, A10220, doi:10.1029/2007JA012368.

Lyons, L. R., and D. J. Williams (1975a), The quiet time structure of energetic (35-560 keV) radiation belt electrons, J. Geophys. Res., 80 (7), 943-950.

Lyons, L. R., and D. J. Williams (1975b), The storm and poststorm evolution of energetic (35-560 keV) radiation belt electron distributions, J. Geophys. Res., 80 (28), 3985-3994.

Schulz, M., and L. Lanzerotti (1974), Particle Diffusion in the Radiation Belts, Springer, New York.

Selesnick, R. S., and J. B. Blake (2002), Relativistic electron drift shell splitting, J. Geophys. Res., 107(A9), 1265, doi:10.1029/2001JA009179.

Sibeck, D. G., R. W. McEntire, A. T. Y. Lui, R. E. Lopez, and S. M. Krimigis (1987), Magnetic field drift shell splitting: Cause of unusual dayside particle pitch angle distributions during storms and substorms, J. Geophys. Res., 92, 13,485–13,497, doi:10.1029/JA092iA12p13485.

Spence, H. E., et al. (2013), Science goals and overview of the energetic particle, composition, and thermal plasma (ECT) suite on NASA's radiation belt storm probes (RBSP) mission, Space Sci. Rev., doi:10.1007/s11214-013-0007-5.

Tsyganenko, N. A. (1989), A magnetospheric magnetic field model with a warped tail current sheet, Planet. Space Sci, 37, 5.

West, H. I., R. M. Buck, and J. R. Walton (1973), Electron pitch angle distributions through the magnetosphere as observed on Ogo5, J. Geophys. Res., 78, 1064–1081.

Zhao, H., X. Li, J. B. Blake, J. F. Fennell, S. G. Claudepierre, D. N. Baker, A. N. Jaynes, D. M. Malaspina, and S. G. Kanekal (2014a), Peculiar pitch angle distribution of relativistic electrons in the inner radiation belt and slot region, Geophys. Res. Lett., 41, doi:10.1002/2014GL059725.

Zhao, H., X. Li, J. B. Blake, J. F. Fennell, S. G. Claudepierre, D. N. Baker, A. N. Jaynes, and D. M. Malaspina (2014b), Characteristics of pitch angle distributions of 100s keV electrons in the slot region and inner radiation belt, submitted to J. Geophys. Res..

Electron and Ion Heating in the Solar Wind Via Whistler Turbulence

R. Scott Hughes

University of Southern California, Los Angeles, CA 90089

S. Peter Gary

Space Science Institute, Boulder, CO 80301

Abstract

Three-dimensional particle-in-cell (PIC) simulations are carried out for a collisionless, homogeneous, magnetized proton-electron plasma in order to investigate the interaction between a spectrum of relatively isotropic whistler fluctuations with the ion population, relative to the interaction of the fluctuations with the electron population. In particular the total amount of heating of the two species is compared as the wavelengths of the initial fluctuations imposed on the system are varied. It is found that as the initial wavelengths increase, the damping rate of the fluctuations decreases. Furthermore the magnitude of electron heating decreases while the magnitude of ion heating increases with increasing wavelength. These results provide support for the hypothesis that observed perpendicular ion heating in the solar wind can, at least in part, be explained by interactions between ions and whistler turbulence.

Keywords: Ion Heating, Whistler Turbulence, Solar Wind

1. Introduction

Assuming that the ion's magnetic moment is conserved as it travels away from the sun, the ion population should form a cold beam structure, such that $T_{i\parallel} \gg T_{i\perp}$, as the solar wind plasma expands in interplanetary space. Here the subscripts $\parallel, \perp$ represent directions parallel, perpendicular to the background magnetic field $\boldsymbol{B}_0$ respectively. At 1 AU, this structure is not observed. In fact most in situ measurements show that the ion temperature is relatively isotropic at 1 AU [*Cranmer*, 2014], demonstrating that the ion magnetic moment is not conserved. This implies that there are mechanisms operating, during the solar wind plasma's journey, which heat the ion population in the direction perpendicular to the ambient magnetic field.

Many explanations for this behavior have been proposed, primarily with the use of Magnetohydrodynamic (MHD) theory, however none of these explanations can completely describe the physics being observed. The true underlying mechanisms which act on the ion population remain unresolved. Recent research has been conducted on the interaction between whistler turbulence and ion heating [*Saito and Nariyuki*, 2014]. In this case the mechanism acting on the ions is one which operates on the microscopic scale, as opposed to the MHD scale. Little investigation has been conducted on this relationship in the past as whistler waves were thought only to have an effect on the electron population, with frequencies typically much higher than that of the ion cyclotron frequency. However in this recent paper it was noted that highly obliquely propagating whistler waves possess large electrostatic components with phase speed comparable to that of the ion thermal speed. These waves have the appropriate characteristics to resonate with a large fraction of the ion population which can potentially lead to bulk ion heating.

In this paper we look closer at the relationship between whistler turbulence, ion heating, and electron heating. We wish to characterize the conditions under which the fluctuations interact with the electrons versus the conditions under which they interact with the ions, and how these conditions influence the final state of the system.

2. Background

There are many proposed explanations as to how ions can be heated as they travel away from the sun. MHD analysis suggests heating of ions through resonance of left hand polarized Alfvén waves with the ion cyclotron orbits. This model is flawed in the sense that measurements suggest that the required resonance conditions aren't present as the frequency of the Alfvén waves is far below that of the inferred ion cyclotron frequencies. One attempt to rectify this discrepancy is through the concept of turbulent cascade which can allow for a flow of energy to higher frequency Alfvén waves. This cascade proceeds primarily in the perpendicular direction however, while the necessary resonant conditions require high frequency parallel propagating Alfvén waves. Another possibility, derived from the large scale (MHD) viewpoint, is that turbulence generates inhomogeneities in the plasma, such as velocity shears, which can result in instabilities and generation of ion cyclotron fluctuations which can heat the ions via resonance.

In a recent publication an explanation for perpendicular ion heating in the solar wind was proposed through the aid of the microscopic (kinetic) viewpoint [*Saito and Nariyuki*, 2014]. In this scenario perpendicular ion heating occurs via Landau resonance with the electrostatic fluctuations of whistler waves of character $k_\perp c/\omega_e > 1$, $k_\parallel c/\omega_e \ll 1$. Saito used particle in cell (PIC) simulations on a 2D spatial grid to investigate this scenario. In this case the results did not show bulk heating of the ion population, but did show local accelerations of individual ions in regions of the domain where there were strong electrostatic fluctuation components. Continuing on the work of Saito and Nariyuki, we extend this investigation to a fully 3D domain, and vary the wavelengths of the initial modes imposed on the system in order to better understand the necessary conditions which will result in bulk ion heating.

3. Methodology

In this investigation we used a 3D relativistic PIC code [*Wang et al*., 1995] to investigate the interactions of whistler turbulence with the electron, proton species of a collisionless, homogeneous, magnetized plasma. In this case all three spatial dimensions are accessible to the plasma, as well as the three velocity dimensions. This allows for a far larger region of phase space to be available for perpendicular interactions between the fluctuations and the ion population, relative to a 2D simulation.

The whistler modes typically represented in these simulations have the property $\Omega_i \ll \omega_r \ll \Omega_e$, where $\Omega_{i,e}$ is the ion, electron cyclotron frequency respectively and ω_r is the real frequency of the fluctuation. From a logical point of view, as one shifts the frequencies of the fluctuations toward one end of this spectrum, there should be more interaction between the fluctuations and the corresponding plasma population. In order to test this hypothesis, we conducted a series of simulations. In this series we held the total initial fluctuation energy of the waves, ϵ, and the plasma β constant, with values of 0.1 and 0.05 respectively, while we varied the wavelengths of the initial fluctuations.

The initial fluctuations were loaded at the onset of the simulation with the property that they were parallel\perpendicular combinations of the three largest modes that fit in the system. With each simulation we doubled the domain size in each direction, and thus allowed for larger initial wavelengths. The number of cells in each simulation was 256^3, 512^3, and 1024^3, with corresponding principal wavenumbers $k_{\perp\backslash\parallel} c/\omega_e = 0.245, 0.123,$ and 0.0614 respectively. Loading a relatively isotropic spectrum of waves, the total number of initial normal modes was 150 in each case. The mass ratio m_i/m_e was chosen to be 400. The reason for selecting an artificial mass ratio was to speed up the dynamics of the ions in order to run the simulation in a reasonable number of simulation steps. It is assumed that the physics should not change as long as $m_i \gg m_e$ apart from a linear scaling of the relative magnitude of the ion response.

As the majority of previous simulations of this type dealt with the characterization of the electron population subjected to whistler turbulence, the electron initial velocities were calculated in a way that generated currents consistent with the initially loaded waves, while the appropriate initialization of the ion population was assumed to be negligible. In our case, however, care was taken to initialize the ions with velocities consistent with the initial waves as well. These drift velocities, calculated from cold plasma wave theory, could be used in conjunction with Ampère's law to calculate more accurate initial velocities for the electrons by allowing for both the ions and electrons to contribute to the current required by the initial waves. In the final step of the velocity initialization the calculated drift velocities for each species were superimposed on a Maxwellian distribution of thermal velocities.

4. Results

Figure 1 shows the magnetic fluctuation spectrum at three simulation times for each case. The spectrum is reduced along one of the perpendicular directions so that the 2D plot shows the cumulative fluctuation energy at each wavenumber in the direction parallel to the magnetic field versus each wave number in the remaining principal perpendicular direction. In each case the relatively isotropic initial spectrum cascades its fluctuation energy primarily to quasi-perpendicular modes. This is a well-established characteristic of whistler turbulence called an anisotropic forward cascade. This cascade results in highly obliquely propagating modes that have the potential to influence the perpendicular velocities of the ions. The magnitude of the cascade varies greatly between the three runs. As the smaller domain reaches much larger wavenumbers than the larger domain, the scale length of the waves approaches that of the electron inertial length. In the case of the larger domain, the bulk of the energy remains outside the range of electron scale lengths. With less interaction with the electron population the fluctuations damp out much slower and more fluctuation energy remains in the system at the end of the simulation. It is apparent that the cascade\damping process is incomplete in the 1024^3 case at $t\omega_e = 2000$. It is also apparent that as the initial wavelengths are increased, less energy is cascaded in the parallel direction. This results in a higher energy density of oblique modes with which the ions can resonate.

Figure 2 compares the characteristics of the ion, electron parallel and perpendicular temperatures as a function of time. Panel 2(d) includes curve fits to the relatively noisy data of the 512^3 and 1024^3 cases. The fits take the form $y = 1 + a[1 - \exp(-bx)]$ and help reveal the asymptotic character of the ion perpendicular temperature. The fitting parameters are presented in table 1. The first four panels of this figure confirm earlier simulation results that whistler turbulence preferentially heats electrons in directions parallel to $\boldsymbol{B}_0$ [*Saito et al*., 2008; *Gary et al*., 2012 *Chang et al*., 2013], and preferentially heats ions in directions perpendicular to the background magnetic field [*Saito and Nariyuki*, 2014]. Comparison of panels (a) and (d) of Figure 1 shows a new result, that the longer wavelength whistler turbulence associated with larger simulation boxes provides less dissipative energy to the electrons but more such energy to the ions. Furthermore, Figure 1(e) shows that, for these three simulations, the total dissipation of the magnetic field fluctuations decreases as the simulation box size (and the overall wavelengths of the turbulence) increases. This is consistent with Fig. 7(b) of *Saito et al.* [2008] which shows linear theory damping of whistlers at quasi-perpendicular propagation decreasing as wavelengths increase. The linear theory damping is due to the Landau wave-particle resonance, and we infer that the same mechanism is heating the electrons and the ions in our simulations although nonlinear processes certainly contribute to the heating as the fluctuation amplitudes increase [e.g., *Chang et al*., 2014].

Figure 3 illustrates the reduced electron parallel velocity distributions and ion perpendicular velocity distributions at selected times for each of the three simulations. The figures show that the transfer of fluctuation energy to both the electrons and ions is indeed a heating process, because the late-time velocity distributions of both species for the most part retain their thermal, Maxwellian-like character even as they gain energy. The primary late-time departures from Maxwellian forms are on the electron parallel velocity distributions in the presence of enhanced high-speed "tails" for the runs at 256^3 and 512^3. This feature is a typical electron response to obliquely propagating whistlers at $\beta_e \ll 1$, and is discussed in detail in *Chang et al.* [2013].

5. Conclusions

We have used three-dimensional, fully kinetic particle-in-cell simulations to examine how decaying whistler turbulence in a low-β collisionless plasma dissipates energy on both electrons and protons. Our computations confirm previous results showing electron heating is preferentially parallel to the background magnetic field $\boldsymbol{B}_0$, and ion heating is preferentially perpendicular to $\boldsymbol{B}_0$. The new results here are that larger simulation boxes and longer initial whistler wavelengths yield weaker electron heating, stronger ion heating, and weaker overall dissipation. The ion heating in the case of large initial wavelengths is of smaller magnitude than the electron heating in the case of small initial wavelengths. This accounts for the weaker dissipation in the large domain runs.

Due to the fact that in the case of large initial wavelengths there is far less electron heating and corresponding fluctuation dissipation, more time is available for the ions to interact with the fluctuations before they damp out. The outcome of this is made apparent in figure 2(d) where the ion heating plateau's quickly for the smaller domain runs, however continues to rise in the largest domain simulation. In the case of smaller initial wavelengths the potential for significant ion heating is present, as there is fluctuation energy propagating quasi-perpendicularly to the background magnetic field; however the electrons consume the fluctuation energy at a high rate in this case. The relatively slow dynamics of the ions do not have sufficient time to interact with the fluctuations before the spectrum has dissipated to magnitudes too low to provide significant heating of the ion population. It would be interesting to

study the evolution of proton and electron temperature in an open system where the fluctuation energy is held in steady state for an extended period of time by allowing for a source of fluctuation energy at long wavelengths, while the sink takes the form of electron heating at small wavelengths created through the cascade process. Such a study would allow for an appropriate direct comparison between the final state of the ion temperature in the simulation and observed ion temperatures in the solar wind.

References

Chang, O., Gary, S. P., Wang, J., "Whistler turbulence and variable electron beta: Three-dimensional particle-in-cell simulations", J. Geophys. Res., 118, 2824, 2013.

Chang, O., Gary, S. P., Wang, J., "Energy dissipation by whistler turbulence: Three-dimensional particle-in-cell simulations", Phys. Plasmas, 21, 052305, 2014.

Cranmer, S., "Ensemble simulations of proton heating in the solar wind via turbulence and ion cyclotron resonance", Ap. J. Supplement Series, in press, 2014.

Gary, S. P., Chang, O., Wang, J., "Forward cascade of whistler turbulence: Three-dimensional particle-in-cell simulations", Ap. J., 755, 142, 2012.

Saito, S., Nariyuki, Y., "Perpendicular ion acceleration in whistler turbulence", Phys. Plasmas, 21, 042303, 2014.

Saito, S., Gary, S. P., Ki, H., Narita, Y., "Whistler turbulence: Particle-in-cell simulations", Phys. Plasmas, 15, 102305, 2008.

Wang, J., Liewer, P., Decyk, V., "3D electromagnetic plasma particle simulations on a MIMD parallel computer", Comput. Phys. Commun., 69, 306, 1995.

Table 1: Fitting parameters for the curve fits to ion perpendicular temperature profiles presented in figure 2(d).

Domain Size	a	b
512^3	0.092	0.0023
1024^3	0.240	0.0011

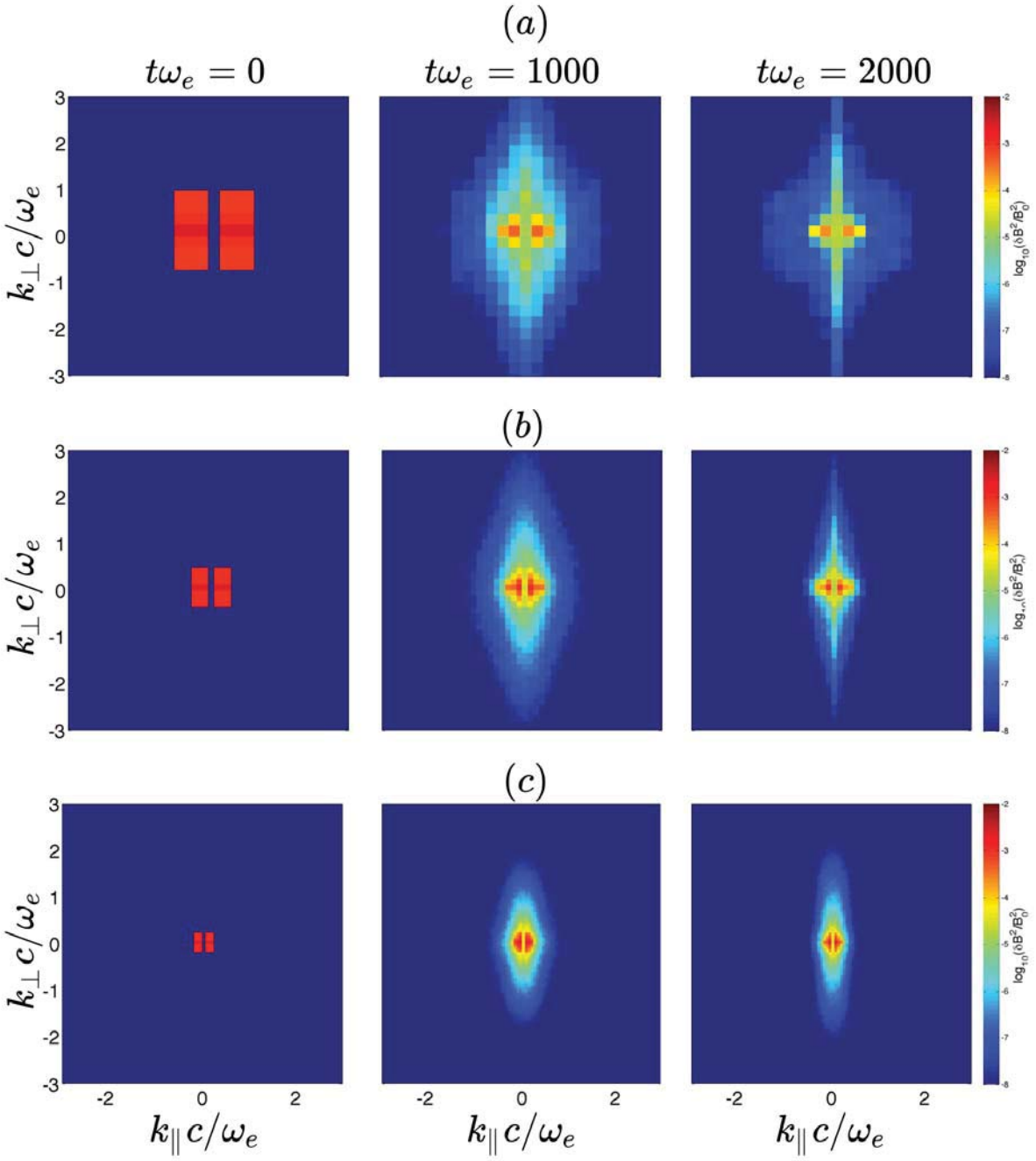

Figure 1: Magnetic fluctuation energy spectrum, $log_{10}(|\delta \boldsymbol{B}|^2/B_0^2)$, as a function of parallel and perpendicular wavenumber, reduced across the third principal direction, at three simulation times for domain size: (a) 256^3, (b) 512^3, (c) 1024^3.

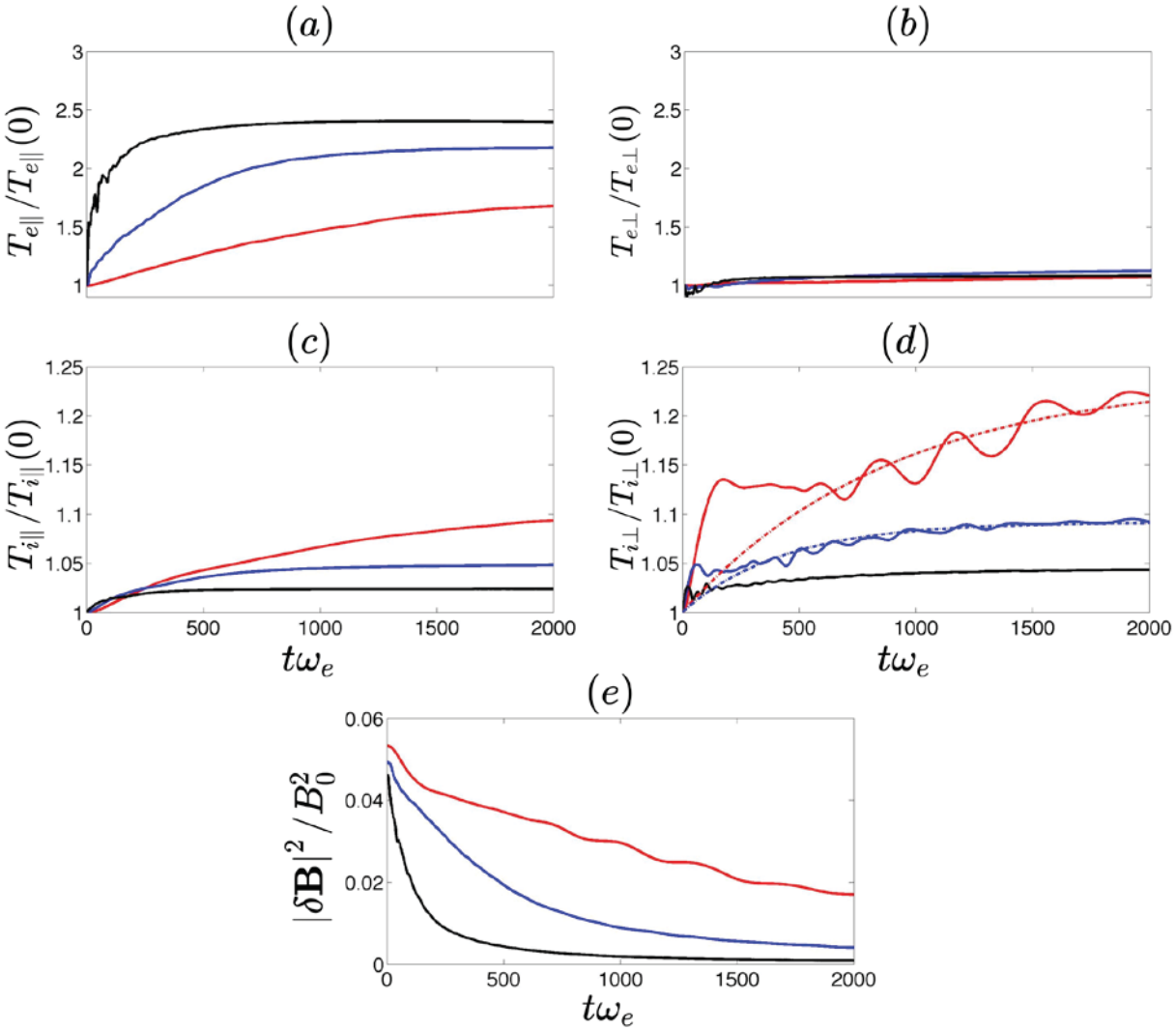

Figure 2: Simulation histories of the (a) parallel electron, (b) perpendicular electron, (c) parallel ion and (d) perpendicular ion temperatures as functions of time from the runs with 256^3 cells (black lines), 512^3 cells (blue lines), and 1024^3 cells (red lines). The dashed lines in panel (d) represent fits to the equation $y = 1 + a[1 - \exp(-bx)]$. (e) Time history of the total magnetic field fluctuation energy for the same three cases.

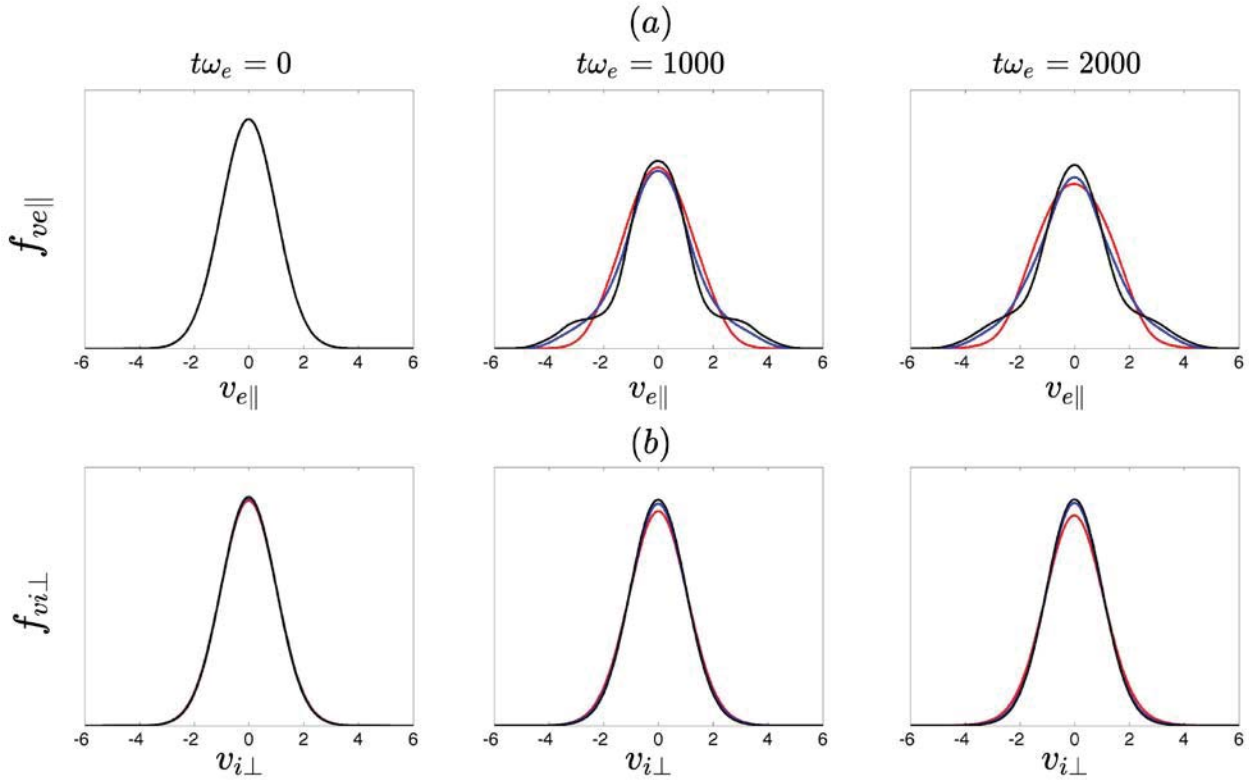

Figure 3: Reduced species velocity distributions at three simulation times. Upper row: electron parallel velocities, lower row: ion perpendicular component velocities. Results are from the runs with 256^3 cells (black lines), 512^3 cells (blue lines), and 1024^3 cells (red lines).

Estimating Source Rate Parameters of Outer Radiation Belt Electrons Using a Kalman Filter Variant: A Progress Report

Quintin Schiller

University of Colorado – Laboratory for Atmospheric and Space Physics, Boulder, CO 80303

Humberto Godinez

Los Alamos National Laboratory, Los Alamos, NM 87545

Abstract

We continue to explore the possibility of estimating source rate parameters of outer radiation belt electrons using a Kalman filter for timescales ~2 hours. We use a one dimensional radial transport equation with an electron phase space density dataset from the Van Allen Probes and THEMIS. Previously, we showed that some source rate parameters can be estimated accurately 'offline' with a simple optimization procedure. The 'offline' estimates are done by finding the minima of a cost function associated with the innovation vector rather than directly estimating the parameters as part of the data assimilation algorithm. Here, we find that the current innovation vector cost function is not a good estimator, and propose an algorithm as an alternative.

Keywords: Data assimilation, Space weather, Magnetospheric physics, Van Allen radiation belts

1. Introduction

Data assimilation procedures have been used to describe the phase space density (PSD) of the outer radiation belts [e.g. Koller et al., 2007]. Specifically, they combine observations of PSD with a one dimensional radial diffusion model to describe the PSD profile for the full radial range. However, data assimilation can be used to estimate state parameters as well, such as the source term of the radial diffusion equation.

The goal of this research is to characterize a Gaussian-shaped source rate term in a simple one-dimensional radial diffusion equation using data assimilation. Our approach is to minimize the innovation vector (y-Hx), where y is the observation vector, H maps the state space into the observational space, and x is the state vector. In this case, x is the phase space density as a function of radial distance and the observations are satellite particle measurements. The innovation vector represents physics that are missing from the physical model, and the theory is that changing state parameters to minimize the innovation vector is a way to estimate those state parameters. However, this method can require many different experiments to be run, since one has to try all the different state parameters to determine which set minimizes the innovation vector.

At the end of my last visit to Los Alamos (Schiller and Godinez, 2012; 2013), we had created a two-dimensional optimization technique to minimize the innovation vector in location,width space. We used a downhill simplex method known as the Nelder-Mead method (Nelder and Mead, 1965). The parameter space can be represented as a cost function

$$J(x,L,\sigma) = \| y - Hx \|_2 \quad (1)$$

where L and σ are the location and width of the source rate term, respectively. Using an optimization technique reduced the number of experiments required by over two orders of magnitude, making a much more efficient use of computation time.

This 2D optimization method was used to estimate the location and width of the source term then estimate the final source rate term parameter, its amplitude (A), directly using the data assimilation and an augmented state vector to include this parameter. However, it was found that the data assimilation had a lag of ~24 hours, and that estimating any state parameters as a direct output of the assimilation would not capture dynamics on timescales shorter than this. We decided to approach the problem by optimizing a three-dimensional cost function

$$J(x,L,\sigma,A) = \| y - Hx \|_2 \quad (2)$$

which would reduce the number of required experiments, from a brute-force full 3D mapping of the cost function, by many orders of magnitude.

2. Methodology

For this visit to Los Alamos, we extended the 2D optimization method to three dimensions. See below for examples. Investigation with simplified identical twin experiments showed that the 3D method was far less robust than the 2D method, as was expected with the inclusion of an additional dimension. Furthermore, the method is extremely sensitive to the initial parameter estimates made. As the method "walks" downhill, if the initial estimates are not on the downward slope to the global minimum, or if the estimates are separated enough in the parameter space that they do not sample the "valley" created by the global minimum, then the method fails to find the global minimum and the result is not close to the true parameter values. To account for this issue, we preconditioned the initial parameter estimates with a Gaussian fit to the radial PSD profile. We used the parameters from the fit to determine the initial estimates. Note on the below plot, the y-axis should read "Phase Space Density", and the x-axis "L".

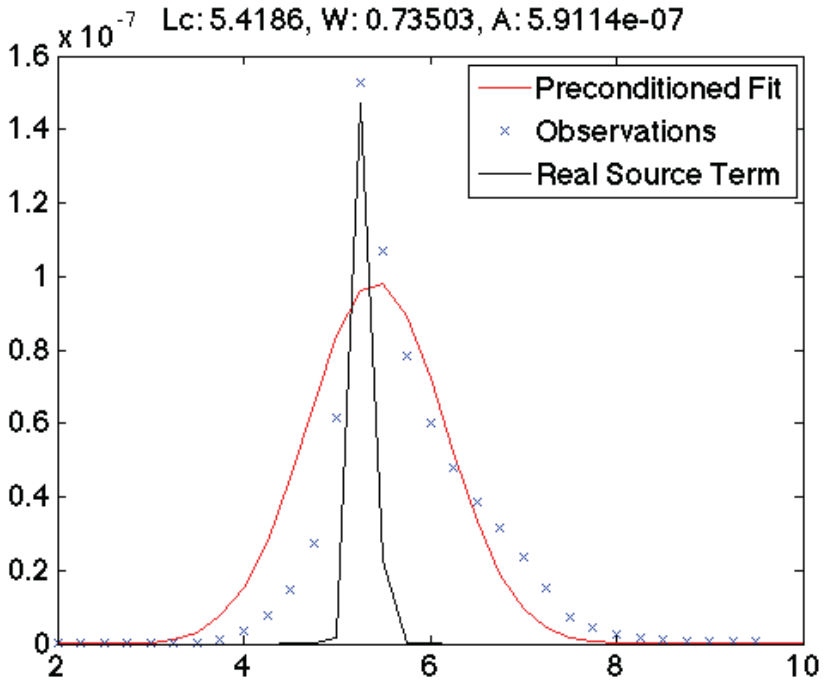

Figure 1: An example of preconditioning to determine the initial estimate for the 3D optimization. The black line is the actual source term over the period, the blue x's are the mean PSD within the period to be analyzed, the red curve is a Gaussian fit to the data, which amplitude, width, and location parameters (at top of the figure) are used to determine the initial parameter estimates for the source term. Notice that the fit Gaussian

does not do a good job of representing the actual source term. However, in general, it is sufficient to condition the initial estimates so that the optimization scheme is able to find the global minimum if it exists.

Using the 3D optimization scheme and preconditioned initial parameter estimates, we ran the method for a series of simplified identical twin experiments. For these experiments, we generated a PSD dataset with realistic loss and diffusion terms, which are Kp and Dst dependent, respectively. We created a simplified source term to include in the model. The full synthesized PSD dataset is depicted below. This dataset is sampled using a 5 spacecraft dataset to represent the Van Allen Probes (~1x6 R_E, 9 hour orbit) and three THEMIS spacecraft (~1x10 R_E, 12 hour orbit). The 'observations' are used in the data assimilation algorithm to attempt to recreate both the PSD for the full radial range as well as the Gaussian source rate term.

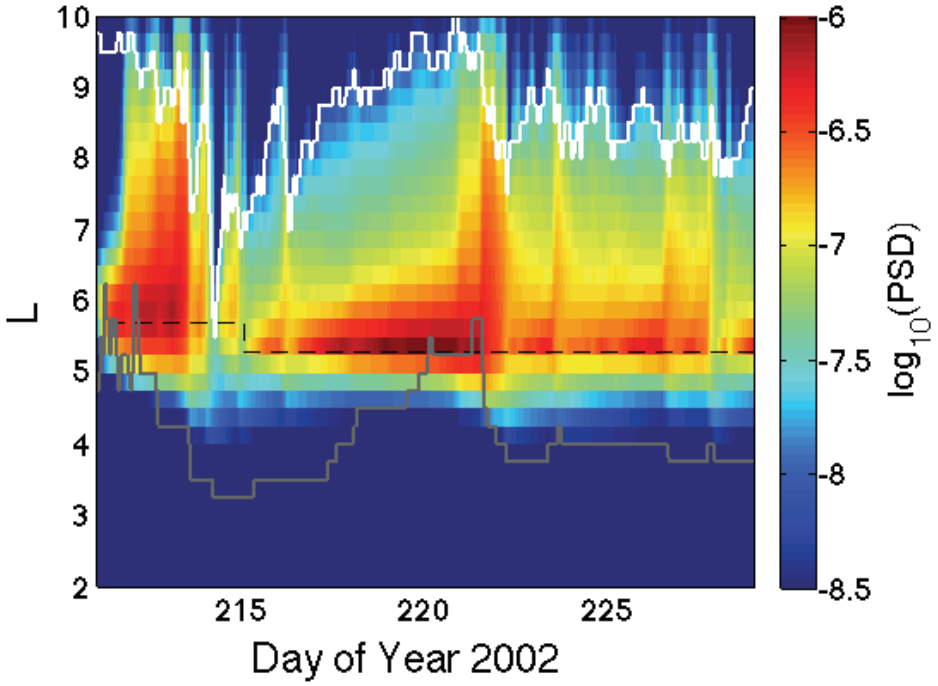

Figure 2: The synthesized PSD dataset. For reference, the last closed drift shell (as determined by Koller and Morley [2010]) is plotted in white, the plasmapause (as determined by O'Brien and Moldwin [2003]) is plotted in grey, and the source term center location in dashed black.

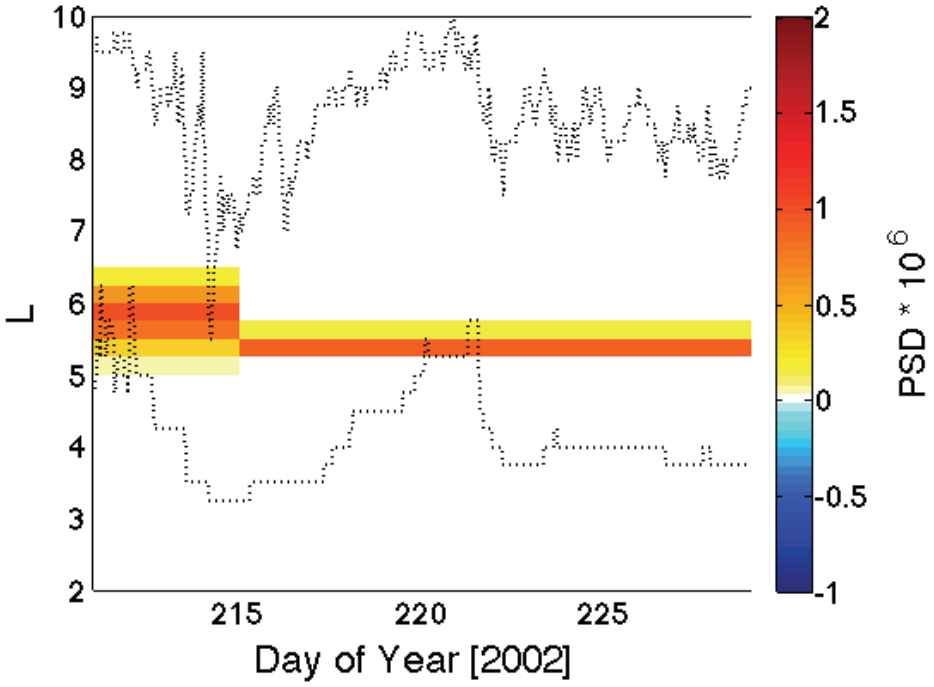

Figure 3: A visualization of the source term included in the PSD dataset. This source term is what this research is attempting to reproduce. The following analysis is focused on the step on DOY 215 from Lc=5.7, σ=0.3, A=1e-6 to Lc=5.3, σ=0.1, A=1e-6.

The 'observations' sample the synthesized dataset at a timescale of 4 minutes, and the filter assimilates the data at comparable timescales. This estimation method attempts to estimate the source term over timescales on the order of ~1 hour, comprising many observation and assimilation cycles. We can vary this period over which to estimate the source term to determine how many observations are required to gather enough information to accurately estimate the source term. The number of observations required depends on the number of dimensions to be estimated. Unfortunately, at least 3(6) hours of observations are required for the 2(3)D estimate, as presented below. In the Path Forward section, we discuss an idea to reduce the estimate timescale to an hour or less.

We assimilated the 'observations' in both the 3D and 2D algorithms to attempt to recreate the source term. All of the following 3D cost function optimization and 2D cost function figures begin on DOY 215, and finish 1-24 hours later, between DOY 215.042 to 216. The results, as explained later, show that the cost functions become more reliable with a longer time analyzed. Note that colorbar for these figures should read "Value of Innovation RMS". The initial parameter estimates are circled. The end criteria for the optimization is when the standard deviation of the most recent estimates fall below a certain threshold. These runs, this threshold is between 1e-13 and 5e-13.

3. Results

3.1. 3D Cost Functions

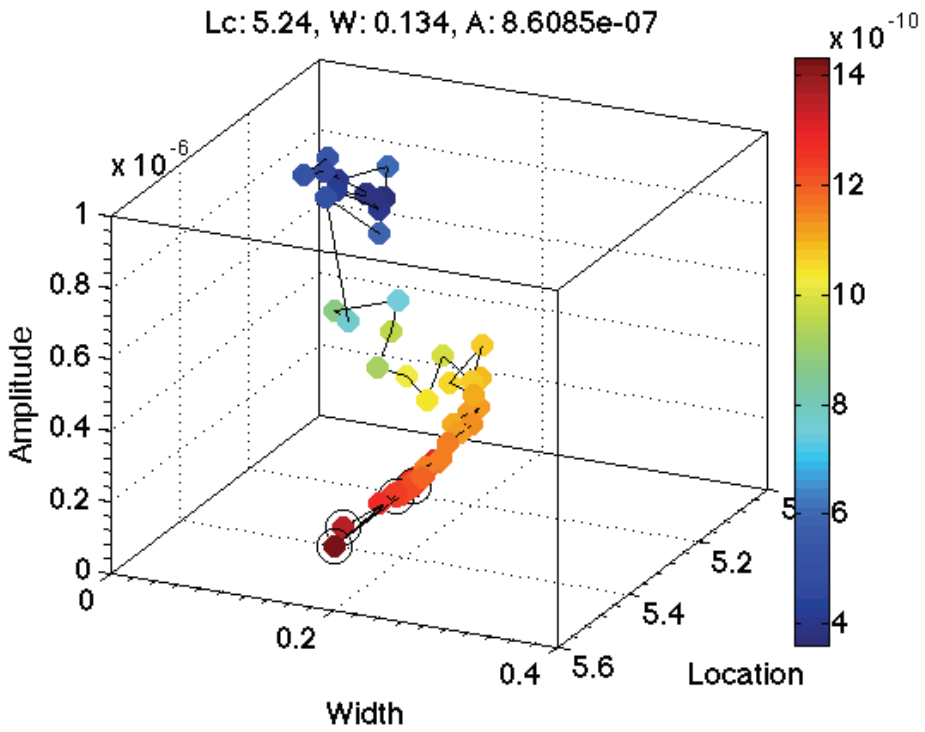

Figure 4: 3D optimization for a 24-hour period.

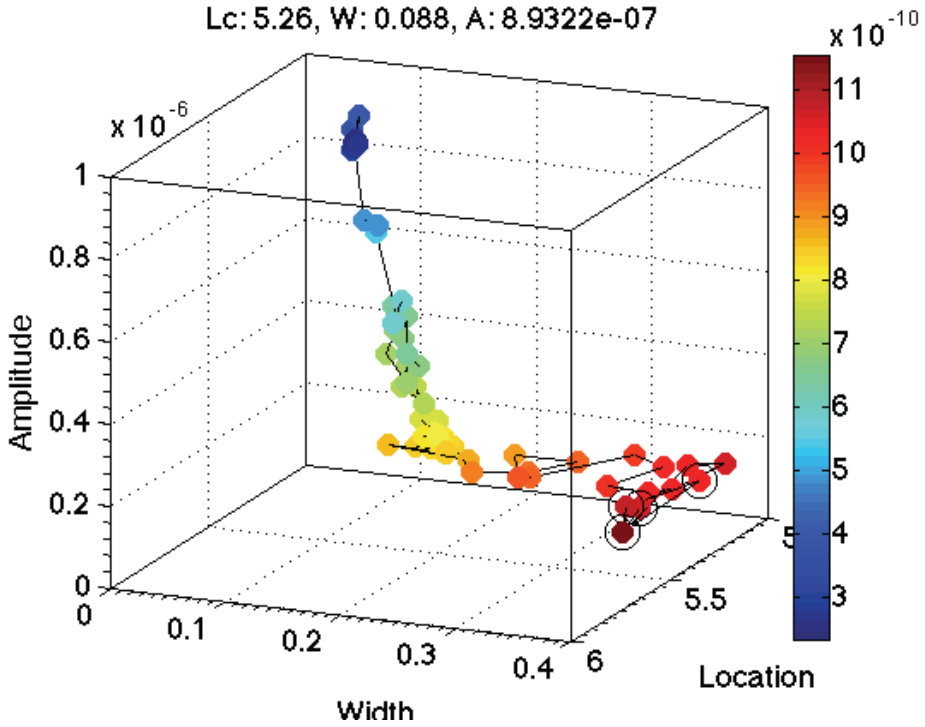

Figure 5: 3D optimization for a 12-hour period.

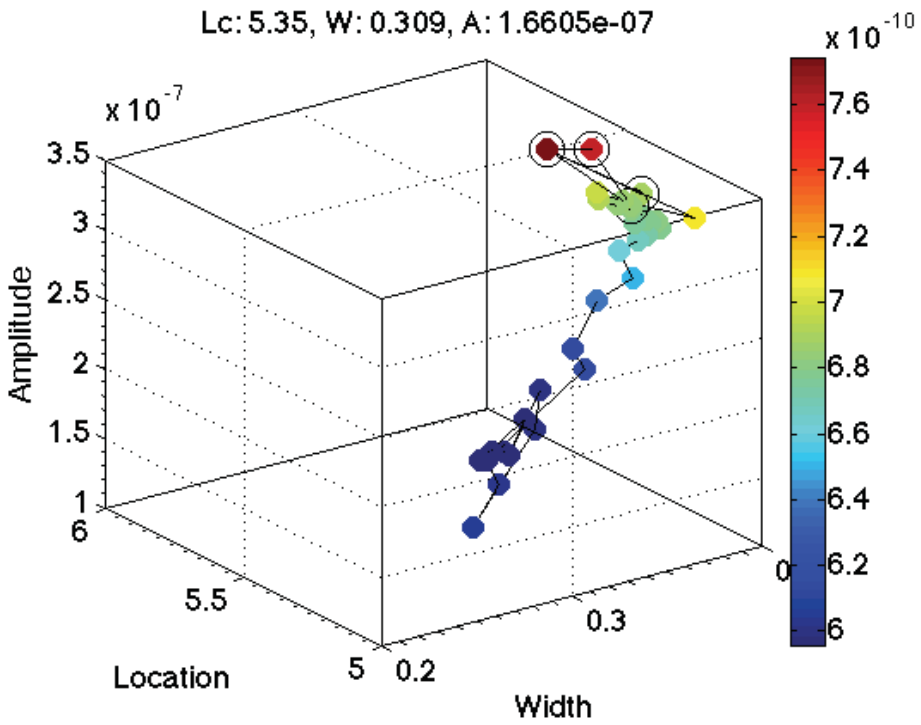

Figure 6: 3D optimization for a 6-hour period.

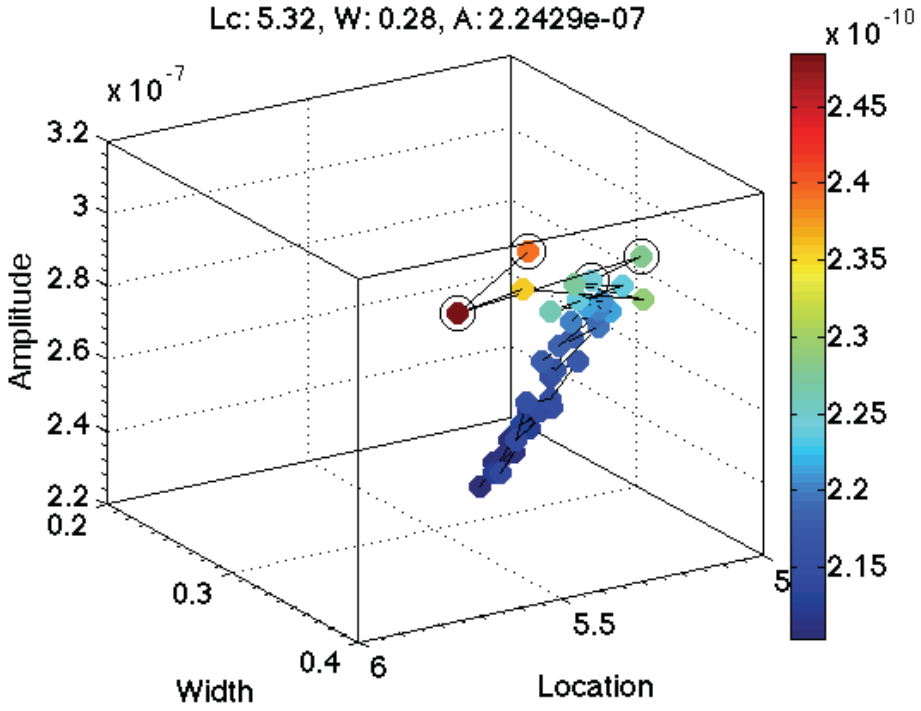

Figure 7: 3D optimization for a 4-hour period.

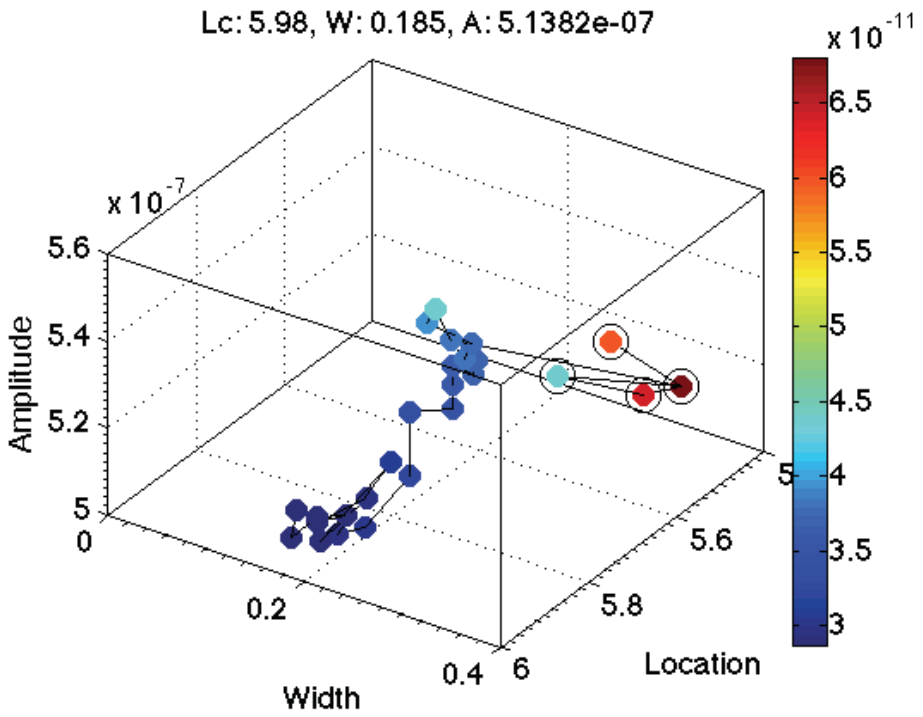

Figure 9: 3D optimization for a 2-hour period.

The previous figures show that the 3D optimization works well for the 12 and 24 hours periods. The method "walks downhill" to find the minimum of the cost function. However, it is not accurate in width or amplitude estimates for 6 or 4 hour periods, and does not estimate accurately at all for the 2 hour period. In short, the 3D cost function (equation 2) is not robust enough to provide an accurate global minimum without more than ~12 hours of data to assimilate. Unfortunately, visualizing the 3D cost function is difficult. In order to understand its behavior, we return to the 2D parameter space where visualizing the entire cost function is both visually and computationally easier.

3.2. 2D Cost Functions

We investigated the 2D cost functions in location-width space. Note that the color bar for these figures should read "Value of Innovation RMS" as the values are absolute, not relative. Furthermore, the parameter space was mapped at coarse resolution, since it's full mapping is computationally consuming. Odd, angular features in the visualizations, as well as imprecise estimates of the location and width, can be artifacts of the coarse resolution.

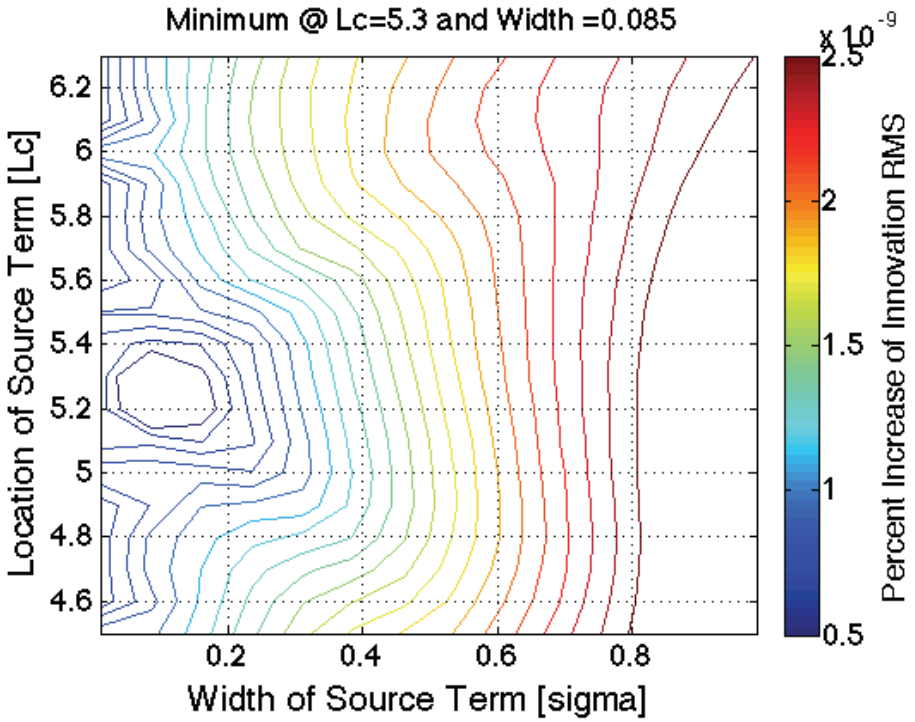

Figure 10: 2D cost function for a 12-hour period.

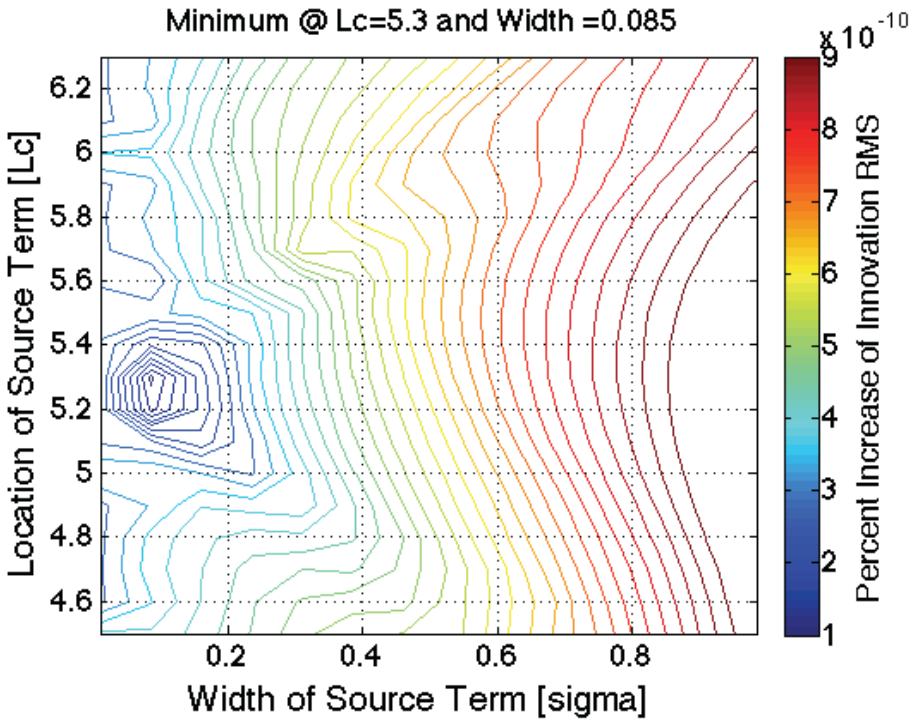

Figure 11: 2D cost function for a 4-hour period.

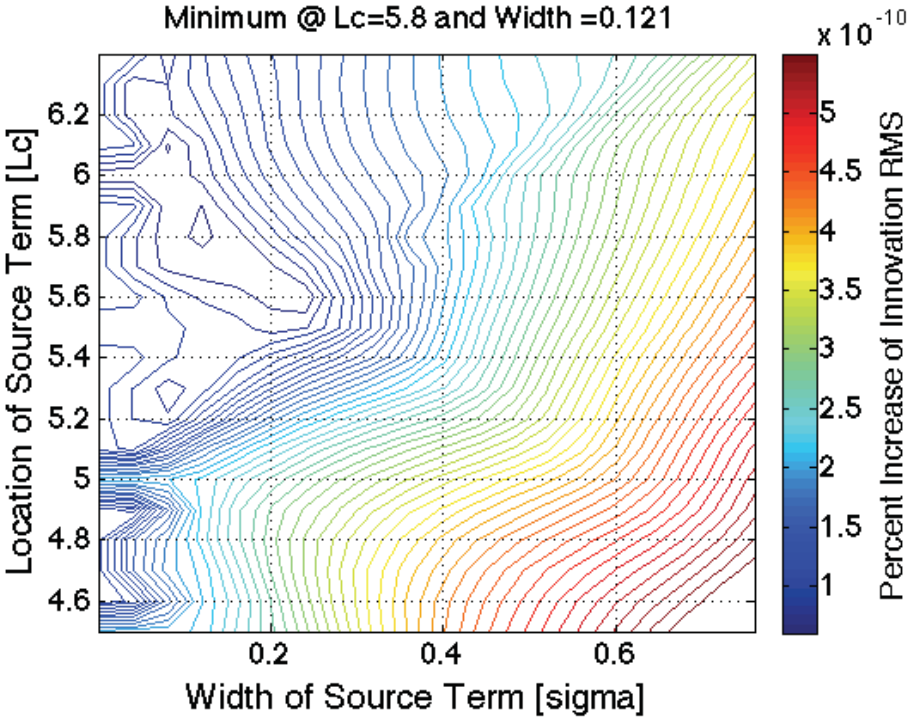

Figure 12: 2D cost function for a 3-hour period.

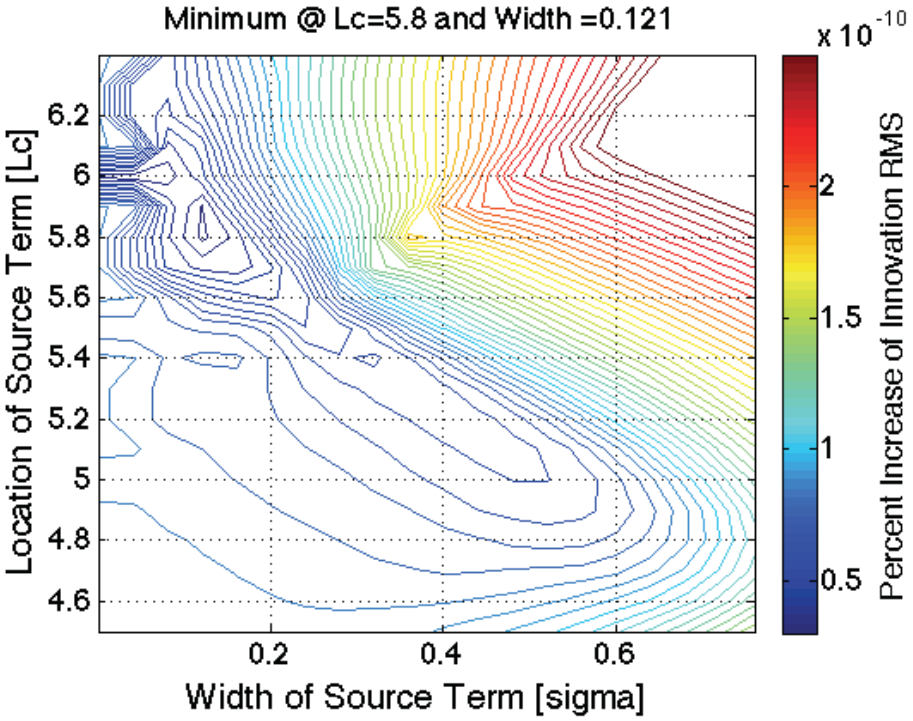

Figure 13: 2D cost function for a 2-hour period.

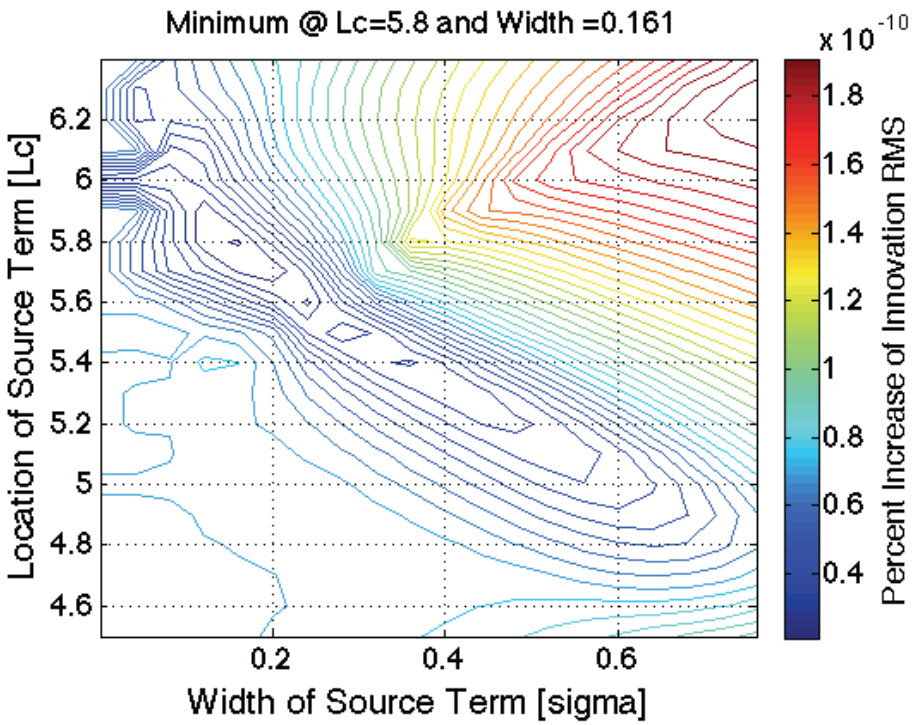

Figure 14: 2D cost function for a 1-hour period.

The 2D cost functions, as presented above, are unable to reproduce the correct source term with less than four hours of data assimilated into the model. As expected, the 2D cost functions are more robust than the 3D cost functions. However, the 2D method is still unable to account for physics occurring on realistic timescales (~1 hour). To address this issue, we have decided to adjust the method to utilize a simpler cost function, with the hope that it will remain robust on shorter timescales.

4. Conclusions and Future Work

With the knowledge that the 3D cost function for analysis is not able to accurately estimate state parameters without at least 6 hours of data assimilated in the Kalman filter, we have decided to change how we define the cost function. If we can create a cost function that has the minimum at the correct source term parameters on shorter timescales, then we can implement the existing optimization scheme.

The short-term path forward is to remove the data assimilation component of the cost function. Instead, of using the Kalman filter to advance the assimilated state to a future timestep (t → t+1) in which to determine the value of the cost function, we will run only the physical model forward. Then, at the future timestep (t+1), we compare the observations to the forecasted state to create the cost function. This method will have to be repeated many times to view the full 2D or 3D cost functions, but can be made more efficient using the optimization scheme to run the model forward for only a handful of different state parameter combinations. Once the correct location, width, and amplitude of the source term are determined through the global minimum in the cost function, then we assimilate the observations and forecasted state at t+1 to create an assimilated state.

In short:

1) Run physical model (1-D radial diffusion with loss + source) on x_a^t to x_f^{t+1}.

2) Determine cost: $J(x,L,sigma,A) = \| y^{t+1} - H\, x_f^{t+1} \|$ for all different L, sigmas and A's. This can be done initially in 2D space to view topography of cost function.

3) Do steps 1) and 2) for different lengths (i.e. 12, 6, 4, 2, 1 hours separating t and t+1) and see if the new cost function is robust at short timescales.

If the method is capable of estimating correct source terms on short timescales, the next steps would be:

4) Assimilate observations (y^{t+1}) and forecasted state (x_f^{t+1}) to create assimilated state (x_a^{t+1}).

5) Set t+1 to t and repeat by returning to step 1).

The idea behind the new method is to remove assimilation between the forecasted state and the observations. Our reasoning is that the data assimilation reduces the impact of the source term by modifying the state vector to conform to the observations. With an incorrect source term in the physical model, it will weight the observations more than the model, thus washing out or hiding the source term in the assimilation. By propagating the state vector forward using only the model, we hope to make the source term more obvious when the forecasted state is compared to the observations, in turn making the cost function more robust and hopefully improving our ability to estimate state parameters.

References

Koller, J., Y. Chen, G. D. Reeves, R. H. W. Friedel, T. E. Cayton, and J. A. Vrugt (2007), Identifying the radiation belt source region by data assimilation, J. Geophys. Res., 112, A06244, doi:10.1029/2006JA012196.

Koller, J., and S. K. Morley (2010), Magnetopause shadowing effects for radiation belt models during high-speed solar wind streams, Abstract SM13A-1787 presented at 2010 Fall meeting, AGU, San Francisco, Calif., 13-17 Dec.

Nelder, John A.; R. Mead (1965). "A simplex method for function minimization". *Computer Journal* **7**: 308–313. doi:10.1093/comjnl/7.4.308.

O'Brien, T. P., and . B. Moldwin (2003), Empirical plasmapause models from magnetic indices, *Geophys. Res. Lett.*, *30(4)*, 1152, doi:10.1029/2002GL016007.

Schiller, Q. and H. Godinez (2013), Determining source rate parameters of energetic electrons in the outer radiation belt using a Kalman filter, in Los Alamos Space Weather Summer School Research Reports, edited by J. Koller and R. D. Gurule, pp. 79-84, LA-UR 13-29060, Los Alamos, N.M.

Schiller, Q. and H. Godinez (2012), Determining source rate parameters of energetic electrons in the outer radiation belt using a Kalman filter, in Los Alamos Space Weather Summer School Research Reports, edited by J. Koller, J. R. Terry, and R. D. Gurule, pp. 51-67, LA-UR 13-23748, Los Alamos, N.M.

Los Alamos Space Weather Summer School
30 Bikini Atoll Rd, ISR-1, MS D466
Los Alamos, NM 87545

http://swx-school.lanl.gov